



THE HONG KONG
POLYTECHNIC UNIVERSITY

香港理工大學

Pao Yue-kong Library

包玉剛圖書館

Copyright Undertaking

This thesis is protected by copyright, with all rights reserved.

By reading and using the thesis, the reader understands and agrees to the following terms:

1. The reader will abide by the rules and legal ordinances governing copyright regarding the use of the thesis.
2. The reader will use the thesis for the purpose of research or private study only and not for distribution or further reproduction or any other purpose.
3. The reader agrees to indemnify and hold the University harmless from and against any loss, damage, cost, liability or expenses arising from copyright infringement or unauthorized usage.

IMPORTANT

If you have reasons to believe that any materials in this thesis are deemed not suitable to be distributed in this form, or a copyright owner having difficulty with the material being included in our database, please contact lbsys@polyu.edu.hk providing details. The Library will look into your claim and consider taking remedial action upon receipt of the written requests.

Pao Yue-kong Library, The Hong Kong Polytechnic University, Hung Hom, Kowloon, Hong Kong

<http://www.lib.polyu.edu.hk>

**PERFORMANCE OF FIBER REINFORCED POLYMER COMPOSITE
CONCRETE PILES IN MARINE SOILS ENDED IN ROCK SOCKETS
UNDER AXIAL CYCLIC AND STATIC LOADINGS**

NUMAN MALIK

PhD

The Hong Kong Polytechnic University

2024

The Hong Kong Polytechnic University

Department of Civil and Environmental Engineering

**Performance of Fiber Reinforced Polymer Composite Concrete Piles in
Marine Soils Ended in Rock Sockets under Axial Cyclic and Static Loadings**

Numan Malik

A thesis submitted in partial fulfilment of the requirements for the degree of

Doctor of Philosophy

November 2023

CERTIFICATE OF ORIGINALITY

I hereby declare that this thesis is my own work and that, to the best of my knowledge and belief, it reproduces no material previously published or written, nor material that has been accepted for the award of any other degree of diploma, except where due acknowledgement has been made in the text.

Signature:

Name: Numan MALIK

Abstract of thesis entitled

Performance of Fiber Reinforced Polymer Composite Concrete Piles in Marine Soils Ended in Rock Sockets under Axial Cyclic and Static Loadings

Traditional pile foundations in harsh marine environment experience steel corrosion, concrete deterioration, and timber degradation, resulting in various issues such as spalling, structural failure, and huge maintenance costs. Besides, consumption of large quantities of river sand and fresh water in the construction industry posing threat to river ecosystems, increased flooding events, and depletion of natural resources. Although seawater and sea-sand which are easily available at offshore construction projects provides an alternative solution, however traditional piling materials may experience corrosion and degradation issues with it due to salinity. The fact that fiber reinforced polymer (FRP) composites do not exhibit significant long-term degradation in typical marine environment makes it a promising alternative to steel as a reinforcing material in seawater sea-sand concrete (SSC). Therefore, replacing steel with FRP composites will be an advantageous approach.

Pile foundations are often subjected to cyclic loadings caused by wind, water currents, waves, earthquakes, traffic loads and ice sheets. For instance, offshore wind turbines generate millions of rotating blade cycles on supporting piles, and pile foundations supporting the transport system always experience significant axial cyclic loads. The cyclic behavior of piles is influenced by major cyclic loading parameters such as frequency, cyclic amplitude, mean load values, the number of cycles and loading history. Although numerous research works have been carried out on the cyclic response of piles in sand, silt and soft soils, the behavior of piles ended in rock-socket under cyclic loading, with emphasis on the shaft friction behavior, is rarely reported.

Apparently, it is necessary to deeply study cyclic loading influence on rock-socketed piles based on systematic tests to provide guidance and potential predictive measures.

Conventional measuring devices like strain gauges and vibrating wire extensometers provide discrete strain data at certain points leading to inadequate information of the entire pile's response. Fiber optic sensing techniques have overcome the limitations by providing distributed strain profiles, long sensing range choices, anti-corrosive, high spatial resolution, easy operation and installation, presenting a better pile monitoring solution.

Given the research limitations, this thesis reports a systematic study to investigate the performance of innovative and sustainable pile foundation design namely fiber reinforced polymer (FRP) composite seawater sea-sand concrete (SSC) piles in marine soils ended in rock sockets, through a series of physical model tests under axial cyclic and static loadings. A total of six model piles with three different structural configurations (FRP tube confined, FRP rebar cage reinforced, and centered FRP rebar reinforced) were tested. A novel hybrid optic sensing technique in which discrete (multiplexed FBGs) and distributed sensors based on optical frequency domain reflectometry (OFDR) with higher spatial resolution of 1mm and high sensing accuracy of $\pm 1\mu\epsilon$ were used to measure strain profiles along the entire length of model piles. The OFDR sensors monitor the distributed strain profiles providing load distribution of the entire pile, identifying any localized regions of weakness, strain concentrations, or pile shaft non-homogeneity with higher accuracy and hence overcoming the limitations of traditional monitoring sensors.

The main findings are listed as follows: (1) The pile head load-displacement response of different model piles presented a similar trend within a loading threshold and was different

(hardening or softening) beyond a transition point. The FRP tube confined pile showed higher ductility and capacity comparatively, suggesting the best solution for field applications in terms of mechanical performance. (2) The strain distribution along the depth of piles showed a similar trend for the model piles with higher strains recorded in the region $(0 - l_d/4)$ from the pile head. The failure of FRP tube confined and centered FRP rebar reinforced SSC piles happened within this region near the pile head. However, the FRP rebar cage reinforced SSC pile showed the maximum deformation in the same region near the pile head and rock surface. (3) The pile body gained cyclic stiffness when the maximum cyclic load level $(Q_{mean} + Q_{cyc})$ was below 30% of Q_{us} , and degradation was observed under higher load conditions. (4) The axial strain profiles within rock-socket were utilized to develop load transfer curves to calculate reliable shaft friction values that may be used in future pile design of similar conditions. (5) The maximum shaft resistance was mobilized up to 4.5 MPa under cyclic loading in the rock socket with higher mobilization observed in the upper one-third region of the socket. The conventional design underestimates the shaft friction along the interface between the rock and the model pile. (6) The distributed circumferential strain profiles provided reliable information of the localized strain concentrations around the pile circumference, showing early detection of pile shaft cracks, lateral deformation, bending direction, and position accurately. (7) The predicted buckling load based on analytical solutions and actual buckling load from tests were in fair agreement with a minor discrepancy due to localized strains near the pile head.

LIST OF PUBLICATIONS DURING THE CANDIDATURE

Journal Papers

Chen, Z., Chen, W. B.*, Yin, J. H., & **Malik, N.** (2021). Shaft friction characteristics of two FRP seawater sea–sand concrete piles in a rock socket with or without debris. *International Journal of Geomechanics*, 21(7), 06021015.

PC Wu, DY Tan, WB Chen, **N Malik**, JH Yin. (2021). Novel fiber Bragg Grating-based strain gauges for monitoring dynamic responses of *Celtis sinensis* under typhoon conditions *Measurement* 172, 108966

P Wu, D Tan, S Lin, W Chen, J Yin, **N Malik**, A Li. (2022). Development of a monitoring and warning system based on optical fiber sensing technology for masonry retaining walls and trees. *Journal of Rock Mechanics and Geotechnical Engineering* 14 (4), 1064-1076

N Malik; W.B Chen; Chen Z; P Wu; JH Yin. (2023). Axial cyclic and static behavior of FRP composite seawater sea-sand concrete piles ended in rock socket. *ASCE's Journal of Geotechnical and Geoenvironmental Engineering*, 10.1061/JGGEFK/GTENG-11529,

N Malik; W.B Chen; P Wu; Chen Z; JH Yin. (2023). Axial and circumferential behavior of rock-socketed FRP-SSC composite piles monitored by distributed optical fiber sensors. *ASCE's Journal of Geotechnical and Geoenvironmental Engineering*, (under review).

Conference papers

N Malik, JH Yin, WB Chen, PC Wu, Z Chen. (2023). Axial Cyclic Behavior of FRP Confined Seawater Sea-Sand Concrete Piles. *ASCE's Geo-Risk 2023*, 366-373

ACKNOWLEDGEMENTS

First and most importantly, I would like to express my heartfelt gratitude and appreciation to my chief supervisor, Chair Professor Jian-Hua Yin, for his enlightening guidance, supervision, and endless support throughout my doctoral study. I am especially thankful to Professor Yin for giving me this unique opportunity to achieve my goals and provide me with his vision, encouragement, patience, and determination throughout these years. I feel privileged to have worked under his supervision and looking forward to implementing my knowledge and experience in future career goals.

I would like to acknowledge my senior colleague, Professor Wen-Bo Chen, for his guidance, patience, and support throughout my candidature. I wish to express my appreciation to my co-supervisor, Professor Zhen-Yu Yin for his enlightenment and encouragement. I am also grateful to my senior colleagues Dr. Wu Peichen, Dr. Ze-Jian Chen, and Dr. Dao-Yuan Tang for their support and guidance in my research work. Many thanks to Dr Lin Shaoqun for his help in fibre optic sensors data analysis. I would also like to thank Mr David Leung, Mr C. K. Leung, Fion Cheng, and Mr Raymond Leung for their help in my experimental works. I would like to acknowledge the board of examiners, for spending their precious time to provide constructive comments and review this thesis thoroughly.

Finally, I would like to express my deepest gratitude to my late father for his utmost support of my career pursuits and life goals. His mentorship, life vision, and invaluable experiences helped me to pursue my dreams and ambitions. I am also grateful to my late mother who endured great hardships in raising and nurturing me to achieve my academic dreams. I would like to thank my other family members for their support and all my friends for their encouragement throughout this journey.

TABLE OF CONTENTS

CHAPTER 1: INTRODUCTION	1
1.1 Background and significance of the study	1
1.2 Research objectives	7
1.3 Methodology	8
1.4 Thesis organization	9
CHAPTER 2: LITERATURE REVIEW	12
2.1 Introduction	12
2.2 Types of pile foundations	13
2.2.1 Based on load carrying mechanisms.....	13
2.2.2 Based on pile functions.....	14
2.2.3 Based on installation techniques.....	16
2.2.4 Types of piles based on materials used for construction.....	17
2.2.5 Composite piles.....	19
2.3 Behavior of FRP composite concrete piles	22
2.3.1 Structural behavior of FRP composite concrete piles under axial loads.....	22
2.3.2 Structural behavior of FRP composite concrete piles under flexural loads	23
2.3.3 Geotechnical behavior of FRP composite concrete piles.....	24
2.3.4 Interface mechanism of FRP composites and soil	24

2.3.5	Confinement mechanism of FRP composites	25
2.4	Axial cyclic behavior of rock-socketed piles	26
2.4.1	Cyclic loads and its influence on piles.....	26
2.4.2	Design of rock-socketed piles.....	27
2.4.3	Negative shaft friction (NSF) mobilization on piles in consolidating soft soils.....	29
2.5	Applications of fiber optic sensors in geotechnical engineering systems	29
2.5.1	Conventional strain measuring instrumentations.....	29
2.5.2	Fiber optic sensors and its classification.....	30
2.5.3	Distributed fibre optic sensing and its applications in geotechnical engineering...	30
2.6	Summary	32
CHAPTER 3: PHYSICAL MODEL PILE SYSTEM, MATERIALS, AND INSTRUMENTATIONS.....		43
3.1	Introduction	43
3.2	Design and setup of the physical model pile system.....	43
3.3	FRP composites.....	44
3.3.1	FRP tubes and rebars.....	44
3.3.2	Compression tests results.....	45
3.4	Seawater sea-sand concrete (SSC)	45
3.4.1	Seawater and sea-sand basic properties	45
3.4.2	SSC unconfined compression tests.....	46

3.5	Hong Kong marine deposits (HKMD)	47
3.5.1	Basic physical properties	47
3.5.2	Oedometer tests.....	47
3.5.3	Triaxial tests	49
3.6	Granite rock-socket and gypsum plaster	50
3.6.1	Rock socket design and roughness	50
3.6.2	Uniaxial compression strength (UCS) tests	50
3.7	Instrumentations	51
3.7.1	Distributed OFDR sensing.....	51
3.7.2	Multiplexed FBGs sensors.....	53
3.7.3	Conventional electronic transducers.....	53
3.8	Summary	54
CHAPTER 4: CYCLIC BEHAVIOR OF THE FRP-SSC MODEL PILES ENDED IN ROCK-SOCKET		78
4.1	Introduction	78
4.2	Model piles preparation and setup	78
4.2.1	Model piles design and installation.....	78
4.2.2	Installation and instrumentation of FBG and OFDR sensors	80
4.3	Cyclic loading testing program	81
4.4	Results and discussion of cyclic stiffness of model piles	83

4.4.1	Cyclic stiffness data analysis	83
4.4.2	Cyclic stiffness of model pile 2	83
4.4.3	Cyclic stiffness of model pile 3	85
4.4.4	Cyclic stiffness of model pile 4 and 5.....	86
4.4.5	Cyclic stiffness of model pile 6	87
4.4.6	Cyclic stiffness of piles in rock-socket section.....	89
4.5	Accumulated deformation results of model piles during cyclic loading	90
4.5.1	Accumulated compression of pile body during cyclic loading.....	90
4.5.2	Permanent accumulated deformation of piles in rock socket section.....	91
4.5.3	Compression of the Pile Section in the Rock Socket during Cyclic Loading	91
4.6	Mobilization of shaft friction under cyclic loadings.....	92
4.7	Summary	95
 CHAPTER 5: STATIC BEHAVIOR OF FRP-SSC MODEL PILES ENDED IN ROCK SOCKET		126
5.1	Introduction	126
5.2	Preliminary elementary tests.....	126
5.2.1	Short columns tests	126
5.2.2	Test setup and instrumentations	127
5.2.3	Compressive strength.....	128
5.2.4	Failure modes.....	129

5.2.5	Axial and lateral stress-strain responses	130
5.3	Model piles static behaviour.....	131
5.3.1	Load-compression response of model piles under static loading	131
5.3.2	Tangent modulus variation of model piles.....	132
5.3.3	Comparison of static behavior of model piles before and after cyclic loading	133
5.4	Axial strain distributions measured with FBGs sensors and failure modes of piles under static loading.....	134
5.4.1	Axial strain distribution along depth of Pile 2	134
5.4.2	Axial strain distribution along depth of Pile 4 and 5	134
5.4.3	Axial strain distribution along depth of Pile 3	135
5.4.4	Failure modes of the model piles under static loading	136
5.5	Shaft friction mobilization of model piles under static loading	136
5.5.1	Shaft friction data interpretation and analysis	136
5.5.2	Mobilized shaft friction in the rock socket of Pile 2.....	138
5.5.3	Mean shaft friction and end bearing of Pile 2.....	139
5.5.4	Mobilized shaft friction in the rock socket of Pile 3.....	139
5.5.5	Mean shaft friction and end bearing of Pile 3.....	140
5.6	Summary.....	141
CHAPTER 6: BEHAVIOUR OF FRP-SSC MODEL PILE IN MARINE SOILS INSTALLED IN ROCK-SOCKET		162

6.1	Introduction	162
6.2	Model pile setup and instrumentations	162
6.2.1	Model pile setup.....	162
6.2.2	Instrumentations.....	163
6.3	Bottom layer HKMD preparation and pre-consolidation results	166
6.3.1	Bottom layer HKMD preparation	166
6.3.2	Pre-consolidation loading system setup and loading program	167
6.3.3	Responses of transducers during pre-consolidation of HKMD	168
6.3.4	Settlement during multi-stage pre-consolidation	169
6.4	Upper layer HKMD preparation and pre-consolidation results.....	169
6.4.1	Upper layer HKMD preparation	169
6.4.2	Pre-consolidation loading system setup and loading program	170
6.4.3	Responses of transducers during pre-consolidation of HKMD	170
6.4.4	Settlement during multi-stage pre-consolidation	172
6.4.5	Review of simplified Hypothesis B method for soft soils under multi-stage loading and unloading.....	172
6.5	Response of both HKMD layers under Consolidation loading	175
6.5.1	Consolidation loading program.....	175
6.5.2	Porewater pressure and vertical stress	175
6.5.3	Settlement of upper and bottom HKMD layers during consolidation	177

6.6 Summary 180

CHAPTER 7: DISTRIBUTED FIBER OPTIC SENSING FOR PILE MONITORING 202

7.1 Introduction 202

7.2 Comparison of axial strain from optic fiber sensing (FBG and OFDR) and conventional LVDTs..... 202

7.2.1 Installation and instrumentation of OFDR optic fibers and FBGs in the model piles
202

7.2.2 Comparison of OFDR and FBG strain profiles of Pile 2..... 205

7.2.3 Comparison of integrated axial strain from OFDR and FBGs with LVDTs for Pile 2
205

7.2.4 Comparison of OFDR and FBG strain profiles of Pile 3..... 206

7.2.5 Comparison of integrated axial strain from OFDR and FBGs with LVDTs for Pile 3
206

7.3 Comparison of axial strain distribution along the depth of model piles from different OFDR fiber sections..... 207

7.3.1 Axial strain profiles from different OFDR fiber sections of Pile 2 207

7.3.2 Comparison of axial strain distribution at peak load of pile 2..... 208

7.3.3 Axial strain profiles from different OFDR fiber sections of Pile 3 208

7.3.4 Comparison of axial strain distribution at peak load of pile 3..... 209

7.4	Comparison of circumferential strain distribution of model piles from different OFDR fiber sections.....	210
7.4.1	Circumferential strain distribution from different OFDR fiber sections of Pile 2	210
7.4.2	Circumferential strain distribution from different OFDR fiber sections of Pile 3	212
7.5	Analysis of axial and circumferential strain localizations in relation to failure mode of model piles.....	213
7.5.1	Comparison of axial and circumferential strain localizations with failure mode of Pile 2	213
7.5.2	Comparison of axial and circumferential strain localizations with failure mode of Pile 3	214
7.6	Comparison with analytical solutions	214
7.7	Summary	217
CHAPTER 8: CONCLUSIONS AND RECOMMENDATIONS.....		238
8.1	Conclusions	238
8.1.1	Axial cyclic stiffness of model piles	239
8.1.2	Static axial behavior of model piles under static loading	240
8.1.3	Strain profiles measured with OFDR and FBG optic sensors comparison.....	241
8.1.4	Shaft friction mobilization in rock-socket	242
8.1.5	Settlement response due to consolidation of HKMD	243
8.2	Recommendations and future studies	243

8.2.1	Behavior of model piles under lateral loading.....	243
8.2.2	NSF for FRP tube confined model pile.....	244
8.2.3	Machine learning methods for interpretation of OFDR distributed monitoring data	
	244	
List of notations and abbreviations.....		255
REFERENCES.....		258

LIST OF FIGURES

Figure 1.1 An overview of the research in this thesis	11
Figure 2.1 Illustration of friction and end bearing pile (dreamcivil.com)	35
Figure 2.2 Illustration of Anchor and fender pile (dreamcivil.com).....	35
Figure 2.3 Driven steel piles in the ground at site	36
Figure 2.4 Bored piling mechanism and machinery (www.skanska.co.uk).....	36
Figure 2.5 Offshore concrete piles (pilebuck.com)	37
Figure 2.6 Group of offshore H shaped steel piles (morrisshea.com)	37
Figure 2.7 Group of driven timber piles in ground (weekesforest.com)	38
Figure 2.8 Composite marine piles (Iskander and Hassan, 1998)	38
Figure 2.9 Stress-strain curve for FRP confined concrete (Saafi et al., 1999).....	39
Figure 2.10 Four-point bending test of FRP composite concrete beam (Fam et al., 2003)	39
Figure 2.11 Cyclic behavior of prestressed and FRP composite pile (Fam et al., 2003).....	40
Figure 2.12 Soil interface responses (Shaia, 2013).....	41
Figure 2.13 Illustration of Confining effect of FRP composites (Shaia, 2013)	41
Figure 2.14 Typical cyclic loading characteristics (ANDERSEN, 2013).....	42
Figure 3.1 Design and photo of the physical model pile system: (a) photo and (b) illustraion....	60

Figure 3.2 Photos of the physical model piles: (a) Pile 1 or 2; (b) Pile 3; (c) Pile 4 or 5; and (d) Pile 6	62
Figure 3.3 GFRP short tubes under compression	62
Figure 3.4 Particle size distribution curves of washed and unwashed sea-sand.....	63
Figure 3.5 Stress-strain curves of measured data, fitting, and Et of SSC	63
Figure 3.6 Variation of vertical strain with time for S1 specimen: (a) loading; (b) unloading (U1 represents the first unloading stage); (c) reloading (R1 represents the first reloading stage); (d) effect of unloading; and (e) effect of reloading (Wu, 2021)	66
Figure 3.7 Variation of vertical strain with time for S2 specimen: (a) loading; (b) unloading (U1 represents the first unloading stage); (c) reloading (R1 represents the first reloading stage); and (d) effect of unloading (Wu, 2021)	69
Figure 3.8 Variation of vertical strain with time for S3 specimen: (a) loading; (b) unloading (U1 represents the first unloading stage); (c) reloading (R1 represents the first reloading stage); and (d) effect of unloading (Wu, 2021)	71
Figure 3.9 Creep response prediction through linear fitting of ψ/V : (a) S1; (b) S2; and (c) S3 (Wu, 2021)	74
Figure 3.10 Triaxial tests results: (a) deviator stress variation with axial strain; (b) porewater pressure variation with axial strain; and (c) effective stress paths from consolidated undrained tests (Wu, 2021)	75
Figure 3.11 Granite rock-socket design	76

Figure 3.12 Plot of axial stress versus axial strain of UC tests on rock specimens	76
Figure 3.13 OFDR sensing principle	77
Figure 3.14 FBG sensing principle	77
Figure 4.1 Cross-section illustrations of (a) vertical profile of Piles 1 and 2; (b) horizontal profile of Piles 1 and 2.....	101
Figure 4.2 Cross-section illustrations of: (a) vertical profile of Pile 3 or 6 (note: Pile 6 is surrounded by 106 cm HKMD inside tank); and (b) horizontal profile of Pile 3 or 6	102
Figure 4.3 Cross-section illustrations of: (a) vertical profile of Pile 4 or 5; and (b) horizontal profile of Pile 4 or 5	103
Figure 4.4 Schematic illustration of loading program	104
Figure 4.5 Variation of pile body stiffness of pile 2 under different cyclic loading series: (a) Series 1; (b) Series 2; (c) Series 3; (d) Series 4; and (e) Series 5	109
Figure 4.6 Variation of cyclic stiffness of Pile 3 under different cyclic loadings: (a) Series 1 and 2; (b) Series 3, 4, and 5; and (c) Series 6 and 7	113
Figure 4.7 Variation of cyclic stiffness of (a) Pile 4 and (b) Pile 5 under cyclic loading	114
Figure 4.8 Variation of cyclic stiffness of Pile 6 under different cyclic loadings: (a) Series 1; (b) Series 2 ; (c) Series 3; and (d) Series 4	118
Figure 4.9 Stiffness variation of the socket under different series of cyclic loadings	119
Figure 4.10 Compression accumulation within pile body under different cyclic loading conditions	120

Figure 4.11 Accumulated compression of Pile 2 within the rock socket under cycling loadings	121
Figure 4.12 Compression of model pile within the socket recorded at static loading and cyclic maximum loading conditions.....	122
Figure 4.13 Mobilization of shaft friction and displacement along depth for different loading cycles on Pile 3: (a) 60-60; (b) 120-60; and (c) 120-90.....	125
Figure 5.1 Short column specimens.....	143
Figure 5.2 (a) Test setup and (b) schematic view of the tested GFRP confined SSC cylinders .	144
Figure 5.3 Stress-strain curves of the different short column specimens	145
Figure 5.4 Mean compressive strengths of the cylinders.....	145
Figure 5.5 Failure modes of the specimens under axial compression: (a)vertical and diagonal cracks; (b) vertical cracks; (c) failure due to buckling of FRP tube; and (d) failure due fibers delamination.....	146
Figure 5.6Axial and lateral strain responses of different cylinders: (a) plain SSC cylinder; (b) SSC with GFRP rebar; (c) GFRP confined SSC cylinder; and (d) GFRP confined SSC cylinder with rebar	149
Figure 5.7 Lateral strain-axial strain responses of the unconfined and confined concrete.....	149
Figure 5.8 Static pile head load-pile body compression relationship of five FRP-SSC model piles	150
Figure 5.9 Tangent modulus versus pile body compression of four FRP-SSC model piles	151

Figure 5.10 Static pile head load-pile body compression relationships of (a) Pile 2, (b) Pile 3, and (c) Pile 4 before and after maximum cyclic loading.....	152
Figure 5.11 Static pile head load-pile compression in rock socket relationships before and after maximum cyclic loading.....	153
Figure 5.12 Strain distribution along the depth of (a) Pile 2, (b) Pile 3, and (c) Pile 5	155
Figure 5.13 Failure modes of FRP-SSC model piles under static loading: (a) Pile 2, (b) Pile 3, and (c) Pile 4	156
Figure 5.14 Shaft friction profiles of Pile 2 calculated from OFDR fiber section data under different loading levels	157
Figure 5.15 Socket response of Pile 2: (a) mean shaft friction and end bearing pressure against applied load, and (b) shaft and base resistance against displacement	158
Figure 5.16 Shaft friction profiles of Pile 3 calculated from OFDR fiber section data under different loading levels	159
Figure 5.17 Socket response of Pile 3 under static loading: (a) mean shaft friction, end bearing and resistance percentage against static load and (b) shaft resistance and base resistance against displacement	161
Figure 6.1 Model pile setup and instrumentation	181
Figure 6.2 Photo of physical model pile and setup.....	182
Figure 6.3 Air cylinders assembly and layout.....	183
Figure 6.4 Photo of air cylinders layout in the physical model	184

Figure 6.5 Porewater pressure transducer protective cotton covering	184
Figure 6.6 Bottom HKMD layer transducers layout.....	185
Figure 6.7 Photo after filling the first layer of HKMD slurry	185
Figure 6.8 PVD band and aluminum mandril.....	186
Figure 6.9 Photo after installing the PVDs	186
Figure 6.10 PVDs layout in the physical model	187
Figure 6.11 Geotextile layer.....	188
Figure 6.12 Pre-consolidation loading setup	189
Figure 6.13 (a) Floating settlement plate design and (b) PPTs and EPCs layout	190
Figure 6.14 Porewater pressure variation at the bottom of tank during pre-consolidation measured with different PPTs	191
Figure 6.15 Porewater pressure variation at the wall of tank during pre-consolidation measured with different PPTs.....	192
Figure 6.16 Vertical stress variation at the bottom of tank during pre-consolidation measured with EPC	192
Figure 6.17 Measured settlement at the surface of bottom layer by LVDTs	193
Figure 6.18 Porewater pressure variation at interface of upper and bottom HKMD layers during pre-consolidation measured with different PPTs	194

Figure 6.19 Porewater pressure variation at the bottom of tank during pre-consolidation measured with different PPTs	194
Figure 6.20 Porewater pressure variation at the wall of tank during pre-consolidation measured with different PPTs.....	195
Figure 6.21 Vertical stress variation at the bottom and interface of upper and bottom HKMD layers during pre-consolidation measured with EPCs	196
Figure 6.22 Measured settlement at the surface of upper layer by LVDTs.....	196
Figure 6.23 Applied surcharge loading for consolidation of HKMD	197
Figure 6.24 Porewater pressure variation at interface of upper and bottom HKMD layers during consolidation measured with different PPTs.....	198
Figure 6.25 Porewater pressure variation at the bottom of tank during consolidation measured with dif.....	198
Figure 6.26 Porewater pressure variation at the wall of tank during consolidation measured with different PPTs.....	199
Figure 6.27 Vertical stress variation at the bottom and interface of upper and bottom HKMD layers during consolidation measured with EPCs.....	200
Figure 6.28 Measured settlement at the surface and interface of upper and bottom HKMD layers by floating settlement plates	201
Figure 6.29 Drag force development at different consolidation loadings along the depth of pile	Error! Bookmark not defined.

Figure 7.1 Cross-section illustrations of Pile 2: (a) vertical profile, (b) horizontal profile	219
Figure 7.2 Cross-section illustrations of Pile 3: (a) vertical profile, (b) horizontal profile	220
Figure 7.3 Comparison of axial strain distribution of Pile 2 measured from OFDR and FBGs.	221
Figure 7.4 Overall integrated axial strain of Pile 2 from measured results from OFDR and FBGs versus the overall strain results from LVDT	222
Figure 7.5 Comparison of axial strain distribution of Pile 3 measured from OFDR and FBGs.	223
Figure 7.6 Pile 3 Overall integrated axial strain from measured results from OFDR and FBGs versus the overall strain results from LVDT	224
Figure 7.7 Axial strain distribution of Pile 2 monitored with different OFDR fiber sections under different loading levels: (a) S1, (b) S9, (c) S11, and (d) S12	226
Figure 7.8 Axial strain profile of Pile 2 monitored with different fiber sections under peak load of 266 kN.....	227
Figure 7.9 Axial strain distribution of Pile I under different loading levels monitored with different OFDR fiber sections: (a) S1, (b) S4, (c) S5, and (d) S6.....	229
Figure 7.10 Axial strain profile of Pile 3 monitored with different fiber sections under peak load of 213 kN	229
Figure 7.11 Circumferential strain distribution of Pile 2 monitored with different OFDR optic fibers at different loading levels; (a) S8; (b) S7; (c) S5; and (d) S2	232
Figure 7.12 Circumferential strain distribution of Pile 3 monitored with different OFDR optic fibers at different loading levels; (a) S8; (b) S9; (c) S12; and (d) S14	234

Figure 7.13 Comparison of axial and circumferential strain profiles of Pile 2 with final failure shape and buckling mode..... 235

Figure 7.14 Comparison of axial and circumferential strain profiles of Pile 3 with final failure shape and buckling mode..... 236

Figure 7.15 Partially embedded pile system: (a) actual pile, and (b) equivalent system based on (after Heelis et al., 2004)..... 237

LIST OF TABLES

Table 2.1 FRP composites confined concrete existing numerical models (Shaia, 2013)	33
Table 3.1 Similarity index of the physical model system	55
Table 3.2 Mechanical properties of the GFRP rebars	55
Table 3.3 Chemical compositions of natural seawater in Chek Lap Kok, Hong Kong	56
Table 3.4 Mix design of SSC	56
Table 3.5 Basic physical properties of HKMD	56
Table 3.6 Loading program of oedometer tests (Wu, 2021)	56
Table 3.7 Quantified compressibility parameters of tested HKMD specimens (Wu, 2021).....	58
Table 4.1 Details of configuration, materials, and instrumentation of six model piles	97
Table 4.2 Cyclic loading program of the model piles	97
Table 5.1 Concrete mix proportion	142

CHAPTER 1: INTRODUCTION

1.1 Background and significance of the study

Bored concrete piles with pile end socketed in bedrock (rock-socketed piles) are commonly adopted for bridges, multi-story buildings, elevated highways and offshore platforms with stringent requirements for bearing capacity and settlement control. In Hong Kong (HK), rock-socketed piles are a prevalent foundation type for medium- or high-rise buildings like the Cullinan (270 m) and Nina Tower (319 m) (Sze, 2015) due to the shallow depth of bedrock in waterfront areas. The bearing capacity of a rock-socketed pile consists of shaft and base resistance which normally will not be mobilized simultaneously (Ng et al., 2001). The load transfer behavior of a rock-socketed pile is dependent on the properties of pile shaft, rock mass stiffness, and the behavior of the pile-rock interface considering elastic solutions. The pile-rock interface usually behaves differently from either the pile or rock material showing a non-linear response. The load transfer behavior of a rock-socketed pile is dependent on the properties of pile shaft, rock mass stiffness, and the behavior of the pile-rock interface considering elastic analysis. Pells and Tumer (1979) provided a design chart of the ratio between bearing capacity and shaft resistance considering varying aspect ratio of socket (socket depth/pile diameter of 0.25~4) and stiffness ratio between pile and rock (0.25~1000). In general, shaft resistance is fully mobilized at a displacement of 0.5-1.5% of pile diameter, while 10-20% is required for base resistance (Haberfield and Collingwood, 2006). Carter and Kulhawy (1988) reported that shaft resistance normally accounts for 80-90% of capacity, provided that the pile is under service loading with relatively small displacement. Extensive efforts (Williams and Pells, 1981; Horvath et al., 1983; Rowe and Armitage, 1987; McVay et al., 1992; Kulhawy and Phoon, 1993; O'Neill

CHAPTER 1: INTRODUCTION

and Hassan, 1993) (Williams and Pells, 1981; Horvath et al., 1983; Rowe and Armitage, 1987; McVay et al., 1992; Kulhawy and Phoon, 1993; O'Neill and Hassan, 1993) have been spent in correlating shaft resistance with the unconfined compressive strength (UCS) of rock or concrete, whichever is lower. Besides, several factors control the development of shaft resistance, including shaft diameter, side surface roughness, rock stiffness and construction practices (e.g., drilling fluid residue and smear), enabling designers to opt to take a conservative approach to estimate shaft resistance. In HK, Geotechnical Engineering Office (GEO) (1996) suggested that the empirical relationship proposed by Horvath et al. (1983) be used to calculate shaft resistance using a minimum mobilization factor of 1.5 in consideration of possible incompetent pile base conditions. According to the Code of Practice for Foundations (Building Department, 2017), the presumed allowable friction between rock and concrete for piles is capped at 700 kPa, which is significantly smaller than the estimated value from the above-mentioned empirical correlations. In-depth study of field tests on grouted piles in sandstone by Klapper et al. (2020) and Manceau et al. (2021) revealed that shaft resistance is inversely proportional to rock socket diameter which was not acknowledged in the previous classical models. For onshore or offshore large diameter grouted, bored, or drilled piles, this ignorance of inverse relationship with diameter is likely to result in an overestimation of shaft resistance. In addition, empirical relationships usually can only be applied to the cases based on which they were proposed, indicating the site-specific essence of those correlations. Given the spatial variability of ground and high cost in field tests, it is challenging to investigate the behavior of shaft resistance under complex applied loadings qualitatively and quantitatively. In this study, physical model tests were adopted by virtue of its advantages in better controlled boundary conditions, including loading and deformation, convenience for parametric studies, etc.

CHAPTER 1: INTRODUCTION

Reinforced concrete materials used for piling in harsh marine environments are susceptible to significant steel corrosion and concrete deterioration. The corrosion of steel reinforcement further induces cracks in concrete and reduces its effective area and its bonding with concrete, resulting in various issues such as spalling, structural failure, and substantial maintenance expenses. For example, Krauss and Nmai (1996) pointed out that most bridges which are along coastlines or offshore and rely on pile foundations will experience premature concrete degradation and steel corrosion in the first 12 years of their service life. Over the last several decades, FRP, a substitute for steel materials, has gained increasing popularity thanks to its high strength-to-weight ratio (one-fifth that of steel) and immunity to corrosion. More than 300 bridges founded on pile foundations were constructed using FRP reinforcement in Canada and the United States in the last three decades (Nolan et al., 2021). Besides that, the tremendous volume of river sand exploitation in the conventional concrete industry poses a serious threat to the environment (Xiao et al., 2017). In view of this, desalted sea-sand has been used in concrete structures worldwide, including in Japan, China and the United Kingdom. However, the extra cost and consumption of freshwater in the desalting process hinder the wide application of sea-sand.

The fact that FRP does not exhibit significant long-term degradation in typical marine environments (Li et al., 2018), making it a promising alternative to steel as a reinforcing material in sea-sand seawater concrete (SSC). Considerable efforts have been put into the structural behavior of concrete-filled FRP composite piles, particularly concrete-filled FRP tube piles

CHAPTER 1: INTRODUCTION

(Mirmiran et al., 1999; Fam et al., 2003; Sakr et al., 2004; Juran and Komornik, 2006; Pando et al., 2006; Park et al., 2011). Filling concrete can provide support to overcome the local buckling of FRP tubes, in turn providing lateral confinement to increase the strength and ductility of concrete. Zyka and Mohajerani (2016) concluded that concrete-filled FRP tube piles possess the advantages of excellent load-bearing capacity, relatively low price compared with other types of composite piles as well as a wide range of available sizes. Additionally, FRP tubes can be designed with different laminated structures to resist various kinds of external load combinations, rendering extra steel reinforcement unnecessary and reducing life-cycle cost. The lightweight of FRP tubes can ease construction to a large extent. Therefore, seawater sea-sand concrete (SSC) reinforced with FRP composites provide an effective and sustainable approach for replacing traditional piling materials in marine environment.

Pile foundations are often subjected to cyclic loadings caused by wind, water currents, waves, earthquakes, traffic loads and ice sheets. Cyclic loadings are variable and repeated in nature with a different range of magnitudes and cycles. For instance, offshore wind turbines generate millions of rotating blade cycles on supporting piles (Jardine et al., 2013), and pile foundations supporting the transport system always experience significant axial cyclic loads (Copsey et al., 1989). Chan and Hanna (1980) found that the cyclic behavior of piles in the sand is influenced by major cyclic loading parameters such as frequency, cyclic amplitude, mean load values, the number of cycles and loading history. The cyclic stiffness, stability diagrams and settlement features of piles in the sand under a variety of axial cyclic loading modes (stable, unstable and metastable modes) were studied. Previous researchers adopted the classical cyclic interaction

CHAPTER 1: INTRODUCTION

loading diagram to characterize the cyclic loading tests based on cyclic stability criteria. This practice has been widely applied in the piles driven in sand and clays (Jardine and Standing, 2012; Tsuha et al., 2012; Rimoy et al., 2013; Buckley et al., 2018) and field tests of drilled and grouted piles in rock (Klapper et al. 2020; Manceau et al. 2021). Helical pulldown micro piles reinforced by fiber-reinforced polymer (FRP)-steel fiber show the degradation of shaft resistance under cyclic loads(Sharnouby M.M. and Naggar M.H., 2012) . On the other hand, (Le Kouby et al., 2004) and (Jardine et al., 2006) claimed that the optimization of cyclic loading amplitude improved the bearing capacity of piles. Bekki et al. (2013) also stated that the shaft friction of piles exhibited strain hardening owing to shear dilatancy under a large number of loading cycles. Zhang et al. (2016) asserted that the cyclic stiffness of soft rock-socketed piles first increases, then decreases and finally tends to level off as the cycle number increases with the progressive damaging process of soft rock interface. Although numerous research works have been carried out on the cyclic response of piles in sand, silt and soft soils, the behavior of piles ended in rock-socket under cyclic loading, with emphasis on the cyclic stiffness variation of pile body and pile-rock interface, is rarely reported. Apparently, it is necessary to deeply study cyclic loading tests on rock-socketed piles based on systematic tests to provide guidance and potential predictive measures.

Fiber optic sensing techniques have overcome the limitations of traditional sensors. These optic sensors provide distributed strain profiles, long sensing range choices, anti-corrosive, high spatial resolution, easy operation and installation, presenting a better pile monitoring solution. Many researchers have applied fiber optic sensors in monitoring geotechnical engineering applications

CHAPTER 1: INTRODUCTION

like natural slopes, diaphragm walls, tunnels, pipelines, pile foundations, bridges, railway and road embankments, and dams (Iten et al., 2008b; D. HAUSWIRTH et al., 2014; Soga, 2014a; Zhang et al., 2015b; Schenato, 2017; Bersan et al., 2018; Pelecanos et al., 2018; Wu et al., 2021; Zheng et al., 2021; P. Wu et al., 2022). Fiber optic sensors include discrete sensors like fiber Bragg gratings (FBG) and distributed fiber optic sensing (DOFS) techniques like Brillouin optical time-domain reflectometry (BOTDR) and optical frequency domain reflectometry (OFDR). The BOTDR sensing technique uses typical spatial resolution (0.5-1.0 m) with wavy strain profiles which needs to be filtered prior to data analysis. Additionally, when differentiating strain profiles to obtain load distribution for calculating shaft friction values, the waviness of the strains leads to difficulty in determining shaft friction with unrealistic fluctuations in raw data (Pelecanos et al., 2018). As a newly developed distributed sensing technique, OFDR is rarely used for monitoring the piles except by Bersan et al. (2018) who applied DOFS for measuring axial strain of an augured cast-in-place pile at a relatively low spatial resolution of 10 mm. However, circumferential strain distribution of the pile provides a better understanding of the interactions between piles and surrounding soil. The presence of any voids, fissures, cracks, or any irregularity in pile body can influence the stress state surrounding pile, which can be detected through circumferential strain distribution curves. Furthermore, these curves can identify potential bending or lateral deformation of pile at certain points under axial load, high strain concentration positions, and variations in underlying soil or rock layers conditions. Therefore, DOFS for axial and circumferential strain distribution is desirable, enabling engineers to understand the behavior of piles under different loading conditions and validate design and assessment analysis assumptions.

1.2 Research objectives

The objective of this thesis is to study the axial cyclic and static behavior of the proposed innovative and sustainable pile design; fiber-reinforced polymer composite sea water sea-sand concrete piles in marine soils ended in rock sockets through a series of physical model tests. The experimental findings of the six physical model piles tests will provide a systematic study of distributed strain profiles, pile settlement, load transfer mechanism, shaft friction mobilization, and bearing capacity of the proposed model piles. The individual objectives of this research work are as follows:

- (a) To design and develop a specialized physical model pile system replicating the actual field conditions in the laboratory
- (b) To investigate the behaviour of FRP composite seawater sea-sand concrete piles ended in rock socket through a series of physical model tests under both axial cyclic and static loadings in marine soils.
- (c) To monitor the distributed strain profiles and load transfer mechanism using advanced fiber optic sensing technology.
- (d) To study the mobilization of shaft friction in rock-socket under cyclic and static loading through monitored distributed strain data by fiber optic sensors
- (e) To investigate the behavior of model pile in consolidating marine soils.
- (f) To compare the experimental results with the analytical solutions.

1.3 Methodology

This thesis adopted a comprehensive and systemic approach including literature review, developing physical model pile system, conducting elementary tests, physical model pile tests, and analytical solution comparison. A total of six model pile tests were conducted to investigate the axial cyclic and static behavior of proposed innovative and sustainable design of FRP composite seawater sea-sand concrete piles in marine soils ended in rock sockets. Three structural configurations (FRP tube confined, FRP rebar cage reinforced, and centered FRP rebar reinforced) were adopted for model piles. Fiber Bragg grating (FBG) optic sensors were used to monitor the discrete static or cyclic strain information along the length of piles inside and above the rock socket. Moreover, a novel fully distributed sensing technology named optical frequency domain reflectometry (OFDR) with a higher spatial resolution of 1 mm and a high sensing accuracy of $\pm 1 \mu\epsilon$ was also used to capture the distributed strain profile of piles inside and above the rock socket. Advantages and applications of each sensing method are emphasized for future studies to advance pile monitoring practices. The strain distribution, axial cyclic stiffness, displacement accumulation, and shaft friction mobilization of piles under static and different modes of axial cyclic loading were analyzed and explored in detail. The test findings are compared with the analytical solutions of partially embedded piles.

1.4 Thesis organization

This thesis is composed of eight chapters which are described and organized as follows:

Chapter 1 is the introduction and overview of whole research work describing the research background, scope and significance, research objectives, methodologies, and thesis organization.

Chapter 2 provides the detailed literature review of different types of piles foundations, behaviour of composite piles, cyclic loads and its influences on piles, and applications of optic fibre sensors in geotechnical engineering.

Chapter 3 presents the physical model pile system design and setup, properties of different materials used for this research, and material elementary tests and its results.

Chapter 4 reports the results of six physical model tests. The cyclic behavior of proposed innovative and sustainable design of FRP composite seawater sea-sand concrete piles in marine soils ended in rock sockets is analyzed and described in detail. The cyclic stiffness variation, deformation accumulation, and shaft friction mobilization under different cyclic loading conditions are discussed in this chapter.

CHAPTER 1: INTRODUCTION

Chapter 5 summarizes the static behaviour of the five physical model piles. In addition, the test results conducted on different types of FRP-SSC short columns under axial compression are reported as well. The axial strain distribution, load-deformation response, shaft friction mobilization and failure modes of model piles under static loading are discussed.

Chapter 6 reports the behaviour of FRP-SSC model pile in marine soil installed in rock-socket. The consolidation response of HKMD, pore water pressure variations, and settlement of the HKMD under different loadings are discussed. The settlement of upper and bottom layers under multistate loading was compared and investigated in detail.

Chapter 7 reports the comparison of optic fibres sensors data comparison of OFDR and FBG optic sensing techniques for pile monitoring. The axial and circumferential strain distributions monitored with different OFDR fibre sections are analysed and discussed in detail. Besides, the experimental results are compared with analytical solutions of partially embedded piles.

Chapter 8 summarizes the main findings and conclusions of this study and proposes recommendations for future related studies.

CHAPTER 1: INTRODUCTION

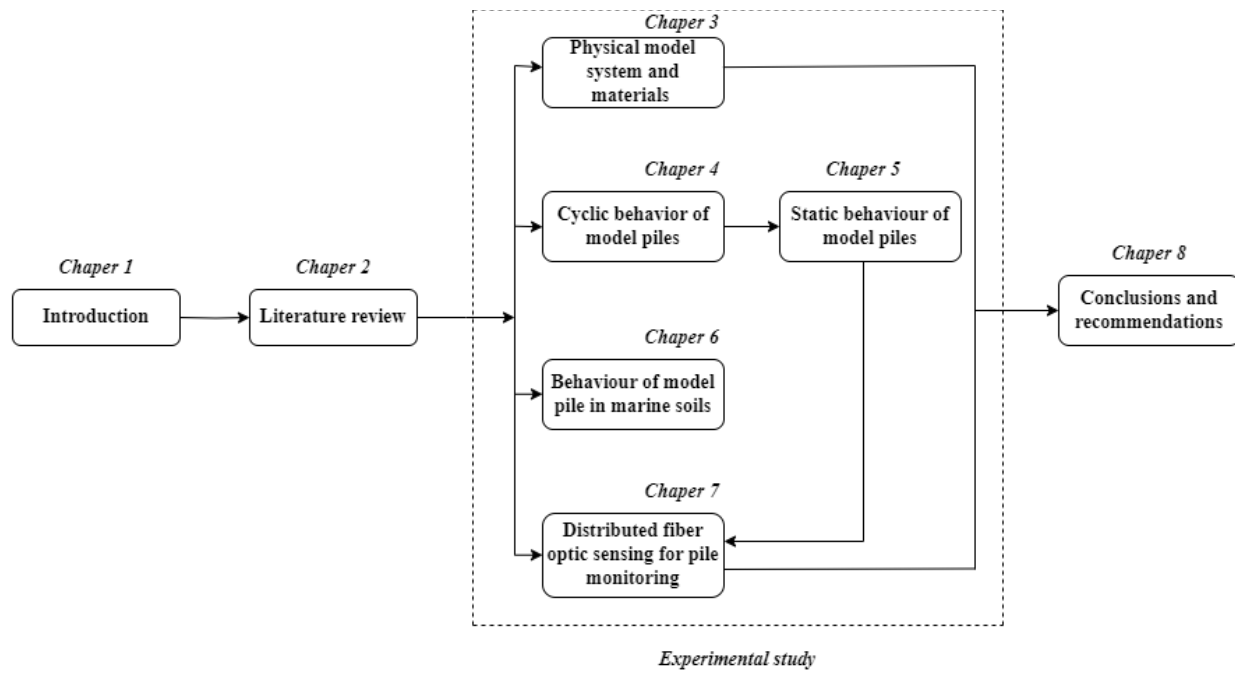


Figure 1.1 An overview of the research in this thesis

CHAPTER 2: LITERATURE REVIEW

2.1 Introduction

In this chapter, the detailed literature review of different types of piles foundations, behaviour of composite piles, cyclic loads and its influences on piles, and applications of optic fibre sensors in geotechnical engineering is presented.

In Civil engineering, the foundation of a structure plays a key role, transferring loads from the superstructure to the ground safely. Generally, foundations are categorized as shallow or deep foundations. Pile foundations are deep foundation systems that transfer structural loads to deeper, stronger soil, and bedrock layers below the ground surface. They are used when shallow foundations are inadequate due to soft soil existence and not able to resist the superstructure loads. The load transfer mechanism of pile foundations to the ground can be either through base resistance in case of end bearing piles or via shaft friction by providing frictional resistance to pile surface in case of friction piles or it can be a combination of both shaft friction base resistance piles. The advantages include the ability to transfer loads to deeper competent layers, enable construction on weak soils, and increase lateral stability for structures in case of shallow foundations which may settle unevenly. The key aspects considered in the pile design include the pile type, required pile length and diameter, and soil bearing capacity based on geotechnical testing. Pile groups are often used to achieve the necessary total bearing capacity or lateral stiffness.

Piles can also be grouped on the basis installation methods which can either be bored or driven.

Driven piles are those which are constructed by forcing the pile head through impulsive forces in the soil, while bored piles are installed in the pre excavated pit of the same size for proper placement. In addition, piles are also classified based on the construction materials. In harsh marine environment the pile foundation made from traditional materials like steel, reinforced concrete, and timber are found to have many problems including deterioration and degradation of concrete, corrosion of steel and durability problems requiring high maintenance costs (Iskander and Stachula, 2002). Therefore, researchers around the globe are looking for alternative materials which are more durable, cost effective and have higher strength in harsh marine environment. It is believed that FRP composites having higher strength, light weight, corrosion resistive and lower maintenance cost have the potential to replace the traditional materials.

2.2 Types of pile foundations

Piles can be categorized based on their load-carrying mechanisms, installation techniques, functions, and materials used for construction, which will be discussed in detail in following section.

2.2.1 Based on load carrying mechanisms

End bearing piles

Piles which transmit loads to the rock or soil stiff layer through pile base/end are considered as end bearing piles. The base of the pile should lie on a strong bearing stratum which can withstand the loads of superstructure and so the end bearing pile work like a column member by

CHAPTER 2: LITERATURE REVIEW

transmitting the loads safely through its end (Aashto, 2002). These piles are often used when the stiff layer of soils or bedrock located at certain depth below the ground surface.

Friction Piles

Friction piles are those whose bearing capacity relies on the shaft resistance induced by the surrounding soils on pile shaft. These kinds of piles are normally constructed in the ground when the hard stratum or stiff layer of soils are deep, and the strength of surrounding soil layers increase with depth below the ground surface. The bearing capacity of friction piles are derived from the surrounding soil resistance mobilized along the whole depth of pile shaft (Aashto, 2002). Piles can also transmit load by both mechanisms, base resistance and shaft resistance and are termed as combined end bearing and friction piles. The difference between friction and end bearings piles are shown in the Figure 2.1.

2.2.2 *Based on pile functions*

Tension piles

Tension piles are designed primarily to resist tensile or uplift forces to anchor structures like buildings, towers, and retaining walls. The uplift forces are resisted by the shaft friction or in combination with end bearing. The piles are often made from steel-H sections, reinforced concrete, or composite materials.

Compaction piles

Compaction piles are used to compact and improve the bearing capacity of loose or compressible soils. They are made of granular materials like sand instead of steel or concrete. Compaction

CHAPTER 2: LITERATURE REVIEW

piles are used for projects on weak soils to reduce settlement risks of overlaying structures. The practical applications include airport railways, stockpile areas, tailing dams and road/rail embankments.

Anchor piles

A special type of pile to anchorage structures against horizontal tensile/pull forces as shown in Figure 2.2. They are designed with or without bracings and its practical applications include retaining wall anchors and mooring for jetties or dolphins.

Fender Piles

Fender piles are specialized type of piles used in waterfront or marine structures to protect the vessels or boats from the impact damage during berthing. During mooring operations, such piles are constructed to absorb the impact induced by kinetic energy of vessels by allowing some elastic deformation. The fender piles are made of materials which allows elastic deformation and can withstand impact forces. The practical fender piles installed in marine structure are shown in the Figure 2.2.

2.2.3 Based on installation techniques

Driven Piles

Piles which are installed in the soil through impact loading or hammering by penetrating them to the required depth are considered as driven piles. Driven piles displace the surrounding soils as it goes deeper in the ground during penetration causing lateral stresses in the ground and make the surrounding soils stiffer. These types of piles cause noise problems at the site due to the impact load or hammering using heavy machinery. To reach the design depth without damaging the pile, accurate specification of hammer energy is essential. The mechanism of driven piles is shown in Figure 2.3.

Bored Piles

Bored piles are constructed in the pre-excavated cavity of the required depth and diameter in the ground. The soils are normally removed from the required position of the pile to be installed and then the reinforcements and cast concrete are placed in the formwork of the pile. This kind of pile is normally constructed in urban areas due to less noise generation and where driven piles are not practicable at the site. Bored piles can carry heavy structural loads and are suitable for both cohesive and cohesionless soils as well as soft soils. Figure 2.4 shows the illustration of bored piles.

2.2.4 Types of piles based on materials used for construction

Concrete Piles

Concrete piles are the most widely used type of pile foundations due its low cost, availability, ease of construction and high stiffness (Xiao et al., 2020). Concrete piles are typically composite structures constructed in combination with steel reinforcements composite rebars, and steel casings. Due to corrosion of steel piles, concrete piles are most common in marine infrastructures and offshore construction works. Generally, bridge piers, caissons retaining walls and large pile groups are supported on concrete piles. These kinds of piles can be either in-situ cast or prefabricated piles in the industry and installed at the site as shown the Figure 2.5. Prefabricated/precast piles are normally manufactured in the industry and then transported to the site for installation. In-situ concrete piles are constructed at the site by pouring concrete in the mould placed in soil fabricated with steel reinforcements.

In harsh marine environments concrete piles experiences steel corrosion, abrasion, and degradation due to water-borne sediments at the seabed. Corrosion of the steel in marine environments is often stimulated by the presence of ions like calcium chloride ions and sodium chloride ions in the seawater. The corrosion of steel leads to cracks in the reinforced concrete caused by the tensile stresses, as concrete is less resistant to tension compared to compression. Apart, freezing and thawing may also induce cracks in the concrete reducing the life span of the piles. However, due to overall good performance and reliability concrete piles are still widely used in the offshore construction.

Steel Piles

Steel piles are commonly used due to its high compressive and tensile strength, durability, and ease of method of installation in the ground. It is highly resistive to damages expected during the driving process and installation process in the ground. Steel pile can stand heavy loads, easy to handle and easily available for installation making them suitable for many pile foundations applications. They can be driven in dense soil according to the required depth and can work as base resistance piles when reach to the strong stratum. Steel piles can be manufactured in different types of shapes according to the requirements such as H-shaped, T shaped, I shaped, circular hollow shaped, and tubed shaped etc. Every shape has its own mechanical properties and can be adopted per the required design. Figure 2.6 shows a group of H-shaped steel piles driven in the soil.

Timber Piles

For thousands of years timber has been used for structural purposes due to its abundant and natural availability. Timber structures are inexpensive and have high strength and low weight compared to other kind of piles. Its low cost and abundant availability make its applications in many countries including northern areas of Canada, Europe, Russia, Turkey, and America for ages. Timber has been used for pile foundations due to its low cost, can be easily cut to required dimensions and easily available. Timber piles varies in diameter from 250-500 mm (Wilkinson, 1968). It can be driven into the ground having natural tapered shape and can be adjusted to required design of shape as well. Timber piles can maximum take a load to 500 kN because of its small diameter and poor derivability in the ground (Fleming et al., 2008). Timber piles can have

longer life span if fully submerged with no exposure to the air (Mandolini et al., 2005). Their durability can be increased by taking advanced preventive measures against deterioration and wood rotting. Figure 2.7 shows a structure fully supported on timber piles in the water.

2.2.5 Composite piles

Composite piles are made of FRP composites or recycled materials which are coupled with concrete providing an alternative to steel reinforcements or protecting it from corrosion resulting in piles with higher strength, longer life span, and low maintenance costs in harsh marine environments. These piles show higher durability as compared to traditional piles foundations. In the late 1980s, composite piles were firstly used at the port of Los Angeles by replacing timber fender piles (Iskander and Hassan, 1998; Zyka and Mohajerani, 2016). Composite piles are of different types such as FRP tube confined concrete piles, FRP rebars reinforced concrete piles, reinforced plastic piles, pultruded piles, steel core piles, and plastic lumber piles. These composite piles are considered structurally favourable and can be applied in practical applications which are shown below in the Figure 2.8.

FRP Piles

The applications of FRP composites have been significantly increased in the past few decades in the field of geotechnical engineering especially in pile foundations (Iskander and Hassan, 1998; Sen and Mullins, 2007). FRP composites are made of two or more phases producing a durable material with improved performance. The typical two phases of FRP composites consist of

CHAPTER 2: LITERATURE REVIEW

matrix and reinforcing phase. The reinforcing phase composed of fibres oriented in desired directions. The fibres can be oriented either in perpendicular directions to each other or multi directions depending upon the purpose of reinforcement. The main purpose of the fibres is to withstand the loads by providing strength, stiffness, mechanical properties, and thermal stability to the FRP composites.

The matrix is typically made of vinyl ester, epoxy, polyester, phenolic elements, and thermoplastics. The main function of the resins is to bind the fibres holding them together and provide a medium to transmit the loads within the fibres. The matrix also protects the fibres from environmental factors and resist the shear loads occurring within the structure of FRP composites itself (Barney, 2004). The fibres and matrix when combined form a composite structure termed as lamina. The matrix can be either reinforced with glass fibres (GFRP), Carbon fibres (CFRP) or aramid fibres (AFRP) and the properties of the composites relies on type of fibres, fibres amount, and its weight fraction. FRP composites are mainly manufactured through three different techniques like filament winding, pultrusion, and moulding process. This study involves three different types of FRP composite piles; FRP tube confined concrete pile, FRP rebar cage reinforced piles and centred FRP rebar piles.

FRP tube confined concrete piles

FRP tube confined concrete piles are the type of piles composed of concrete and FRP tube, in which the FRP tube act as a permanent casing as well providing confinement to the concrete. The concrete infilled is without any steel reinforcements because the FRP tube provides confinement effect, lateral tensile strength, and barrier to harsh external environmental effects to the concrete

CHAPTER 2: LITERATURE REVIEW

and the concrete itself provides compressive strength making it a durable structure (Fam et al., 2003). The FRP tube outer surface act as an interface boundary with the surrounding soil and protects the pile from harsh environment factors like corrosion, abrasion and hence increases the service life of the piles. The piles made of FRP composite tubes are found to have comparable performance with reinforced concrete structures under axial compressive loading conditions (Mirmiran et al., 1999). It is found that the FRP tube improves the ductility and strength of the member due its confinement pressure and durability (Fam et al., 2003). The renovation and maintenance of the bridges proved that concrete filled FRP tube piles has increased their structural performance significantly (Pando et al., 2006).

FRP rebars reinforced concrete piles

FRP composite piles can be designed in a similar way like steel reinforced concrete structures, in which the steel rebars are replaced with FRP rebars. The substitution of traditional steel bars with FRP rebars is a novel approach to avoid steel corrosion from chloride attack, pile deterioration, maintenance costs in marine environments. Many studies have investigated the structural and geotechnical behavior of FRP rebars reinforced concrete piles and its applications in the offshore marine structures have increased significantly in past few decades. The structural behavior and flexure strength of GFRP rebars reinforced concrete piles was investigated by Mousa et al. (2018) and analyzed the deformation accumulation and ductility under different tests. Tests conducted by P. Wu et al. (2020) to examine the flexural behavior of pre-stressed high strength concrete reinforced with steel and FRP rebars. The findings showed FRP rebars reinforced piles exhibited higher flexure capacity compared to steel rebars reinforced piles. Han et al. (2003)

conducted an analysis of existing design approaches for traditional pile foundations and its applicability for FRP composite piles and proposed a new design methodology for FRP composite piles under lateral and axial load conditions.

2.3 Behavior of FRP composite concrete piles

2.3.1 Structural behavior of FRP composite concrete piles under axial loads

It has been found by many researchers that FRP confined concrete structures behave bilinearly under axial loading ((Mirmiran and Shahawy, 1997; Lau and Hui, 2002). Two distinct regions reflect the bilinear response as shown in Figure 2.9. The first part shows identical behaviour like unconfined concrete, as at initial stage the lateral expansion of the infilled concrete is relatively small. When the axial load gets higher, the FRP composites creates confining pressure and stiffness at a constant uniform rate restraining the expansion of concrete. This behaviour mainly depends on the mechanical properties of the FRP tube such fibres orientation and amount, and matrix properties. The section OX and OL of the stress-strain curve shows the first linear part in axial and hoop directions, respectively. The XY and LP depicts the second linear part in the axial and hoop directions, respectively. In this region, the confining pressure and compressive stress are the parameters that varies and attaining their ultimate values when the FRP composites reach failure stage.

2.3.2 Structural behavior of FRP composite concrete piles under flexural loads

Pile foundation provides support to the structure carrying both flexural and axial loads. Pile act like a column structurally carrying and transferring flexural loads and axial loads. In the offshore foundations, piles are subjected to axial loads from the structure and flexural loads from the waves, snowflakes, earthquakes, water currents and wind loads. The confinement effect of the FRP tubes and FRP wraps are relatively low against flexural loads as compared to axial loads. However, other advantages of FRP composites like permanent formwork as stay in place, ease of construction and speedy erection of the structures make them attractive and alternative solution. They can be used as flexural members in piles, poles, overhead sign structures, piles and tunnels and bridge girders etc.

Firstly, FRP confined concrete beams were produced by casting concrete into the FRP boxes (Fardis and Khalili, 1981). Large-scale FRP tubes and hollow GFRP and steel tubes were tested under flexure loading shown in the Figure 2.10 (Fam et al., 2003). The findings showed that the flexural behaviour of FRP tube confined concrete members were primarily dependent on the tube diameter to thickness ratio and stiffness, however, showed less dependency on concrete compressive strength. Additionally, FRP tube confined concrete were investigated experimentally to observe the flexural behaviour using four-point bending tests (Fam and Rizkalla, 2003). It was concluded that concrete provide more strength for low stiffness tubes in bending as compared to strength provided in the axial loadings for the same stiffness tubes by preventing local buckling of the fibres. The flexural strength of FRP composite structures can be enhanced by increasing its thickness.

2.3.3 Geotechnical behavior of FRP composite concrete piles

FRP composite piles have relatively less literature due to their novelty and new material as compared to the traditional piling materials. During installation and service life of the FRP composite piles, Han et al. (2003) monitored the critical buckling loads and found that it depends on the lateral soil stresses, boundary conditions, shear effect coefficient, critical pile length, and embedment ratio in the soil. A full-scale FRP tube confined concrete pile load test and prestressed concrete piles have been conducted by Pando et al. (2006). The study revealed a decrease in the axial geotechnical capacities, with prestressed concrete piles exhibiting the highest capacity, followed by FRP tube confined concrete piles. In other study conducted by Mirmiran and Shahawy (1997), the objective was to investigate the influence of drivability of FRP composite piles. The findings showed that neither debonding between concrete core and FRP tube nor pile head damage were observed for both prestressed and FRP tube confined concrete piles. A full-scale field test of prestressed concrete pile and FRP tube confined concrete pile under axial loads were conducted after pile driving in soil and the findings of the tests for three cycles of loading are shown in Figure 2.11 (Fam et al., 2003).

2.3.4 Interface mechanism of FRP composites and soil

In pile foundations interface shear resistance between the soil and the structural materials like concrete, FRP composites, and steel is the key parameter in soil structure interaction and geotechnical designs. Interface response of some of the structures for consideration in geotechnical design problems are shown in the Figure 2.12. In pile foundations, the pile capacity depends on either the shaft resistance or base resistance or combination of both. The resisting

loads are initially generated by the mobilization of shaft friction at low relative displacement between the pile shaft and surrounding soil. However, as the applied loads on the pile and relative displacement increases, the base resistance starts contributing to resist the applied load. Both the shaft resistance and base resistance strongly depends on the physical properties of the surrounding soil and piling material. The interface shaft friction is defined as:

$$\tau = \sigma \times \tan \delta$$

where τ , σ , and δ represents shear strength, applied normal stress and interface friction angle between soil and pile.

2.3.5 Confinement mechanism of FRP composites

In the FRP tube confined concrete structures, the lateral confinement of the FRP composites is passive in nature. During axial compression of the concrete expands in lateral direction which is confined by FRP tube subjecting it to the tensile strains in hoop direction. The FRP tube provides confinement until it reaches its hoop tensile strength and fails. Figure 2.13 illustrates the confining effect of the FRP tube confined concrete under axial compression. It is found that structural response of the FRP tube confined concrete structures mainly dependent on the mechanical properties of the concrete and FRP composites such as fibre orientation, thickness, and type of the fibre used. Many researchers have worked on the assessment of strength enhancement of FRP tube confined concrete and presented different numerical models as shown in Table 2.1. Most of these mathematical models are developed on the concept presented by (Richart et al., 1929) which is based on the concrete failure strength confined by hydrostatic pressure.

$$f'_c = f_c \left[1 + k_1 \frac{f_l}{f_c} \right]$$

where " f'_c " and " f_c " represents the compressive strength of the FRP tube and unconfined concrete, respectively. " f_l " and " k_1 " denotes lateral confining pressure and confinement coefficient of the FRP tube, respectively.

When the FRP tube or wrap reaches its failure state as the infilled concrete fails, the maximum confining pressure induced is determined by the given relation:

$$f_l = \frac{2t \times f_{FRP}}{d}$$

Where "t" and "d" represents the thickness and diameter of FRP composites respectively, while " f_{FRP} " represents tensile strength of the FRP tube in the lateral direction.

2.4 Axial cyclic behavior of rock-socketed piles

2.4.1 *Cyclic loads and its influence on piles*

Pile foundations are crucial to cyclic loadings caused by wind, water currents, waves, earthquakes, traffic loads, and ice sheets etc. Previous studies show that the influence of cyclic loadings need to be considered in the design when determining the bearing capacities, and stiffness of the piles. Cyclic loadings are generally variable in nature and have repeated patterns in the form of cyclic amplitude, frequency, and cycles. The characteristics of normally occurring cyclic loadings are shown in Figure 2.14. Cyclic loading's frequencies and cycles numbers vary for different types of loads. The earthquake loads are very critical and last for a very shorter time

duration with minimum cycles among all. Generally, for designing offshore or onshore pile foundations, the most common pattern of loading adopted has certain cyclic amplitude, mean load level, and fixed frequency. This type of cyclic loading pattern is sinusoidal in nature, with mean load (Q_{mean}), cyclic loading amplitude (Q_{cyc}), number of cycles (N), and time period (T). In this study, sinusoidal loading pattern with different cyclic amplitude, mean load, and cycles have been considered for the investigating the behavior of model piles.

2.4.2 Design of rock-socketed piles

Cast-in-place bored concrete piles socketed into rock with the applied load resisted by socket shaft resistance and end bearing resistance are widely used for bridges, high rise buildings, and offshore structures. These piles provide versatile and sustainable foundation solutions due to high bearing capacity, minimal noise, less ground vibration, and high flexibility in length and diameter. Traditionally, the design of such rock socketed piles is based on one of the following four methods: empirical correlations based on unconfined compressive strength (UCS) of rock and concrete, shaft diameter, and socket roughness, standard code of practice, rational method based on settlement analysis and bearing capacity, or field static load tests (Zhan and Yin, 2000).

Many researchers have proposed empirical correlations predicting the shaft resistance of rock-socketed piles measured in static load tests. Field load tests on small diameter (200-610 mm) piles conducted by Rosenberg and Journeaux (1976) showed that shaft resistance is mainly dependent on bond strength of concrete rock interface and UCS of rock. In 1979, Horvath and Kenney reviewed 49 load tests of rock-socketed piles with diameters (between 410 to 1220 mm) conducted in UK, USA, Canada, and Australia, and observed that socket shaft resistance was

CHAPTER 2: LITERATURE REVIEW

fully mobilized at approximately 6 mm (0.5-1.5% of pile diameter) displacement. And they also correlated shaft resistance with UCS of rock. Furthermore, O'Neill et al. (1996) compared the empirical correlations based on UCS of weaker material (concrete or rock) developed by different researchers (Kaderabek and Reynolds, 1981; Williams and Pells, 1981; Rowe and Armitage, 1987; Carter and Kulhawy, 1988; Reese, 1988; Toh et al., 1989) with an international database of 137 rock socketed pile load tests and concluded that none of the correlations worked satisfactorily with the database results. Unlike previous empirical models, Seidel and Collingwood (2001) developed an analytical method for determining the shaft resistance of drilled and grouted piles socketed in rock, which was validated using extensive database covering a wide variety of rocks. This method incorporated major factors influencing shaft friction like socket roughness, rock mass stiffness, socket diameter, and normal stress at rock-concrete interface. However, quantifying the effect of construction techniques, effect of drilling slurries, debris smear, bonding type and drilling practices were not incorporated in developing the correlations which possibly influence the shaft friction mobilization.

The use of load-transfer curves based on maximum allowable settlement and bearing capacity provides an approach for the design of pile foundation, but remarkable experience and engineering judgment will be required to implement such curves in the field whose conditions differ distinctly with that where these curves were obtained. Although fully instrumented static load tests recommended by standard design codes provide a rational design approach, it might be limited to high profile projects with sufficient budget in field testing. Therefore, physical model tests were employed in this study to investigate the complex interaction between pile shaft and rock, identify potential design issues, and validate numerical models to be used for parametric studies in future.

2.4.3 Negative shaft friction (NSF) mobilization on piles in consolidating soft soils

In soft consolidating soils, interface shaft friction between the pile shaft and surrounding soils is mobilized when the soil settles more than the pile. This kind of shaft friction drags down the pile in the downward direction and is known as negative shaft friction (NSF). The development of NSF results in two different effects on the pile. Firstly, it leads to the generation of drag force, which subsequently contributes to the excessive settlement of the pile. NSF acts as an additional load on a pile under service load conditions reducing the structural capacity of the pile. It exhibits a time dependent behavior due to its dependency on soil consolidation and creep and keep increasing until the soil reaches full consolidation stage. The calculation of the NSF in soft consolidating soils on a pile is a complex scientific issue that has been extensively studied by many researchers in the past (Broms, 1988; Khare and Gandhi, 2001; Lee and Ng, 2004). However, there is a lack of research that investigates the NSF mobilization on piles in soft soils and ended in rock-socket. This study focuses on the NSF development of model piles in soft consolidating soils installed in rock-sockets.

2.5 Applications of fiber optic sensors in geotechnical engineering systems

2.5.1 Conventional strain measuring instrumentations

Conventional measuring devices like strain gauges and vibrating wire extensometers provide discrete strain data at only certain points, which have limitations. Firstly, the shaft friction values calculated from strain profile and load distribution curves based on discrete point measurement

data would differ from actual values. Secondly, using conventional sensors would suffer from cable congestion, high cost and data acquisition equipment constraints for offshore rock socketed piles which penetrate through the full depth of seawater. Thirdly, marine corrosive environment would be a challenge for the durability and functionality of these resistance-based sensors (De Battista et al., 2016). Therefore, novel measuring techniques are required to measure reliable strain distribution and response of the piles.

2.5.2 Fiber optic sensors and its classification

The applications of fibre optic sensors (FOS) technology have been increased significantly over the past few decades. In comparison to the traditional sensors the usage of FOSs provides many advantages such as resistance to electromagnetic interference, higher spatial resolution, accuracy, resistant to water, long term stability and durability in harsh marine environments, and low cost of operation. In addition, their capabilities of being multiplexed over a larger number of points and long-distance sensing measurements show their remarkable characteristics. Therefore, FOSs can be used where spatial resolution and large number of sensing points measurement are required.

2.5.3 Distributed fibre optic sensing and its applications in geotechnical engineering

The FOS can generally be categorized as discrete point sensors like Fibre Bragg Grating (FBG) sensors and fully distributed optic fibre sensor (DOFS). In the FBG sensing technology many sensors can be fabricated along the length of fibre at discrete points and due to effectiveness have been used for decades in many applications. The DOFS technology measures the strain and temperature variations along the whole length of fibre to range of 1000 meters. The

CHAPTER 2: LITERATURE REVIEW

manufacturing process of these fibres are simple and cheap as compared to FBG which need special sensing element for strain measurement while in DOFS the sensing elements are not required and the fibre itself work as a sensor. This type of optic sensor depends mainly on the elastic and inelastic interaction of propagating light from the data logger and the fiber material itself. In DOFSs three types of light reflection generate these interactions, known as Brillouin, Ramen, and Rayleigh scattering. During the propagation of light in the optical fiber, some of the light signals are reflected by any of the above-mentioned mechanisms. This back propagating light scattering is received by the reading equipment interrogate it in the form of strain and/ or temperature measurement of the object of interest. Rayleigh and Brillouin scattering of the reflected light in the fiber is sensitive to strain and temperature while ramen scattering is sensitive only to temperature changes. This combined sensitivity makes it difficult for the sensors to differentiate between the temperature or strain. Therefore, to avoid discrepancy assume either one of the two required parameters constant. Regarding the accuracy and spatial resolution, their capabilities are different like Raleigh scattering provides higher spatial resolution in the range of millimeters and measurement accuracy of $\pm 1 \mu\epsilon$. In the case of Brillouin and Ramen scattering, the spatial resolution is in the range of 0.1 to 10 meters with 1-10 $\mu\epsilon$ sensing accuracy.

The applications of optical fiber sensors have been increased recently in geotechnical engineering, such as monitoring of piles, tunnels, pipelines, natural slopes, retaining walls and dams (Iten et al., 2008a; D Hauswirth et al., 2014; Soga, 2014b; Zhang et al., 2015a; Hong et al., 2016). Many researchers have applied DFOS for monitoring the piles in literature and mostly Brillouin optical time domain reflectometry (BOTDR) was adopted having typical spatial

resolution of 1 m for data analysis and data acquisition equipment (Soga, 2014b; Mohamad and Tee, 2015; De Battista et al., 2016; Hong et al., 2016; Pelecanos et al., 2018).

2.6 Summary

This chapter introduces different types of pile foundations based on their load-carrying mechanism, installation technique, function, materials used for construction. In addition, structural and geotechnical behaviour of composite piles, cyclic loads and its influences on piles, and applications of optic fibre sensors are reviewed in detail. The previous studies and observations in field conditions showed that the traditional pile materials like steel, reinforced concrete, and timber in harsh marine environment experiences deterioration and degradation of concrete, corrosion of steel, and durability problems which consume high maintenance costs. Therefore, an alternative pile foundation design which is sustainable, durable, cost effective, and non-corrosive in harsh marine environment is required to be adopted for the future field applications. It is widely recognized and accepted that structural materials such as FRP composites when coupled with sea sand seawater concrete have the potential to replace the traditional piling materials. FRP composites do not exhibit significant long-term degradation in typical marine environments making it a promising alternative to steel as a reinforcing material in sea-sand seawater concrete (SSC). The axial cyclic and static behavior of FRP composite SSC piles ending in rock sockets are absent in the literature, therefore systematic experimental studies under a wide range of loadings using distributed optic fiber sensing technologies are needed.

CHAPTER 2: LITERATURE REVIEW

Table 2.1 FRP composites confined concrete existing numerical models (Shaia, 2013)

Author	Fibre type	Ultimate strength (f'_c)	Ultimate axial strain (ϵ'_c)
Fardis and Khalili, (1981)	GFRP	$f_c + 4.1f_l$	$\epsilon_c + 0.001\left(\frac{E_{FRP}}{df_c}\right)$
Saadatmanesh et al. (1994)		$f_c \left[-1.254 + 2.254 \sqrt{1 + \frac{7.94f_l}{f_c}} - 2\left(\frac{f_l}{f_c}\right) \right]$	$\epsilon_c \left[1 + 5\left(\frac{f'_c}{f_c} - 1\right) \right]$
Karbhari and Gao (1997)		$f_c \left[1 + 2.1\left(\frac{f_l}{f_c}\right)^{0.87} \right]$	$\epsilon_c + 0.01\left(\frac{f_l}{f_c}\right)$
Mirmiran, (1997)		$f_c + 4.269.f_l^{0.587}$	-----
Samaan and Shahawy (1998)		$f_c + 6.0 f_l^{0.7}$	-----
Saafi et al. (1999)		$f_c \left[1 + 2.2\left(\frac{f_l}{f_c}\right)^{0.84} \right]$	$\epsilon_c \left[1 + (537\epsilon_{l+}2.6)\left(\frac{f'_c}{f_c} - 1\right) \right]$
Toutanji (1999)		$f_c \left[1 + 3.5\left(\frac{f_l}{f_c}\right)^{0.85} \right]$	$\epsilon_c \left[1 + (310\epsilon_{l+}1.9)\left(\frac{f'_c}{f_c} - 1\right) \right]$
Lam and Teng (2003)		$f_c \left[1 + 3.5\left(\frac{f_l}{f_c}\right) \right]$	$\epsilon_c \left[1.75 + 5.53\left(\frac{f_l}{f_c}\right)\left(\frac{\epsilon_l}{\epsilon_c}\right)^{0.45} \right]$
Teng et al. (2007)		$f_c \left[1 + 3.3\left(\frac{f_l}{f_c}\right) \right]$	$\epsilon_c \left[1 + 17.5\left(\frac{f_l}{f_c}\right) \right]$

Notes: f_c and ϵ_c represents compressive strength and ultimate strain of unconfined concrete, respectively. f'_c and ϵ'_c denotes compressive strength and ultimate strain of the confined concrete,

CHAPTER 2: LITERATURE REVIEW

respectively. ε_l and f_l denotes lateral or hoop strain and confining pressure of the confined concrete, respectively. E_{FRP} stands for the elastic modulus of FRP composites.

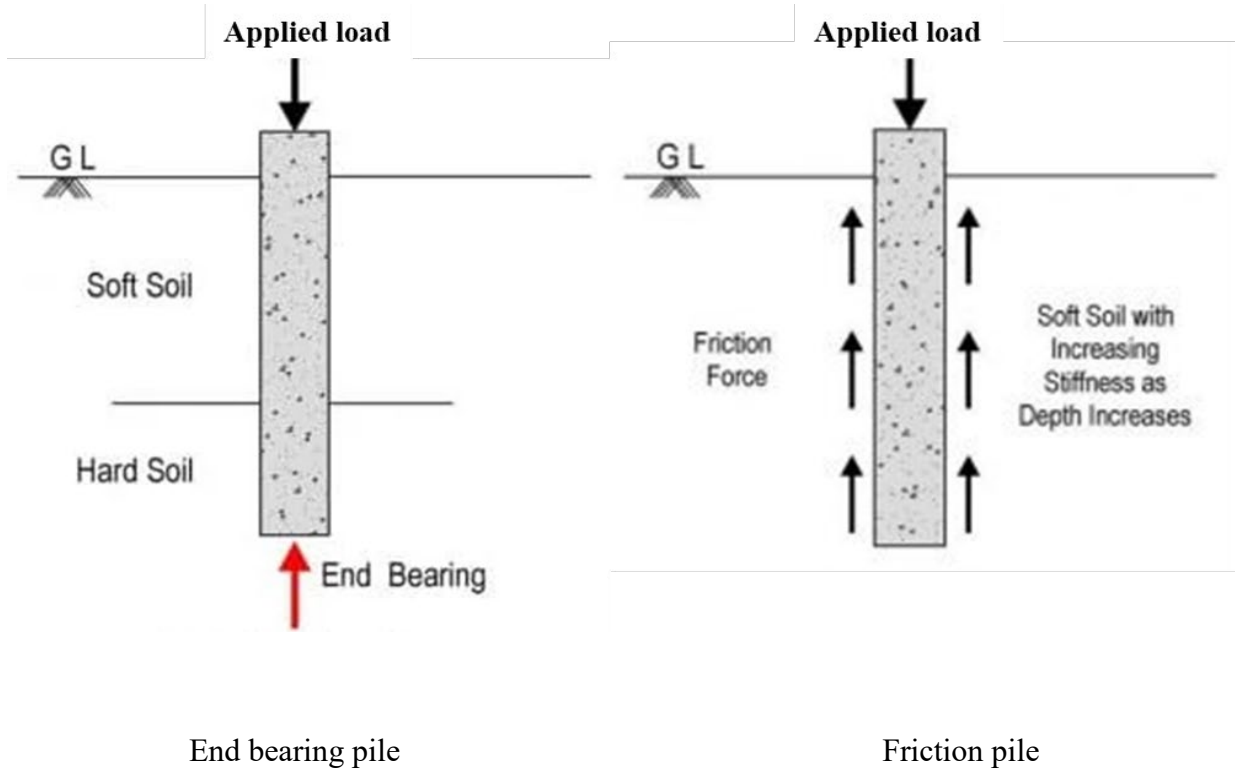


Figure 2.1 Illustration of friction and end bearing pile (dreamcivil.com)

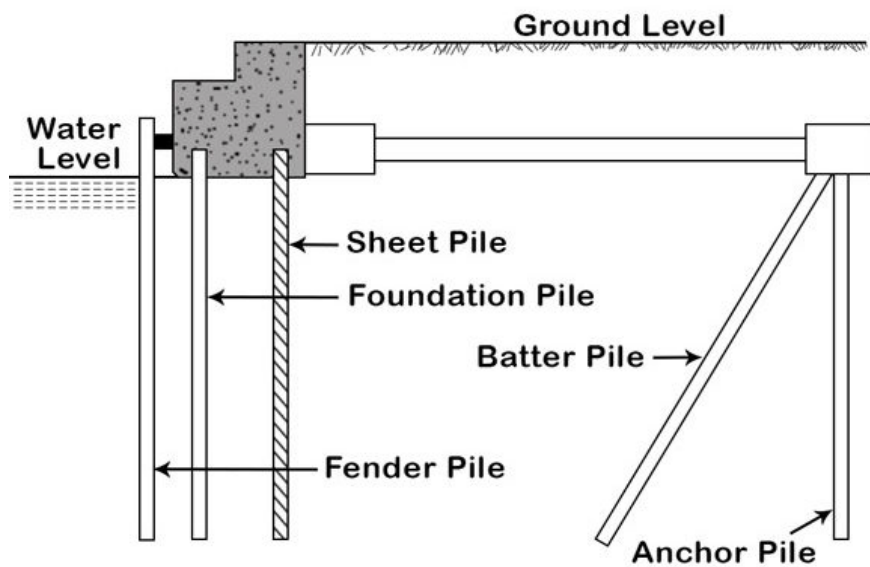


Figure 2.2 Illustration of Anchor and fender pile (dreamcivil.com)

CHAPTER 2: LITERATURE REVIEW



Figure 2.3 Driven steel piles in the ground at site (shortspansteelbridges.org)

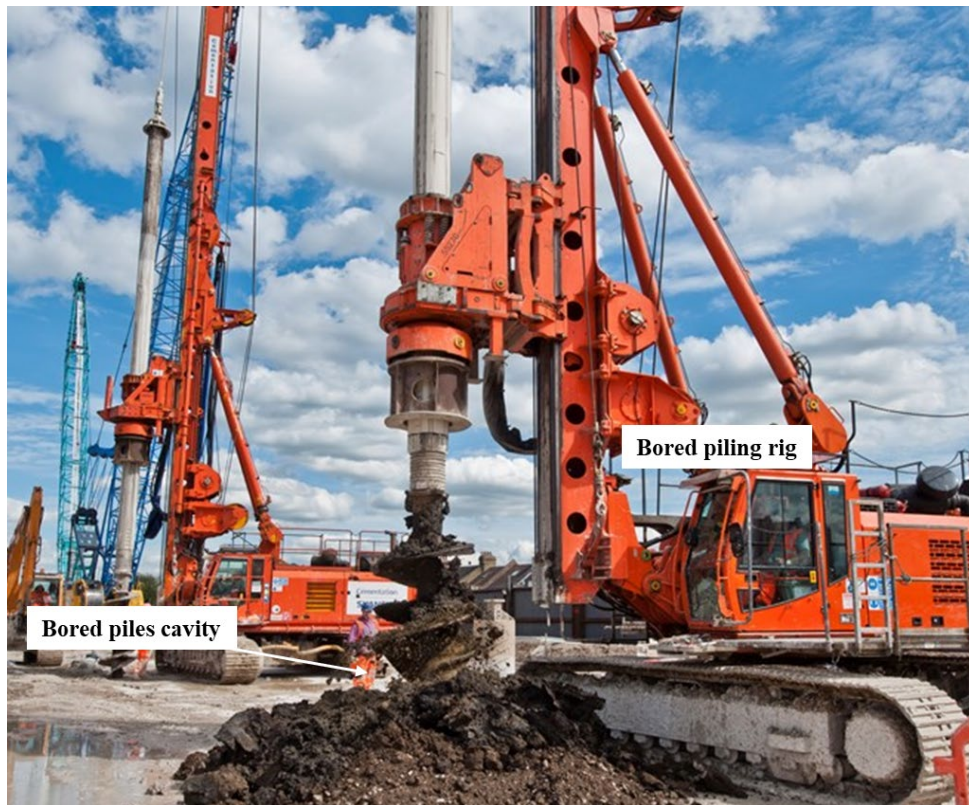


Figure 2.4 Bored piling mechanism and machinery (www.skanska.co.uk)

CHAPTER 2: LITERATURE REVIEW



Figure 2.5 Offshore concrete piles (pilebuck.com)



Figure 2.6 Group of offshore H shaped steel piles (morrisshea.com)



Figure 2.7 Group of driven timber piles in ground (weekesforest.com)

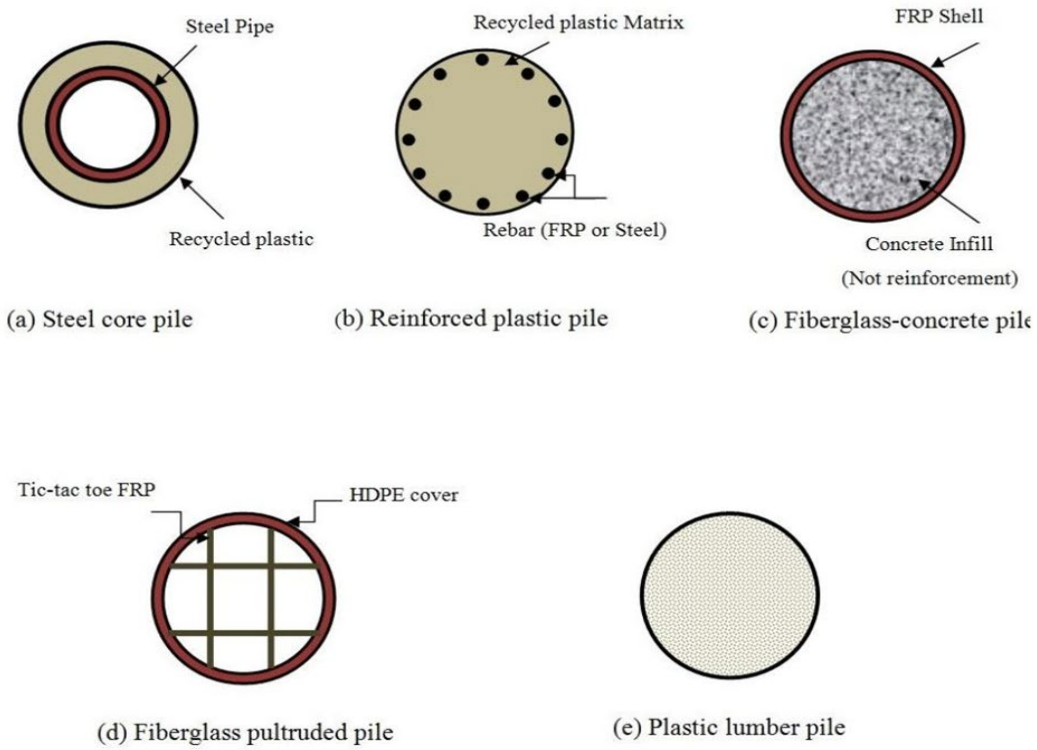


Figure 2.8 Composite marine piles (Iskander and Hassan, 1998)

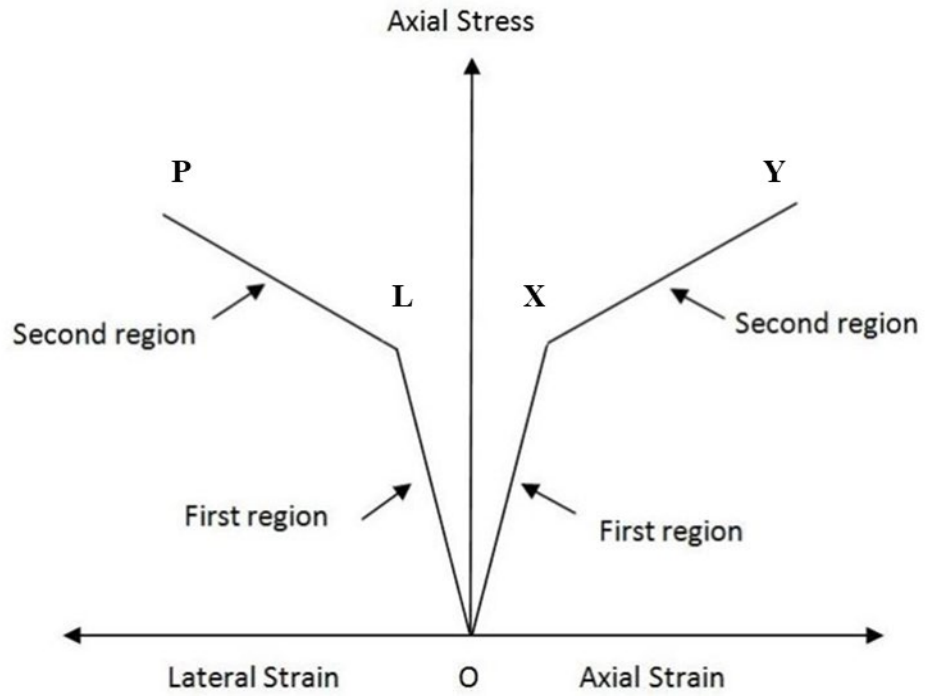


Figure 2.9 Stress-strain curve for FRP confined concrete (Saafi et al., 1999)



Figure 2.10 Four-point bending test of FRP composite concrete beam (Fam et al., 2003)

CHAPTER 2: LITERATURE REVIEW

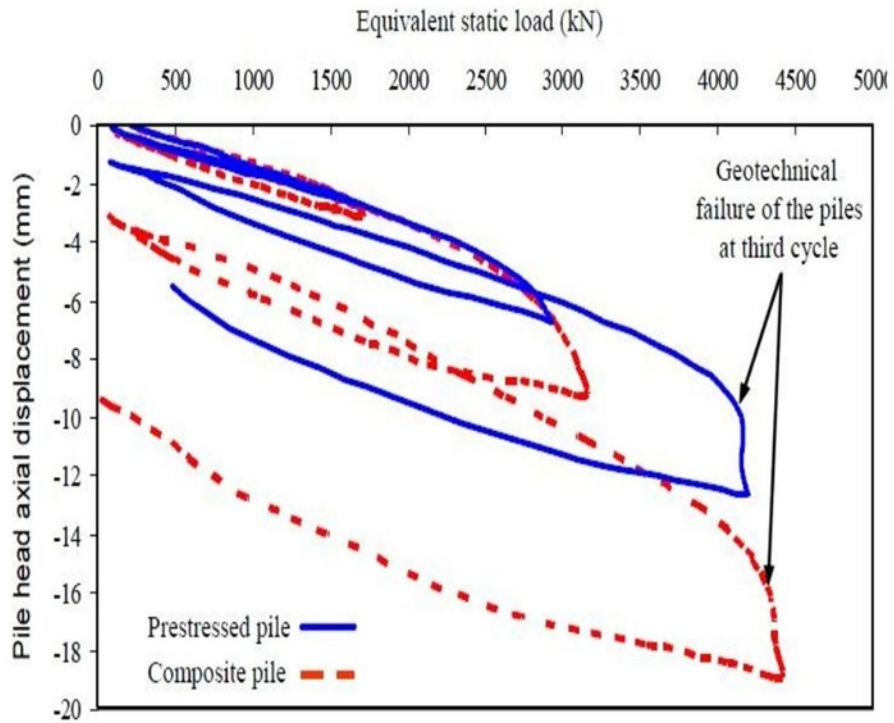
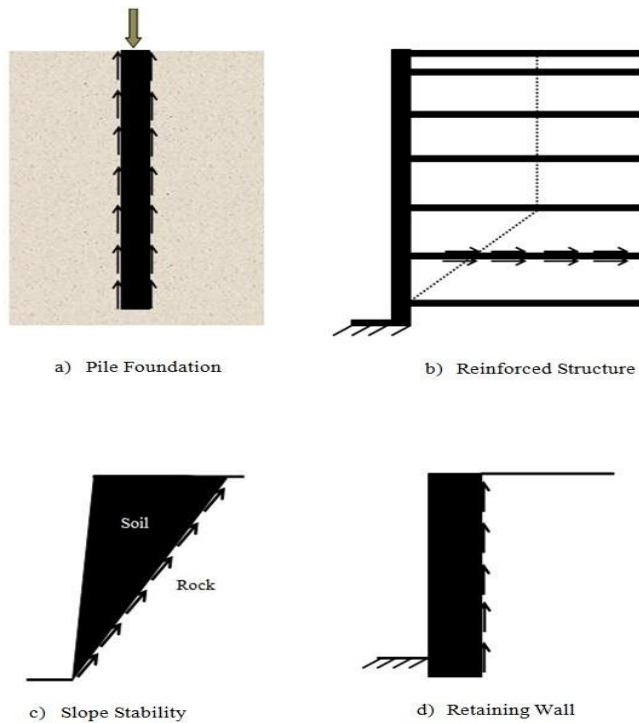


Figure 2.11 Cyclic behavior of prestressed and FRP composite pile (Fam et al., 2003)



CHAPTER 2: LITERATURE REVIEW

Figure 2.12 Soil interface responses (Shaia, 2013)

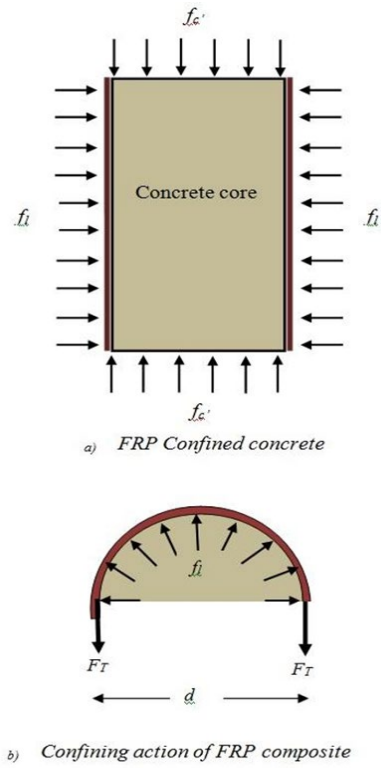


Figure 2.13 Illustration of Confining effect of FRP composites (Shaia, 2013)

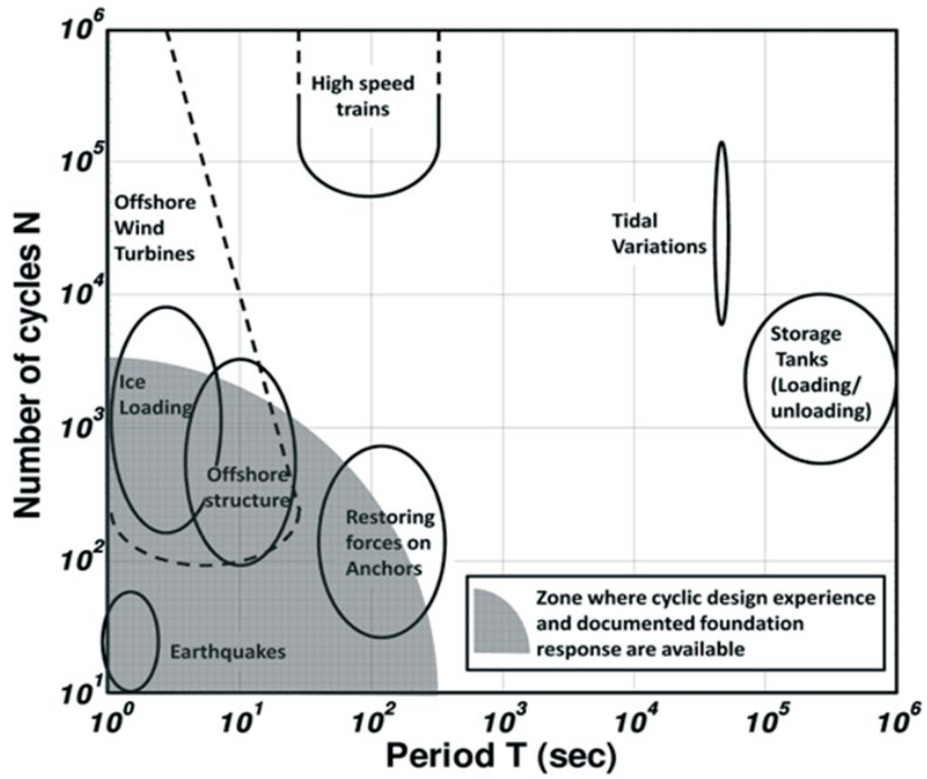


Figure 2.14 Typical cyclic loading characteristics (ANDERSEN, 2013)

CHAPTER 3: PHYSICAL MODEL PILE SYSTEM, MATERIALS, AND INSTRUMENTATIONS

3.1 Introduction

In this chapter, the setup and design of the physical model pile system especially developed for this study are described. The materials properties and instrumentations used for the physical model piles tests are presented. The basic physical properties of sea sand, sea water, SSC, and Hong Kong marine deposits are introduced. The granite rock-socket design, its mechanical properties, and roughness are then described. At the end, different instrumentations used for monitoring model pile tests are discussed.

3.2 Design and setup of the physical model pile system

An innovative physical model was designed and built at the Soil Mechanics Laboratory of The Hong Kong Polytechnic University (PolyU), as shown in Figure 3.1. This system is composed of a hydraulic loading actuator (GCTS, the United States of America) that can apply both static and cyclic loads axially on the pile head. A steel reaction frame was designed to support the hydraulic loading actuator. Model piles were constructed in a steel tank which has an inner diameter of 1 m and an inner depth of 1.326 m. A hardened gypsum layer was laid at the bottom of the steel tank in order to position and hold the granite rock at the center. A socket with a diameter of 100 mm and a depth of 160 mm was drilled into the rock with the inbuilt roughness of 5 mm based on Monash Roughness Model (Seidel and Collingwood, 2001).

CHAPTER 3: PHYSICAL MODEL PILE SYSTEM, MATERIALS, AND INSTRUMENTATIONS

A total of six model piles as shown in Figure 3.2 were tested for which geometric similarity was considered in the design. Table 3.1 presents the similarity relations for the model and prototype with a scaling ratio, n , which is defined by the ratio of diameter range of full-scale piles in the field to that in the physical model. Therefore, in this study, n varies from 6 to 25, as the common range of rock socketed pile diameter is from 0.6 to 2.5 m in Hong Kong (Zhan and Yin, 2000; Chen et al., 2021). The effects of density, gravity and rate dependency on the scaled model were not investigated in this study. Two linear variable differential transformers (LVDTs) were fixed to an independent reference frame near the pile head to monitor the overall pile head displacement of model piles under axial loading,

3.3 FRP composites

3.3.1 FRP tubes and rebars

A type of FRP composite called glass fiber reinforced polymers (GFRP) composites were used for different configuration of model piles. Three structural configurations (FRP tube confined, FRP rebar cage reinforced, and centered FRP rebar reinforced) were adopted for model piles. For Pile 1 and 2, a GFRP tube was used for the confinement of the SSC. For Pile 3 and 6, GFRP rebars cage fabricated with longitudinal rebars and circular stirrups were used. For Pile 4 and 5, a centered FRP rebar of 19 mm diameter was used. The GFRP rebars are made from unsaturated polyester resin and E-glass fiber coated with sand. The mechanical properties of 9.5 mm rebars used in pile 3 and 6 are listed in Table 3.2, provided by the manufacturer. The GFRP tubes used

CHAPTER 3: PHYSICAL MODEL PILE SYSTEM, MATERIALS, AND INSTRUMENTATIONS

in this study were filament-wound tubes made from E-glass fiber and vinyl ester resin with a fiber orientation of $\pm 45^\circ$.

3.3.2 Compression tests results

Axial compression tests were conducted on small specimens of FRP tubes cut from the same tube used in the model pile having 60 mm height and 3.5 mm thickness as shown in Figure 3.3. The specimens were instrumented with both axial and hoop strain gauges to measure the axial and hoop deformation under axial compression. A wet layup of FRP mixed with epoxy resins was applied on both upper and lower edges of the tube specimens to avoid fibers damage at the edges during compression. The axial and hoop elastic moduli obtained were 11.3 GPa and 10.1 GPa respectively. The FRP tubes with the same fiber orientation were observed to have the same mechanical properties in the hoop and axial directions.

3.4 Seawater sea-sand concrete (SSC)

3.4.1 Seawater and sea-sand basic properties

Sea sand and seawater were collected from Chek Lap Kok area of Hong Kong. Previous research studies indicated that sea-sand contains high contents of silt or clay particles which affect the workability and strength of concrete. Therefore, sea-sand was washed first to remove the clay particles and afterward it was kept in oven at 105 °C for 48 hours. The dried sand was then sieved through a 5 mm sieve to remove the unwanted large aggregates. The particle size distribution

CHAPTER 3: PHYSICAL MODEL PILE SYSTEM, MATERIALS, AND INSTRUMENTATIONS

curve of washed and unwashed sea-sand is presented in Figure 3.4. Besides, the natural seawater has PH and salinity of 7.92 and 32.241 g/L respectively. Table 3.3 shows the results of ion composition from ion chromatography (IC) tests.

3.4.2 *SSC unconfined compression tests*

A specially designed mix ratio of SSC was used for constructing model piles, as shown in Table 3.4. To increase workability and sustainability, superplasticizer and fly ash were employed in the mix design. To check the mechanical properties of the SSC, uniaxial compressive tests were carried out on cylindrical specimens with a height of 100 mm and a diameter of 50 mm. Strain gauges were adopted to measure the strain of each specimen. Figure 3.5 shows the axial stress-strain curve measured with strain gauges fitted well with the Comité Euro-International du Béton–Fédération International de la Précontrainte (CEB-FIP) Model Code (Code, 1990) developed on the relations formulated by (Sargin and Handa, 1969):

$$\frac{\sigma_c}{f_{cm}} = \frac{A\eta - \eta^2}{1 + (A-2)\eta}, \eta = \frac{\varepsilon_c}{\varepsilon_{cm}}, A = \frac{E_c}{f_{cm} / \varepsilon_{cm}} \quad (3.1)$$

where σ_c represents axial stress; f_{cm} stands for the peak stress ($f_{cm} = 31$ MPa); ε_c refers to axial strain; ε_{cm} denotes the strain at f_{cm} ($\varepsilon_{cm} = 0.00344$); E_c is the initial elastic modulus ($E_c = 22.9$ GPa). The tangent modulus $E_t = \frac{d\sigma_c}{d\varepsilon_c}$ varied according to Eq. (1), which was adopted for

calculating the axial force of piles based on the strain value measured by optic fiber sensors.

3.5 Hong Kong marine deposits (HKMD)

3.5.1 Basic physical properties

Hong Kong marine deposits are found in the sea surrounding Hong Kong SAR and based on the properties, it is considered a typical soft soil. Several infrastructure projects have been developed on the HKMD, one of which is the construction of the third runway at Hong Kong International Airport. Extensive research has been conducted in the past decades on the stress-strain behaviour of HKMD (Koutsoftas et al., 1987; Yin and Graham, 1999; Yin et al., 2002; Feng and Yin, 2017). The findings indicate that HKMD possess significant rheology effects and a highly plastic soil.

The HKMD used in this study was collected from the coastal area of Lantau Island in Hong Kong, which is dark grey in color with small amount of shell fragments. To prevent any potential disturbance and uncertainty in the experiments, particles and shells of size 2 mm or larger were removed prior to testing. Table 3.5 listed the basic properties of HKMD used in this study. HKMD used in this study was from same origin and similar properties as that used by Wu (2021). Therefore, the oedometer and triaxial test data was adopted from Wu (2021) work.

3.5.2 Oedometer tests

The compressibility properties of HKMD were determined through a series of multi-stage loading (MSL) oedometer tests in the laboratory. The multi-stage loading tests details are listed in the Table 3.6. The specimens used in oedometer tests were collected from three different locations of HKMD subsurface. The vertical strain responses with time of the HKMD specimens (S1, S2, and S3) under different loading stages are shown in Figures 3.6 to 3.9. Different

CHAPTER 3: PHYSICAL MODEL PILE SYSTEM, MATERIALS, AND INSTRUMENTATIONS

researchers and studies define and represent the compression and rebounding parameters of oedometer tests in different ways, however Feng and Yin (2017) notations and definitions will be adopted in this study for the interpretation of results. Under typical loading conditions, the slope of the linear part of the strain with log scaled effective stress curve is defined as compression index and is given as:

$$\frac{C_c}{V} = \frac{\Delta \varepsilon}{\Delta \log(\sigma'_z)} \quad (3.2)$$

where $\Delta \varepsilon$ denotes the strain increment; V represents the specific volume and can be defined as; $V = 1 + e_0$. In over-consolidated conditions, the slope of the strain with log scaled effective stress curve is defined as rebounding index, C_r/V . The oedometer tests results can also be interpreted in terms of compression parameter λ/V and rebounding parameter κ/V with a relationship given as:

$$\frac{\lambda}{V} = \frac{C_c}{\ln(10)V} = \frac{C_c}{2.3V} \quad (3.3)$$

$$\frac{\kappa}{V} = \frac{C_r}{\ln(10)V} = \frac{C_r}{2.3V} \quad (3.4)$$

Longer-duration testing can be utilised to calculate the creep coefficient, ψ/V , and is determined from the slope of the linear fitting line of vertical strain with time (ln scale). The relationship between creep coefficient and secondary consolidation coefficient C_{ae}/V is defined by Yin and Graham (1994) and Feng and Yin (2017) in their studies, given as:

$$\frac{\psi}{V} = \frac{C_{ae}}{\ln(10)V} = \frac{C_{ae}}{2.3V} \quad (3.5)$$

CHAPTER 3: PHYSICAL MODEL PILE SYSTEM, MATERIALS, AND INSTRUMENTATIONS

The results of linear fitting of “ ψ/V ” for creep behaviour of tested specimens, S1, S2, and S3 are shown in Figure 3.9. Table 3.7 lists the average values of ψ/V of the tested specimens.

3.5.3 Triaxial tests

Following the British standard BS 1377-8 (1990), consolidated undrained (CU) triaxial tests were carried out on HKMD specimens. The porewater pressure and deviator stress results with axial strain under different confining pressures are shown in the Figure 3.10. Similarly, under different confining pressures, effective stress paths in relation to mean effective stress, p' , and deviator stress, q , are shown in the Figure 3.10(c). The relations for mean effective stress and deviator stress are given as:

$$p' = \frac{(\sigma'_1 + 2\sigma'_3)}{3} \quad (3.6)$$

$$q = \sigma'_1 - \sigma'_3 \quad (3.7)$$

where σ'_1 and σ'_3 represents the effective major and minor principal stresses.

3.6 Granite rock-socket and gypsum plaster

3.6.1 Rock socket design and roughness

A socket 100 mm in diameter and 150 mm long was drilled at the centre of the granite rock. The rock socket was manufactured from an intact rock mass with very high strength and stiffness workshop with predetermined roughness as specified in Figure 3.11. Thus, the roughness of socket for each model pile was kept identical. The average roughness of 5 mm was determined by Monash Roughness Model as introduced by Seidel and Collingwood (2001). The ratio of socket length to diameter = 1.5 which is within a common range in engineering practice recommending minimum socket length of 1 to 2 times the pile diameter (Ng et al. 2001; BD 2017). The rock base was fixed at centre on the bottom of the steel tank by hardened gypsum plaster. The rock base was designed to be much larger than the piles to allow stresses to distribute uniformly in a similar way as in the field.

3.6.2 Uniaxial compression strength (UCS) tests

The granite rock properties were determined according to ASTM C469 under uniaxial compressive tests on four granite rock specimens in height and diameter of 100 mm and 50 mm respectively. Two vertical strain gauges and one horizontal strain gauge were glued properly on each specimen to accurately measure strain development under compression. The modulus and strength were determined based on the average values of four compressive tests.

The Young's modulus of 42 GPa was determined for granite rock through four uniaxial compression tests. Based on the compression curve, granite specimens experienced crack closing

CHAPTER 3: PHYSICAL MODEL PILE SYSTEM, MATERIALS, AND INSTRUMENTATIONS

and linear elastic stages in sequence, then followed by a sudden failure after crack initiation, as shown in Figure 3.12. Considering that the relatively low shaft friction in the physical model compared to the loading level in UCS test, the secant modulus at the transition point connecting crack closing and linear elastic stages was calculated as the Young's modulus (42 GPa). The compressive strength of 177 MPa was determined based on the average values at which loading the specimens failed suddenly. The rock was classified as Grade I rock (Geoguide 3, HK) based on the UCS results. Similarly based on ASTM C469, the Young's modulus and uniaxial compressive strength through six specimens of the gypsum plaster were determined as 22 GPa and 66 MPa, respectively.

3.7 Instrumentations

3.7.1 Distributed OFDR sensing

Among the DOFS techniques, OFDR is an advanced sensing method based on the principle of Rayleigh backscattering. The Rayleigh scattering light is quasi-elastic scattering light whose frequency will not drift during scattering in the fiber. When a small strain or temperature variation occurs in the fiber, it causes a change in refractive index inducing shift in the local spectrum. Figure 3.13 illustrates that when a light emits from a tunable laser source, it is divided into two branches (i.e., the reference light and measurement light) through an optical coupler. Rayleigh backscattered light is generated when the measurement light passes through measuring fiber and combines with the backscattered light from reference branch creating an interference signal which can be detected and demodulated by optical detector. The Rayleigh backscattering

CHAPTER 3: PHYSICAL MODEL PILE SYSTEM, MATERIALS, AND INSTRUMENTATIONS

spectrum shifts with the changes in strain and temperature of the optical fiber, expressed by the given relation:

$$\Delta\nu = C_\varepsilon\Delta\varepsilon + C_T\Delta T \quad (3.8)$$

where $\Delta\nu$ is Rayleigh spectrum shift; $\Delta\varepsilon$ represent strain change; ΔT stands for temperature change; and C_ε and C_T are the calibration coefficients of strain and temperature change, respectively, calibrated as $-0.15 \text{ GHz}/\mu\varepsilon$ and $-1.25 \text{ GHz}/^\circ\text{C}$, respectively (J. Wu et al., 2020). The strain or temperature dependent spectrum can be calculated relatively between the reference signal (data measured under zero strain and room temperature condition) and measurement signal (data measured when strain or temperature changes). In this study the temperature change was neglected due to constant temperature conditions kept in the laboratory where tests were conducted.

In this study, OFDR based interrogator (OSI-I, Junlong Technology Ltd., China) was used. The interrogator operates in two different modes relying on the maximum length of fiber. In standard mode, it can provide strain reading at each 1 mm which is the spatial resolution for maximum 50 m length of fiber (sensing range). In long range mode, the spatial resolution of the interrogator reduces to 10 mm for the maximum sensing range of 100 m. For both modes, a high strain sensing accuracy of $\pm 1 \mu\varepsilon$ can be achieved. The data acquisition rate depends on the sensing range of the fiber and required spatial resolution. For example, in 1 mm spatial resolution mode, the interrogator approximately takes around 6 seconds to sample strain data for 30 m length of the fiber. A smaller sampling time can be achieved by decreasing the length of fiber or by reducing spatial resolution.

3.7.2 *Multiplexed FBGs sensors*

Multiplexed FBGs were also instrumented in model piles on account of their high resolution and data acquisition frequency for cyclic loads (Chen et al. 2021; Hong et al. 2022). A multiplexed FBG system consists of multiple Fiber Bragg Gratings (FBGs) inscribed in a single optical fiber at different positions. Each FBG reflects light at a specific wavelength, enabling strain and temperature measurements at various locations along the fiber.

The sensing principle of FBG optic sensors depends on the wavelength λ shift of the light which passes through the grating section of the fiber as shown in Figure 3.14. A specific wavelength of light is reflected called Bragg's wavelength caused by the variations in strain and temperature of the optical fiber with correlation given as

$$\frac{\Delta\lambda}{\lambda_i} = c_1\Delta\varepsilon + c_2\Delta T \quad (3.9)$$

where i is the initial state; $\Delta\lambda$ stands for wavelength change; ΔT refers to temperature change; $\Delta\varepsilon$ denotes the change in strain; c_1 and c_2 are the coefficients of strain and temperature change, respectively. In this study, the value of c_1 was taken as 0.78 whereas temperature change was neglected due to constant temperature conditions in the laboratory.

3.7.3 *Conventional electronic transducers*

In the sixth physical model pile test, the consolidation behaviour of the HKMD was monitored with conventional transducers which operates on voltage signals. Three different types of transducers were used such as pore pressure transducers (PPTs), earth pressure cells (EPCs), and

CHAPTER 3: PHYSICAL MODEL PILE SYSTEM, MATERIALS, AND INSTRUMENTATIONS

linear variable differential transformers (LVDTs). The specifications and details of these transducers are discussed in Section 6.2.2 of Chapter 6.

3.8 Summary

The setup and design of the physical model pile system and material's basic properties are introduced in this chapter. Under uniaxial compression tests, the FRP tubes with the same fiber orientation were observed to have the same mechanical properties in the hoop and axial directions. Natural seawater has a PH and salinity of 7.92 and 32.241 g/L respectively. The axial stress-strain curve of small concrete cylinders tests measured with strain gauges fitted well with the Comite Euro-International du Beton–Federation International de la Precontrainte (CEB-FIP) Model Code (Code, 1990). The basic properties of HKMD show significant rheological effects indicating it as a highly plastic soil. For the rock-socket, the average roughness of 5 mm was determined by Monash Roughness Model as introduced by Seidel and Collingwood (2001) and the rock was classified as Grade I rock (Geoguide 3, HK) based on the UCS results.

CHAPTER 3: PHYSICAL MODEL PILE SYSTEM, MATERIALS, AND INSTRUMENTATIONS

Table 3.1 Similarity index of the physical model system

Physical parameter	Dimension	Model/ Prototype
Diameter of pile	L	$1 / n$
Length of pile	L	$1 / n$
Area	L^2	$1 / n^2$
Displacement	L	$1 / n$
Axial force	MLT^{-2}	$1 / n^2$
Strength	$ML^{-1}T^{-2}$	1
Young's modulus	$ML^{-1}T^{-2}$	1
Shear modulus	$ML^{-1}T^{-2}$	1

Table 3.2 Mechanical properties of the GFRP rebars

Material	Diameter (mm)	Failure load (kN)	Tensile strength (MPa)	Modulus of elasticity (GPa)	Ultimate strain
GFRP Rebar	9.5	71.6	600	50.8	0.0199

CHAPTER 3: PHYSICAL MODEL PILE SYSTEM, MATERIALS, AND INSTRUMENTATIONS

Table 3.3 Chemical compositions of natural seawater in Chek Lap Kok, Hong Kong

Ion	Cl ⁻	Br ⁻	SO ₄ ²⁻	Li ⁺	Na ⁺	K ⁺	Mg ²⁺	Ca ²⁺	Salinity
(g/L)	18.153	0.066	1.675	0.0007	10.419	0.354	1.215	0.358	32.24

Table 3.4 Mix design of SSC

Cement	Fly ash	Seawater	Sea-sand	Superplasticizer
0.75	0.25	0.6	3.25	0.013

Table 3.5 Basic physical properties of HKMD

Specific gravity, G_s	Liquid limit, LL (%)	Plastic limit, PL (%)	Plasticity index, PI (%)
2.65	43.2	22.6	20.6

Table 3.6 Loading program of oedometer tests (Wu, 2021)

Test specimen	Applied			Duration of			Applied			Duration of		
	No.	loading (kPa)	each loading (day)	No.	loading (kPa)	each loading (day)	No.	loading (kPa)	each loading (day)	No.	loading (kPa)	each loading (day)
S1	1	5	3	8	10	1	15	100	1			

CHAPTER 3: PHYSICAL MODEL PILE SYSTEM, MATERIALS, AND INSTRUMENTATIONS

	2	10	3	9	20	1	16	50	1
	3	20	3	10	50	1	17	100	1
	4	50	3	11	100	1	18	200	1
	5	100	7	12	200	7	19	400	1
	6	50	1	13	400	7	20	800	6
	7	20	1	14	200	1	Total test duration of 51 days		
<hr/>									
	1	5	1	8	50	1			
	2	10	1	9	100	1			
	3	20	1	10	200	7			
S2	4	50	1	11	400	10			
	5	100	1	12	200	1			
	6	50	1	13	100	1			
	7	20	1	14	50	1	Total test duration of 29 days		
<hr/>									
	1	5	1	8	50	1			
	2	10	1	9	100	1			
	3	20	1	10	200	7			
S3	4	50	1	11	400	10			
	5	100	1	12	200	1			
	6	50	1	13	100	1			

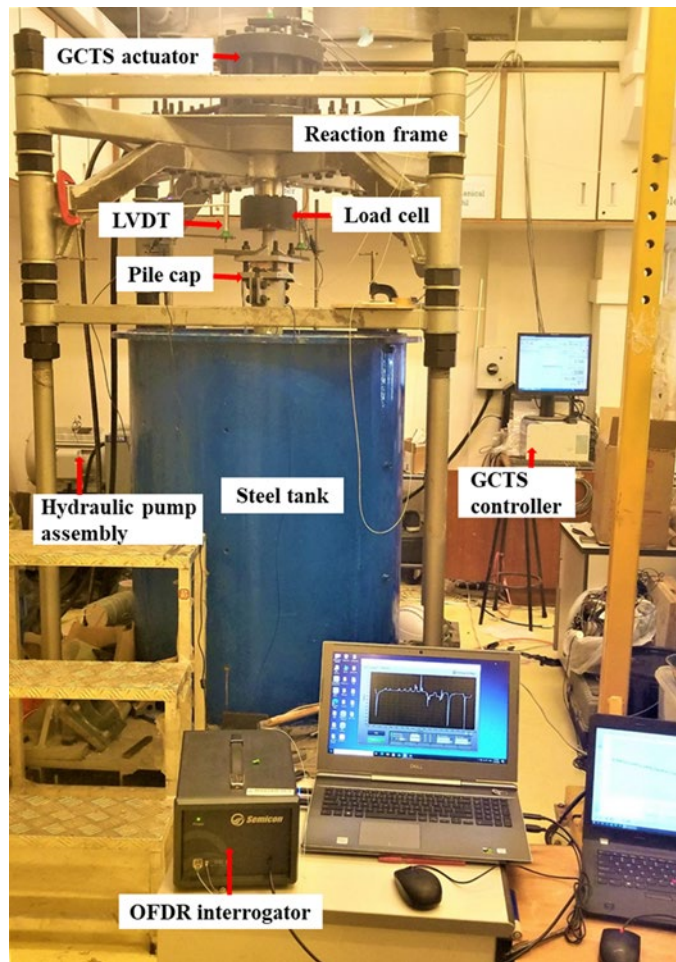
CHAPTER 3: PHYSICAL MODEL PILE SYSTEM, MATERIALS, AND INSTRUMENTATIONS

7 20 1 14 50 1 Total test duration of 29 days

Table 3.7 Quantified compressibility parameters of tested HKMD specimens (Wu, 2021)

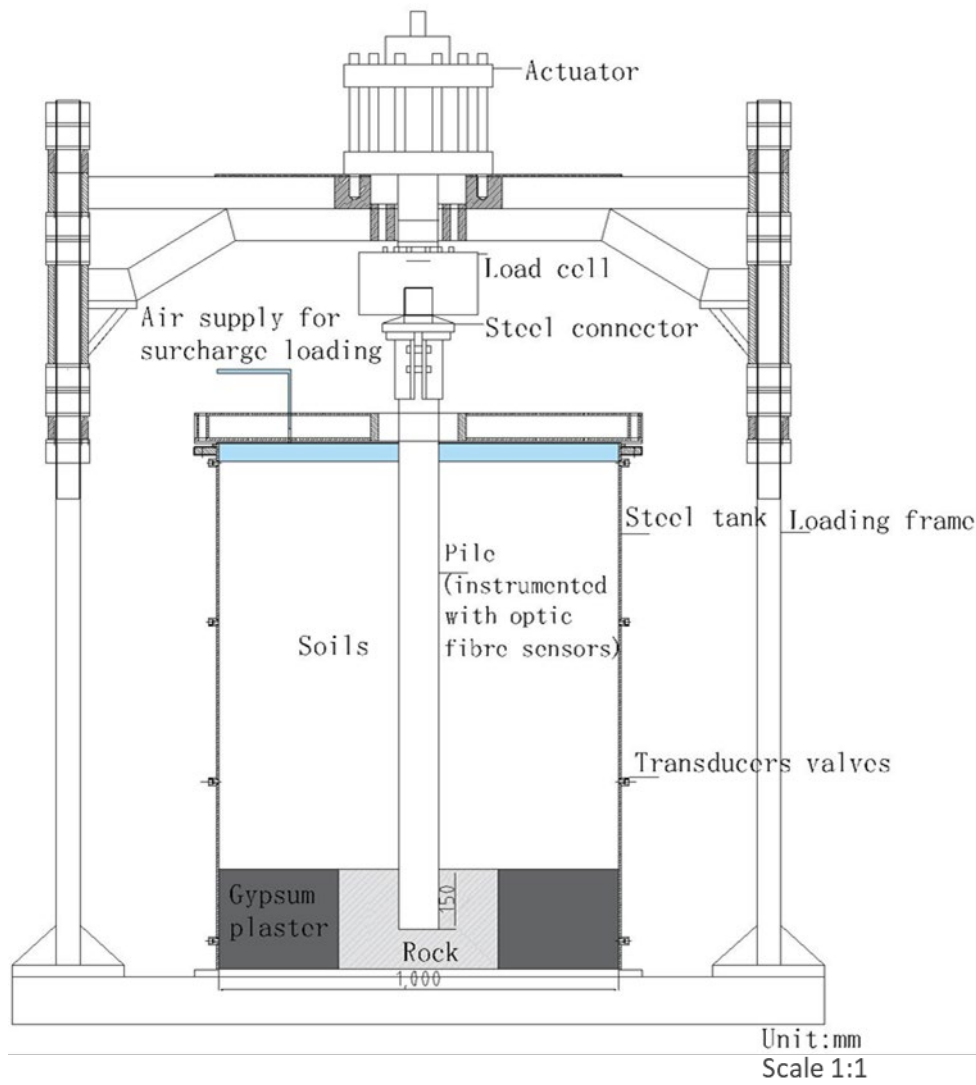
Specimen	κ/V	λ/V	ψ/V	C_r/V	C_c/V	C_{ae}/V	C_{ae}/C_c
S1	0.0119	0.1159	0.0016	0.0274	0.2666	0.00071	0.00266
	0.0163			0.0375			
S2	0.0108	0.0991	0.0021	0.0248	0.2279	0.00092	0.00404
	0.0158			0.0363			
S3	0.0095	0.1051	0.0024	0.0219	0.2418	0.00102	0.00422
	0.0167			0.0384			

CHAPTER 3: PHYSICAL MODEL PILE SYSTEM, MATERIALS, AND INSTRUMENTATIONS



(a)

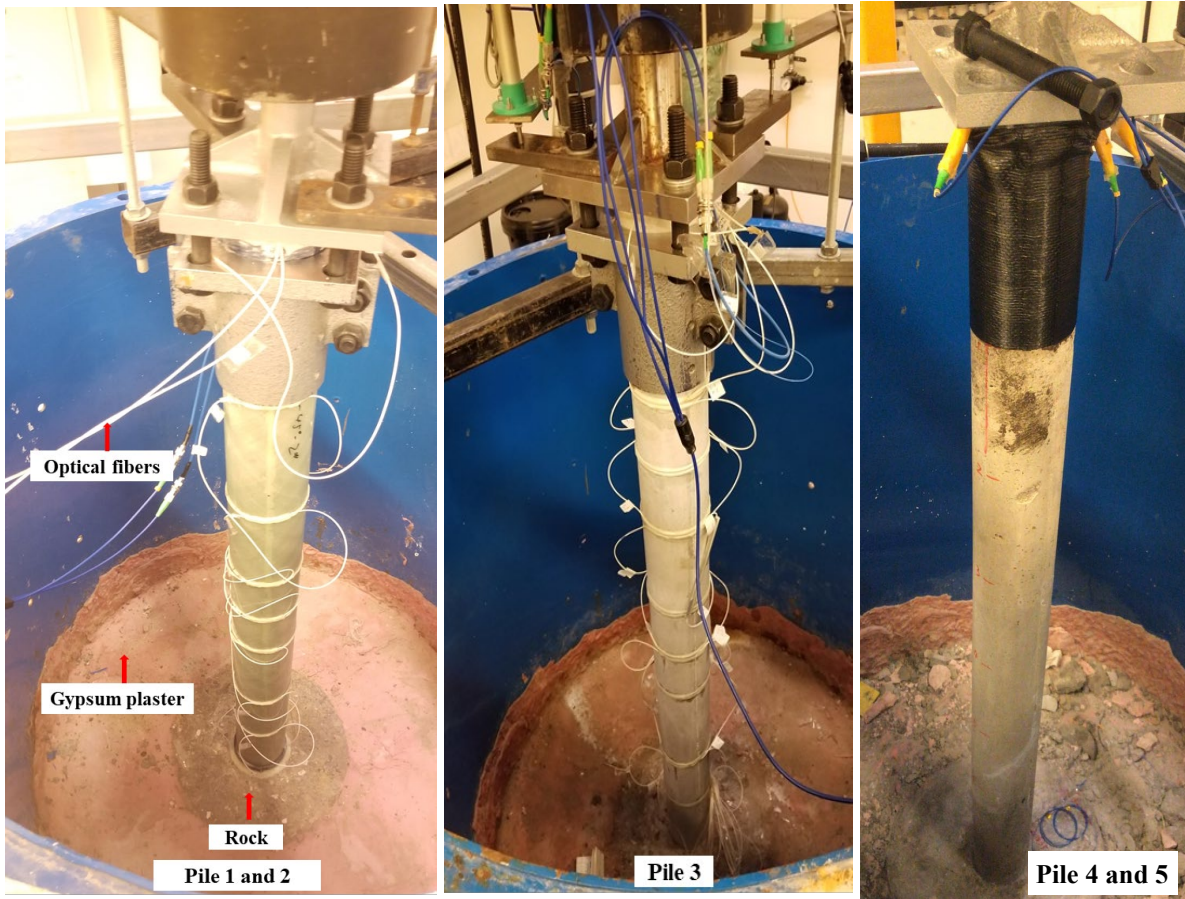
CHAPTER 3: PHYSICAL MODEL PILE SYSTEM, MATERIALS, AND INSTRUMENTATIONS



(b)

Figure 3.1 Design and photo of the physical model pile system: (a) photo and (b) illustration

CHAPTER 3: PHYSICAL MODEL PILE SYSTEM, MATERIALS, AND INSTRUMENTATIONS

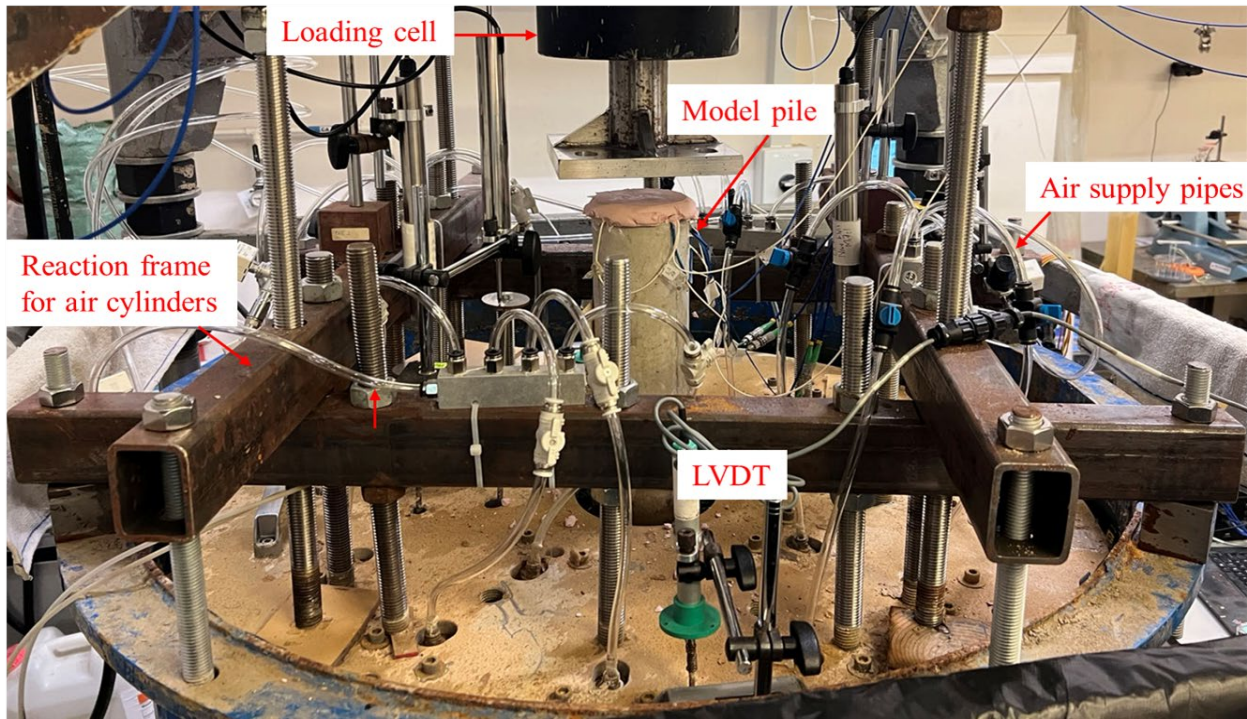


(a)

(b)

(c)

CHAPTER 3: PHYSICAL MODEL PILE SYSTEM, MATERIALS, AND INSTRUMENTATIONS



(d)

Figure 3.2 Photos of the physical model piles: (a) Pile 1 or 2; (b) Pile 3; (c) Pile 4 or 5; and (d) Pile 6

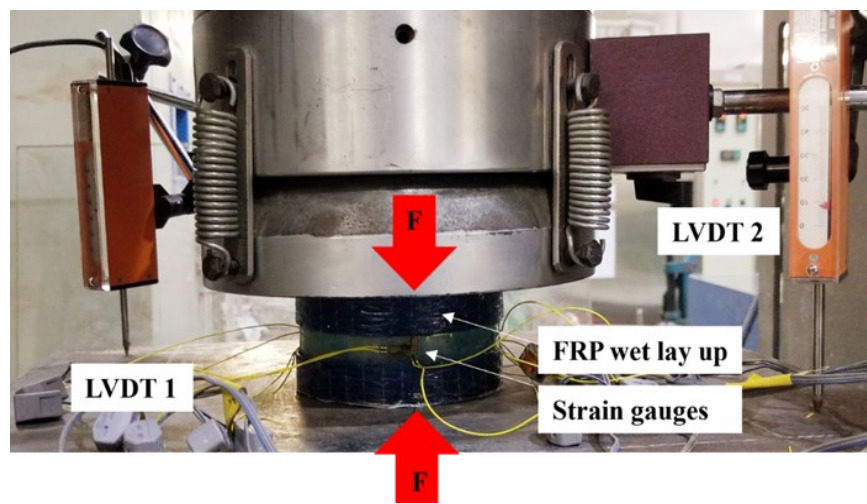


Figure 3.3 GFRP short tubes under compression

CHAPTER 3: PHYSICAL MODEL PILE SYSTEM, MATERIALS, AND INSTRUMENTATIONS

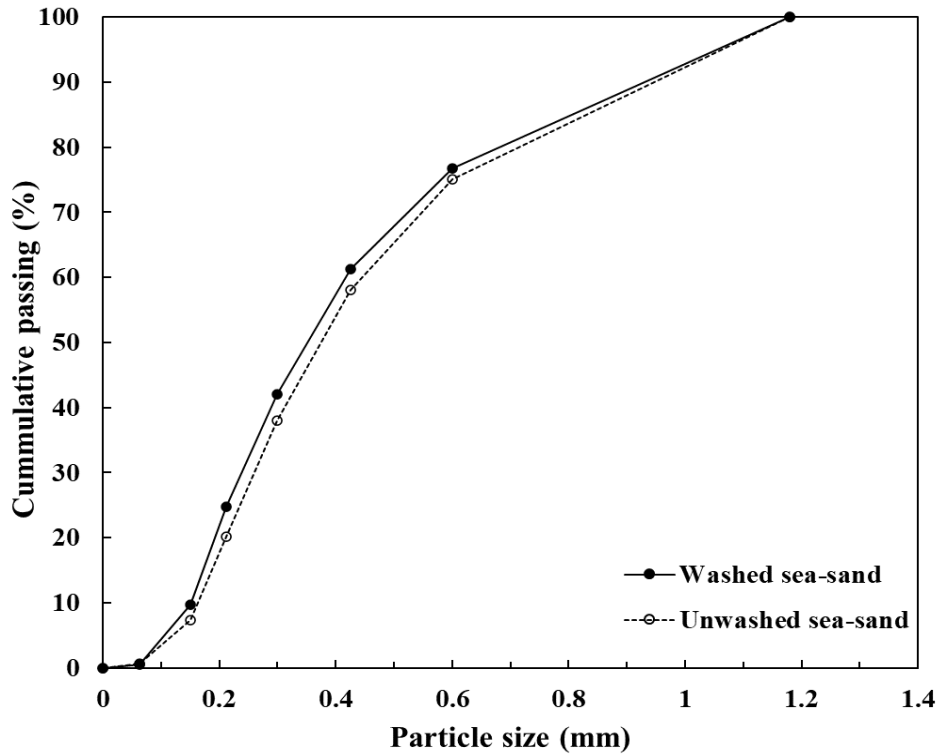


Figure 3.4 Particle size distribution curves of washed and unwashed sea-sand

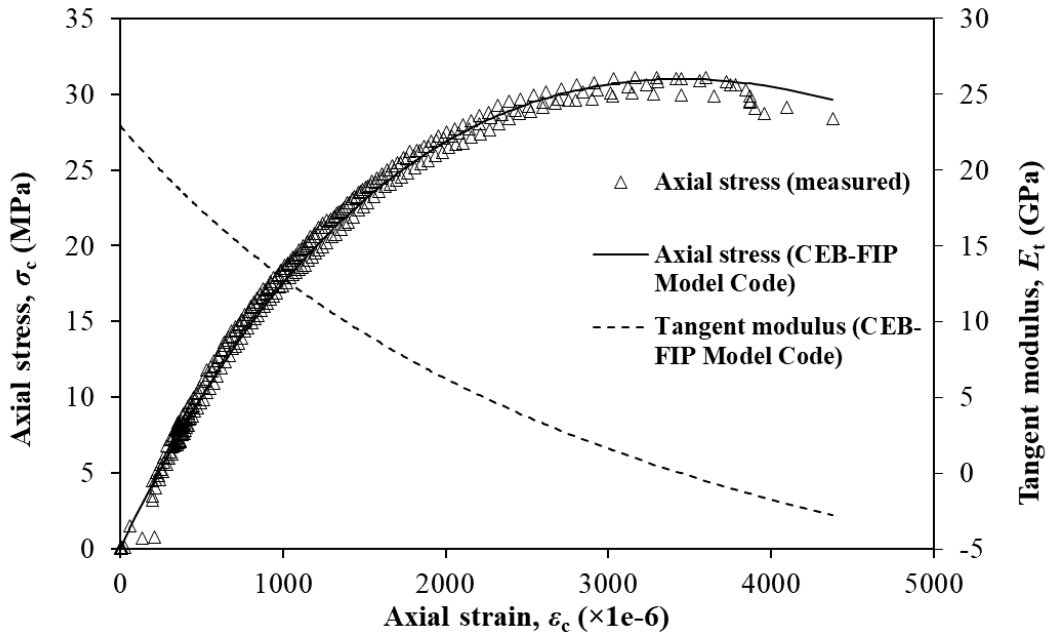
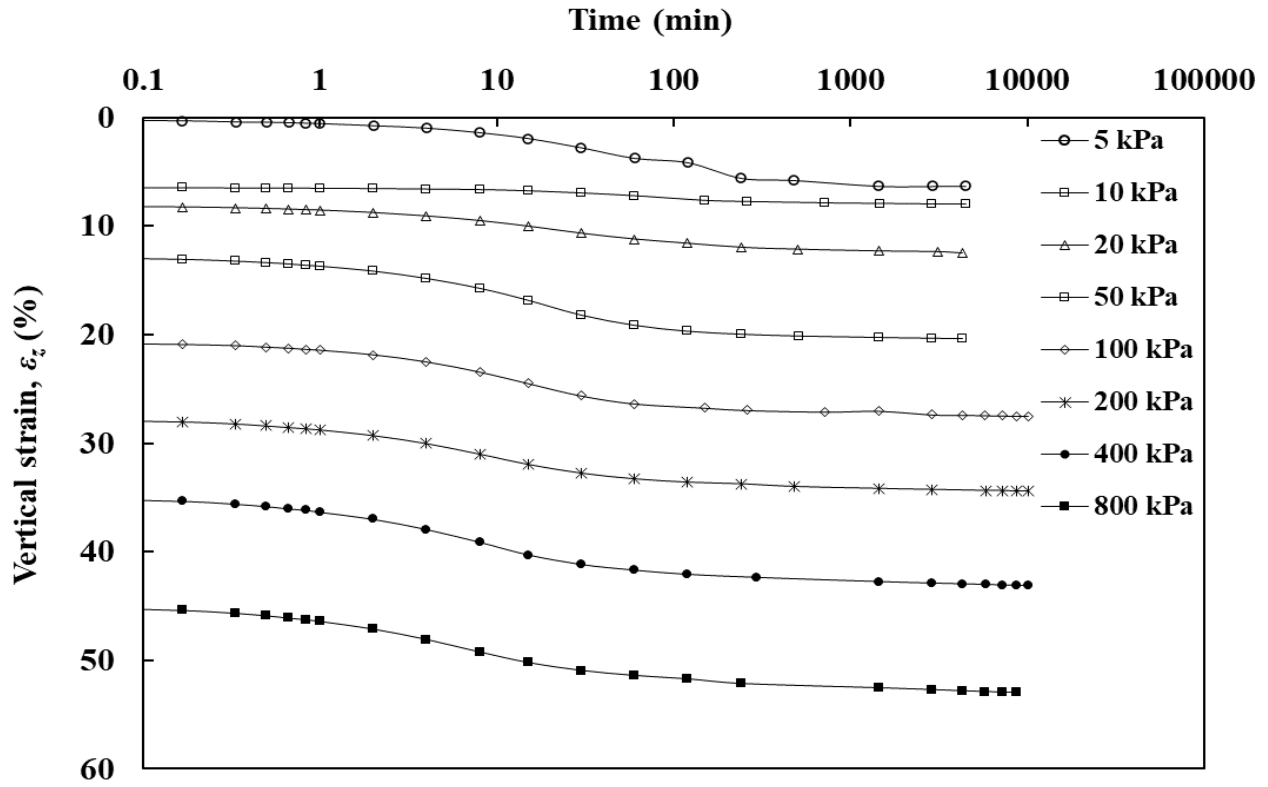
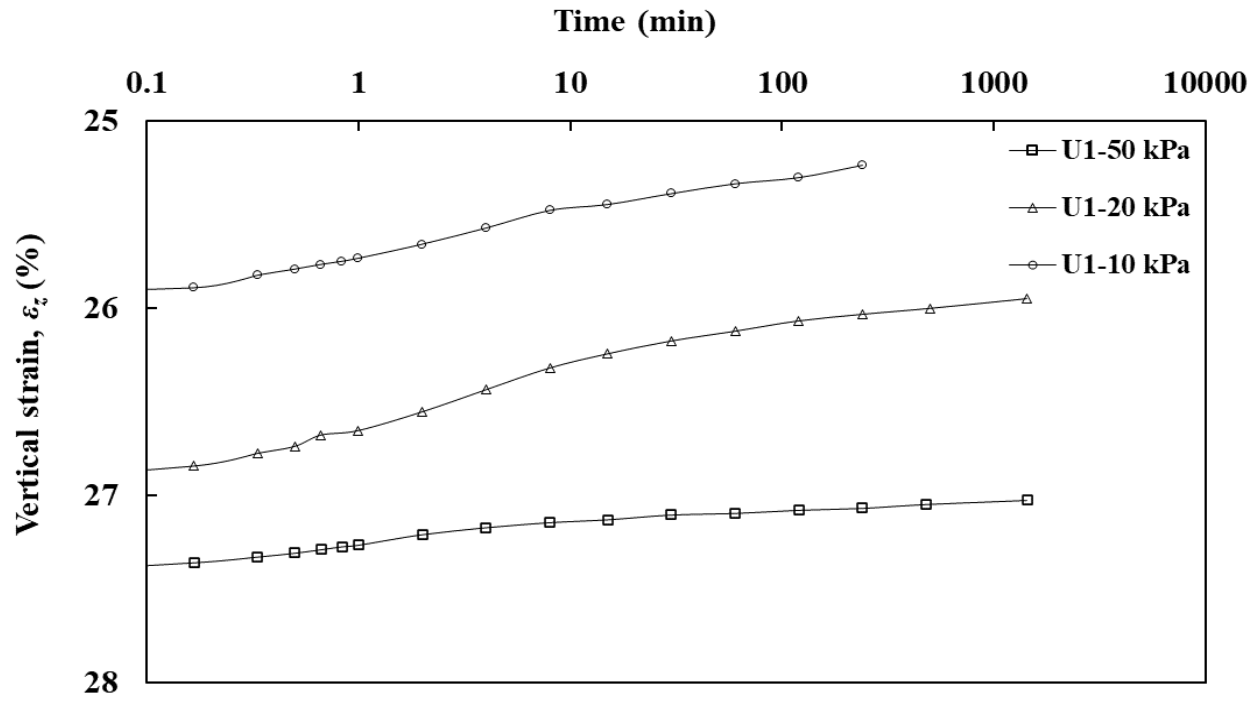


Figure 3.5 Stress-strain curves of measured data, fitting, and E_t of SSC

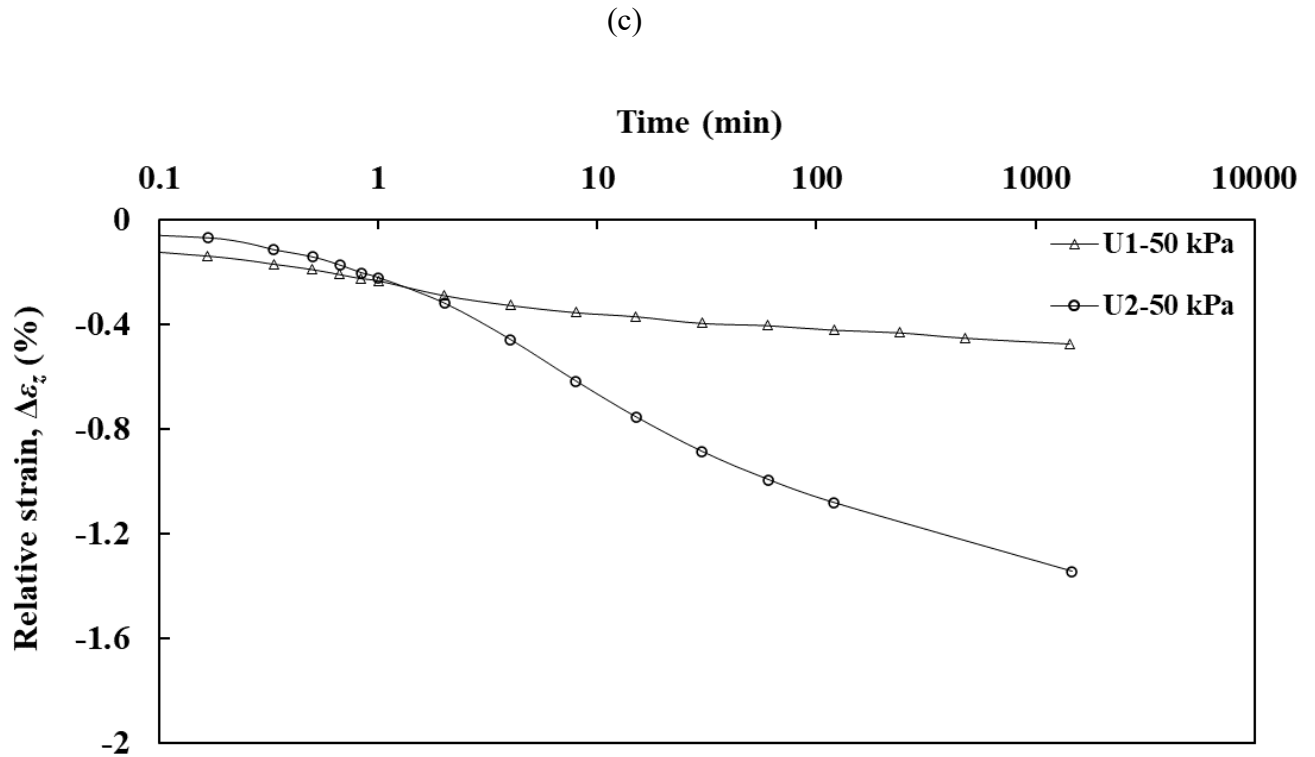
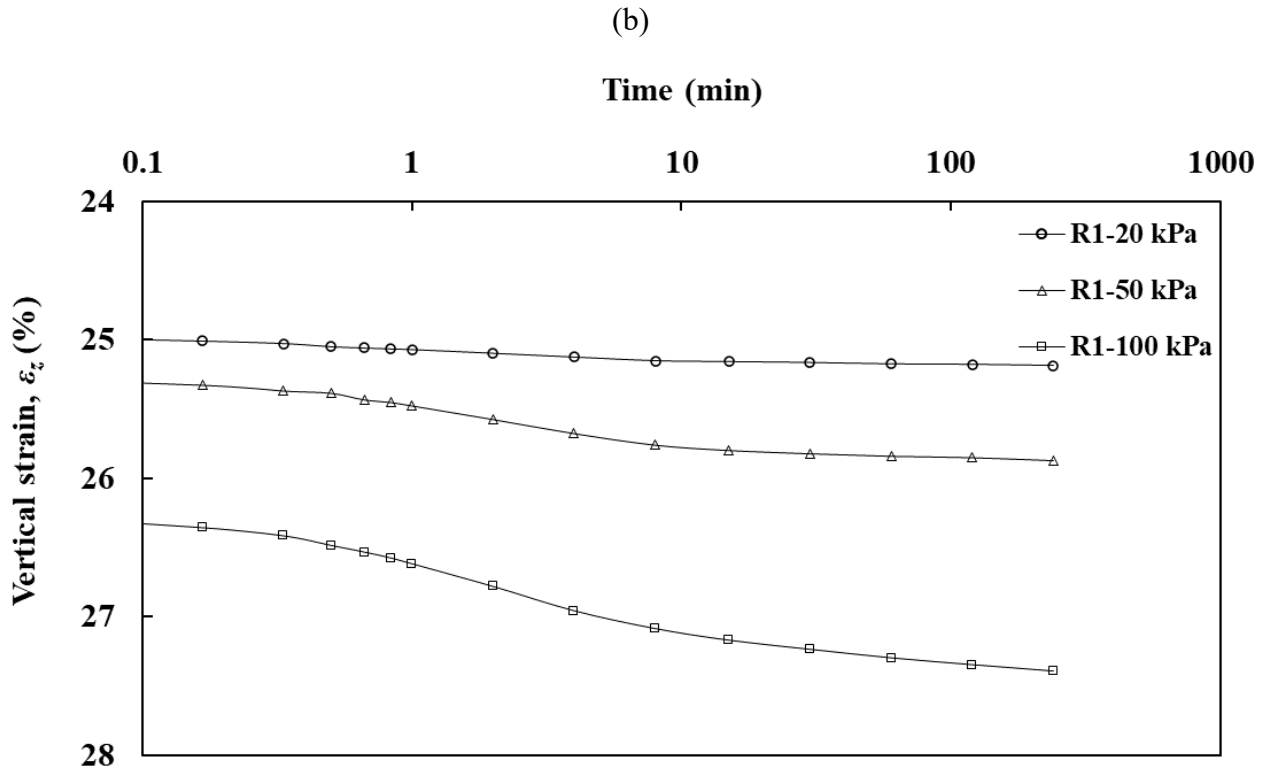
CHAPTER 3: PHYSICAL MODEL PILE SYSTEM, MATERIALS, AND INSTRUMENTATIONS

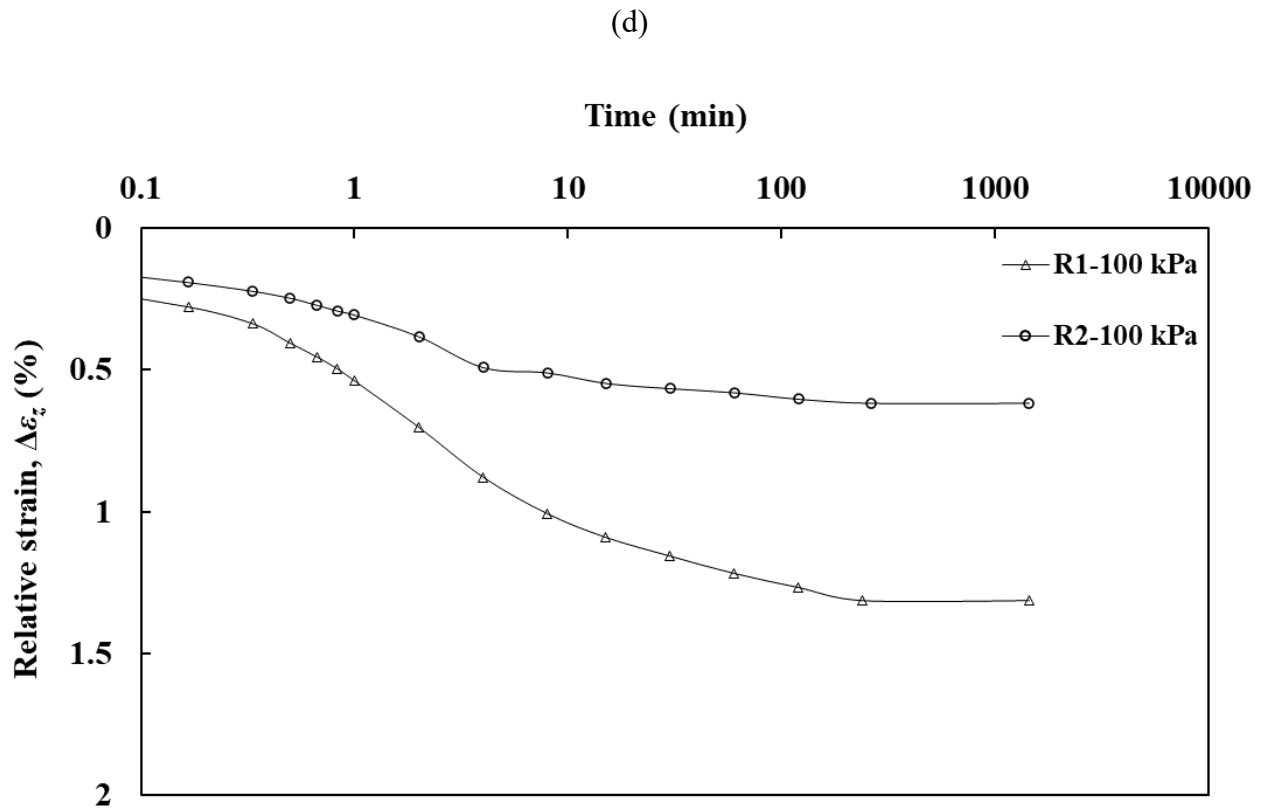


(a)



CHAPTER 3: PHYSICAL MODEL PILE SYSTEM, MATERIALS, AND INSTRUMENTATIONS

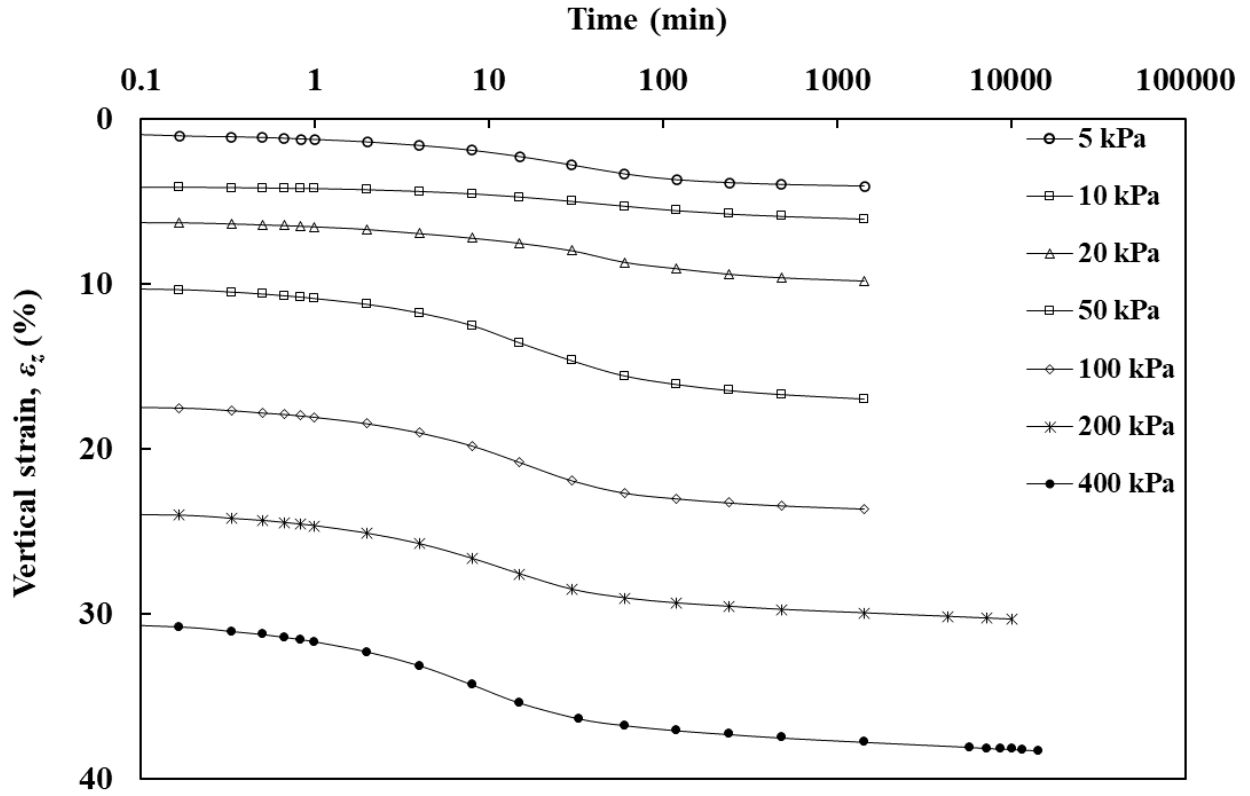




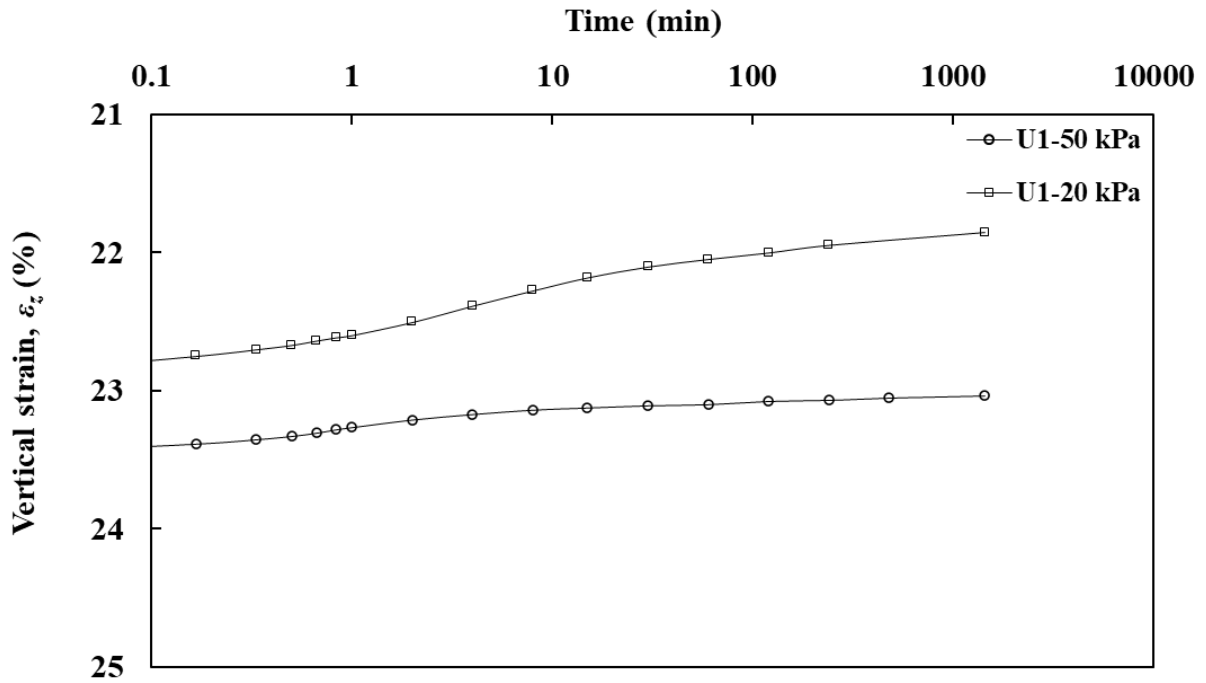
(e)

Figure 3.6 Variation of vertical strain with time for S1 specimen: (a) loading; (b) unloading (U1 represents the first unloading stage); (c) reloading (R1 represents the first reloading stage); (d) effect of unloading; and (e) effect of reloading (Wu, 2021)

CHAPTER 3: PHYSICAL MODEL PILE SYSTEM, MATERIALS, AND INSTRUMENTATIONS

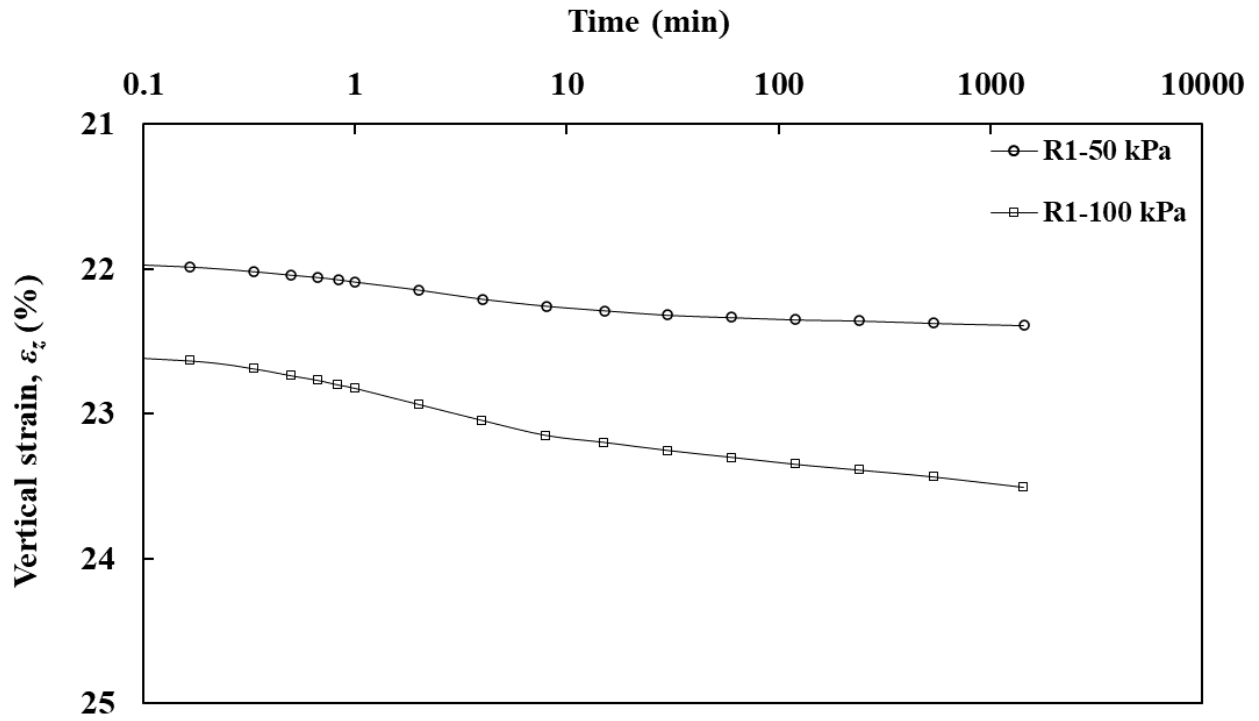


(a)

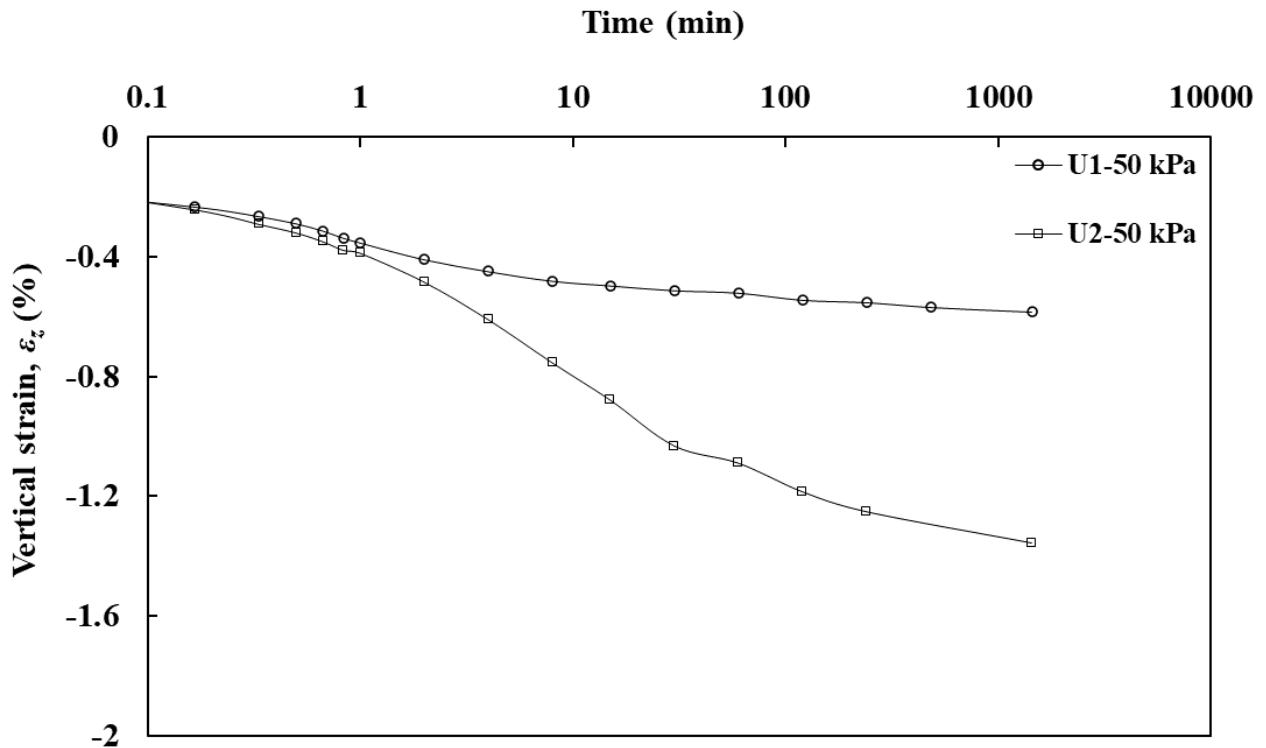


CHAPTER 3: PHYSICAL MODEL PILE SYSTEM, MATERIALS, AND INSTRUMENTATIONS

(b)



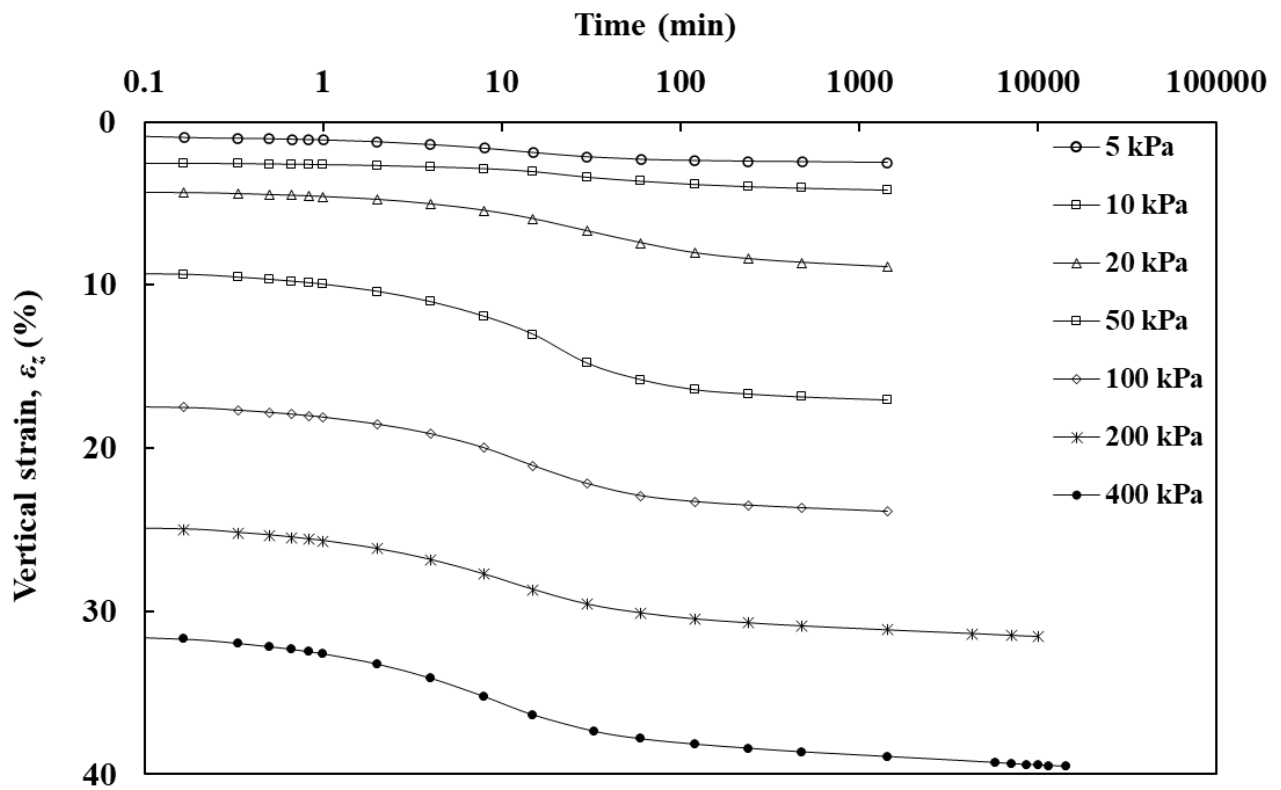
(c)



CHAPTER 3: PHYSICAL MODEL PILE SYSTEM, MATERIALS, AND INSTRUMENTATIONS

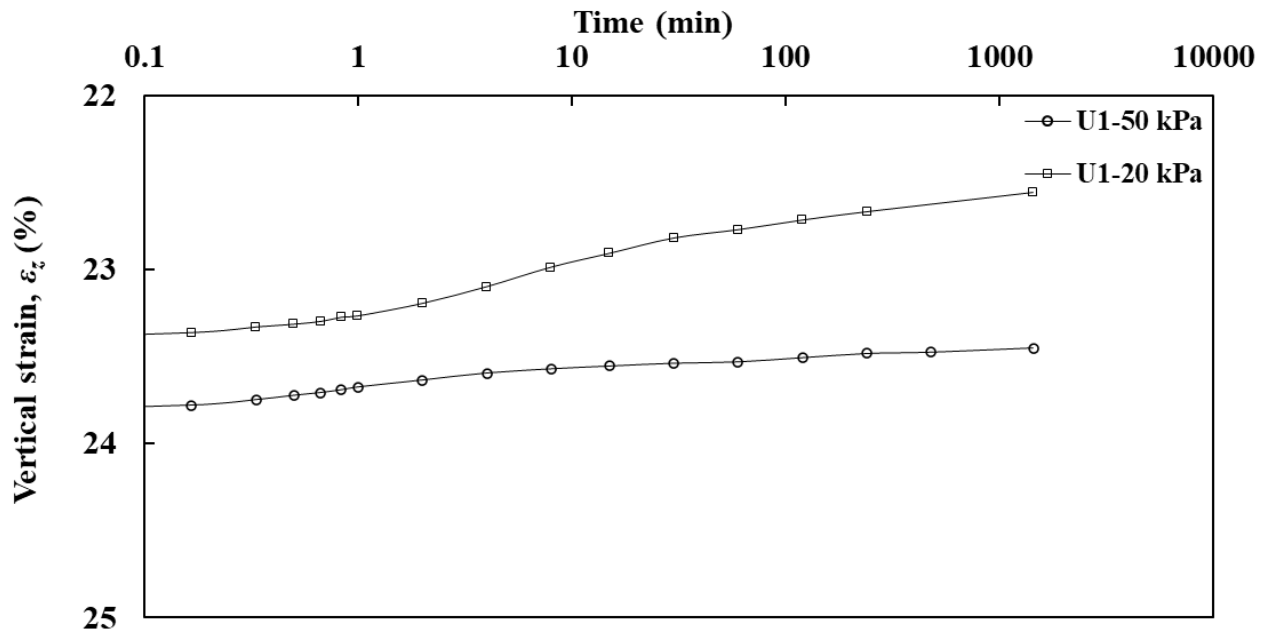
(d)

Figure 3.7 Variation of vertical strain with time for S2 specimen: (a) loading; (b) unloading (U1 represents the first unloading stage); (c) reloading (R1 represents the first reloading stage); and (d) effect of unloading (Wu, 2021)

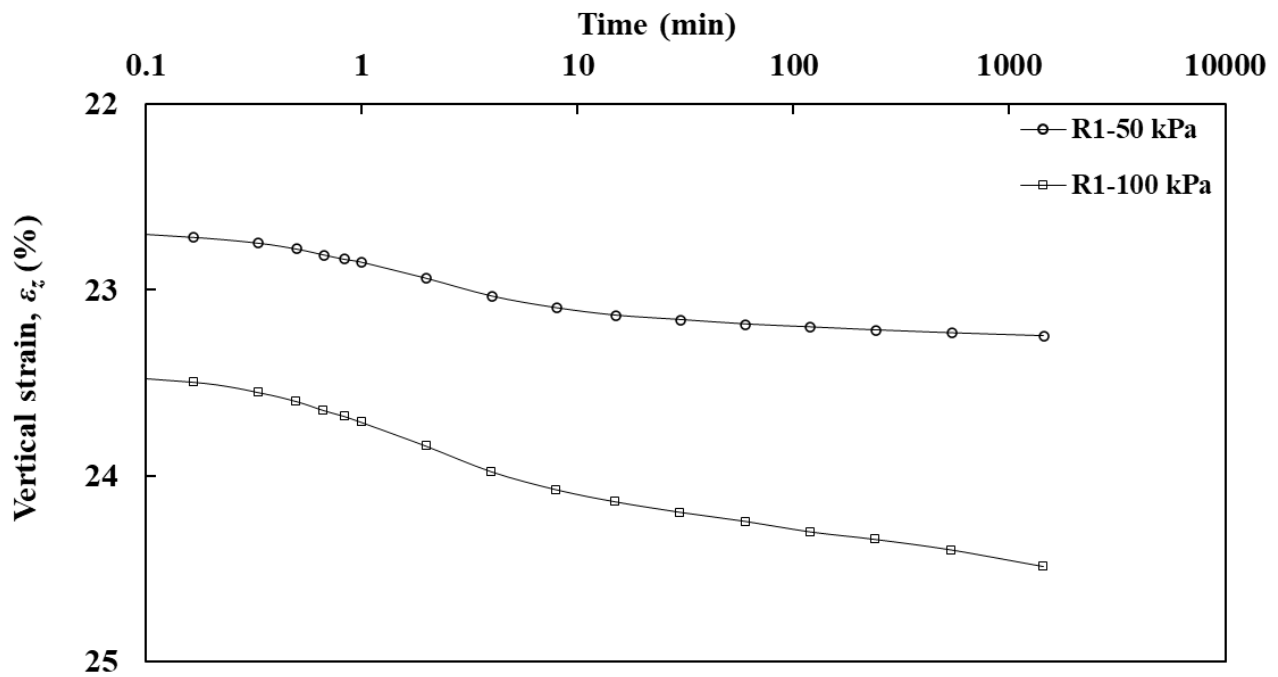


(a)

CHAPTER 3: PHYSICAL MODEL PILE SYSTEM, MATERIALS, AND INSTRUMENTATIONS

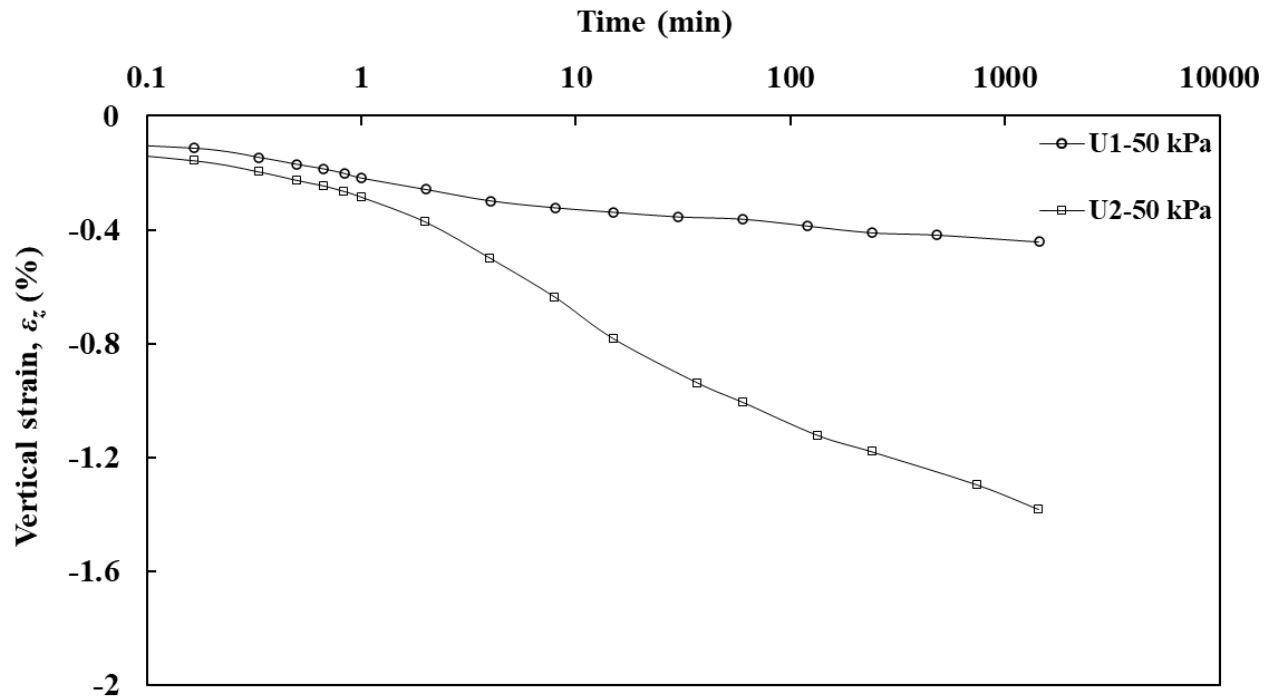


(b)



(c)

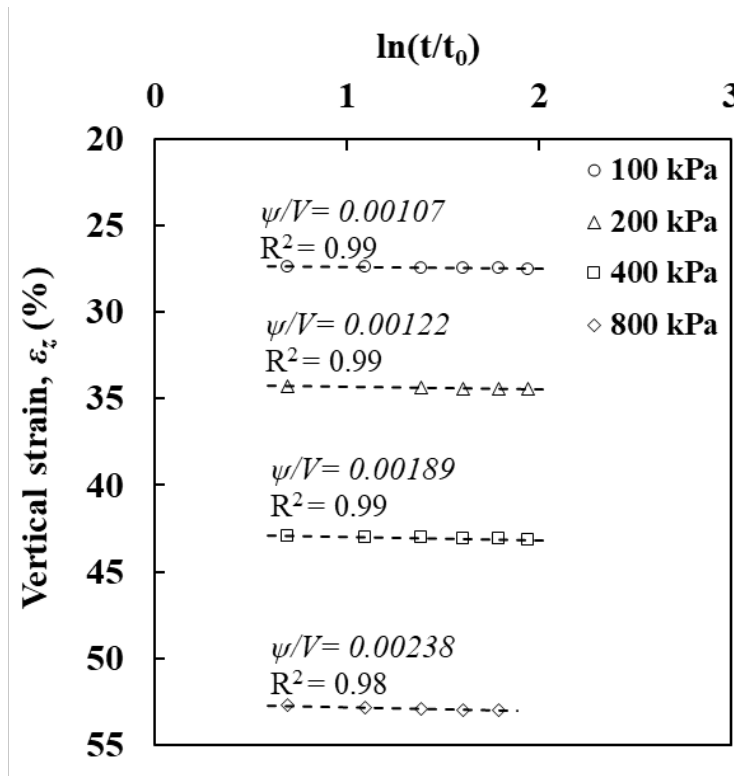
CHAPTER 3: PHYSICAL MODEL PILE SYSTEM, MATERIALS, AND INSTRUMENTATIONS



(d)

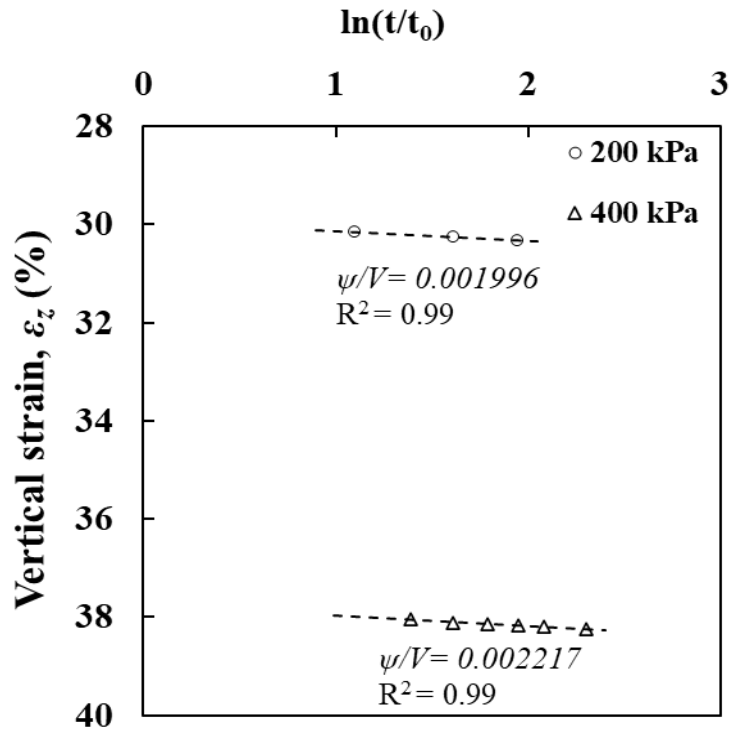
Figure 3.8 Variation of vertical strain with time for S3 specimen: (a) loading; (b) unloading (U1 represents the first unloading stage); (c) reloading (R1 represents the first reloading stage); and (d) effect of unloading (Wu, 2021)

CHAPTER 3: PHYSICAL MODEL PILE SYSTEM, MATERIALS, AND INSTRUMENTATIONS

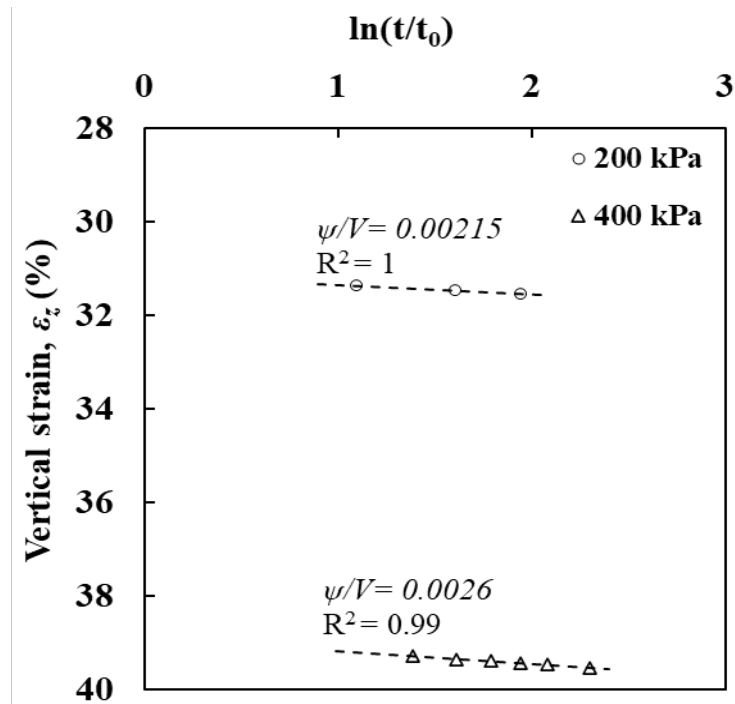


(a)

CHAPTER 3: PHYSICAL MODEL PILE SYSTEM, MATERIALS, AND INSTRUMENTATIONS



(b)

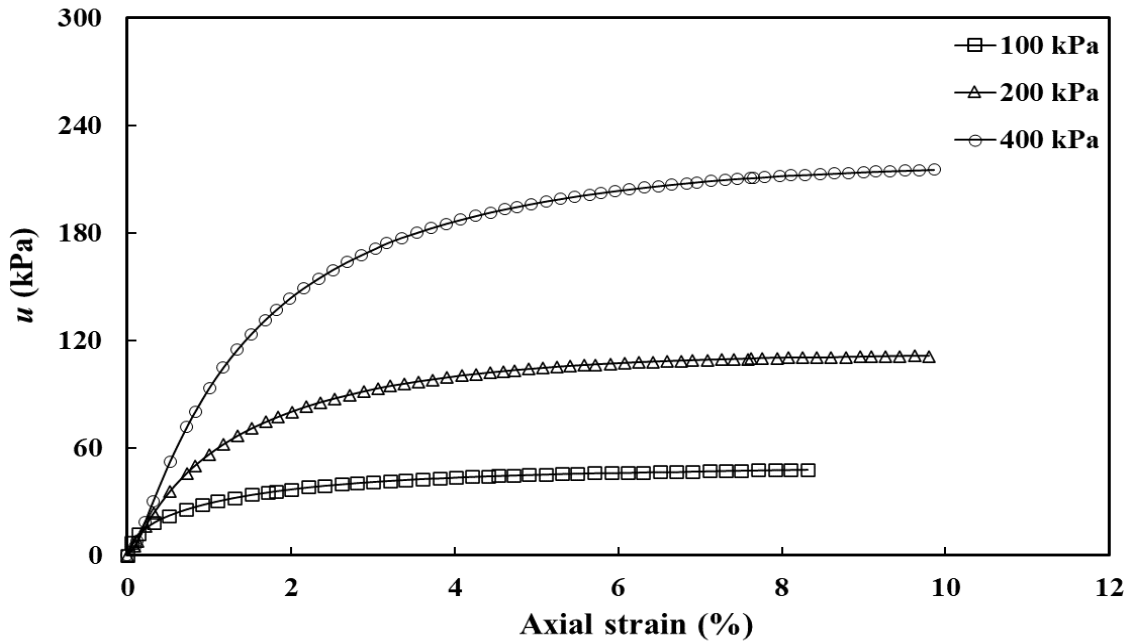
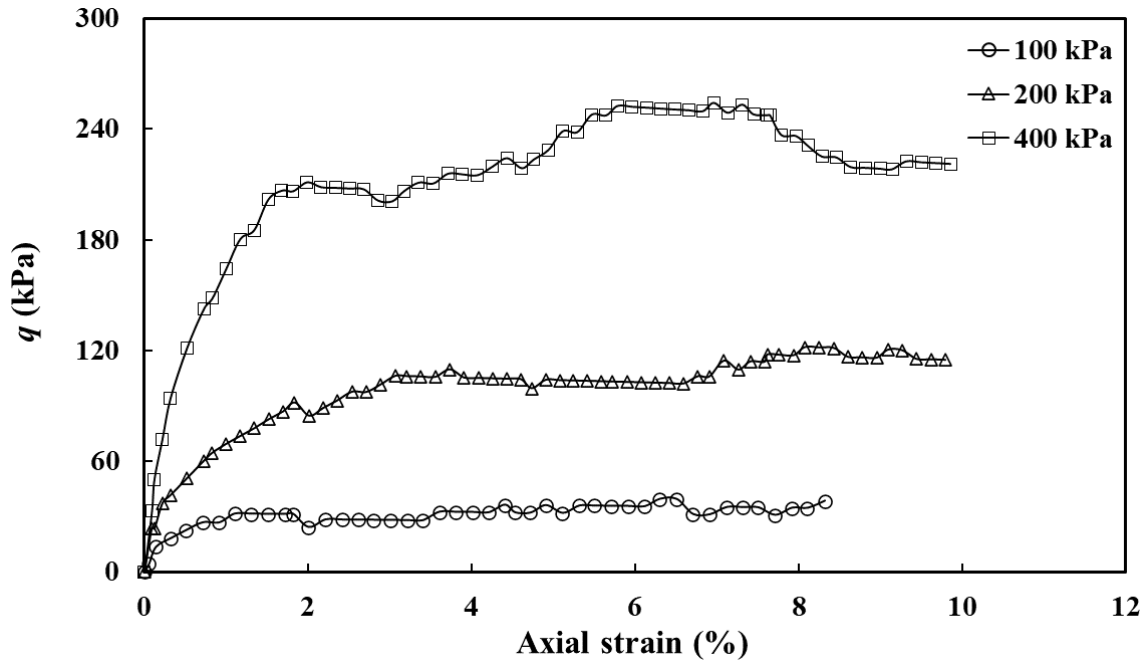


CHAPTER 3: PHYSICAL MODEL PILE SYSTEM, MATERIALS, AND INSTRUMENTATIONS

(c)

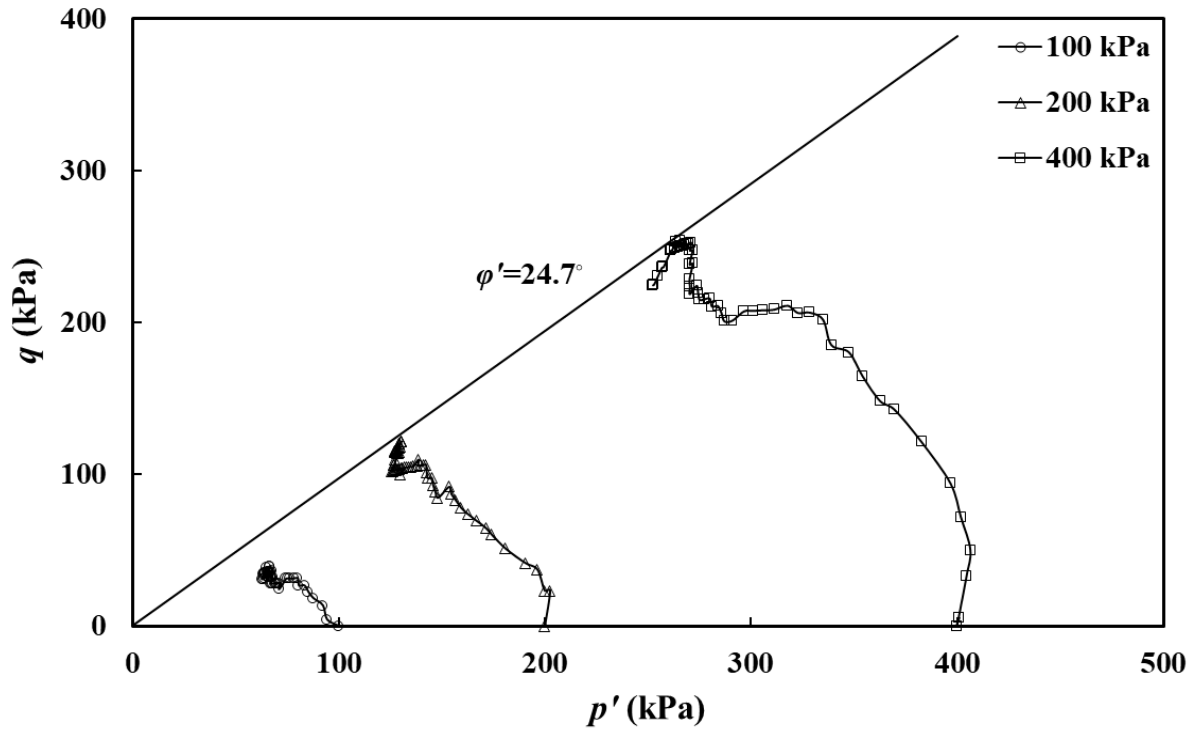
Figure 3.9 Creep response prediction through linear fitting of ψ/V : (a) S1; (b) S2; and (c) S3

(Wu, 2021)



(a)

(b)



(c)

Figure 3.10 Triaxial tests results: (a) deviator stress variation with axial strain; (b) porewater pressure variation with axial strain; and (c) effective stress paths from consolidated undrained tests (Wu, 2021)

CHAPTER 3: PHYSICAL MODEL PILE SYSTEM, MATERIALS, AND INSTRUMENTATIONS

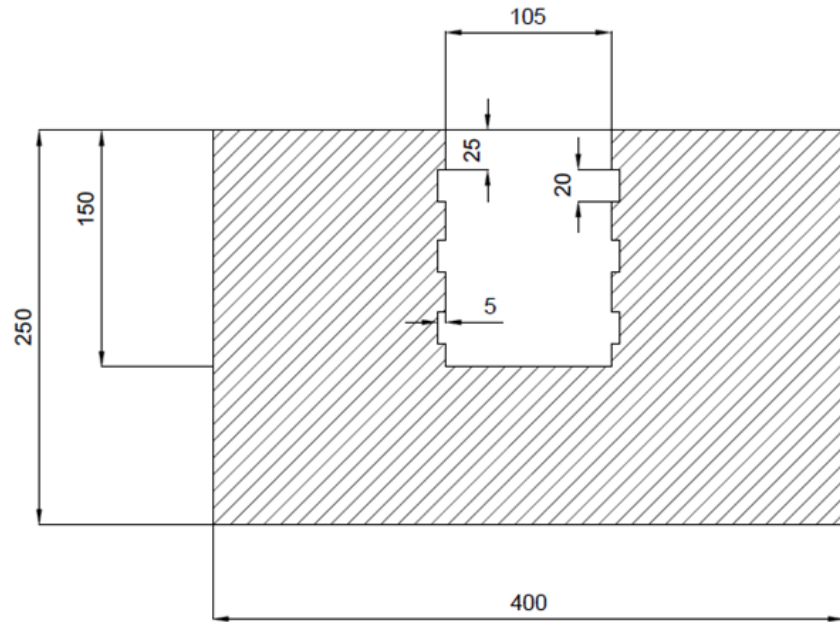


Figure 3.11 Granite rock-socket design

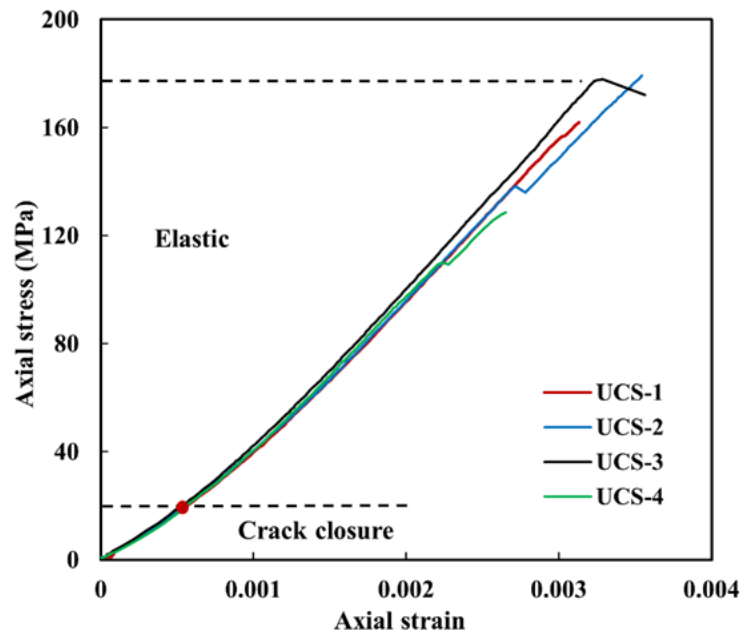


Figure 3.12 Plot of axial stress versus axial strain of UC tests on rock specimens

CHAPTER 3: PHYSICAL MODEL PILE SYSTEM, MATERIALS, AND INSTRUMENTATIONS

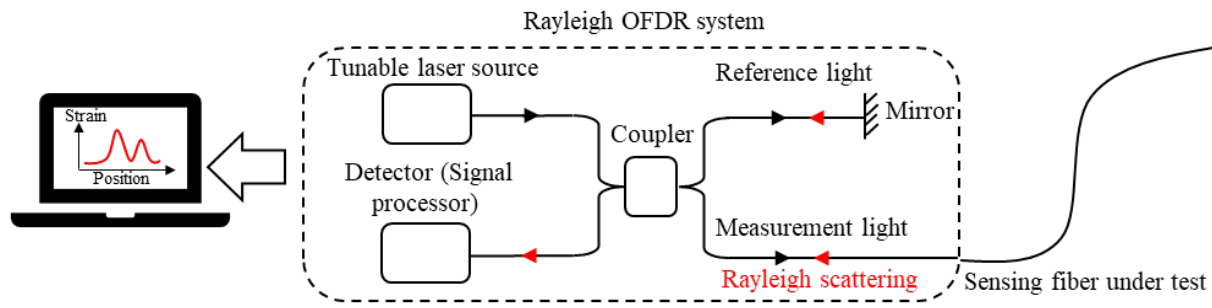


Figure 3.13 OFDR sensing principle

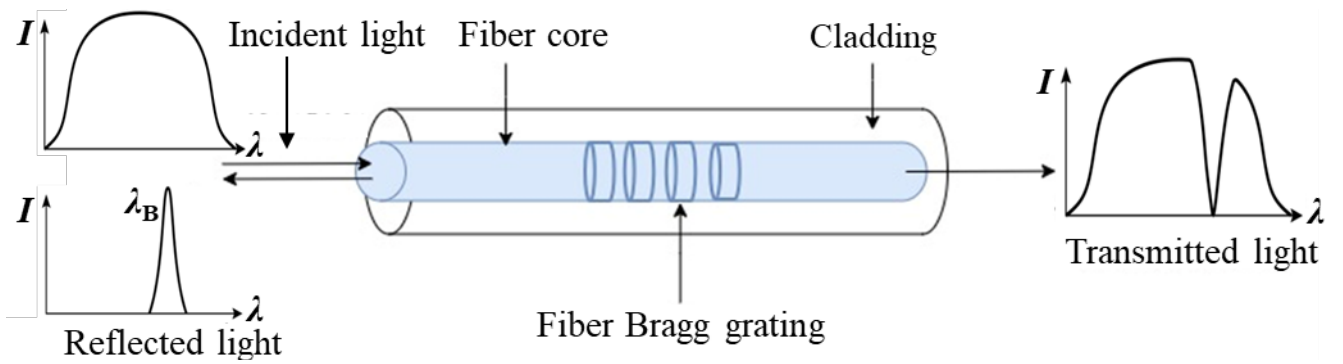


Figure 3.14 FBG sensing principle

CHAPTER 4: CYCLIC BEHAVIOR OF THE FRP-SSC MODEL PILES ENDED IN ROCK-SOCKET

4.1 Introduction

In this chapter, the cyclic performance of the proposed innovative and sustainable design of FRP-confined SSC model piles installed in a rock socket is investigated through a series of physical model tests. Physical model piles with different typical configurations are cast in a rock socket and subjected to cyclic loadings of different cyclic amplitudes and mean loads to determine the characteristics of cyclic stiffness, accumulated deformation, and shaft friction mobilization. The effects of cyclic loading history on the compression behavior of piles under repeated cyclic loadings is analyzed and investigated. A hybrid optic sensing technology of discrete (FBGs) and fully distributed sensing named optical frequency domain reflectometry (OFDR) with a higher spatial resolution of 1 mm and a high sensing accuracy of $\pm 1 \mu\epsilon$ is used to capture the continuous strain profile of piles inside the rock socket for calculating the shaft friction profiles. The findings of this study will assist geotechnical designers in determining the cyclic response of FRP-SSC composite piles ended in rock sockets for future design considerations.

4.2 Model piles preparation and setup

4.2.1 *Model piles design and installation*

Model piles with different configurations were investigated in this study. Table 4.1 lists the details of configuration, materials, and instrumentation of six model piles. All of them have a

CHAPTER 4: CYCLIC BEHAVIOR OF THE FRP-SSC MODEL PILES ENDED IN ROCK-SOCKET

length of 1460 mm, of which 160 mm was embedded in the rock socket and 1,300 mm was above the rock surface. Piles 1 and 2 comprise an SSC column confined by a glass fiber reinforced polymer (GFRP) tube possessing a thickness of 3.5 mm, an internal diameter of 100 mm and a total length of 1300 mm, as shown in Figure 4.1. Note that a specially designed clamp collar was fixed at tube bottom to increase the base stability of tube and steel wires attached to the tank were used to fix tube horizontally such that the GFRP tube was kept firmly, and annual inner wall of tube can be aligned with rock socket almost perfectly. In addition, the GFRP tube was sealed with water-resistant adhesives, that would be removed after SSC curing, near the rock surface to prevent any gap between the tube and the rock surface. Figure 4.2 shows that Pile 3 and 6 were made of SSC that is 100 mm in diameter with four longitudinal GFRP rebars embedded (a diameter of 9.5 mm and a length of 1460 mm). Above the rock socket, rebars were confined by circular stirrups of an outer diameter of 90 mm with a center-to-center spacing of 70 mm. Model piles 3 and 6 were designed in same way, except that Pile 6 was confined with HMKD of height 106 cm above the rock surface. In model Pile 4, a longitudinal GFRP rebar with a diameter of 19 mm was positioned at the center and surrounded by the SSC column with a diameter of 100 mm, as shown in Figure 4.3. Pile 5 was designed in the same way as Pile 4, except that a 10 mm debris (loose completely decomposed granite with diameter smaller than 10 mm) was placed at the socket bottom of the former to simulate debris in common construction site.

For the model pile 3 and 6, the rebar cage was first fabricated and then fixed in the rock socket within the polyvinyl chloride formwork casing, followed by the casting of the SSC inside. For

CHAPTER 4: CYCLIC BEHAVIOR OF THE FRP-SSC MODEL PILES ENDED IN ROCK-SOCKET

model pile 6, after curing the pile for 28 days, HKMD slurry was filled in the tank into two layers with a height of 106 cm above the rock surface. In the design of model piles, the GFRP tube was considered confinement to the SSC in both axial and hoop directions and worked as a permanent casing. The longitudinal rebars along with concrete contributed to the capacity of the pile against axial loads. Circular ties provided confinement to avoid the buckling and shear failure of longitudinal rebars. The SSC was filled using a small trowel into the rock socket and in the GFRP tube from the upper side. The filled SSC was vibrated manually with an aluminum rod (1 cm diameter) during casting process without any changes in the optical sensors position.

4.2.2 Installation and instrumentation of FBG and OFDR sensors

Model piles were instrumented with both FBG sensors and OFDR fibers along the length. FBGs were employed to monitor the cyclic loading behavior of model piles due to the high frequency of data acquisition. Regarding Piles 1, 2, 4 and 5, arrays of multiplexed FBGs were attached to an aluminum channel and embedded inside the concrete, as shown in Figures 4.1(b) and 4.3(b). The aluminum channel was designed to protect vulnerable optical fibers and form a quasi-distributed sensing strip with a finite number of FBGs. For Pile 3 and 6, the FBGs were attached to the rebar protected with glue, as shown in Figure 4.2(b). For each of the model piles, eight FBGs were placed in the pile body above the rock socket and four FBGs within the rock socket, with a spacing of 160 and 35 mm, respectively.

CHAPTER 4: CYCLIC BEHAVIOR OF THE FRP-SSC MODEL PILES ENDED IN ROCK-SOCKET

As to Piles 1 and 2, OFDR sensing fibers were embedded longitudinally in the SSC with six sections marked as “S1 to S6”, as shown in Figure 4.1(b). As for Pile 3, two independent fibers were installed on the rebars and within the SSC, with six sections (S1 to S6, and F1-F6) for each fiber in the cross-section of the pile, as shown in Figure 4.2(b). Since all the fibers worked as a sensor along the whole length, a section of the fiber (the slack fiber section) was kept free in the air to separate each measuring fiber. Slack fiber sections were mechanically strain-free, allowing locating the position of the measured strain from the strain distribution curves of the entire fiber. Measuring fibers were first pre-tensioned and then glued on the GFRP tube and rebars using an ultra-high-strength epoxy adhesive to protect sensing fibers and ensure a good bond between the fiber and surface. Pre-tensioning the measuring fibers ensures a stable state prior to loading. A pre-tension within the range of 50 to 100 micro strain was applied which was measured and recorded with OFDR interrogator. A 3 mm notch was made on GFRP rebars to properly place the sensing fiber, as shown in Figure 4.2(b).

4.3 Cyclic loading testing program

Model piles were cured with seawater under room temperature for 28 days and then subjected to a series of cyclic loading tests applied by a GCTS hydraulic loading system. Before loading, all the model piles were capped with high-strength gypsum to make sure that stresses were evenly distributed over the pile head. The cyclic testing programs with different cyclic amplitudes and mean loads are summarized in Table 4.2. In practice, piles do experience multi-round loadings with irregular loading levels. In this study, we take the influence of earlier loading tests as one of

CHAPTER 4: CYCLIC BEHAVIOR OF THE FRP-SSC MODEL PILES ENDED IN ROCK-SOCKET

the main focuses. We investigated the loading sequence (increasing, decreasing, or repetitive) on the change of static or cyclic deformation resistance, particularly the cyclic stiffness, of pile body and rock socketed pile section, considering the effect of pile configuration. The first intention of the test design is to investigate the effect of increasing loading levels. The second intention is to see the effects of a prior larger cyclic loading level on the cyclic response of pile under subsequent lower cyclic loading level. The third intention is to reveal the effect of loading-unloading to zero on the pile deformation, which is relatively less investigated.

The Sine function cyclic loading applied to the model pile head is presented in Figure 4.4. Generally, pile foundations experience cyclic loadings with frequencies ranging from 0.0001 to 0.1 Hz and 10 to 105 cycles (Puech, 2013). The frequency adopted in this study is 0.01 Hz in general with some tests with (0.02, 0.1, and 0.2 Hz) with 100 cycles for each loading case with some tests conducted up to 1000 cycles. Model piles were unloaded after each stage of cyclic loading and finally subjected to axial monotonic compression under the condition of load control till failure. The major considerations in cyclic loading tests are: (a) ensuring sufficient bearing capacity; (b) making sure that cyclic displacements are tolerable; (c) assessing whether long term settlements due to permanent displacements during cyclic loading are tolerable; (d) considering also cracks and significant stiffness variations developed cycling; and (e) assessing how the rock socket and pile shaft reaction developed during cyclic loadings. These aspects are discussed in more detail by Andersen (2004).

4.4 Results and discussion of cyclic stiffness of model piles

4.4.1 Cyclic stiffness data analysis

The stiffness of a pile plays a crucial role in determining the load transfer mechanism and the distribution of strains along its length. The experimental results on pile stiffness can be used to validate and improve numerical models and theoretical predictions which can contribute to design of piles in the future. The cyclic stiffness of model piles was calculated by the following equation:

$$k_{cyc,pb} = 2 \frac{Q_{cyc}}{u_{cyc,pb}} \quad (4.1)$$

$$u_{pb} = \int_0^{l_a} \varepsilon(z) dz \quad (4.2)$$

where $k_{cyc,pb}$ represents the cyclic stiffness of the pile body above the rock socket determined in each cycle; $u_{cyc,pb}$ refers to the recoverable deformation at pile head when peak load is released back to the valley value in the respective cycle. The deformation was calculated by integrating the strain measured with eight FBGs in the pile body (l_a), as shown in Equation 4.2. The stiffness was calculated in the unit of kN/mm in this study.

4.4.2 Cyclic stiffness of model pile 2

The variations in the $k_{cyc,pb}$ of Pile 2 under different cyclic loading conditions against cycle number are presented in Figure 4.5. Stiffness increased almost linearly during the first loading

CHAPTER 4: CYCLIC BEHAVIOR OF THE FRP-SSC MODEL PILES ENDED IN ROCK-SOCKET

(60-60) in the first series, as shown in Figure 4.5(a). When the second loading of 120-60 was applied, the stiffness obtained a sudden increase from 175 to 180, then showed a quick degradation in the initial 10 cycles followed by a slight increasing trend till the 100th cycle under the loading. It can be observed that the pile showed higher stiffness under this intermediate loading (120-60) in all series as shown in Figures 4.5(a)-4.5(d) compared with the higher or lower loadings (120-90 and 60-60). This can be attributed to a certain load threshold within which strain hardening occurs. The deformation of SSC, at this stage, is mainly contributed by elastic compression of aggregates and closure of micro cracks, which is enhanced by the confinement of GFRP tube. While as the load keeps increasing, the FRP tube underwent some fiber breakage or delamination due to cyclic loading (Schoeppner and Abrate, 2000; Pitarresi et al., 2019), the micro cracks in SSC develop in size and propagate, and cementitious products exhibit plastic flow behavior, thereby reducing stiffness.

Note that the axial load was released to zero between two consecutive loading stages. Stiffness in first three series generally increased with cycle number, while stabilized during the fourth. It can be concluded that the pile body had adapted to the loading levels after several loading-unloading cycles were applied. On the other hand, the stiffness under each loading level kept increasing from Series 1 to Series 4. For example, the pile gained stiffness of up to 6% from the minimum 166 kN/mm in the first series to the maximum stiffness of 185 kN/mm in the fourth series for the 120-60 loading, indicating that the unloading-reloading cycle strengthened the deformation resistance of FRP tube confined concrete pile for which confinement action from the FRP tube was activated with the deformation accumulated. In Series 5, as shown in Figure 4.5(e), under

CHAPTER 4: CYCLIC BEHAVIOR OF THE FRP-SSC MODEL PILES ENDED IN ROCK-SOCKET

higher cyclic loading applied the stiffness of Pile 2 achieved a large value of around 187 kN/mm then degraded quickly within the initial 25 cycles and afterwards stabilized at a level of 177.5 kN/mm, which is lower than that under 120-60 in first four series. Interestingly, the stiffness, however, still obtained gradual increase with the loading sequence, which should be mainly attributed to the microstructure adjustment resulted from unloading-reloading cycles between each two consecutive loading cases and continuous enhancement in stiffness due to the confinement development of FRP tube.

4.4.3 Cyclic stiffness of model pile 3

The stiffness variations of Pile 3 over cycles under different cyclic loading conditions are shown in Figure 4.6. During the loading 60-60 in series 1, stiffness showed a stable trend. When the load was increased, however, a slowly increasing trend was observed in the first 30 cycles, followed by a stable behavior with cycle number for the first two 120-60 tests, as shown in Figure 4.6(a). In contrast, degradation was marked in the first 12 cycles during the third 120-60 repeated test but reached a similar level of stiffness of Series 2 in the following cycles. For the same mean load and cyclic amplitude, the repeated tests resulted in gains of 5% in stiffness, which could be attributable to the strain hardening effect. When cyclic amplitude was further increased in test 120-90 shown in Figure 4.6(b), the pile showed less stiffness compared with that in test 120-60. It can be possibly expected that if cycling would continue for the same test (120-90) or higher load, stiffness could presumably show a further decrease. Compared with the further increase trend of FRP tube confined concrete pile (Pile 2) under 180-60 loading, the FRP rebar cage showed a less confining enhancement effect on the pile. Then, the loading conditions

CHAPTER 4: CYCLIC BEHAVIOR OF THE FRP-SSC MODEL PILES ENDED IN ROCK-SOCKET

were reduced back to investigate the effect of high loading history on the stiffness behavior of pile body when subjected to subsequent lower cyclic loadings. As shown in Figure 4.6(b), stiffness overall degraded from 162 kN/mm for 120-60 loading to 130 kN/mm for 60-30 loading. However, as shown in Figure 4.6(c), a slight gain of stiffness was observed in the repeated tests 60-60 in Series 5 compared with that in Series 4. Combined with results of Pile 2, it can be concluded that the pile body preloaded by a higher loading around strain hardening threshold would gain slightly in stiffness. The stiffness under 90-60 and 90-90 loadings laid between 60-60 and 120-60 cases, which possibly indicates that the maximum cyclic loadings ($Q_{cyc}+Q_{mean}$) is the main influencing factor for the cyclic stiffness, provided that the loading level is more or less within the strain hardening threshold.

4.4.4 Cyclic stiffness of model pile 4 and 5

The variations in the stiffness of Piles 4 and 5 under cyclic loadings with increasing cycle numbers are shown in Figure 4.7. Initially, Pile 4 showed almost constant stiffness with the increase of cycle number under low-level cyclic loading 30-30. However, when the pile was unloaded and retested under increased loading conditions 60-60, stiffness degradation was observed in the first 50 cycles, followed by a constant stiffness trend. As a result of being reinforced with the centered FRP rebar of a high modulus of elasticity and high strength, the pile showed no significant change in stiffness. Additionally, Q_{cyc} and Q_{mean} were kept under 30 % of post-cyclic monotonic capacity Q_{ps} , which is below the load threshold capable of inducing the significant stiffness degradation of the pile. During the first cyclic loading 30-30 on Pile 5, stiffness showed an initial degradation of 3% in the first 40 cycles. Then, it linearly increased to

CHAPTER 4: CYCLIC BEHAVIOR OF THE FRP-SSC MODEL PILES ENDED IN ROCK-SOCKET

the initial value at $N = 108$ and degraded again till 400 cycles, followed by a constant trend. This variation in stiffness can be attributed to the rearrangement and compaction of the slag under compression in the rock socket, destabilizing the behavior of the pile in the initial loading stage. During test 60-60, stiffness degraded slowly in the first 200 cycles, followed by a constant trend of nearly similar value 156 kN/mm as in the previous test 30-30 till $N = 1,000$. The cyclic loading tests on Piles 4 and 5 suggest that applying the maximum cyclic load ($Q_{cyc} + Q_{mean}$) below 35% of the post cyclic capacity of the pile for 1,000 cycles may not significantly change the stiffness of the pile with a center positioned FRP rebar.

4.4.5 Cyclic stiffness of model pile 6

The stiffness variations of the Pile body over cycles under different cyclic loading conditions are shown in Figure 4.8. During the loading 30-30 in series 1, stiffness showed a slight decreasing trend initially in the first 30 cycles and then followed a slower increasing trend till 1000 cycles. When the load was increased, however, a slowly decreasing trend was observed in the first 30 cycles, followed by a stable behavior with cycle number for the 60-30 loading test, as shown in Figure 4.8(a). A slower degradation trend with cycles number was marked in the first loading test of Series 2 i.e, 60-60-1 as shown in Figure 4.8(b). However, upon repeated test in 60-60-2 the stiffness showed a stable constant trend with cycles. Further repeated tests (60-60-3, 60-60-4) in Series 2 showed a similar stiffness level with constant stable trends with cycles. For the same mean load and cyclic amplitude in Series 2, the repeated tests resulted in gains of 3% in stiffness, which could be attributable to the strain hardening effect. The influence of cyclic amplitude keep a same mean load and repetition of cyclic loading tests is shown in the Figure 4.8(c). During the

CHAPTER 4: CYCLIC BEHAVIOR OF THE FRP-SSC MODEL PILES ENDED IN ROCK-SOCKET

loading 90-30 in Series 3, the stiffness followed a stable trend with cycles but showed higher stiffness value compared to the 60-60 loading tests of Series 2, even $(Q_{cyc}+Q_{mean})$ is higher, this could possibly be due to the strain hardening effect. When the cyclic amplitude was increased keeping the mean load same in loading 90-60-1, the stiffness decreased to 191 kN/mm and showed a decreasing trend in the first 12 cycles and afterward followed a stable trend with cycle number. Further repeated tests (90-60-2, 90-60-3) in Series 3 showed a similar stiffness level with constant stable trends with cycles. For the same mean load and cyclic amplitude in Series 3, the repeated tests resulted in gains of 2.5% in stiffness, which could be attributable to the strain hardening effect. Upon further increasing of the cyclic amplitude to 90 kN in the Series 3, the stiffness of the pile decreased to 183 kN/mm in the 90-90 loading test.

The evolution of pile cyclic stiffness with cycles under increased mean load and cyclic amplitude is presented in Figure 4.8(d). In the first loading test 120-60-1 of Series 4, the stiffness initially decreased in the first 12 cycles and then followed a stable trend. Upon repeating the same loading tests, the stiffness gained of 3% increase and showed a constant stable trend with similar stiffness of 190 kN/mm in 120-60-2 and 120-60-3 tests. When the cyclic amplitude was further increased to 90 kN in Series 4, the stiffness decreased significantly and followed decreasing trend with cycles until complete failure in the 57th cycle showing the maximum cyclic capacity of the pile.

4.4.6 Cyclic stiffness of piles in rock-socket section

Figure 4.9 presents how the cyclic stiffness of the pile in the rock socket evolved under various cyclic loading conditions. In Series 1, stiffness increased linearly with the increase of cyclic loading at a slow rate. A higher cyclic stiffness of 8,915 kN/mm was recorded under 120-60 loading in Series 2 due to the strain hardening caused by the load within the threshold value, as discussed in Section 3.1. For each of tests 60-60, 120-60 and 120-90 from Series 1 to 4, stiffness increased with cyclic loading, achieving gains of up to 4.3%, 8.4% and 2.85%, respectively. Then, stiffness increased slowly under higher cyclic loading in Series 5, achieving gains of only 3.68% from 8,421 to 8,731 kN/mm with repeated testing. Based on the theoretical framework introduced by Manceau et al. (2021), the shaft resistance is mainly governed by the rock socket roughness, shear modulus of rock, and pile diameter. Initially, small gaps between asperities of rock and pile shaft may have existed. As the cyclic loading continued, dilation at the rock-pile interface developed, leading to an increase in normal stress, which induced a higher cyclic stiffness. However, when the load was increased and cycle number accumulated, partial wears and damage of asperities contacts between rock and pile occurred, that reduced the dilation and normal stress at the interface. With the further increase of loading, the debris from asperity fracture would be compressed again, thereby inducing denser packing and dilation again. Since the shaft resistance has a negative correlation with pile diameter (Manceau et al., 2021), the effect of external loading on the shaft resistance behavior would be less obvious for the large-diameter piles. Therefore, precautions should be taken when applying the observed trends in practical design.

4.5 Accumulated deformation results of model piles during cyclic loading

4.5.1 Accumulated compression of pile body during cyclic loading

The accumulated pile compression $u_{acc,pb}$ is the compression accumulated in the pile body over l_a from the first cycle to the last during cyclic loading. The accumulated compression of Pile 2 under different maximum cyclic loadings ($Q_{cyc}+Q_{mean}$) in different series is shown in Figure 4.10. Compression accumulation was maximum during the first cyclic loading series, with a higher value of 200 μm observed in test 120-60. In the very first cyclic loading series, the conditioning of the pile may change and respond differently to cyclic loading. Each subsequent series from 1 to 3 showed a reduction in pile compression accumulation, but a nearly similar response was recorded during Series 3 and 4, which can be attributed to the effect of load history. During the cyclic loading tests 60-60, 120-60 and 120-90 from Series 1 to 4, compression accumulation was reduced by roughly 70%, 86% and 67%, respectively, leading to the gains in stiffness. The pile accumulated the maximum compression of 400 μm during the first test (180-60) in Series 5 but exhibited a nearly 77% of reduction in compression accumulation under the same loading conditions from the first to fourth tests in this series.

Therefore, it is generally observed that cyclic loading history reduced compression accumulation for the following loading stages with the same cyclic loading conditions. As the main component to sustain compressive cyclic loading, SSC, in the initial loading conditions, contributes to the major compression accumulation due to the formation and distribution of microcracks. However, as the loading continues the stresses are redistributed evenly across the concrete achieving a

CHAPTER 4: CYCLIC BEHAVIOR OF THE FRP-SSC MODEL PILES ENDED IN ROCK-SOCKET

balanced state, which helps to distribute the applied loads effectively and leading to reduction in the rate of compression accumulation. Besides, the enhanced confinement from the FRP tube restrained SSC laterally and increased its deformation resistance through inhibiting the damage propagation and crack growth in SSC (Lam and Teng, 2003). Hence, it was advisable to take the effect of cyclic loading into consideration in ultimate state design when examining piles with competent confinement, like the FRP tube.

4.5.2 Permanent accumulated deformation of piles in rock socket section

The total accumulation of compression in the pile socket as a consequence of a series of cyclic loadings is presented in Figure 4.11. Compression accumulated at a high rate with the increase of loading, whose accumulation however was less marked on retesting in the following series due to the gains in stiffness. A total of 12 μm permanent compression accumulated within the socket as a result of cyclic loading from Series 1 to the end of series 5. The high strength of the rock resulted in less compression within the rock socket compared with that within the pile body.

4.5.3 Compression of the Pile Section in the Rock Socket during Cyclic Loading

In this section, the compression of the piles within the rock socket under static loading (Q_{mean}) before cyclic loading and post-cyclic stages was analyzed. The variation in the compression of the pile in the socket when it was subjected to static and cyclic loadings is presented in Figure 4.12. The compression under static loading showed a linear response with the increase of load magnitude. Under the same static loads of 60 and 120 kN in each series, compression was kept

CHAPTER 4: CYCLIC BEHAVIOR OF THE FRP-SSC MODEL PILES ENDED IN ROCK-SOCKET

nearly constant for each test with a value of 8 and 16 μm , respectively. At a higher static load of 180 kN in Series 5, compression increased linearly to 23 μm and showed no obvious change during the retests in the same series.

The compression of the socketed section of pile after cyclic loading showed a different phenomenon. As shown in Figure 4.12, the compression accumulation under cyclic loading evolved at a slower rate compared with that under static loading. This can be explained by the repetitive shearing dilation at the rock-concrete interface due to the increased confinement resulting from the breakage of interface asperities and their rearrangements, corresponding to the theoretical framework proposed by Manceau et al. (2021) and their field test results of drilled and grouted piles in rock. Within the first series, the socket deformed more compared with other series under the same loading conditions and showed a high compression of 17.7 μm under 120-60 loading within Series 1 to 4. Compression kept almost constant for each respective test in Series 2, 3 and 4 as the results of the conditioning effect of cyclic loading in Series 1. Moreover, it experienced a maximum compression of 25 μm under higher cyclic loading of 180-60 but increased at a lower rate under the same loading conditions in subsequent tests as a result of the cyclic conditioning effect from prior loadings.

4.6 Mobilization of shaft friction under cyclic loadings

The shaft friction f inside the rock socket between the granite rock and the pile was measured from the load distribution in the pile body inside the socket. And the load distribution was

CHAPTER 4: CYCLIC BEHAVIOR OF THE FRP-SSC MODEL PILES ENDED IN ROCK-SOCKET

calculated from the distributed strain data of pile measured with OFDR optic fibers rather than FBG. As a discrete sensing element, the FBG adopted in this study has a length of 15 mm, which indicates it will measure the average strain within this range. However, one of the FBG sensors in the pile locates at the level of rock surface such that the stuck effect, induced by the imperfect matching between the pile and the drilled socket hole, would affect the accuracy of that specific FBG sensor. On the other hand, OFDR provides more detailed profile of shaft friction along socket depth due to its full distribution nature. Rock quality designation (RQD) was kept the same for all the model piles. Piles 4 and 5 were not instrumented with OFDR optic fibers and OFDR optic fibers in Pile 2 could not provide data along entire length in socket. Hence, the shaft friction results of Pile 3 were discussed as a representative pile. The following relation was used to calculate the shaft resistance in the rock socket:

$$f = \frac{\Delta F}{\Delta h \cdot \pi \cdot D} = \frac{\Delta \sigma_c A_c + \Delta \sigma_f A_f}{\Delta h \cdot \pi \cdot D} \quad (4.3)$$

where Δh is the distance between the two sensing points; D represents pile diameter; A_c and A_f denote the cross-section areas of concrete and FRP rebars, respectively. In the case of Pile 3, four GFRP rebars along with the SSC were placed in the rock socket. To calculate the axial stress σ_c of concrete, the tangent modulus E_t discussed in Section 3.4.2 was adopted by considering concrete as a non-linear elastic-plastic material. FRP was treated as an elastic material, and the incremental axial stress along the depth was calculated as $\Delta \sigma_f = \Delta \varepsilon E_f A_f$, where E_f is the modulus of FRP.

CHAPTER 4: CYCLIC BEHAVIOR OF THE FRP-SSC MODEL PILES ENDED IN ROCK-SOCKET

The variations of mobilized shaft friction f and displacement along the depth in the rock socket at cycles $N = 3, 25, 50$ and 100 in different cyclic loading tests are shown in Figure 4.13. The displacement in the socket was calculated as the change of longitudinal distance of each point relative to the point near the rock surface. It was observed that the behavior of mobilized rock shaft friction was non-linear with some fluctuations along the depth in the socket. Shaft resistance evolved with cycles, showing gains of up to 15% from $N = 3$ to $N = 100$ at the depth of 10 mm of the socket for 60-60 loading in Series 1. The increase in shaft friction attenuated with the increase of depth, with almost no significant change at pile base. Following a smooth curve with a maximum displacement of $3 \mu\text{m}$ in the region 0-20 mm, displacement decreased non-linearly along the depth and showed a nearly similar trend with cycles.

For the 120-60 loading as shown in Figure 4.13(b), the mobilized shaft friction decreased generally with depth. It should be noted that the ratio of shaft friction at 10 mm depth under 120-60 loading and 60-60 loading was 2.5, while the ratio decreased to 1.88 at the pile base. In comparison with the previous test 60-60, displacement increased with cycles, rising from 5.8 to $7 \mu\text{m}$ at $N = 100$. The maximum shaft friction of 4.6 MPa was observed at $N = 100$ under test 120-90 (Figure 4.13(c)). Generally, shaft resistance increased with an increase in $Q_{cyc} + Q_{mean}$. However, when $Q_{cyc} + Q_{mean}$ increased by 10% for 120-60 case to 120-90 case, the maximum shaft friction increased by 23%. And the shaft frictions at the depths at 90 mm and 110 mm showed no difference for these two loading cases. The shaft frictions at 130 mm and 145 mm were even smaller for the 120-90 case. It can be speculated that the pile-rock interface at upper portion mobilized at a large extent with significant asperities breakage and obvious increase in

CHAPTER 4: CYCLIC BEHAVIOR OF THE FRP-SSC MODEL PILES ENDED IN ROCK-SOCKET

confinement from rock to pile due to the dilation effect of broken-out small particles. The magnitude changed less markedly with cycles in the lower section of the rock socket but increased with an increase in cycle number at the upper portion.

4.7 Summary

This chapter introduces a series of physical model tests on rock socketed FRP composite SSC model piles with different configurations under various axial cyclic loadings. FBG and OFDR sensing technologies were used for measuring the strain profile within model piles to investigate axial cyclic stiffness, accumulated deformation, and shaft friction mobilization between SSC and rock. The main findings can be summarized as follows:

- (a) The pile body gained cyclic stiffness when the maximum cyclic load level ($Q_{mean} + Q_{cyc}$) was below 30% of Q_{us} , and degradation was observed under higher load conditions. The stiffness of the pile body showed gains of up to 5% for the mentioned load levels with the maximum stiffness observed on the FRP tube confined pile.
- (b) Pile 6 surrounded by HKMD showed 20 % higher stiffness compared to Pile 3 under same cyclic loading conditions which can be attributed to the confinement provided by HKMD.
- (c) The cyclic stiffness of the socket section increased linearly with the increase in cyclic load levels due to the high modulus and strength of the rock.
- (d) The accumulation of compression was influenced by both Q_{mean} and Q_{cyc} levels with the maximum compression accumulated within the pile body during test 120-60, which is around the threshold loading for the FRP tube confined pile.

CHAPTER 4: CYCLIC BEHAVIOR OF THE FRP-SSC MODEL PILES ENDED IN ROCK-SOCKET

(e) Shaft resistance in rock socket increased with $(Q_{mean} + Q_{cyc})$. The pile-rock interface at upper portion mobilized at a large extent with more significant asperities breakage and obvious increase in confinement from rock to pile due to the dilation effect of broken-out small particles. The magnitude changed less markedly with cycles in the lower section of the rock socket but increased with an increase in cycle number at the upper portion.

CHAPTER 4: CYCLIC BEHAVIOR OF THE FRP-SSC MODEL PILES ENDED IN ROCK-SOCKET

Table 4.1 Details of configuration, materials, and instrumentation of six model piles

Model Piles	Pile Configuration	Materials	Instrumentation	Length
Pile 1	FRP tube confined SSC pile	GFRP tube and SSC	FBG and OFDR sensors, LVDTs	
Pile 2	FRP tube confined SSC pile	GFRP tube and SSC	FBG and OFDR sensors, LVDTs	Total 1460 mm
Pile 3	FRP rebars cage reinforced SSC pile	GFRP rebars, stirrups, and SSC	FBG and OFDR sensors, LVDTs	(160 mm within granite rock
Pile 4	Centered FRP rebar reinforced SSC pile	GFRP rebar and SSC	FBG sensors, LVDTs	socket and 1300 mm above rock
Pile 5	Centered FRP rebar reinforced SSC pile	GFRP rebar, SSC, and debris	FBG sensors, LVDTs	surface)
Pile 6	FRP rebars cage reinforced SSC pile	GFRP rebar, SSC, and HKMD	FBG sensors, LVDTs	

Table 4.2 Cyclic loading program of the model piles

Model pile	Loading series	Test Code ¹	Q_{mean} (kN)	Q_{cyc} (kN)	Cycle number, N	Loading frequency, f (Hz)	Post-cyclic failure load Q_{us} (kN)
Pile 1	-	60-60	60	30	100	0.01	-
		120-60	120	30	100		

CHAPTER 4: CYCLIC BEHAVIOR OF THE FRP-SSC MODEL PILES ENDED IN ROCK-SOCKET

		120-90	120	45	50		
		180-60	180	30	7 ²		
		60-60	60	30			
	Series 1	120-60	120	30			
		120-90	120	45			
		60-60	60	30			
	Series 2	120-60	120	30			
		120-90	120	45			
		60-60	60	30			
Pile 2	Series 3	120-60	120	30	100	0.01	266
		120-90	120	45			
		60-60	60	30			
	Series 4	120-60	120	30			
		120-90	120	45			
		180-60-1	180	30			
		180-60-2	180	30			
	Series 5	180-60-3	180	30			
		180-60-4	180	30			
	Series 1	60-60	60	30			
		120-60-1	120	30			
		120-60-2	120	30	100		
Pile 3	Series 2	120-60-3	120	30		0.01	213
		120-90-1	120	45			
	Series 3	120-90-2	120	45	57		

CHAPTER 4: CYCLIC BEHAVIOR OF THE FRP-SSC MODEL PILES ENDED IN ROCK-SOCKET

		60-30-1	60	15			
	Series 4	60-30-2	60	15			
		60-30-3	60	15			
	Series 5	60-60-1	60	30	100		
		60-60-2	60	30			
	Series 6	90-60-1	90	30			
		90-60-2	90	30			
	Series 7	90-90	90	45	72		
Pile 4	-	30-30	30	15	1000	0.1	239
		60-60	60	30			
Pile 5	-	30-30	30	15	1000	0.1	208
		60-60	60	30			
Model pile	Loading series	Test Code ¹	Q_{mean} (kN)	Q_{cyc} (kN)	Loading frequency, f (Hz)	Cycle number, N	Post-cyclic failure load Q_{us} (kN)
	Series 1	30-30	30	15	0.01	1000	
		60-30	60	15	0.02		
		60-60	60	30	0.02		
Pile 6	Series 2	60-60	60	30	0.01		-
		60-60	60	30	0.1	100	
		60-60	60	30	0.2		
	Series 3	90-30	90	15	0.02		
		90-60	90	30	0.01		

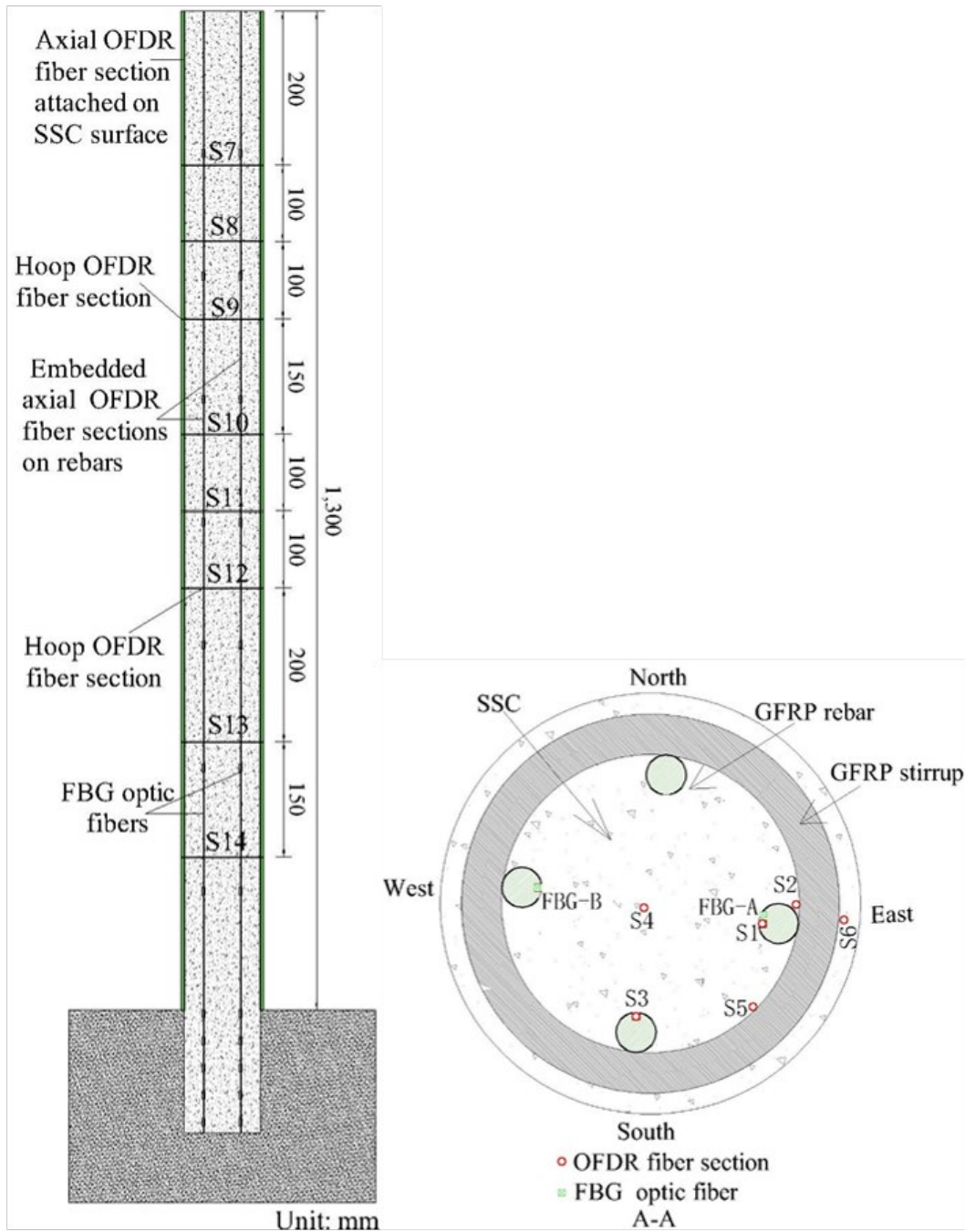
CHAPTER 4: CYCLIC BEHAVIOR OF THE FRP-SSC MODEL PILES ENDED IN ROCK-SOCKET

	90-60	90	30	0.1	
	90-60	90	30	0.2	
	90-90	90	45	0.02	
	120-60	120	30	0.01	
Series 4	120-60	120	30	0.1	
	120-60	120	30	0.2	
	120-90	120	45	0.01	

Note 1. The first value represents Q_{mean} , second value refers to $2Q_{cyc}$, and if any third number, it represents the serial number of repeated tests within one series with respect to time (1 refers to the first test and so on).

Note 2. The pile failed unexpectedly due to the technical failure of the load transferring plate between the model pile and actuator during cyclic loading.

CHAPTER 4: CYCLIC BEHAVIOR OF THE FRP-SSC MODEL PILES ENDED IN ROCK-SOCKET



(a)

(b)

Figure 4.2 Cross-section illustrations of: (a) vertical profile of Pile 3 or 6 (note: Pile 6 is surrounded by 106 cm HKMD inside tank); and (b) horizontal profile of Pile 3 or 6

CHAPTER 4: CYCLIC BEHAVIOR OF THE FRP-SSC MODEL PILES ENDED IN ROCK-SOCKET

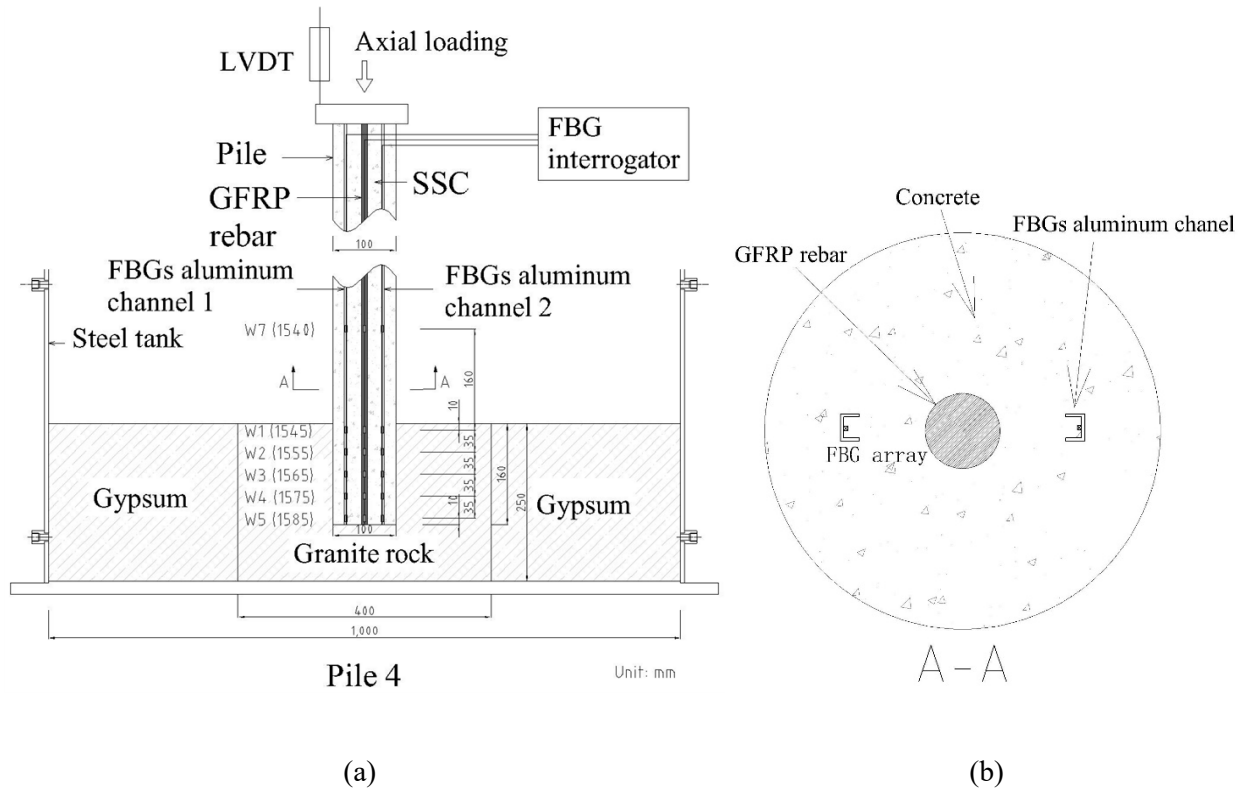


Figure 4.3 Cross-section illustrations of: (a) vertical profile of Pile 4 or 5; and (b) horizontal profile of Pile 4 or 5

CHAPTER 4: CYCLIC BEHAVIOR OF THE FRP-SSC MODEL PILES ENDED IN ROCK-SOCKET

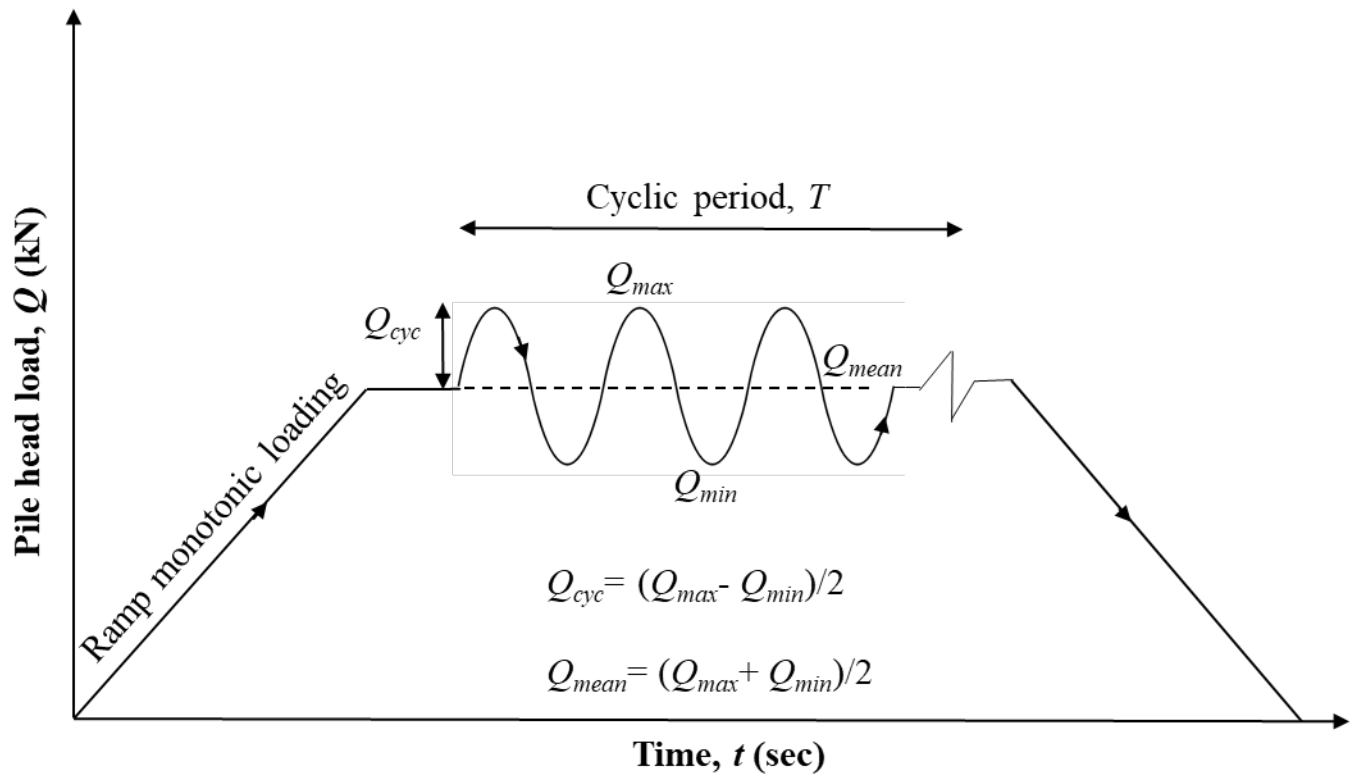
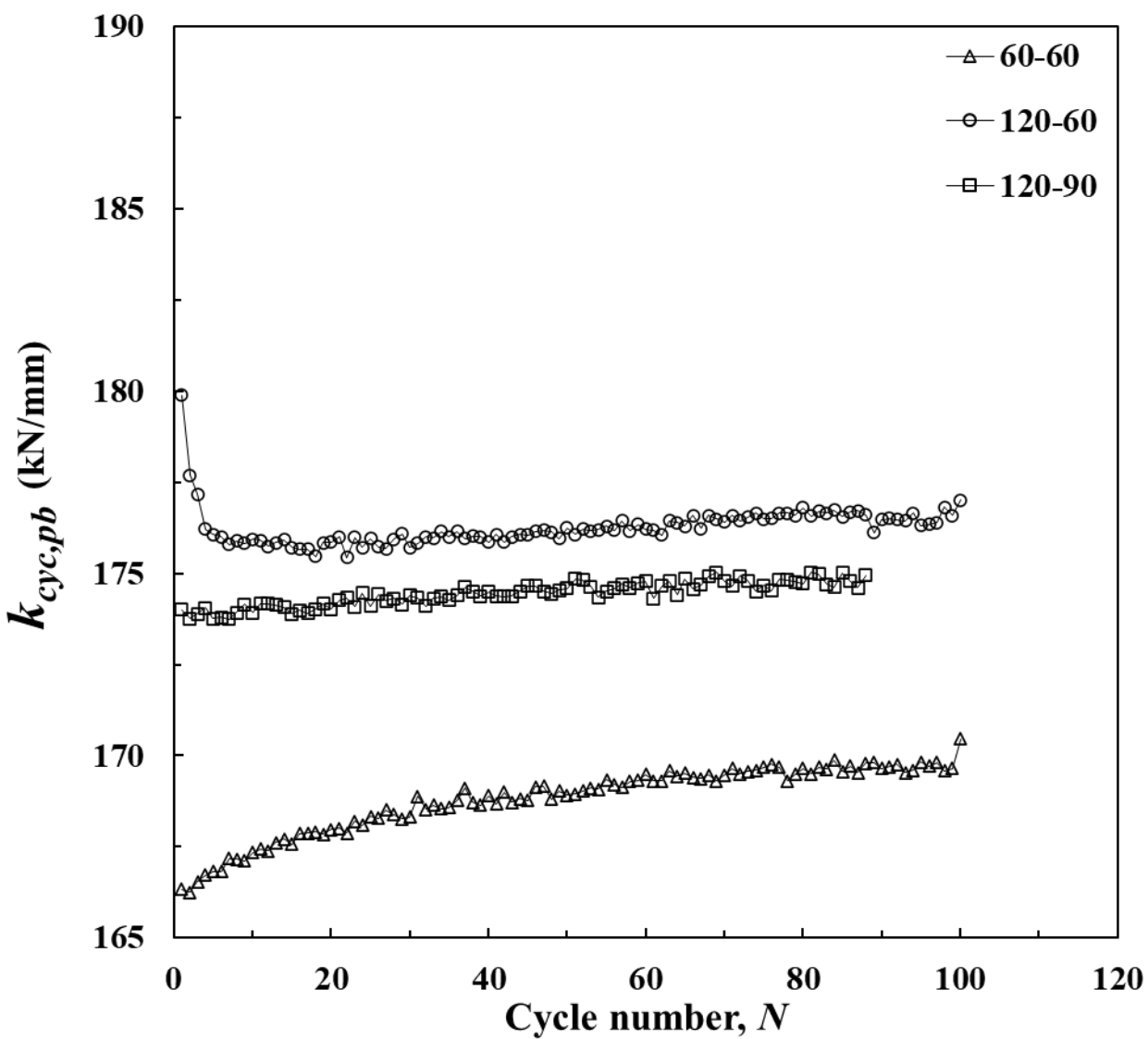
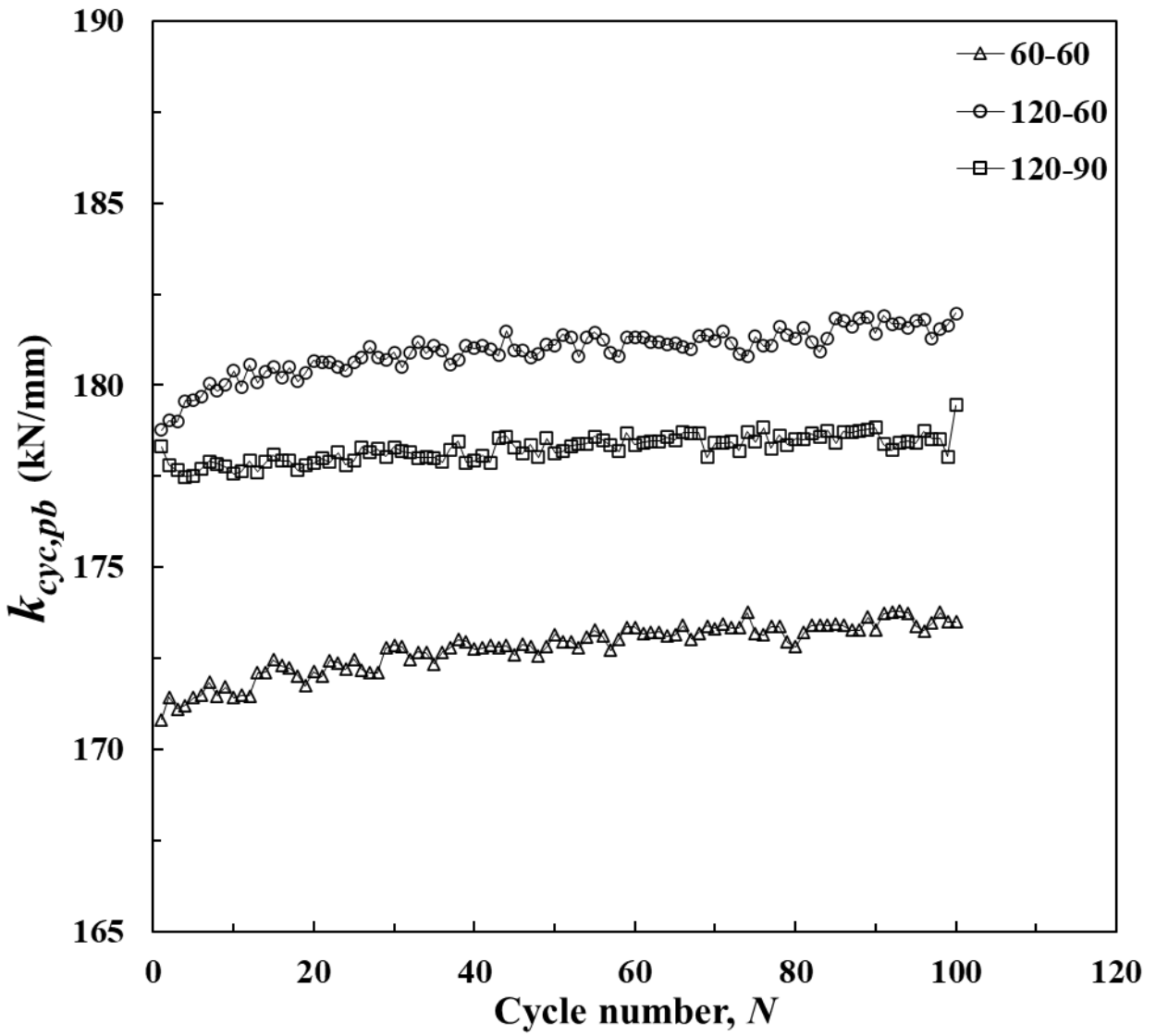


Figure 4.4 Schematic illustration of loading program

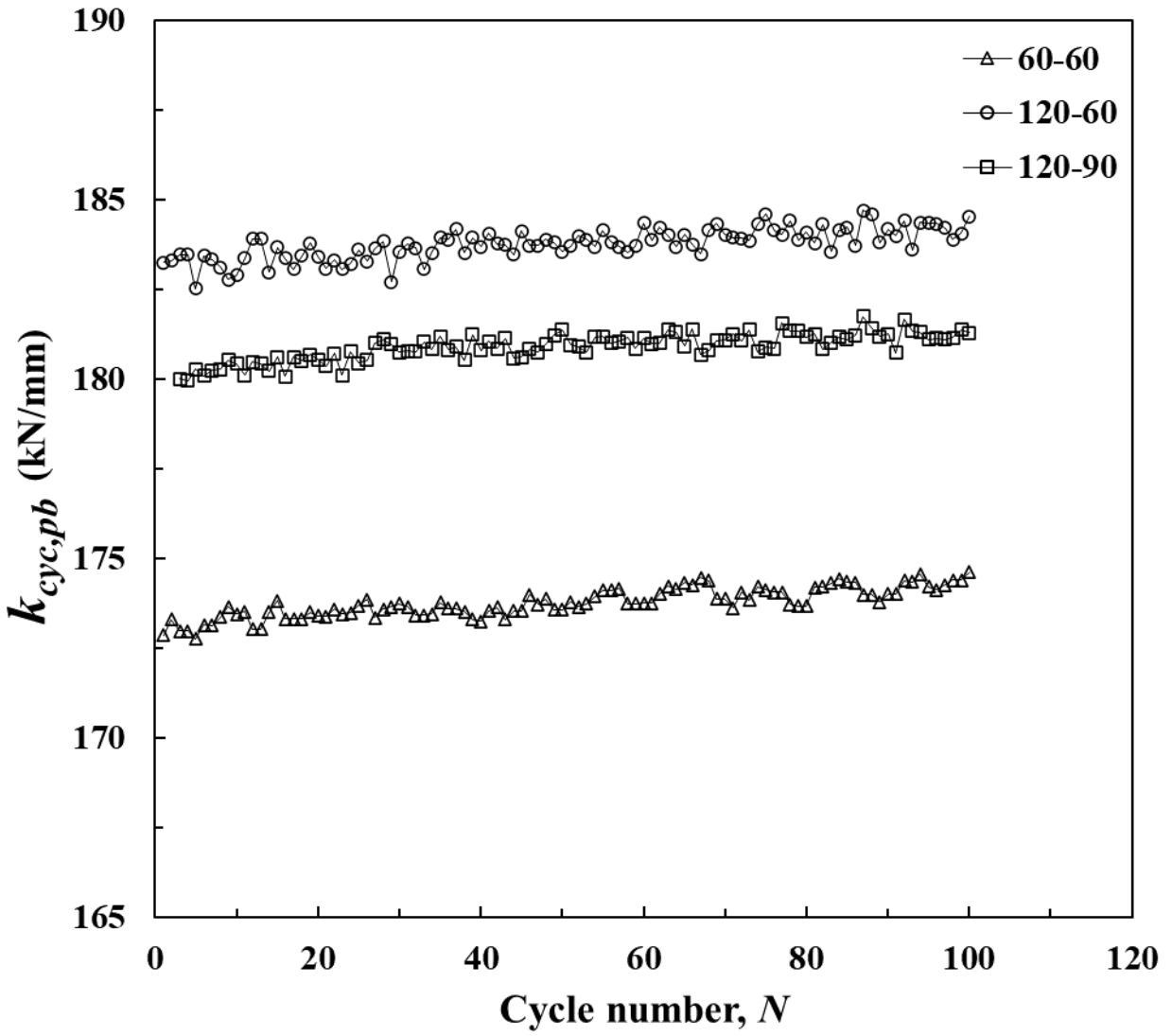


(a)



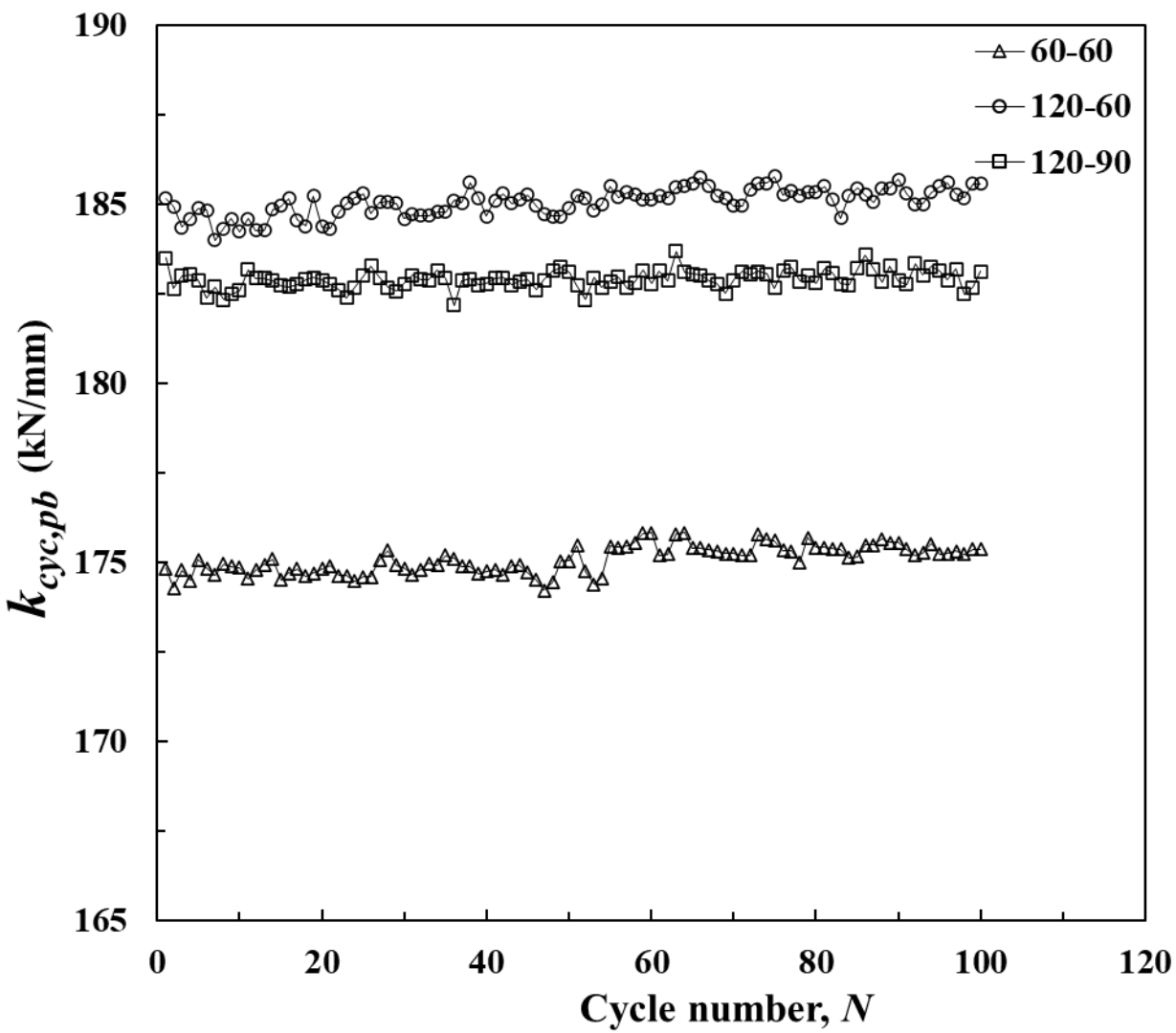
(b)

CHAPTER 4: CYCLIC BEHAVIOR OF THE FRP-SSC MODEL PILES ENDED IN ROCK-SOCKET

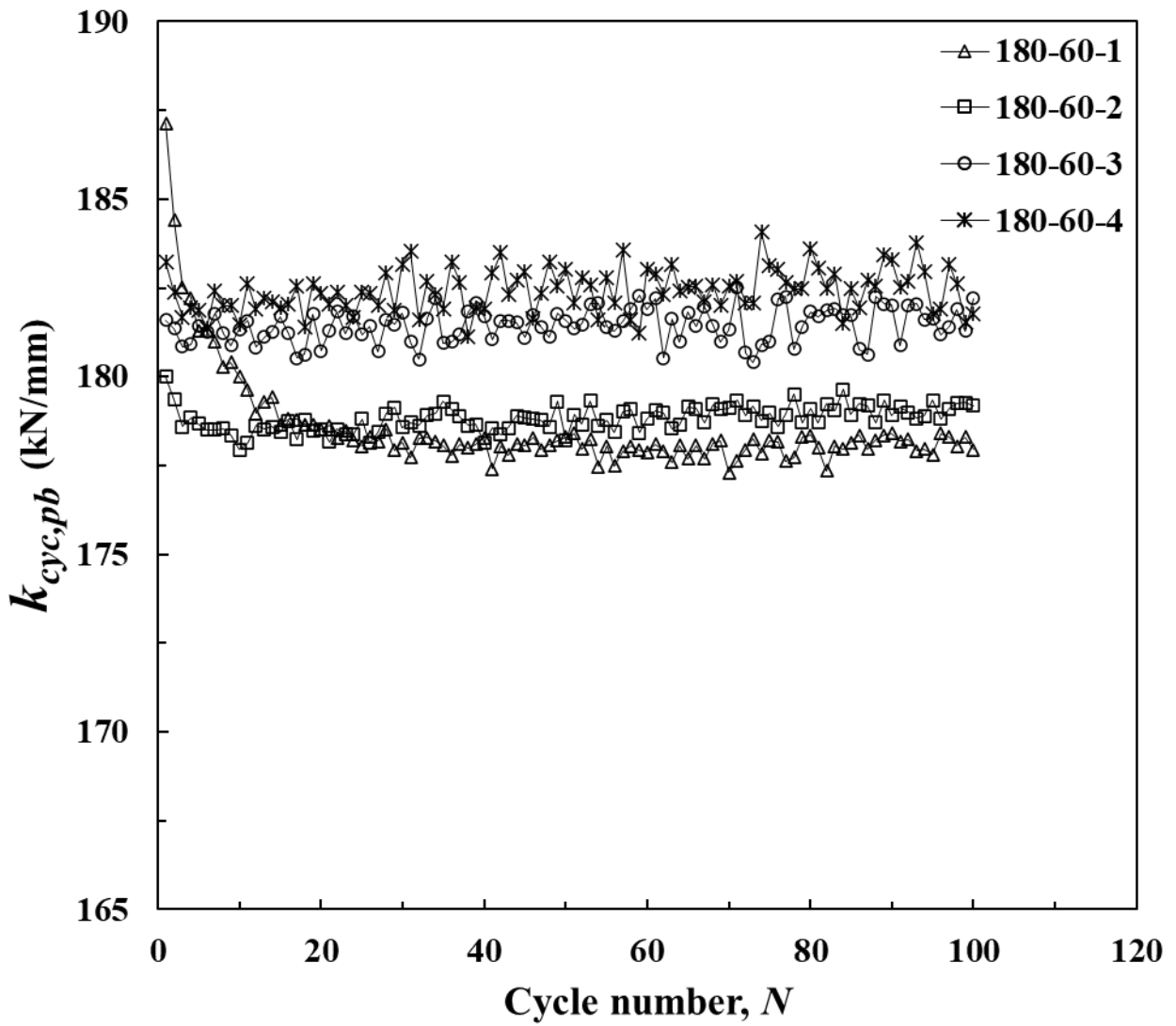


(c)

CHAPTER 4: CYCLIC BEHAVIOR OF THE FRP-SSC MODEL PILES ENDED IN ROCK-SOCKET



(d)

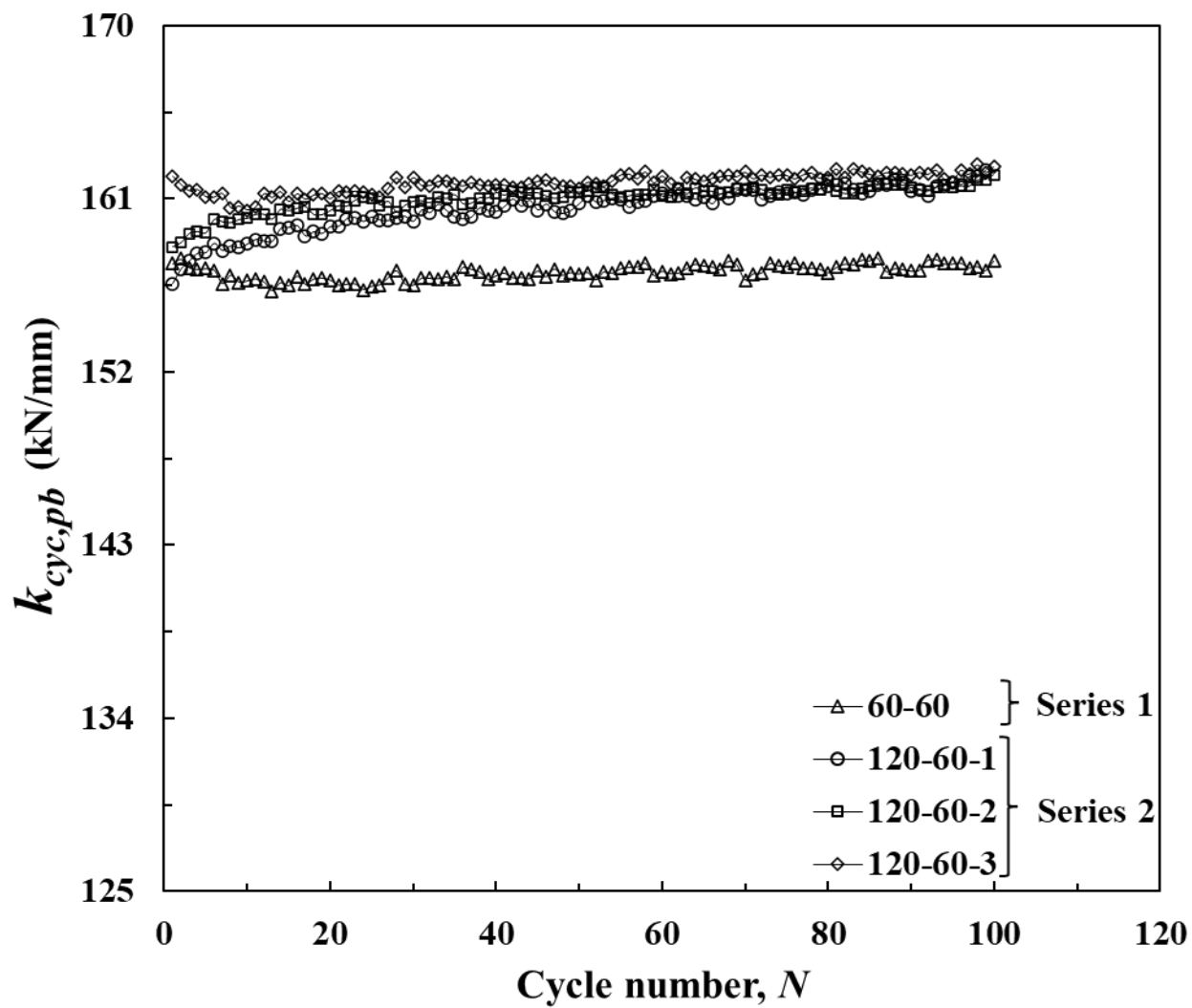


(e)

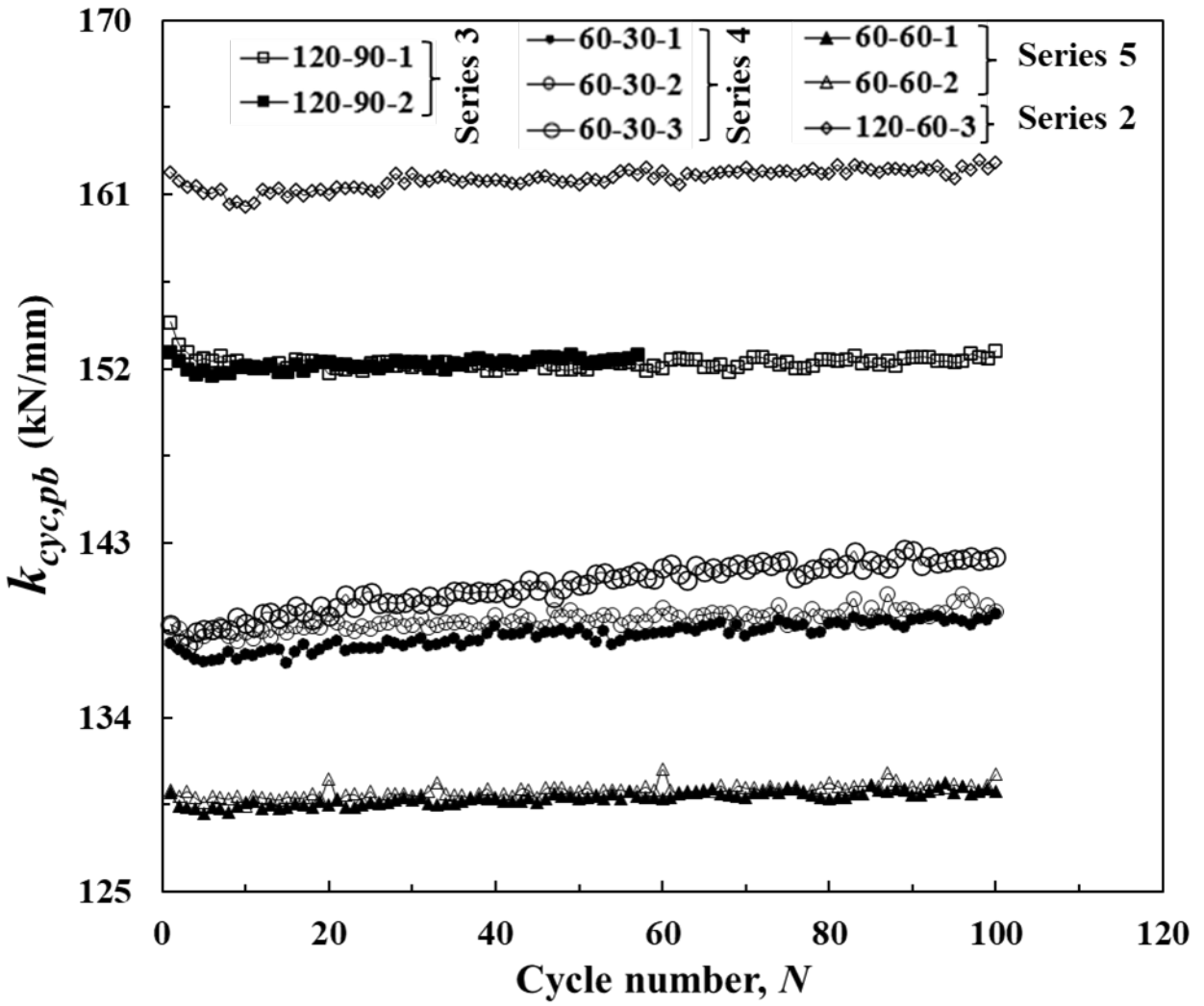
Figure 4.5 Variation of pile body stiffness of pile 2 under different cyclic loading series: (a)

Series 1; (b) Series 2; (c) Series 3; (d) Series 4; and (e) Series 5

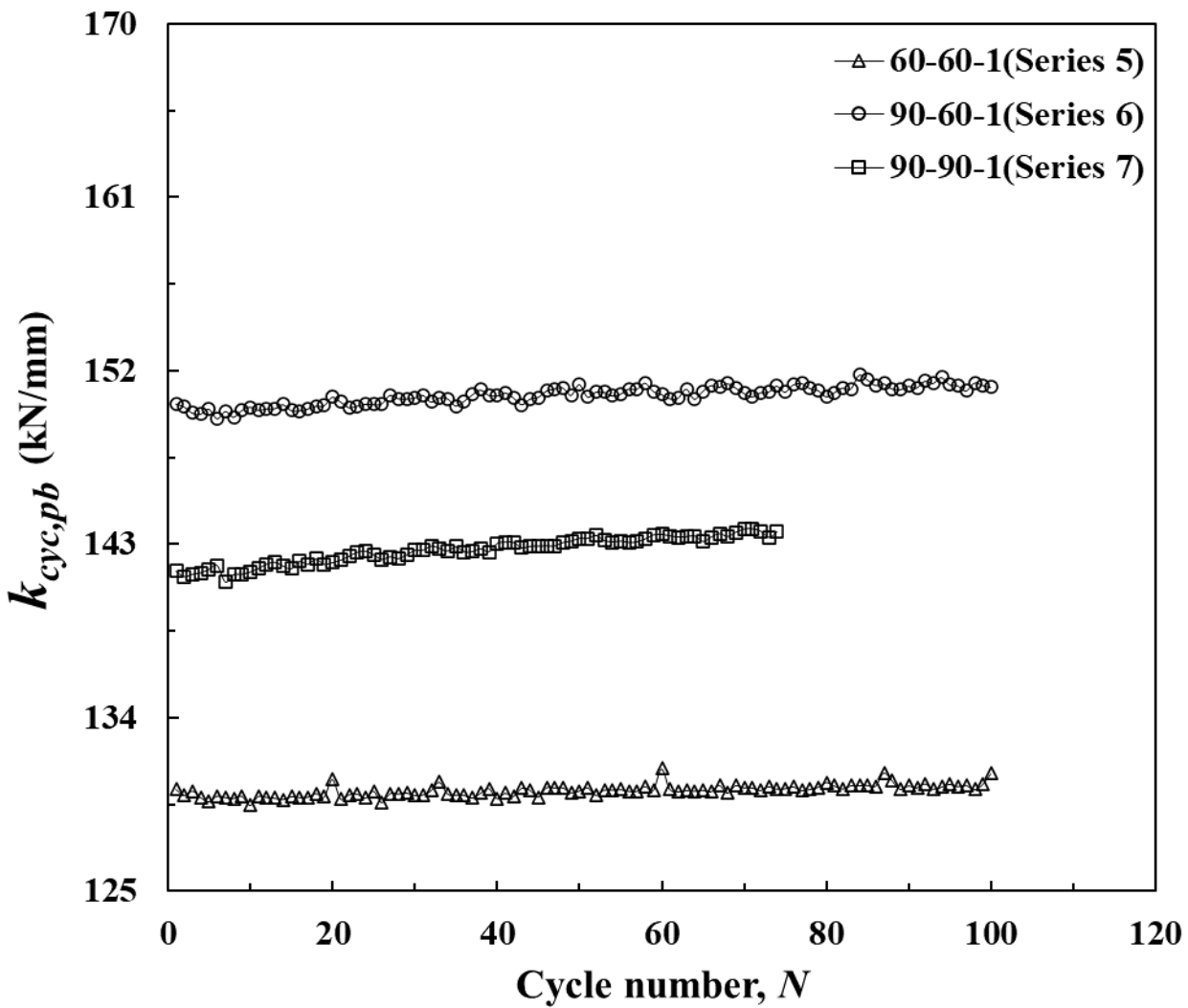
CHAPTER 4: CYCLIC BEHAVIOR OF THE FRP-SSC MODEL PILES ENDED IN ROCK-SOCKET



(a)



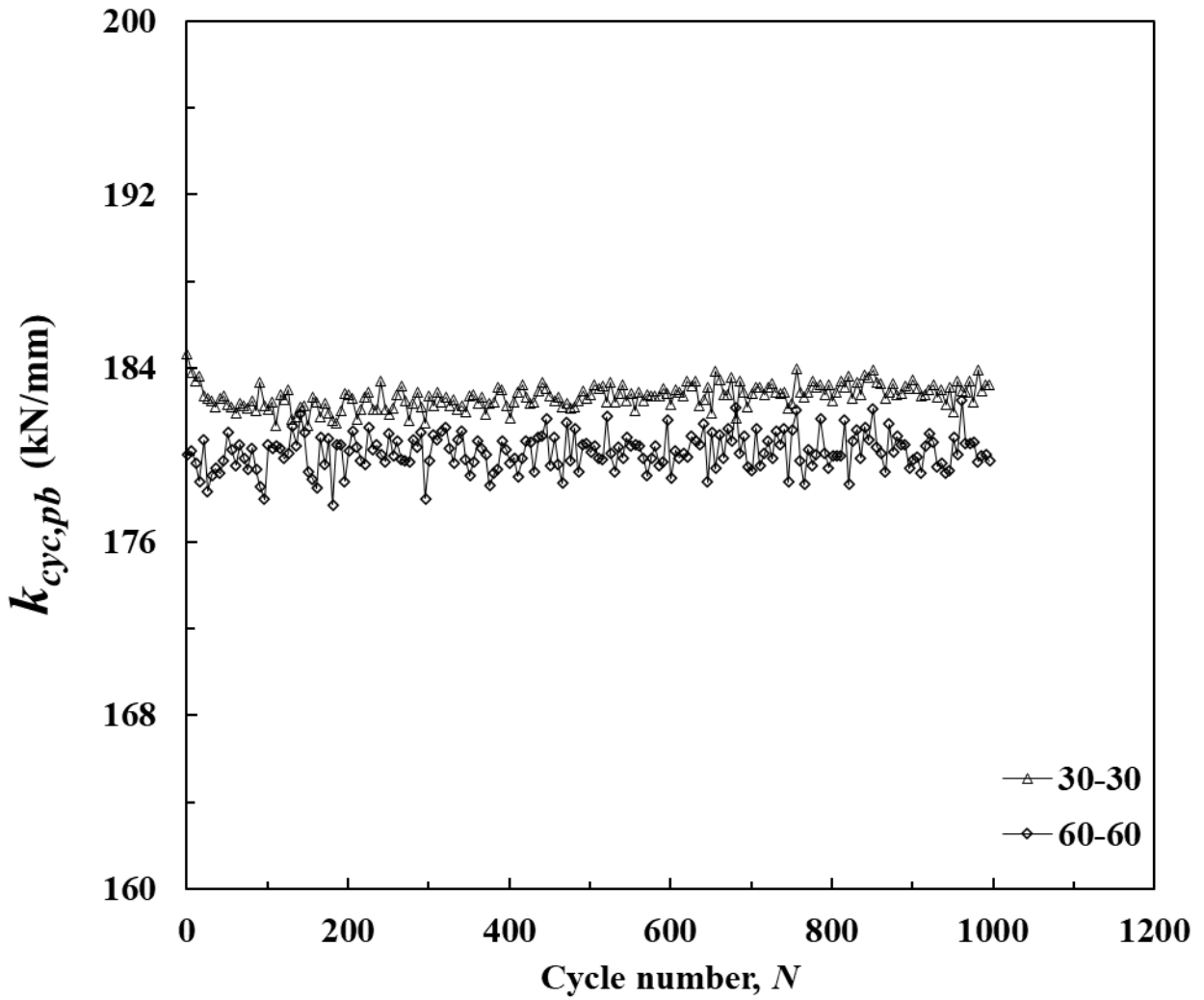
(b)



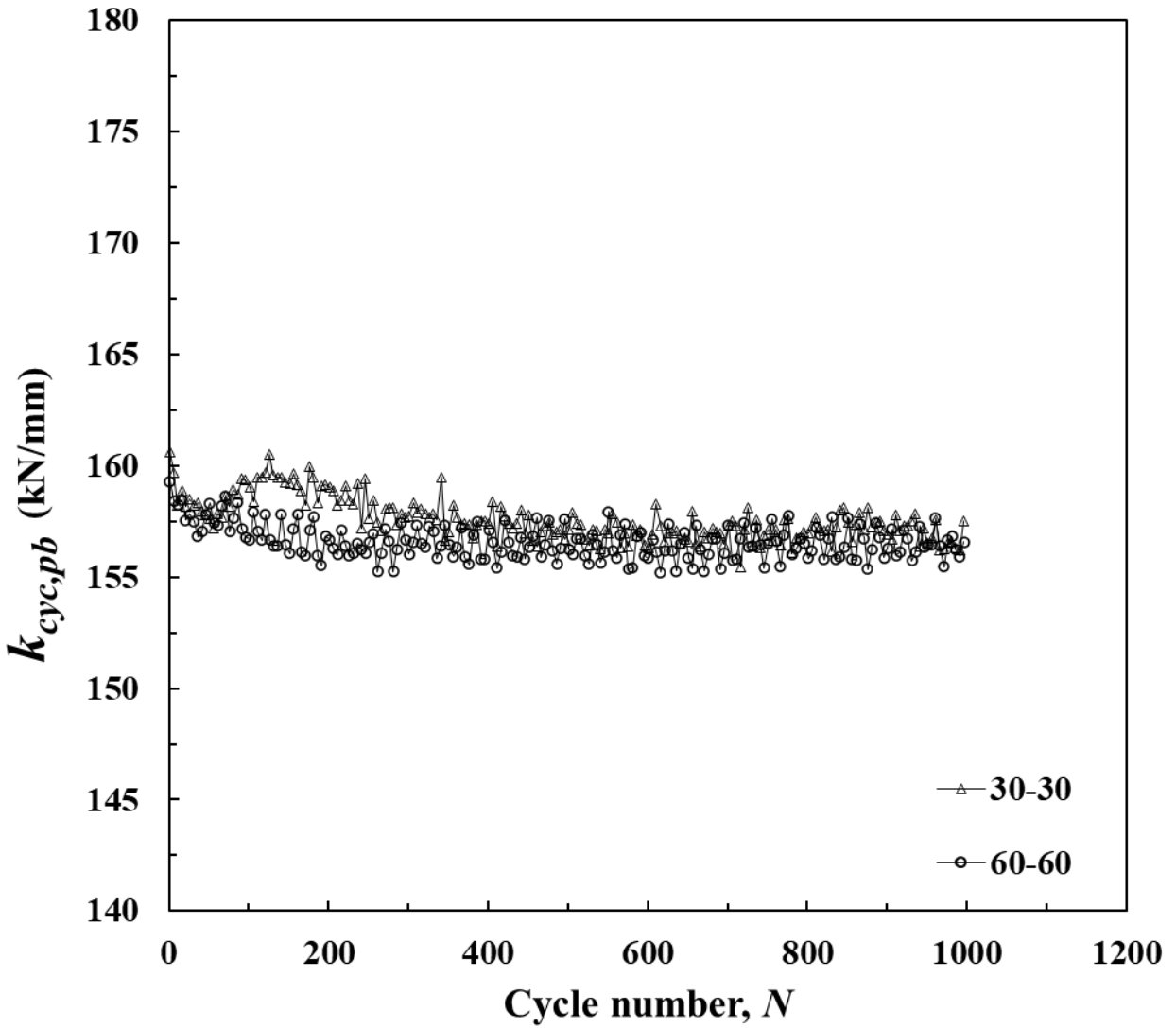
(c)

CHAPTER 4: CYCLIC BEHAVIOR OF THE FRP-SSC MODEL PILES ENDED IN ROCK-SOCKET

Figure 4.6 Variation of cyclic stiffness of Pile 3 under different cyclic loadings: (a) Series 1 and 2; (b) Series 3, 4, and 5; and (c) Series 6 and 7

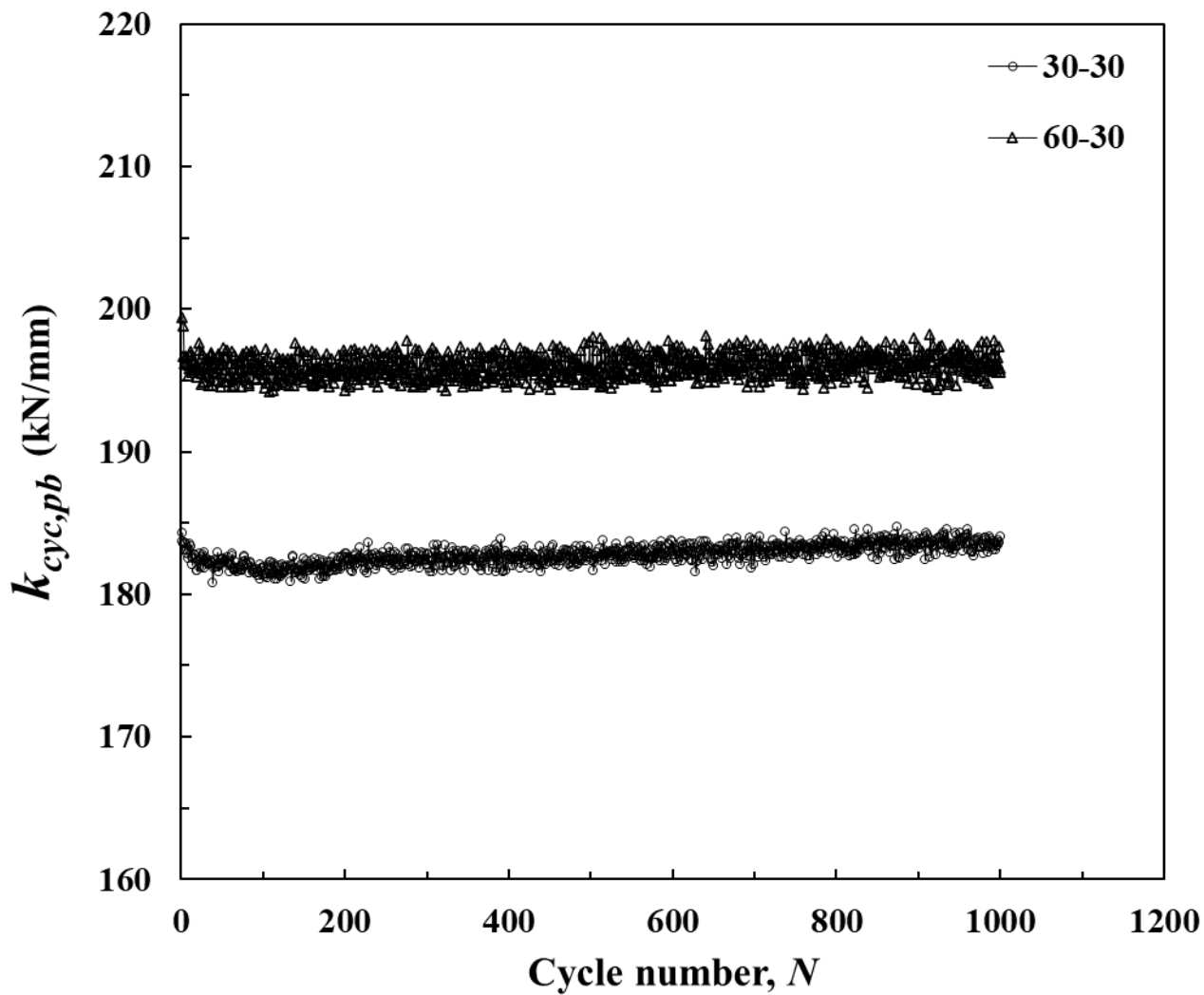


(a)



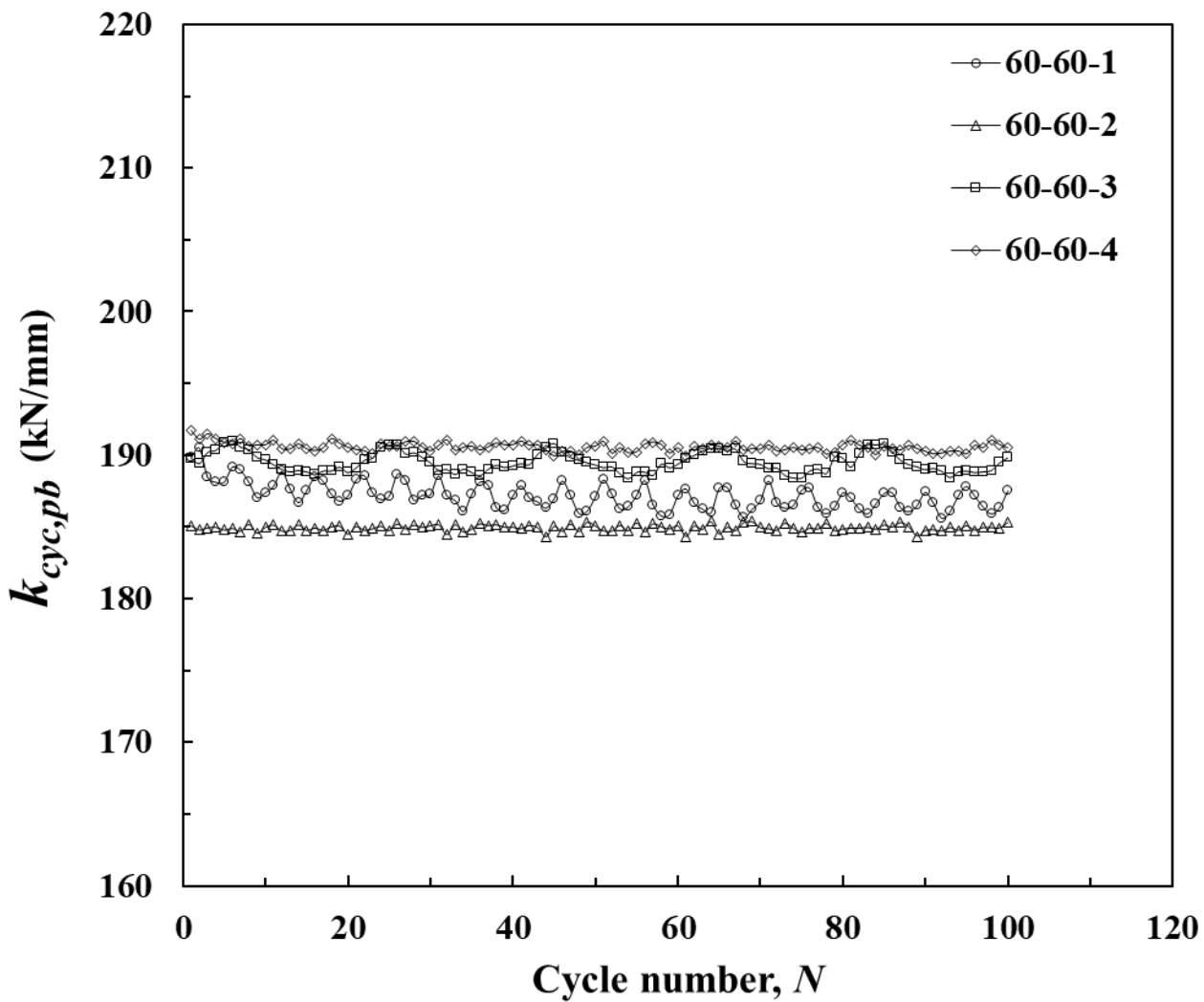
(b)

Figure 4.7 Variation of cyclic stiffness of (a) Pile 4 and (b) Pile 5 under cyclic loading



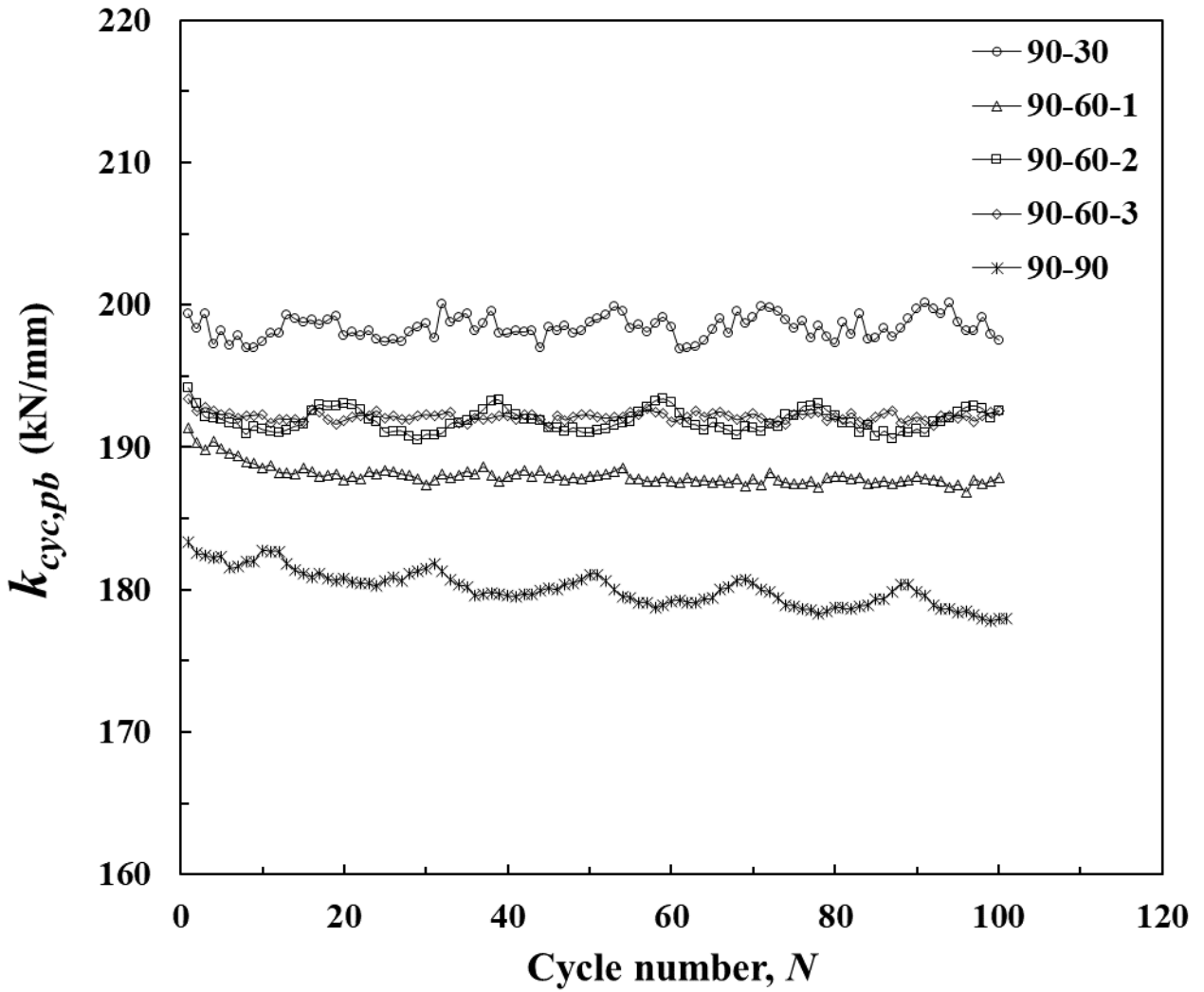
(a)

CHAPTER 4: CYCLIC BEHAVIOR OF THE FRP-SSC MODEL PILES ENDED IN ROCK-SOCKET

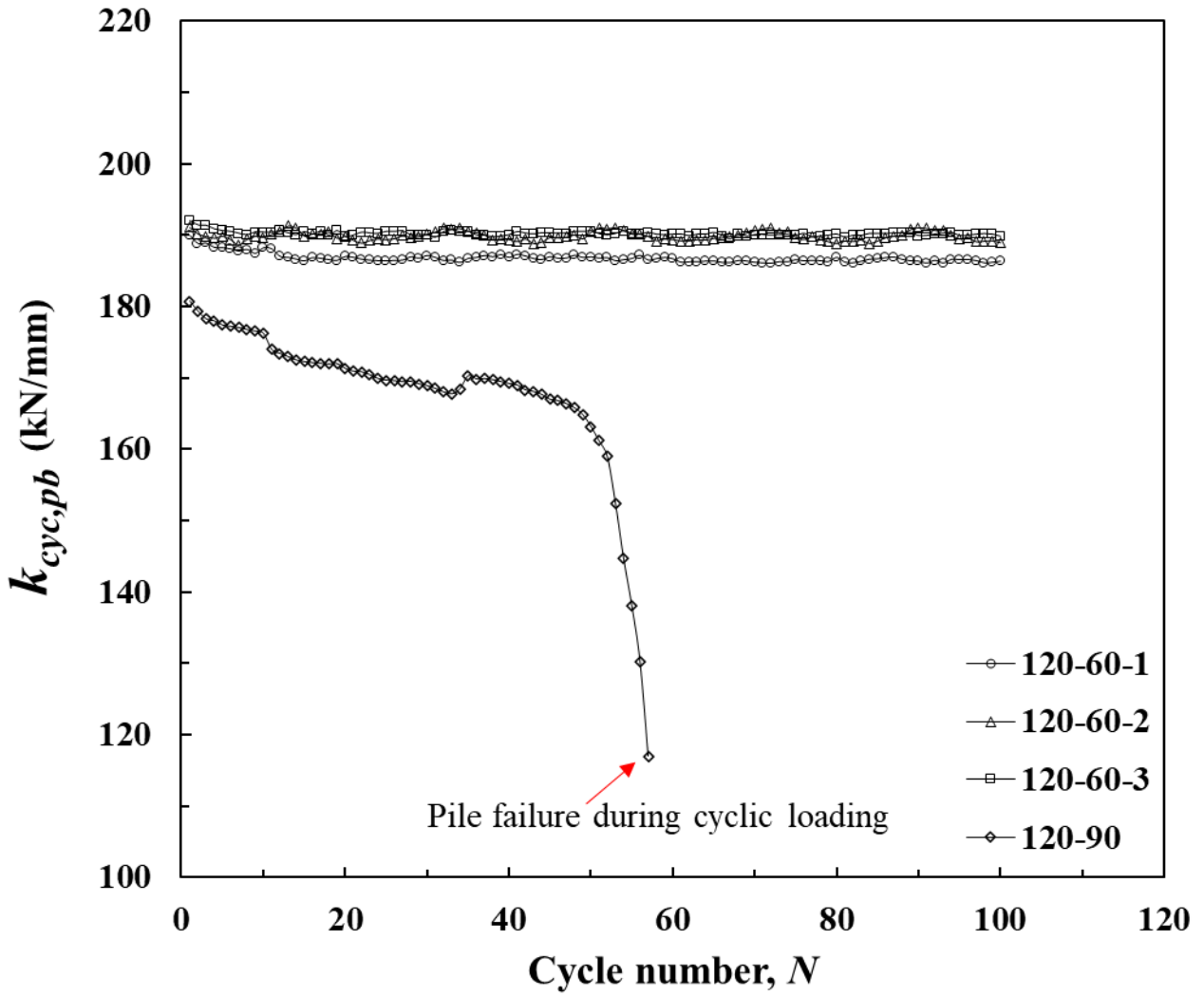


(b)

CHAPTER 4: CYCLIC BEHAVIOR OF THE FRP-SSC MODEL PILES ENDED IN ROCK-SOCKET



(c)



(d)

Figure 4.8 Variation of cyclic stiffness of Pile 6 under different cyclic loadings: (a) Series 1; (b) Series 2; (c) Series 3; and (d) Series 4

CHAPTER 4: CYCLIC BEHAVIOR OF THE FRP-SSC MODEL PILES ENDED IN ROCK-SOCKET

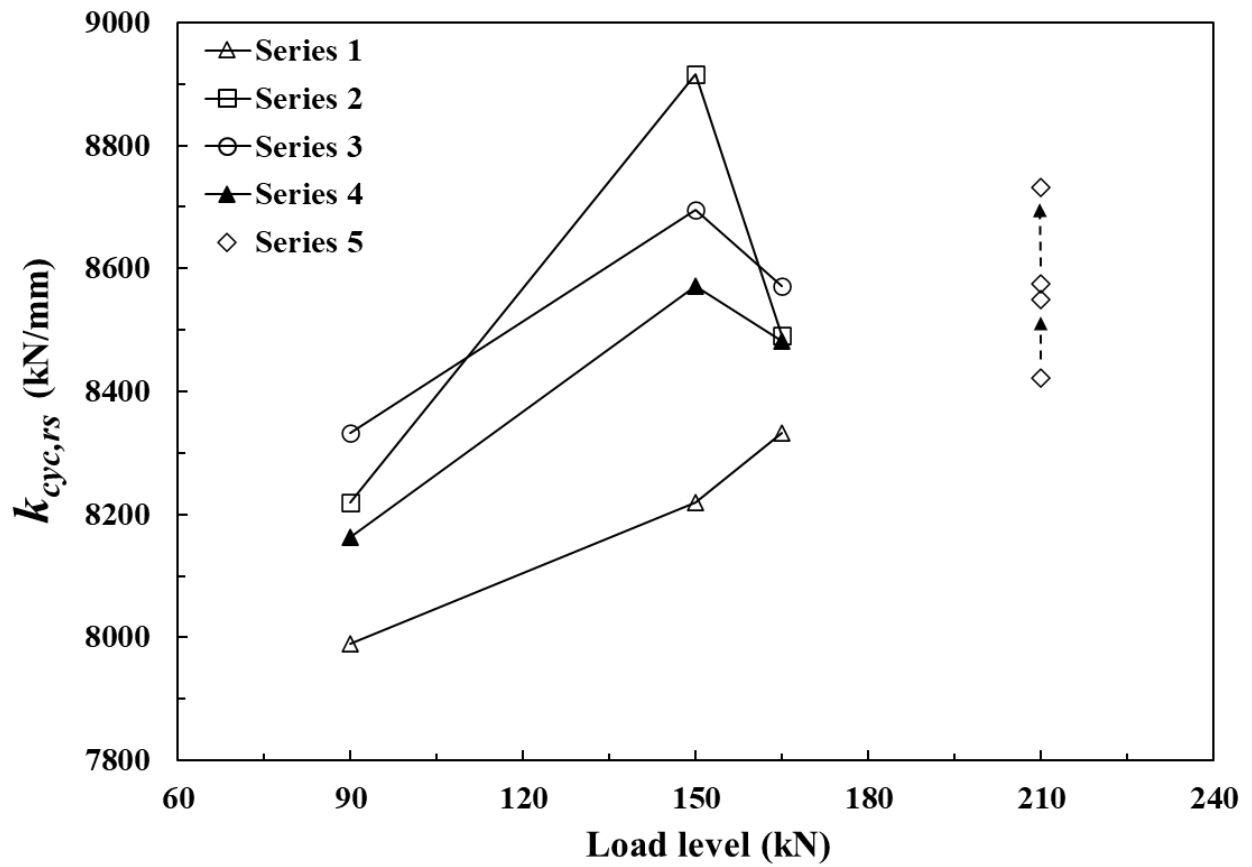


Figure 4.9 Stiffness variation of the socket under different series of cyclic loadings

CHAPTER 4: CYCLIC BEHAVIOR OF THE FRP-SSC MODEL PILES ENDED IN ROCK-SOCKET

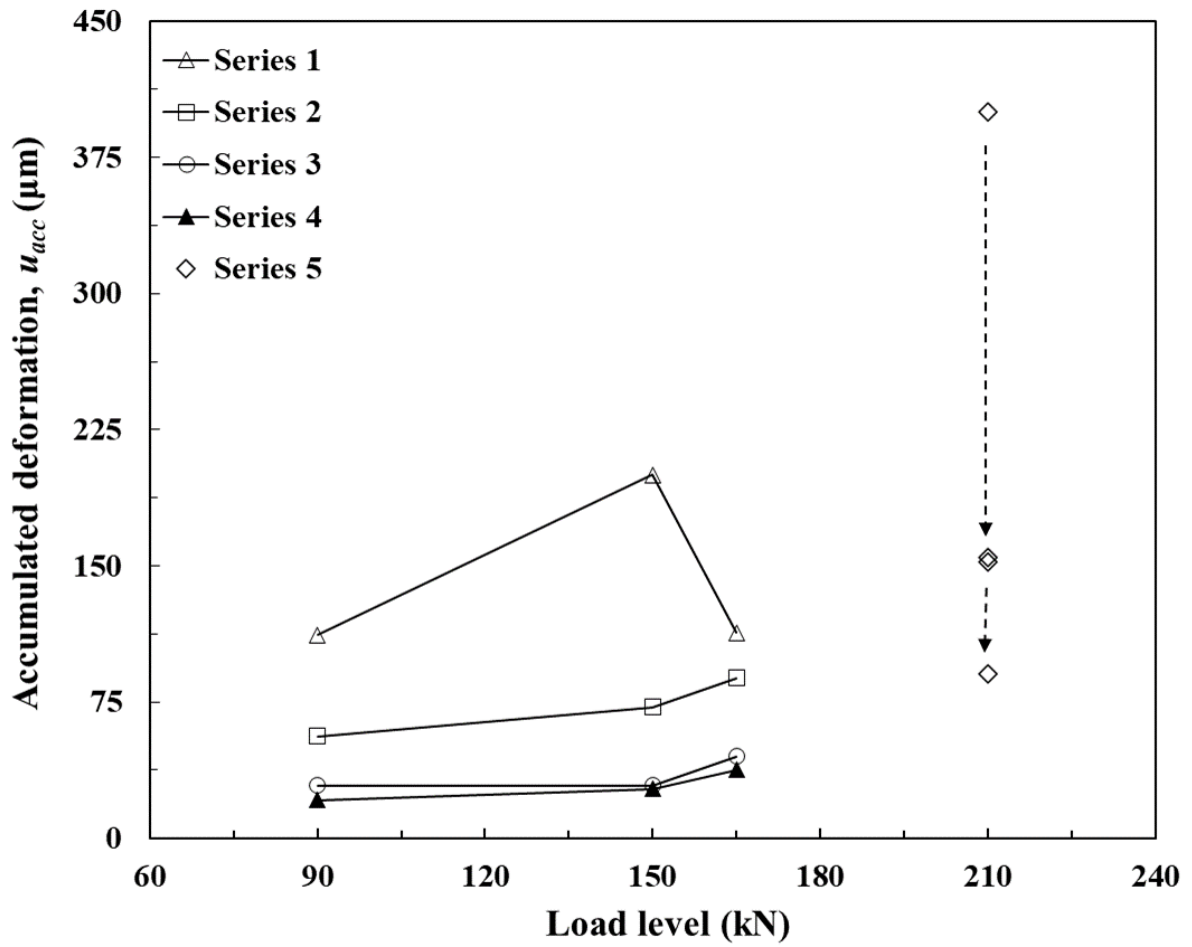


Figure 4.10 Compression accumulation within pile body under different cyclic loading conditions

CHAPTER 4: CYCLIC BEHAVIOR OF THE FRP-SSC MODEL PILES ENDED IN ROCK-SOCKET

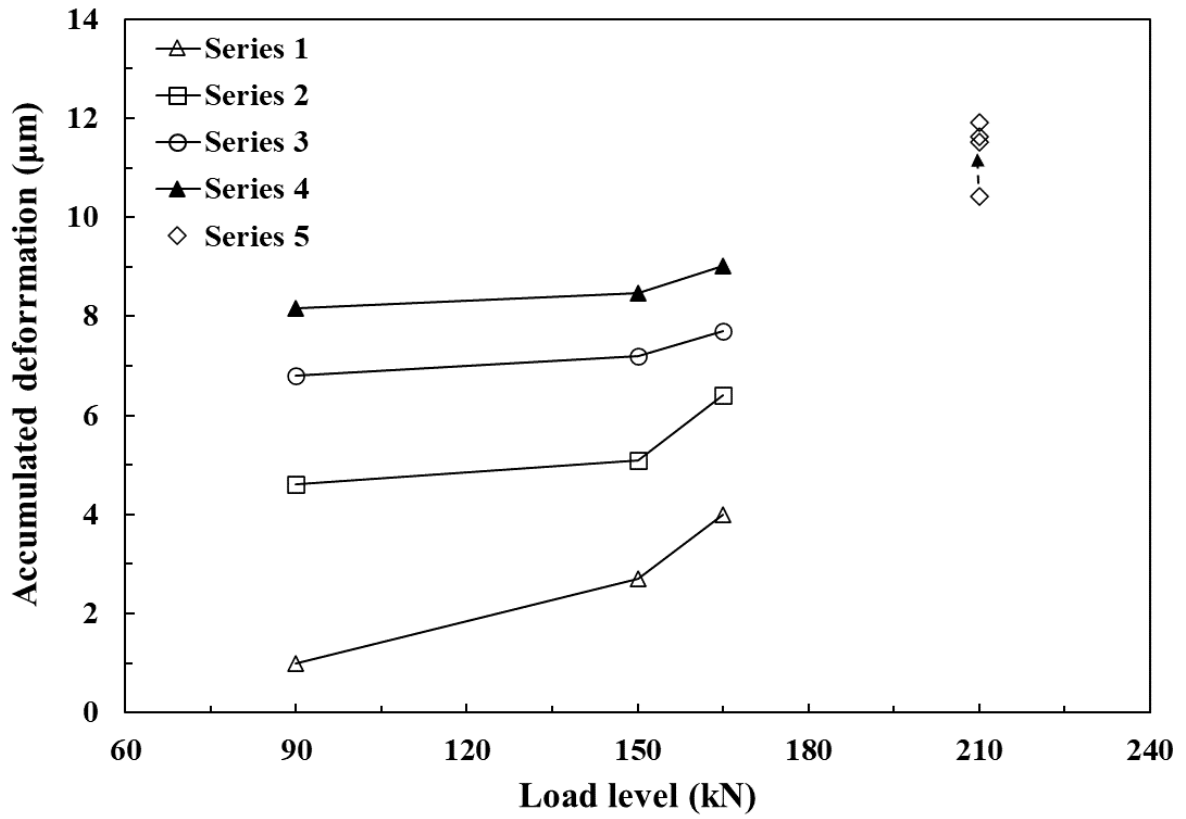


Figure 4.11 Accumulated compression of Pile 2 within the rock socket under cycling loadings

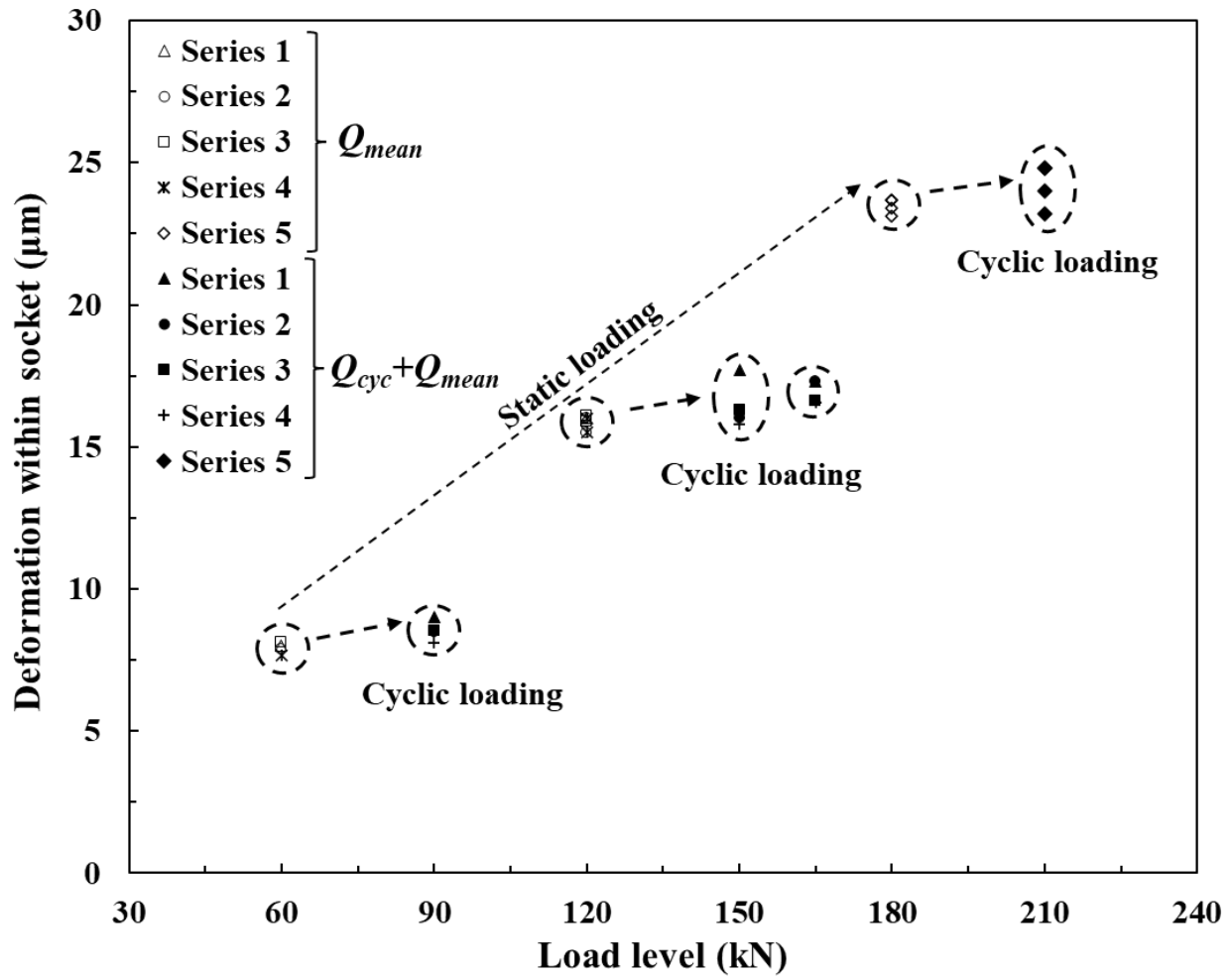
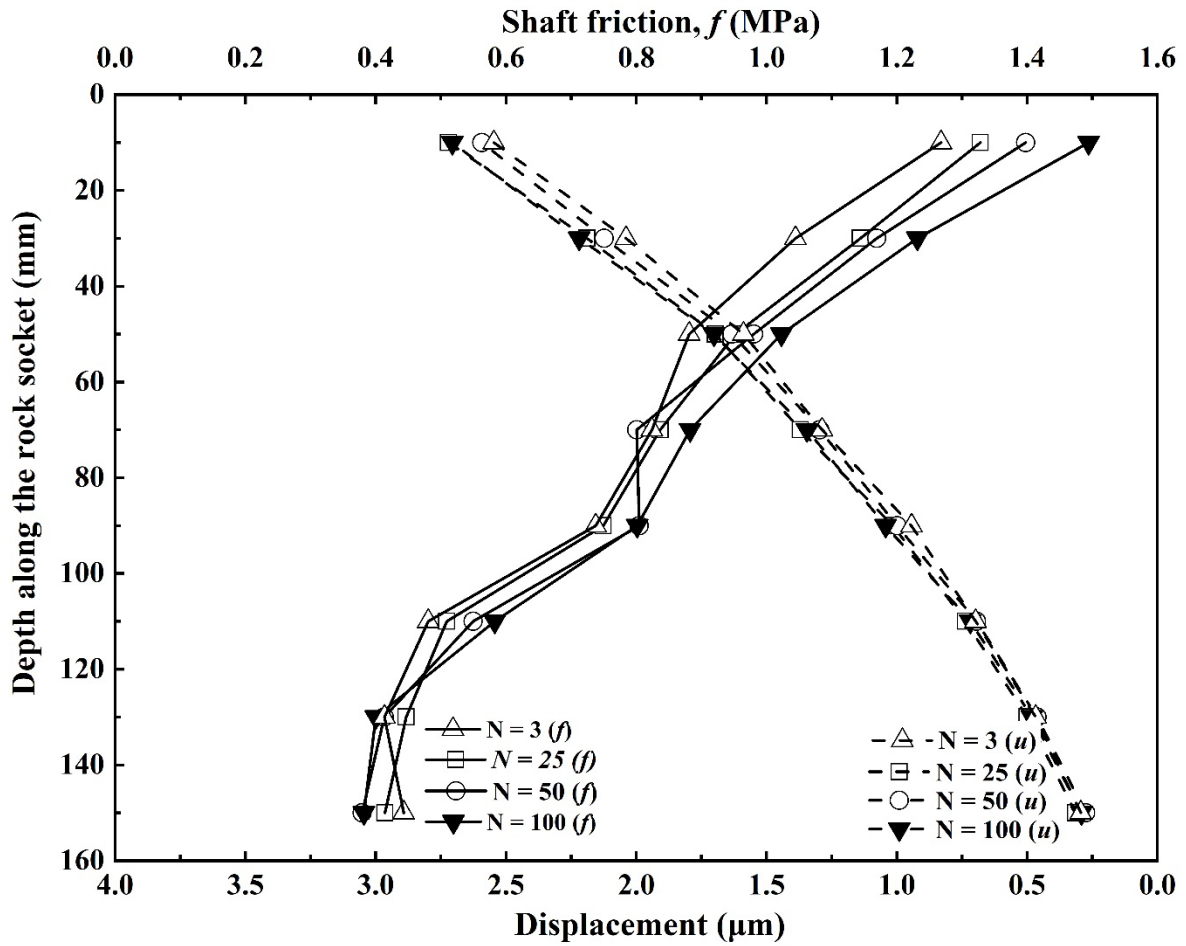


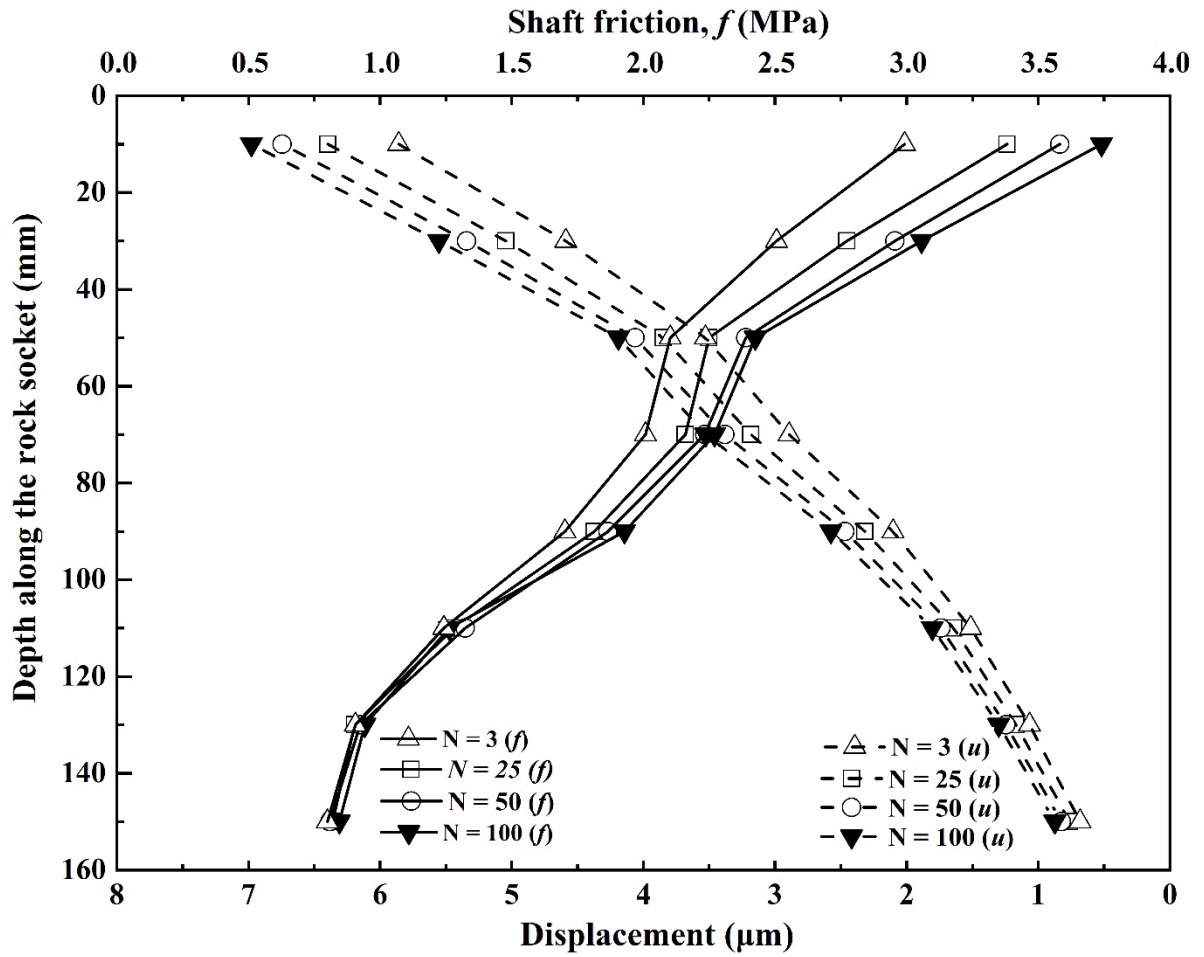
Figure 4.12 Compression of model pile within the socket recorded at static loading and cyclic maximum loading conditions

CHAPTER 4: CYCLIC BEHAVIOR OF THE FRP-SSC MODEL PILES ENDED IN ROCK-SOCKET

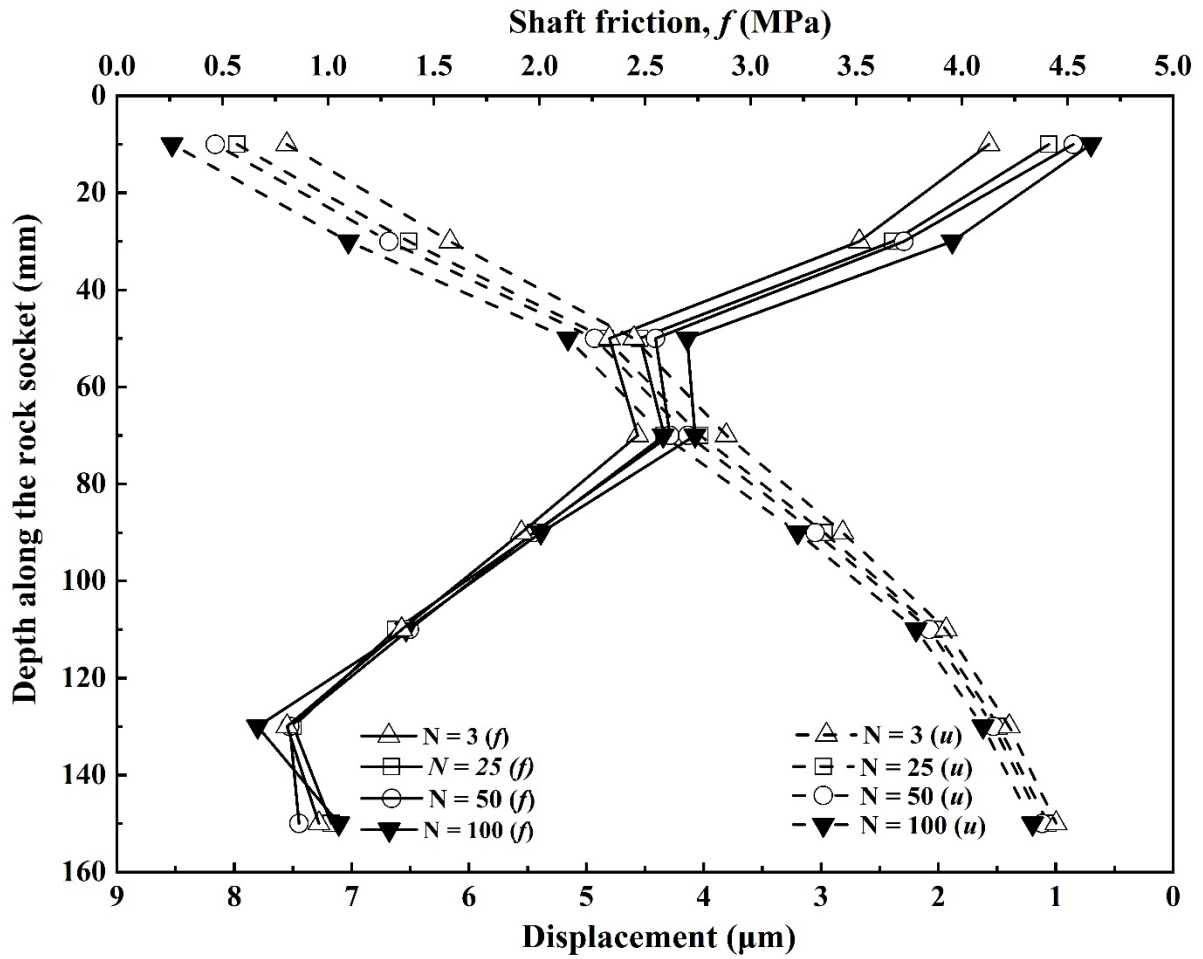


(a)

CHAPTER 4: CYCLIC BEHAVIOR OF THE FRP-SSC MODEL PILES ENDED IN ROCK-SOCKET



(b)



(c)

Figure 4.13 Mobilization of shaft friction and displacement along depth for different loading cycles on Pile 3: (a) 60-60; (b) 120-60; and (c) 120-90

CHAPTER 5: STATIC BEHAVIOR OF FRP-SSC MODEL PILES ENDED IN ROCK SOCKET

5.1 Introduction

In this chapter, firstly the behavior of FRP composite sea water sea sand concrete (SSC) short columns were investigated under static axial compression. A total of twelve short column specimens having different configurations were tested to study their compressive behavior. Secondly the static behavior of the proposed innovative and sustainable design of FRP-confined SSC model piles installed in a rock socket is presented. The static loading to failure of the model piles were conducted after the cyclic loading tests. The static loading tests aim to reveal load-displacement response and tangent modulus variation of model piles. The static response of piles before and after cyclic loading is compared to reveal loading history effects. Axial strain distributions measured with FBGs sensors and failure modes of model piles under static loading are discussed in detail. Moreover, the mobilization of shaft friction in the rock socket calculated from the strain monitored with OFDR optic fiber sensors is analyzed.

5.2 Preliminary elementary tests

5.2.1 Short columns tests

A total of twelve short column specimens having a diameter of 100 mm and height of 200 mm were prepared as shown in Figure 5.1 and tested under axial compression. The behavior of GFRP composite sea water sea sand concrete (SSC) short columns were investigated in detail. All the specimens were prepared from the same SSC mix as shown in Table 5.1. The specimens were

categorized into four different groups. For each group, three specimens were tested. The first group comprised of three unconfined plain concrete cylinders named (SSC-P) and considered as a reference for the remaining specimens. The second group consists of concrete filled GFRP tube (CFFT) columns, in which the SSC was confined with GFRP tube named (GFRP-SSC), while in the third group plain concrete cylinder were reinforced with centered GFRP rebar named (SSC-R). In the fourth group the CFFT specimens were reinforced with a centered GFRP rebar named (GFRP-SSC-R). All the specimens were cured for 28 days in the sea water to simulate marine environment under room temperature.

The GFRP tube used for these specimens has an inner diameter of 100 mm and thickness of around 3.5 mm while GFRP rebar has 19 mm diameter. The properties of the GFRP tube and rebar are discussed in section 3.3. The filament winding process was adopted for the manufacturing of the GFRP tube using E-glass fibers and vinyl ester resins. The fibre orientation to reinforce the tube was kept $\pm 45^\circ$ along the longitudinal axis. This orientation of fibres provides stiffness both in longitudinal and hoop directions.

5.2.2 Test setup and instrumentations

The top and bottom of all the cylinders were capped with gypsum to provide uniform surface for even stress distribution uniformly under axial loading. All the specimens were subjected to uniaxial compression using hydraulic press machine (MTS 815) till failure. The specimens were placed in the middle vertically between the loading plates of the MTS machine as shown in Figure 5.2(a). To record the axial and hoop deformations of the specimens, conventional 30 mm

strain gauges were used. Four strain gauges were installed on the outer surface at the middle height of each specimen for monitoring the axial and hoop strains as illustrated in Figure 5.2(b).

5.2.3 Compressive strength

Figure 5.3 shows stress-strain curves of all types of specimens being tested. The axial stress-strain curves show two major regions, one is elastic and the other is plastic region. The initial linearly elastic slope region is called elastic region, this region is common for all type of cylinders. The plain SSC and SSC with rebar specimens behave elastically till reach the ultimate unconfined compressive strength and then the curve descends reaching the crushing failure of concrete. However, in the case of GFRP tube confined SSC specimens the curve ascends after the transition zone transforms to the plastic region. During the compression, the concrete exhibits vertical cracks due to the tensile stresses which lead the concrete to expand laterally subjecting the confining GFRP tubes to resist the expansion of concrete by tensioning the GFRP tube in hoop direction.

At this stage, the confinement provided by the GFRP tubes gets activated and this the region referred to as a plastic region of the axial stress-strain curve. In this region, the SSC is fully crushed, and all the stress is carried by the GFRP tubes by fully providing the confinement. The confinement effect of the GFRP tubes increased the average strength and ductility significantly. Figure 5.4 shows the mean compressive strengths of all four short column groups being tested. The GFRP tube increased the ultimate load capacity by 56%, while the use of only rebar

enhanced the capacity by 17% over the plain SSC specimens. However, the combination of both GFRP tube and rebar increased the ductility and ultimate axial load capacity by around 100%.

5.2.4 Failure modes

All the specimens were kept in the sea water for 28 days under room temperature. In general deterioration was not observed in all the specimens due to the harsh marine environment. The plain SSC cylinders failed in a typical way under compression with generation of vertical and slightly diagonal cracks as shown in Figure 5.5(a). These cracks occurred when the distributed stress in lateral direction exceeded the allowable strength of the concrete. The white scales on the surface of SSC cylinder appeared due to alkaline action of seawater during curing. The cracks for the SSC-rebar specimen have mostly vertical cracks due to the reinforcement of the rebar as shown in Figure 5.5(b).

The GFRP tube confined cylinders failed due to the higher tensile stresses in hoop direction resulted in the rupture of the GFRP tube as shown in Figures 5.5(c) and 5.5(d). The rupture of the fibres occurred in the $\pm 45^\circ$ due to the same fabricated orientation of the fibres. During early to the middle stages of the loading, popping sounds of the micro cracking of concrete due to concrete core dilation in lateral direction were observed. The GFRP tubes completely ruptured at higher loads near ultimate capacity and the concrete was disintegrated at this stage failing immediately. The ultimate rupture failure was very noisy and sudden with no signs of warning for all GFRP confined specimens. The failure pattern shows that GFRP tubes provided significant contribution to the stiffness, strength, and ductility.

5.2.5 Axial and lateral stress-strain responses

The stress-strain response of the confined concrete depends largely on the level and mechanical properties of FRP composites confinement. Figure 5.6 shows the relationship between axial stress as a function of axial and lateral strain. The right side shows the plot between the axial stress and axial strain while the left side shows axial stress and lateral strain based on different type of the specimens. The axial strain and lateral strain curves of the confined SSC specimens shows same behaviour due the confinement action provided by GFRP tube. The fibre orientation $\pm 45^\circ$ provides uniform stiffness and strength to both axial and lateral strains. The lateral strain curves behave identically like axial strain curves comprising of both elastic and plastic regions which has been discussed in the previous section in detail.

The normalized lateral and axial strain response of all the specimens is shown in the Figure 5.7. Initially, all the specimens behaved identically showed linearity, except the SSC-R specimen responded slightly non-linearly. This can be explained by the fact in early loading conditions mostly the load is resisted by the concrete until concrete have no cracks. When the cracks develop in the concrete it starts to expand laterally and hence the load is distributed to the GFRP tube which provides confinement and axial stiffness as well. For the SSC-R specimen, the axial strain is more as compared to the lateral strain for the same axial stress, due to the absence of confinement in the lateral direction.

5.3 Model piles static behaviour

5.3.1 Load-compression response of model piles under static loading

The pile body compression u_{pb} was calculated by integrating the strain measured by eight FBGs along the depth of the model piles above the rock surface using the following equation:

$$u_{pb} = \int_0^{l_a} \varepsilon(z) dz \quad (5.1)$$

where l_a represents the length from the pile head to the rock surface; $\varepsilon(z)$ stands for the strain at the position with a distance of z to the pile head; the subscript “ pb ” denotes pile body.

The pile head load-pile body compression curves of the model piles monitored during post-cyclic monotonic loading are illustrated in Figure 5.8. With the same structural configuration, Piles 1 and 2 presented a similar trend in the load-compression response under a load of 130 kN. When the load was increased beyond 130 kN, however, Pile 1 significantly deformed due to a technical problem, i.e., by the failure of the circular steel transferring case resulting in the tilting of the pile. Hence, Pile 2 was discussed in detail in the following sections for the configuration of the FRP tube confined concrete pile. It can be observed that the FRP tube confined pile (Pile 2) withstood a higher load value of 240 kN compared with 215 kN of the FRP rebar cage reinforced pile (Pile 3) under the condition of the same compression value. Pile 2 exhibited more ductile behavior with the further increase of load because of the lateral confinement from the FRP tube, greatly improving the ductility and strength of concrete. Under the same loading magnitude, Pile 5 showed larger compression compared with Pile 4 due to the presence of debris in the rock socket

which reduced the pile stiffness resulting from the collapse and crushing of debris particles under higher loading levels (Chen et al. 2020).

5.3.2 Tangent modulus variation of model piles

In Figure 5.9, the variation of tangent modulus for Piles 2, 3, 4, and 5 with increasing pile body compression is presented. Before reaching a compression value of 0.75 mm, Piles 4 and 5 demonstrate significantly higher loading resistance compared to the other model piles. This can be attributed to the high modulus of the centered FRP rebar in these piles (50 GPa) in contrast to the modulus of concrete (22 GPa). However, starting from a compression of 0.5 mm, the tangent modulus of Piles 4 and 5 rapidly degrades, likely due to local buckling of the centered FRP rebar. In the case of Piles 2 and 3, there is an initial sharp decrease in tangent modulus, followed by a turning point at compressions of 0.14 mm for Pile 2 and 0.24 mm for Pile 3. Subsequently, both piles exhibit a period of strain hardening until reaching compression levels of approximately 1.2 mm to 1.3 mm. Throughout this range, the tangent modulus of Pile 2 remains consistently higher than that of Pile 3, indicating that the FRP tube provides greater confinement to SSC. The superior ductility of Pile 2 over Pile 3 is demonstrated by a larger compression value at which the tangent modulus starts to degrade rapidly, occurring at 1.71 mm for Pile 2 and 1.24 mm for Pile 3. Furthermore, it is noticeable that Piles 4 and 5 exhibit a slower degradation of modulus in the residual stage, followed by Pile 3 with FRP rebar stirrups, and then Pile 2 with FRP tube confinement. Pile 2 almost experiences brittle failure after the rupture and buckling of the FRP tube. These findings highlight the importance of pile configuration, specifically the presence of

different types of FRP components, in influencing the load response and compression behavior of the piles.

5.3.3 Comparison of static behavior of model piles before and after cyclic loading

The comparison of static loading behavior before and after cyclic loading tests can be made to investigate the effect of cyclic loading history on pile body (Figure 5.10) and shaft resistance (Figure 5.11) development. It can be generally concluded that Pile 2 showed no significant change in the strength development under static loading after 120-90 cyclic loading was applied, which possibly indicated that the pile capacity almost kept stable when cyclic loading is within a certain threshold. However, after 180-60 cyclic loading was applied, the strength mobilization rate of Pile 2 obviously degraded, as shown in Figure 5.10(a). On the contrary, Pile 3 started to degrade after 120-90 cyclic loading was applied (Figure 5.10(b)). This difference between Pile 2 and Pile 3 is due to the difference in confinement, which is also confirmed by the tangent modulus degradation as shown in Figure 5.10(b). Pile 4 generally showed less change after 60-60 cyclic loading was applied (Figure 5.10(c)). As shown in Figure 5.11, the deformation resistance in rock socket kept improving with cyclic loading level smaller than 120-90, while kept almost stable when cyclic loading level increased to 180-90.

5.4 Axial strain distributions measured with FBGs sensors and failure modes of piles under static loading

5.4.1 Axial strain distribution along depth of Pile 2

The axial strain of Pile 2 at different depths along the pile body under different monotonic load levels is shown in Figure 5.12(a). When the load level was lower than the ultimate value, the strain of the pile presented a generally similar pattern along the pile depth under different load levels, with a peak value at the depth of 340 mm and a minimum value at the level of the rock surface. The strain value increased with the increase in load level. At depths of 340 mm and 980 mm, strain value showed a variation and experienced a sudden increase at an ultimate load of 266 kN. This increase in strain could be ascribed to the local buckling of the FRP tube and concrete crushing observed at the failure stage of the pile. The Euler's buckling is more likely to occur when the slenderness ratio (λ) is high which governs the failure of the member (Tomblin and Barbero, 1994). The slenderness ratio of a member can be defined as the ratio of the length of a member to its diameter under the condition of end fixity. Because of having high λ , the model pile failed in buckling near the pile head because of the low-end fixity of the pile head.

5.4.2 Axial strain distribution along depth of Pile 4 and 5

The axial strains of Pile 3 measured at different load levels are displayed in Figure 5.12(b). The strain profile appeared to have constant values along the depth from the pile top to the level of rock surface. Under increasing load, strain value increased and followed a similar trend with smooth curves for different load levels. Initially, the increase in strain with the increase of load

varied slightly under a load of 120 kN, but strain response showed significant variations under 180 kN and higher loading conditions. The maximum load taken by the pile before failure was 213 kN, and the load resisting ability of the pile dropped afterwards. The strain response at 213 kN showed variations between 180 and 340 mm. Markedly higher localized strain values were observed and confirmed by the appearance of cracks in concrete. Similarly, the high values of strain were recorded at 980 mm owing to the breakage of FRP rebars and the shedding of the concrete cover.

5.4.3 Axial strain distribution along depth of Pile 3

The axial strain response monitored during the monotonic loading of Pile 5 is shown in Figure 5.12(c). Since Piles 4 and 5 have an identical structural configuration above the rock surface, only the latter was discussed here. The strain value increased with the increase of load and showed constant strain response under the same load along the depth of the pile except for the obvious smallest value on the rock surface. The strain variation under lower load levels was relatively slight with smooth curves. However, strain increased significantly with the increase of load when the load was increased beyond 120 kN. At a maximum load level of 208 kN, the strain response showed a sudden increase at 340 mm. Cracks in the concrete and breakage of the rebar resulted in the shedding of concrete from the rebar and the failure of the pile at this location.

5.4.4 Failure modes of the model piles under static loading

All the model piles failed at the same position $0 \sim l_d/4$ near the pile head on account of low-end fixity at the pile head with the exception of obvious damage between $0 \sim l_d/4$ from the pile bottom in the case of Pile 3, as shown in Figure 5.13. Pile 2 failed due to the rupture and buckling of the FRP tube shown in Figure 5.13(a). It can be found from Figure 5.13(b) that the rupture of longitudinal FRP rebars and cracks in the concrete cover led to spalling and the failure of Pile 3. Piles 4 and 5 failed due to the separation of concrete from FRP rebars and the breakage of FRP rebars which resulted in brittle failure, as shown in Figure 5.13(c).

5.5 Shaft friction mobilization of model piles under static loading

5.5.1 Shaft friction data interpretation and analysis

The shaft friction f inside the rock socket between the granite rock and the pile was measured from the load distribution in the pile body inside the socket. And the load distribution was calculated from the distributed strain data of pile measured with OFDR optic fibers rather than FBG. As a discrete sensing element, the FBG adopted in this study has a length of 15 mm, which indicates it will measure the average strain within this range. However, one of the FBG sensors in the pile locates at the level of rock surface such that the stuck effect, induced by the imperfect matching between the pile and the drilled socket hole, would affect the accuracy of that specific FBG sensor. On the other hand, OFDR provides more detailed profile of shaft friction along socket depth due to its full distribution nature. Rock quality designation (RQD) was kept the same for all the model piles. Piles 4 and 5 were not instrumented with OFDR optic fibers and

Pile 6 failed during cyclic loading hence Pile 2 and 3 shaft friction results were discussed as representative piles. The following relation was used to calculate the shaft resistance in the rock socket:

$$f = \frac{\Delta F}{\Delta h \cdot \pi \cdot D} = \frac{\Delta \sigma_c A_c + \Delta \sigma_f A_f}{\Delta h \cdot \pi \cdot D} \quad (5.2)$$

where D is the pile diameter; Δh is the distance between two strain measuring points and ΔF is the force difference between two consecutive surfaces with distance of Δh , and the force applied on the cross section can be determined by

$$F(y) = E(y) A \varepsilon(y) \quad (5.3)$$

where EA is the axial rigidity of pile (E is the Young's modulus and A is the cross-sectional area). The Young's modulus of the pile was determined from the moduli of the materials used in the pile (i.e FRP and concrete) given as

$$E = \frac{E_c A_c + E_f A_f}{A_c + A_f} \quad (5.4)$$

where E_c and E_f are the moduli of concrete and FRP respectively; A_c and A_f represents the area of the concrete and GFRP respectively. The GFRP rebars were considered as linear elastic materials with an elastic modulus of 50 GPa. However, the concrete was considered a non-linear elastic-plastic material and the stress-strain curve measured by strain gauges of small cylindrical specimens fitted well with the equation specified in Comité Euro-International du Béton–Federation International de la Précontrainte (CEB-FIP) Model Code (FIP 1993) :

$$\frac{\sigma_c}{f_{cm}} = \frac{A\eta - \eta^2}{1 + (A-2)\eta}, \eta = \frac{\varepsilon_c}{\varepsilon_{cm}}, A = \frac{E_c}{f_{cm} / \varepsilon_{cm}} \quad (5.5)$$

where σ_c represents axial stress; f_{cm} stands for the peak stress ($f_{cm} = 31$ MPa); ε_c refers to axial strain; ε_{cm} denotes the strain at f_{cm} ($\varepsilon_{cm} = 0.00344$); E_c is the initial elastic modulus ($E_c = 22.9$ GPa). The tangent modulus $E_t = \frac{d\sigma_c}{d\varepsilon_c}$ varied according to Eq. (7), which was used for calculating the load distribution of piles.

5.5.2 Mobilized shaft friction in the rock socket of Pile 2

The strain profile monitored by the OFDR fiber section S12 embedded in the concrete was utilized for calculating the load transfer curves. The load-transfer curves were used for the calculation of mobilized shaft friction within the socket using Equation 5.2 given in section 5.5.1. The fiber section monitored the strain till 120 mm depth of the socket, and beyond it the fiber was not able to detect the signals due to fiber sharp angle at the base within the socket. The shaft friction profiles at different loading levels along the depth within the socket are presented in Figure 5.14. In general, shaft friction increased with increasing loading level and decreased along depth for same loading magnitude. Higher shaft friction mobilization took place in the socket's upper region (0–50 mm), relative to the lower portion due to the small strain values near the base. Under the loading of 266 kN, the maximum shaft friction of 5.6 MPa mobilized in the 0–20 mm zone. The shaft friction decreased to 4.68 MPa in the 40–50 mm region and followed by a faster decreasing rate along the depth reaching 0.9 MPa near the base for the same load.

5.5.3 Mean shaft friction and end bearing of Pile 2

The mean shaft friction and bearing pressure evolution with the applied load are shown in Figure 5.15(a). The mean shaft friction was calculated based on the shaft friction profiles calculated from the optic fiber data discussed in the previous section. The mean shaft friction showed approximately a linear response with the applied load reaching ultimate value of 4 MPa under the applied load of 266 kN. The rock socket used in this study had higher stiffness, therefore the mean shaft friction increased linearly at uniform rate. However, the end bearing pressure showed a nonlinear response comparatively and reached an ultimate value of 5.5 MPa. The mobilization of shaft and base resistance with the displacement at the upper cross-section of the socket near rock surface is presented in Figure 5.15(b). The shaft resistance mobilized early at small displacements and increased linearly, providing around 77% contribution to resist the applied load. In contrast, the base resistance mobilized slowly at higher loads, reaching a maximum value of 52.7 kN when the displacement reached 9.5 μm . The base resistance accounted for around 23% of the applied load at the ultimate loading conditions.

5.5.4 Mobilized shaft friction in the rock socket of Pile 3

Shaft friction profiles at different loading levels were calculated using Equation 5.4 based on the strain profiles measured by different fiber sections. According to Equation 5.4 the modulus of the pile can be calculated based on the moduli of FRP and concrete, hence fiber sections (S1 and S3) attached to independent longitudinal FRP rebars and one fiber section (S4) embedded in the concrete were considered for determining shaft friction profiles development. The curves in Figure 5.16 show the mobilized shaft friction profiles under different loading levels measured

with different fiber sections along the depth within the rock socket. Generally, the shaft friction decreased along the depth for same loading magnitude and increased with increase in loading level. The maximum shaft friction of 5.5 MPa under 213 kN was mobilized in the region of 0-20 mm and dropped to 4 MPa in the region of 20-40 mm and decreased slowly along the depth under the same load. The shaft friction profiles showed smooth curves which can be used for evaluation and determination of mean shaft friction for the predictive and design tools

5.5.5 Mean shaft friction and end bearing of Pile 3

The axial load of piles ended in a rock socket is supported by combined shaft resistance and base resistance. The ultimate post-cyclic static monotonic load capacity Q_{us} of each model pile is shown in Table 4.2. For all the piles, the failures were observed in the pile body above the rock socket, indicating the higher capacity of pile within the rock socket. The mean shaft friction, end bearing, and the load percentage taken by shaft and base in the rock socket against the applied load are presented in Figure 5.17(a). The mean shaft friction increased almost linearly with the increase in load however the end bearing showed a non-linear response. Around 78.4-88.9 % of the load was resisted by the pile shaft and 11.1-21.6 % was resisted by the pile base showing the major contribution by shaft resistance, corresponding to a ratio of shaft resistance over total loading of around 10% based on the design chart provided by Pells and Tumer (1979). When the applied load was increased beyond 20 kN, the percentage contributed by shaft resistance decreased gradually while that of base increased. The contributions of shaft and base resistance against the displacement of pile at the top cross-section of rock socket are shown in Figure 5.17(b). The shaft resistance mobilized at a small relative displacement between the rock and pile

hence significant portion of the applied load on rock-socketed piles was transferred to the rock-pile interface at the side. It can be observed that when the displacement exceeded 3 μm , the pile base resistance started to mobilize and increased with the increase in applied load.

5.6 Summary

A distributed sensing technique, i.e., distributed OFDR and multiplexed FBG sensors were employed to monitor the fully distributed axial strain profiles, end bearing, and shaft friction mobilization under static monotonic loading which contributed to the design of pile foundation. The strain distribution along the depth of piles showed a similar trend for the model piles with higher strains recorded in the region $(0 - l_a/4)$ from the pile head. The failure of FRP tube confined and centered FRP rebar reinforced SSC piles happened within this region near the pile head. However, the FRP rebar cage reinforced SSC pile showed the maximum deformation in the same region near the pile head and rock surface. The axial strain profiles within rock-socket were utilized to develop load transfer curves to calculate reliable shaft friction values that may be used in future pile design of similar conditions. The maximum shaft friction was mobilized in the upper one-third region of the socket. The mean shaft friction mobilized early at smaller displacement with maximum up to 3.3 MPa and 4 MPa compared to end bearing pressure which mobilized at higher displacement with maximum up to 4.85 MPa and 5.5MPa for Pile 3 and 2 respectively). The observed shaft friction values between the rock and pile shaft were higher compared to conventional designs showing underestimation of actual values.

Table 5.1 Concrete mix proportion

	Portland cement	Fly Ash	Sea sand (<5 mm)	Sea water	Super plasticizer
Proportion	0.75	0.25	3.25	0.6	0.01

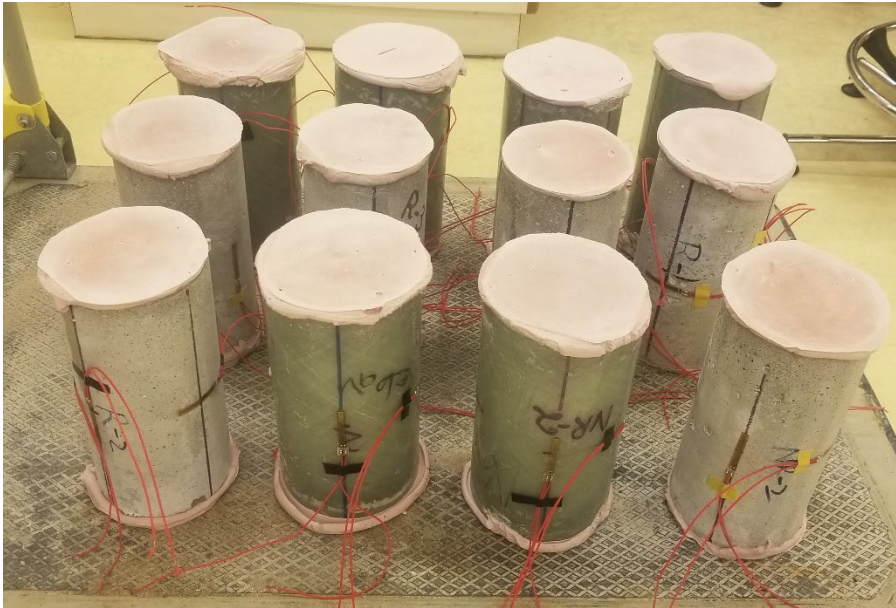
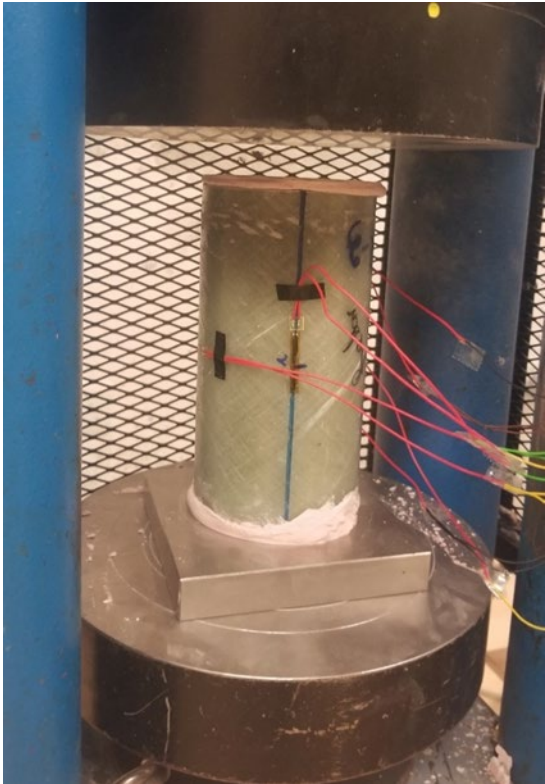
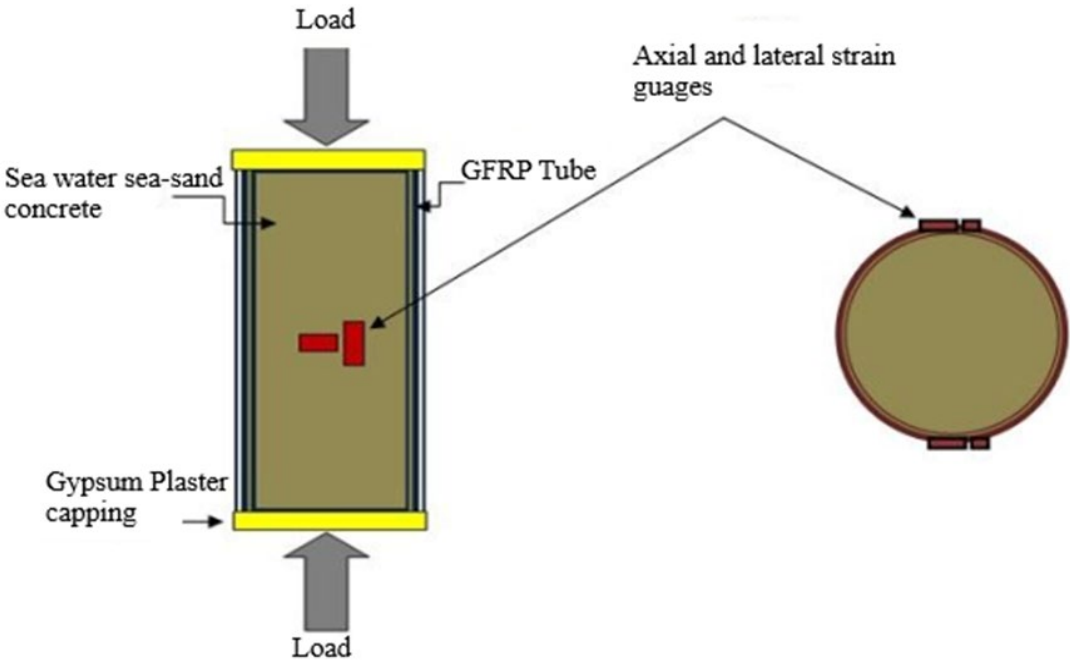


Figure 5.1 Short column specimens



(a)



(b)

Figure 5.2 (a) Test setup and (b) schematic view of the tested GFRP confined SSC cylinders

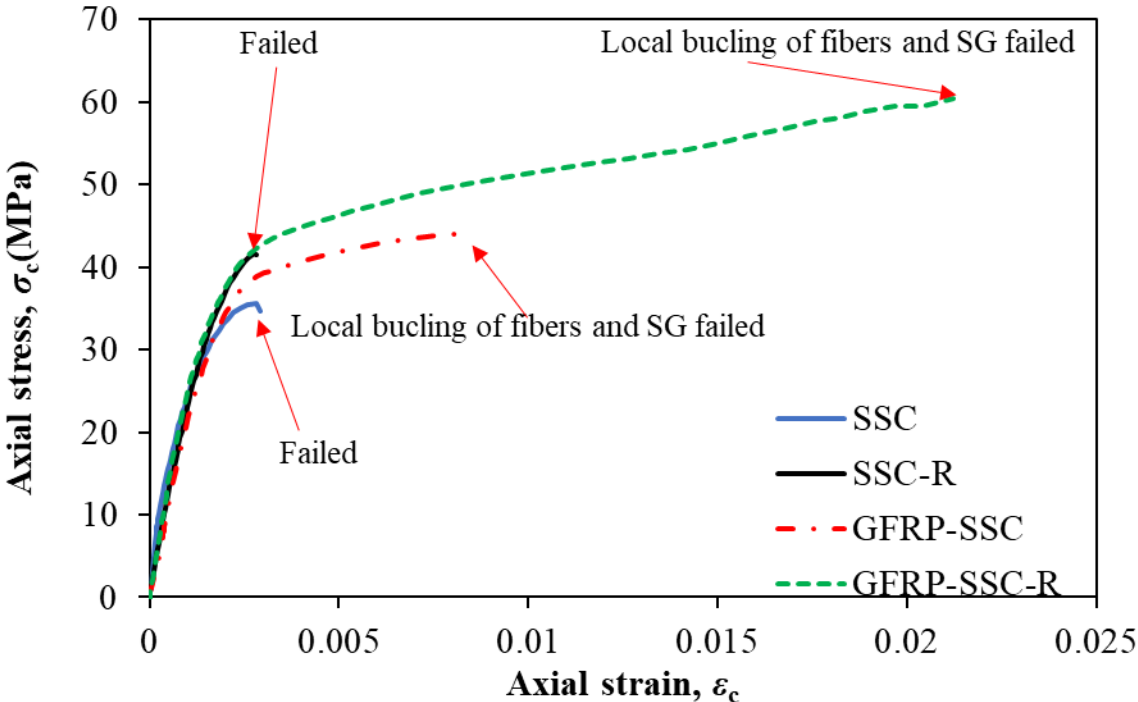


Figure 5.3 Stress-strain curves of the different short column specimens

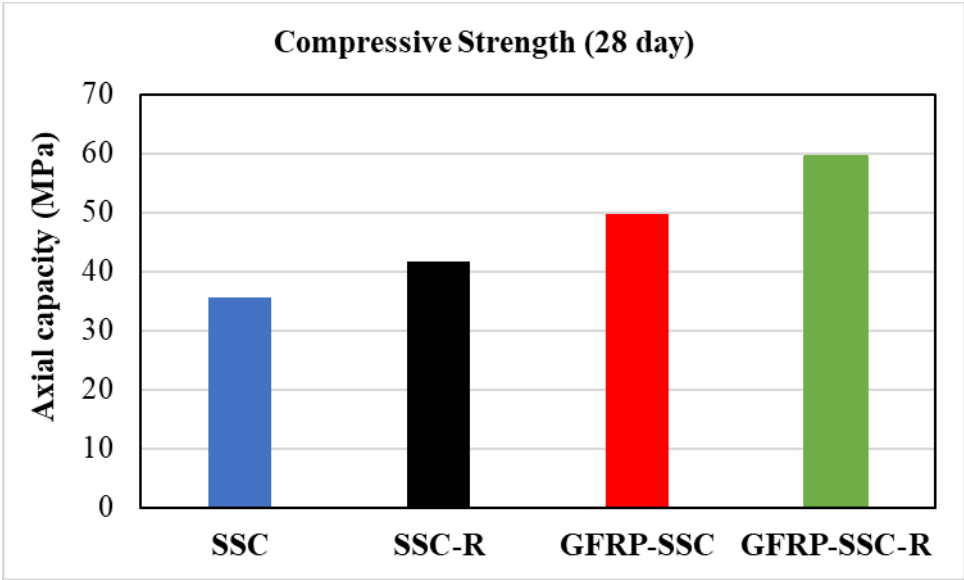
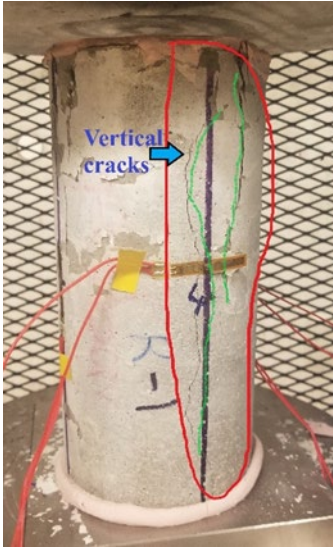


Figure 5.4 Mean compressive strengths of the cylinders



(a)



(b)

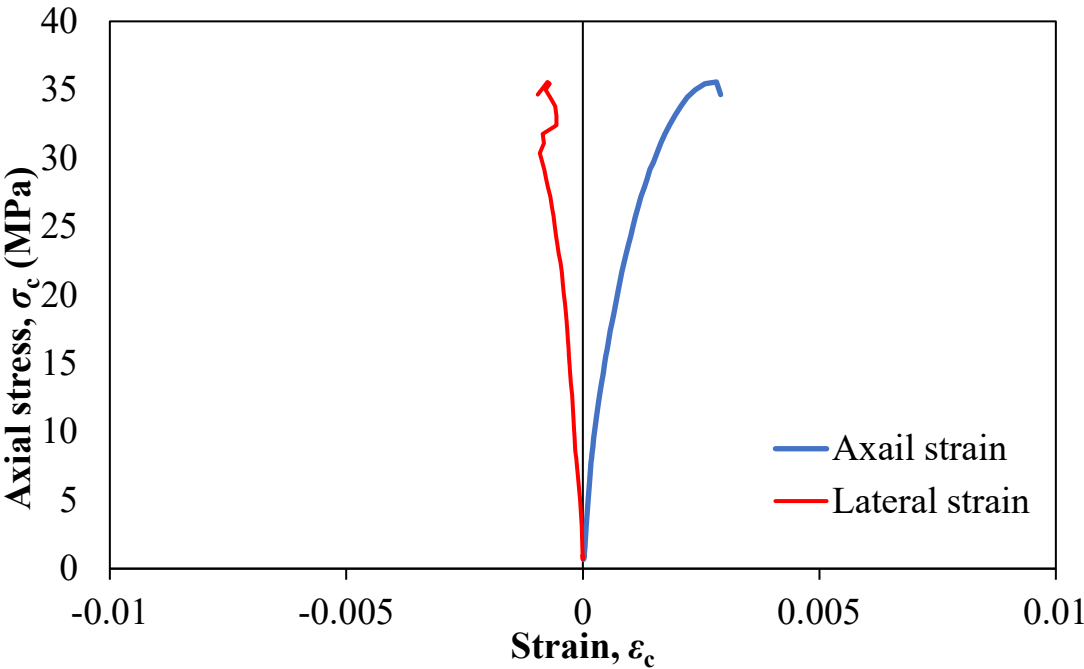


(c)

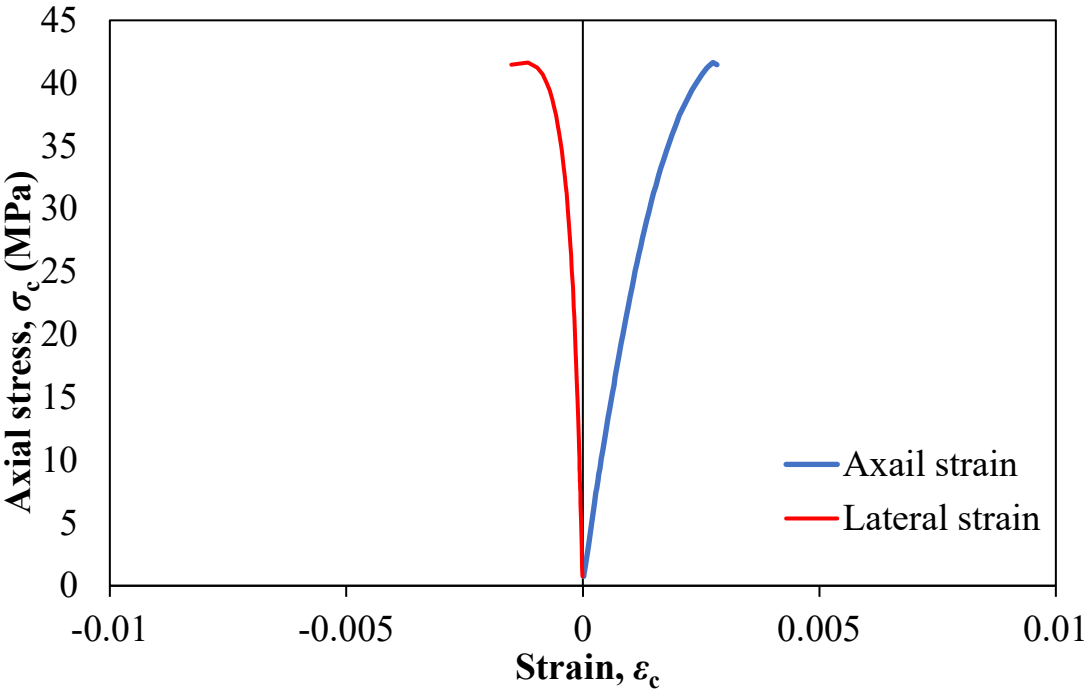


(d)

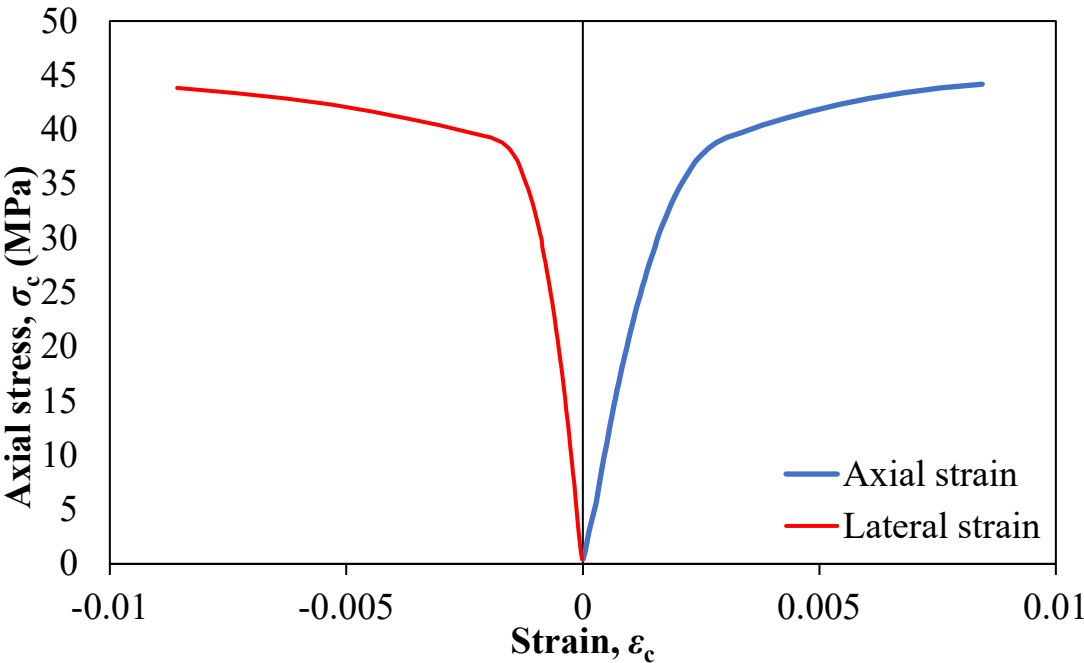
Figure 5.5 Failure modes of the specimens under axial compression: (a)vertical and diagnol cracks; (b) vertical cracks; (c) failure due to bucking of FRP tube; and (d) failure due fibers delamination



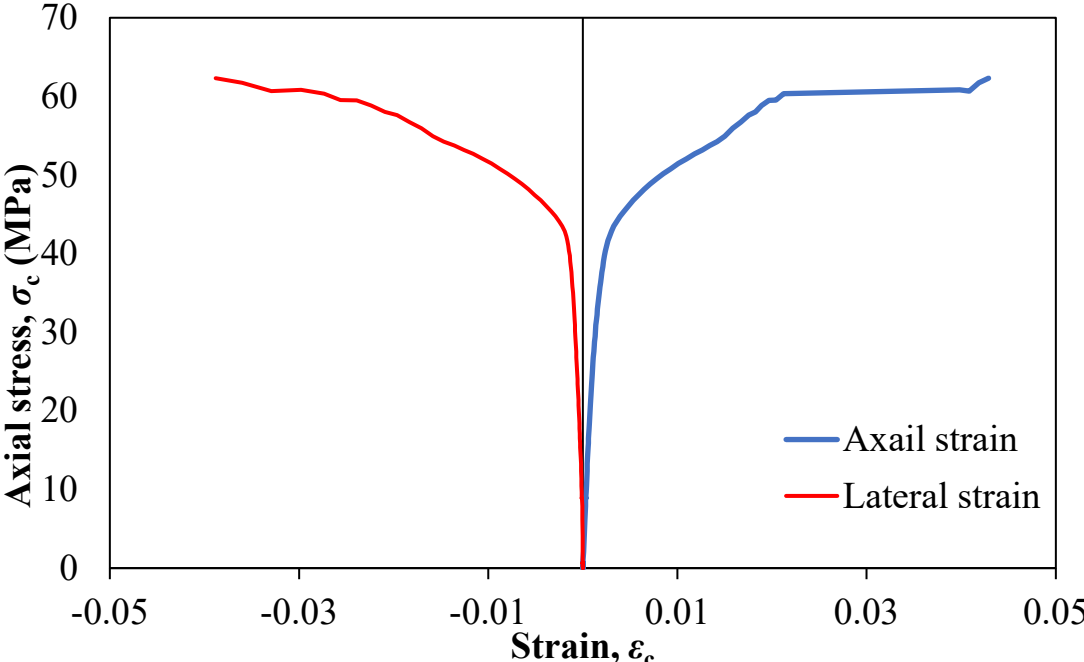
(a)



(b)



(c)



(d)

Figure 5.6 Axial and lateral strain responses of different cylinders: (a) plain SSC cylinder; (b) SSC with GFRP rebar; (c) GFRP confined SSC cylinder; and (d) GFRP confined SSC cylinder with rebar

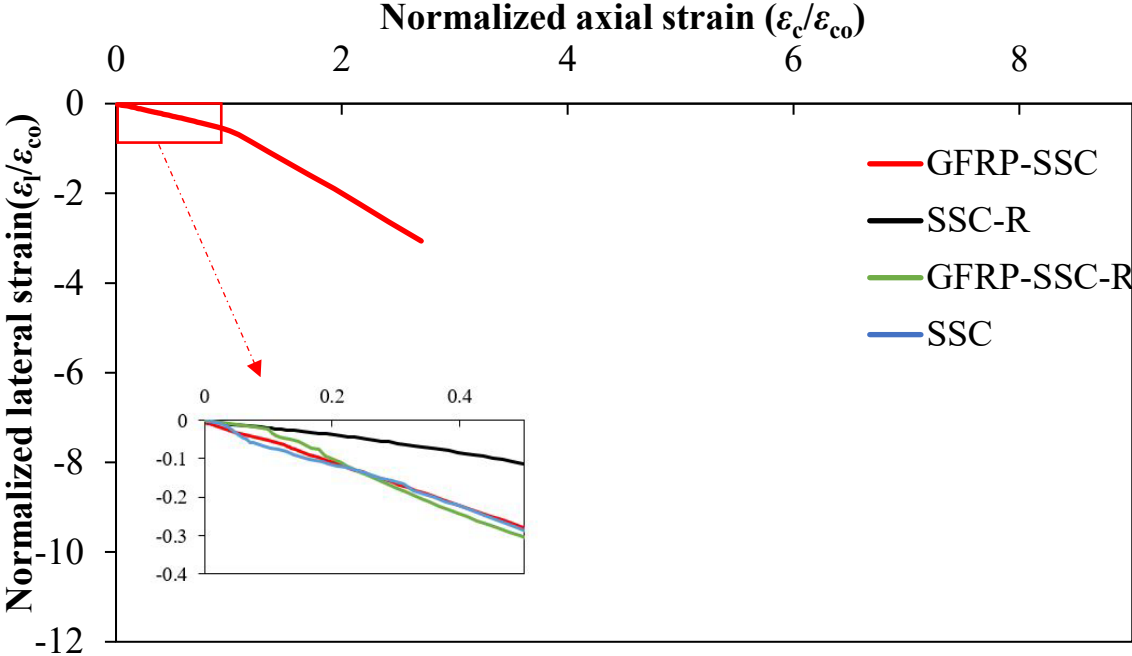


Figure 5.7 Lateral strain-axial strain responses of the unconfined and confined concrete

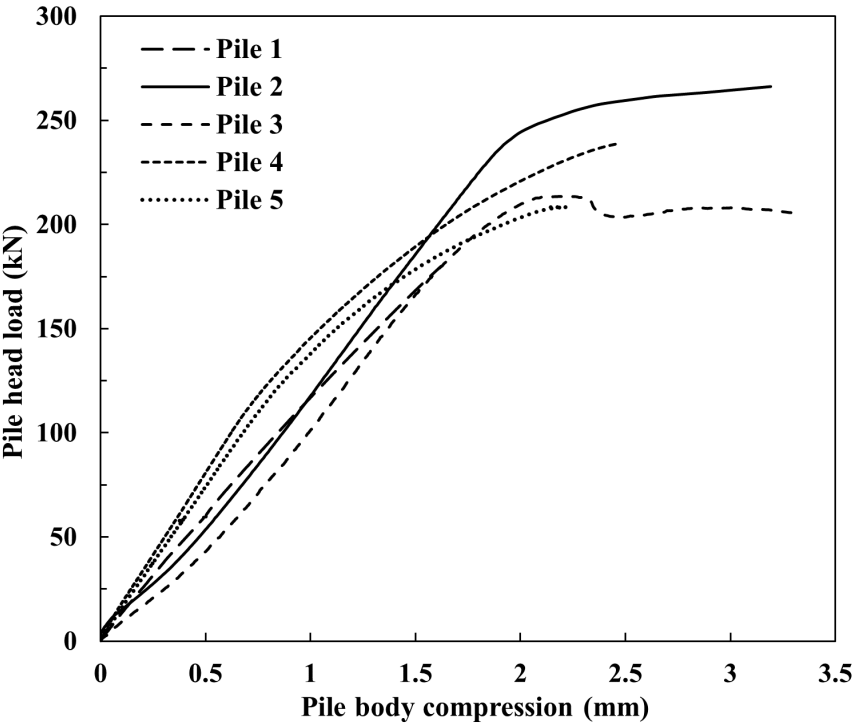


Figure 5.8 Static pile head load-pile body compression relationship of five FRP-SSC model piles

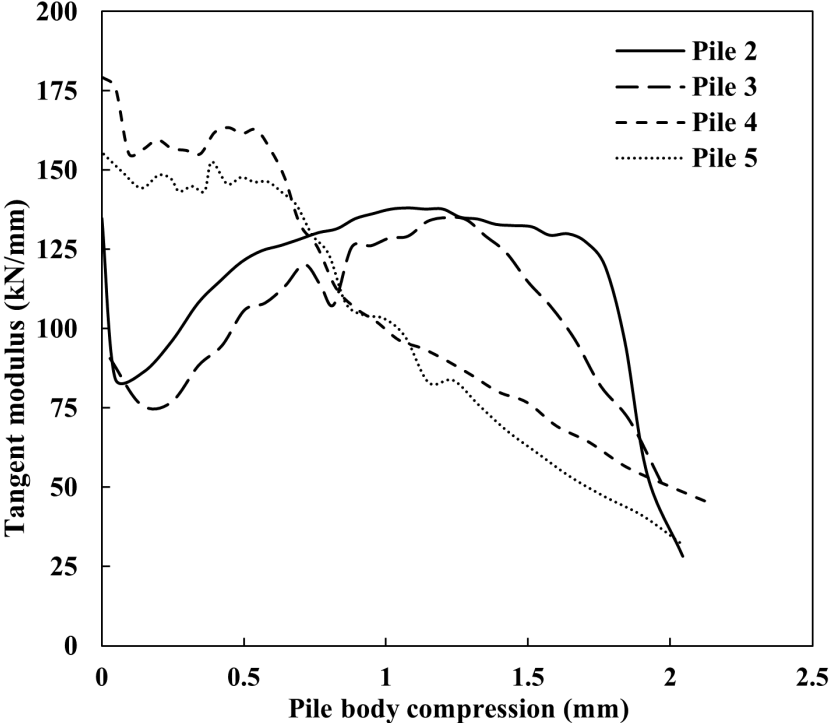
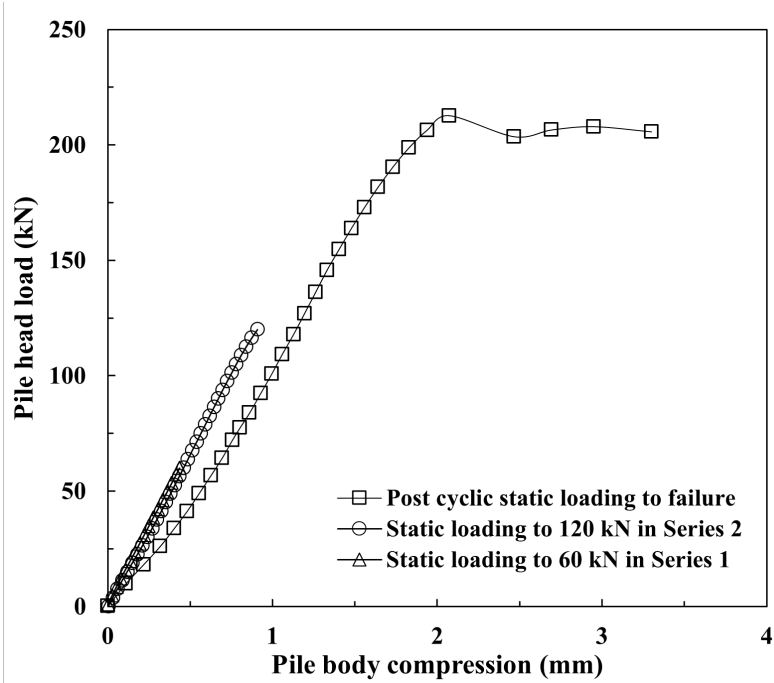
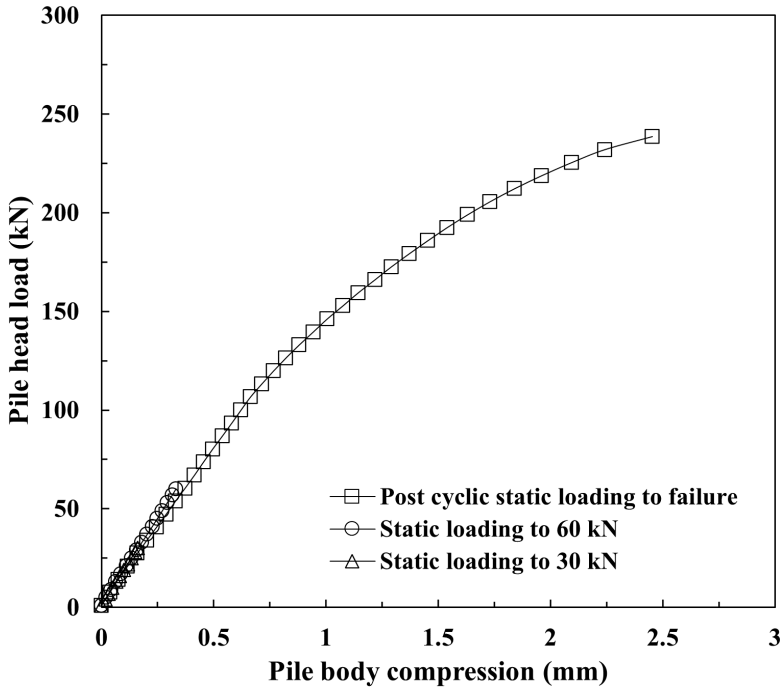


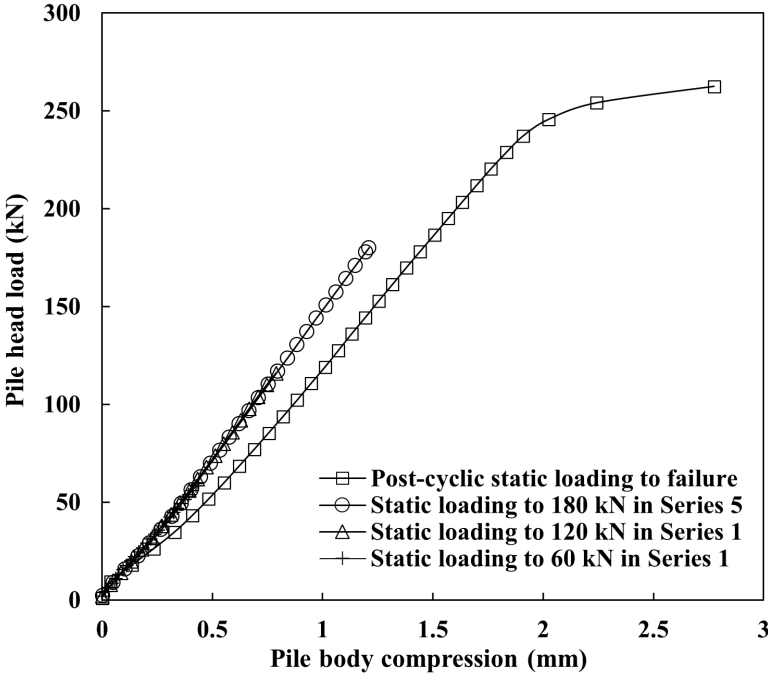
Figure 5.9 Tangent modulus versus pile body compression of four FRP-SSC model piles



(a)



(b)



(c)

Figure 5.10 Static pile head load-pile body compression relationships of (a) Pile 2, (b) Pile 3, and (c) Pile 4 before and after maximum cyclic loading

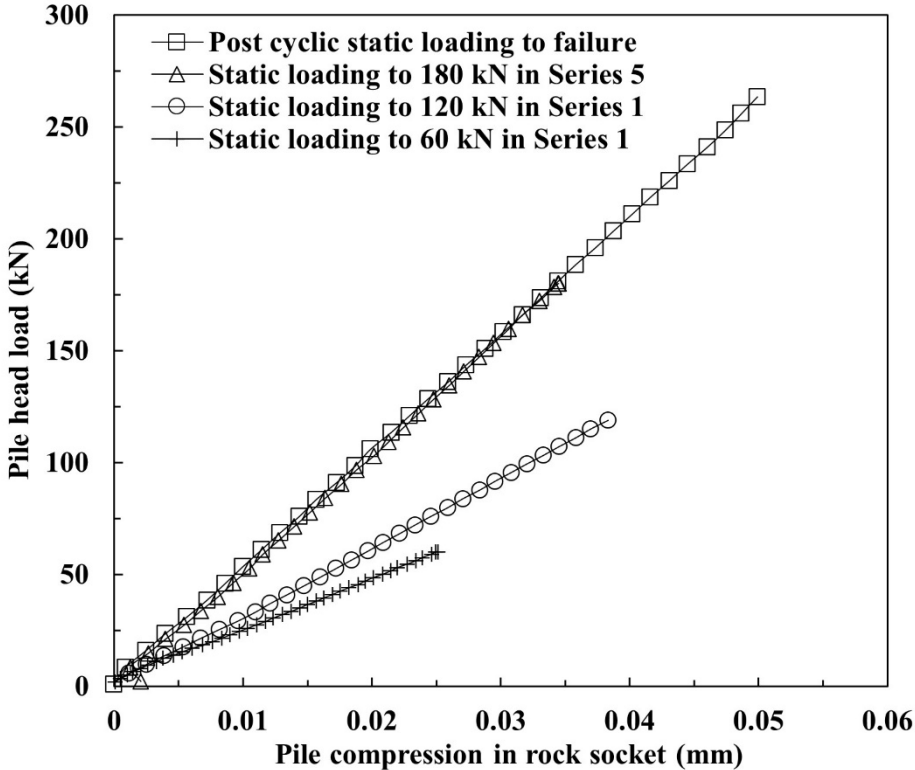
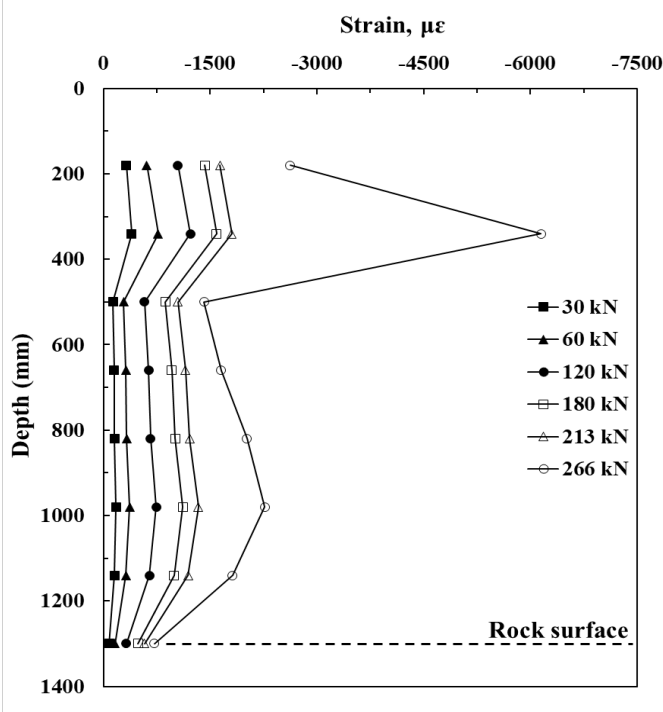
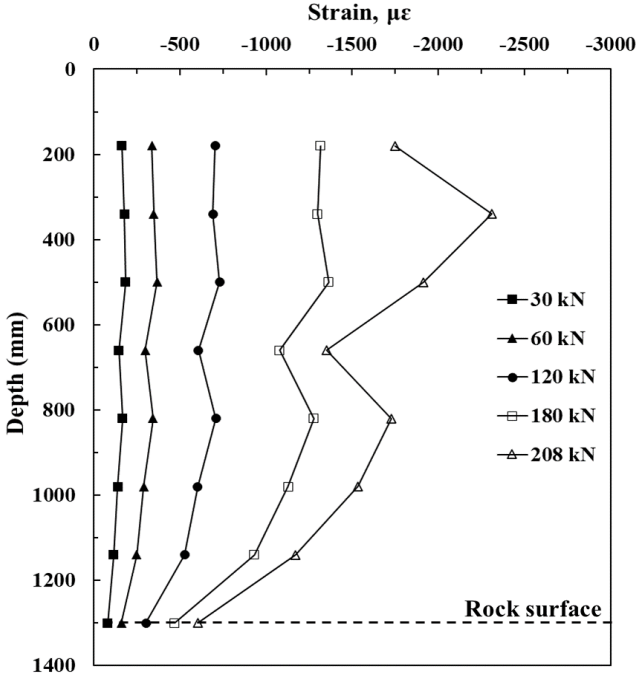


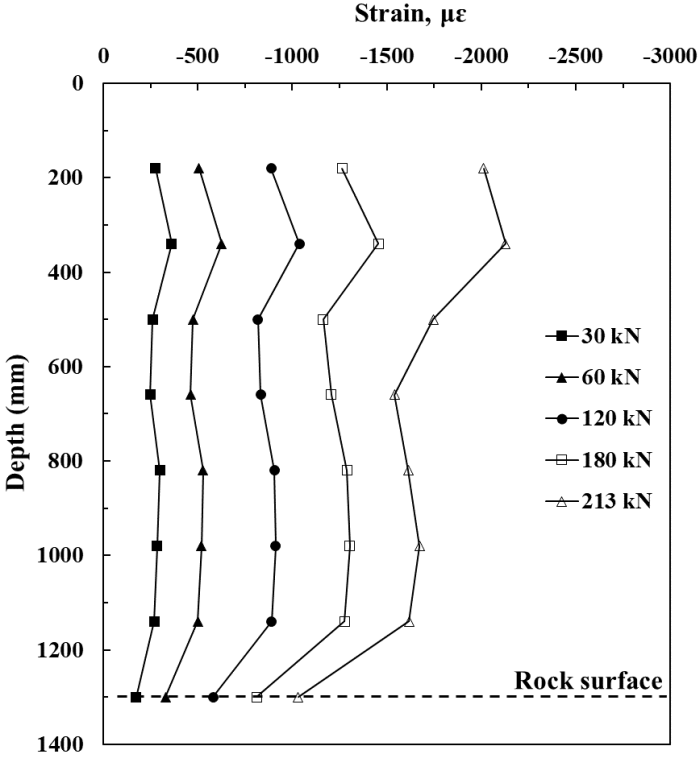
Figure 5.11 Static pile head load-pile compression in rock socket relationships before and after maximum cyclic loading



(a)



(b)



(c)

Figure 5.12 Strain distribution along the depth of (a) Pile 2, (b) Pile 3, and (c) Pile 5



(a)

(b)

(c)

Figure 5.13 Failure modes of FRP-SSC model piles under static loading: (a) Pile 2, (b) Pile 3, and (c) Pile 4

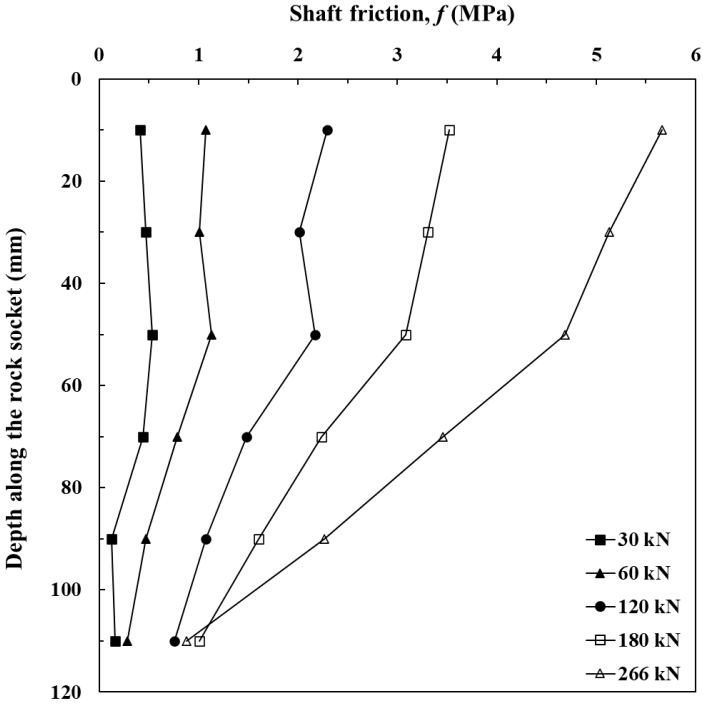
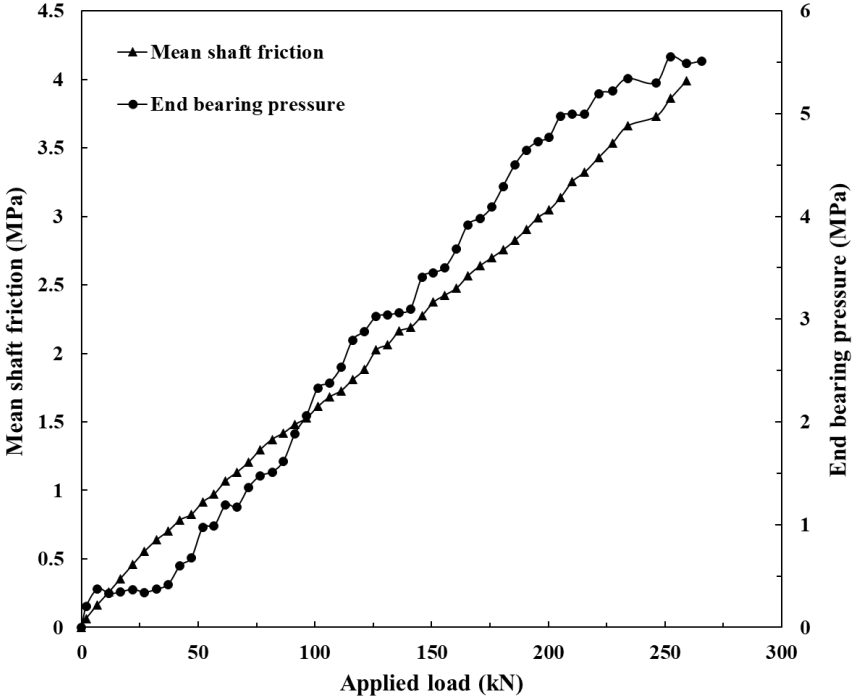
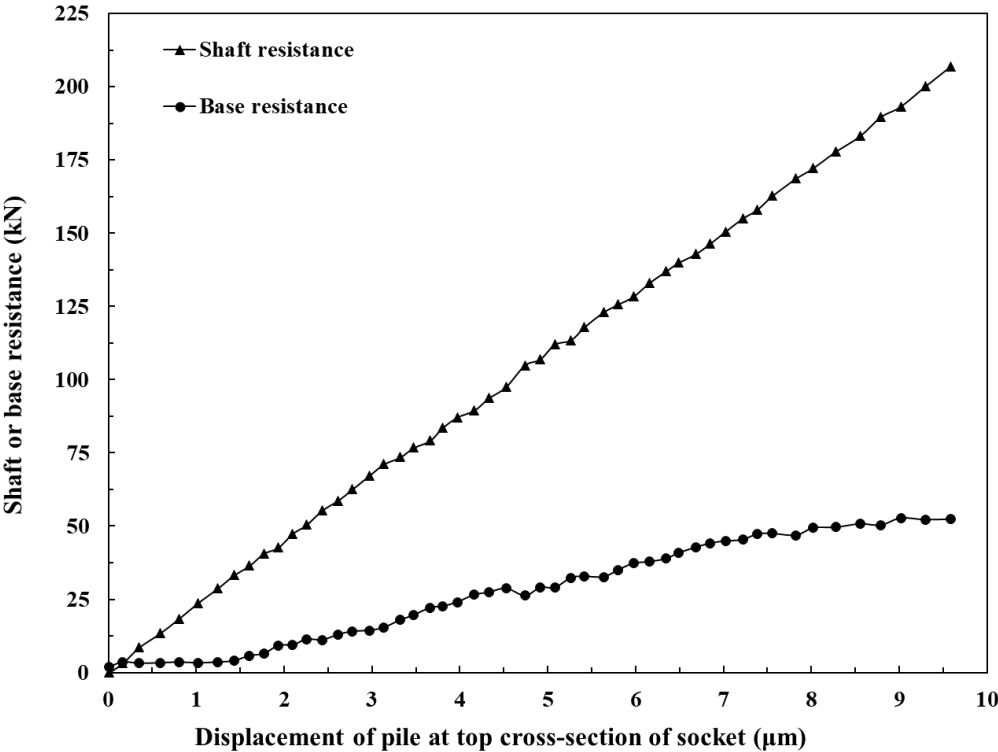


Figure 5.14 Shaft friction profiles of Pile 2 calculated from OFDR fiber section data under different loading levels



(a)



(b)

Figure 5.15 Socket response of Pile 2: (a) mean shaft friction and end bearing pressure against applied load, and (b) shaft and base resistance against displacement

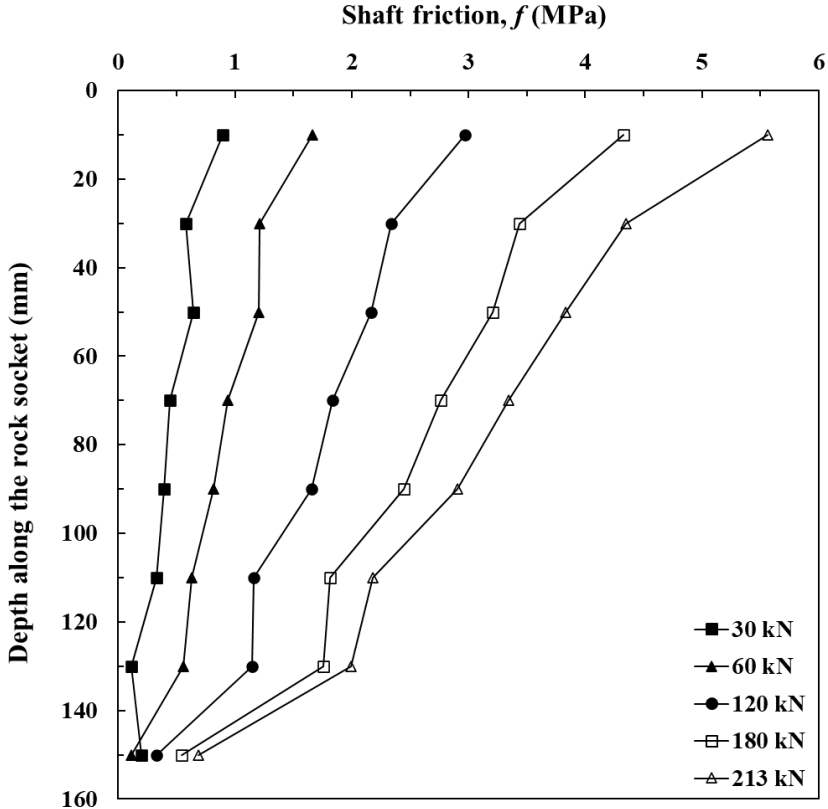
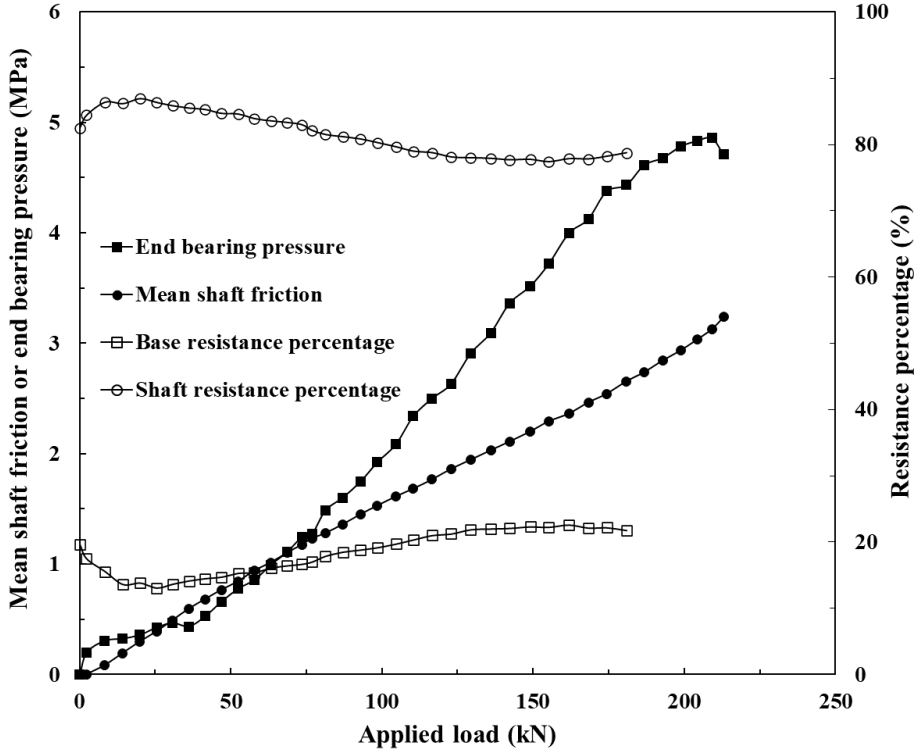
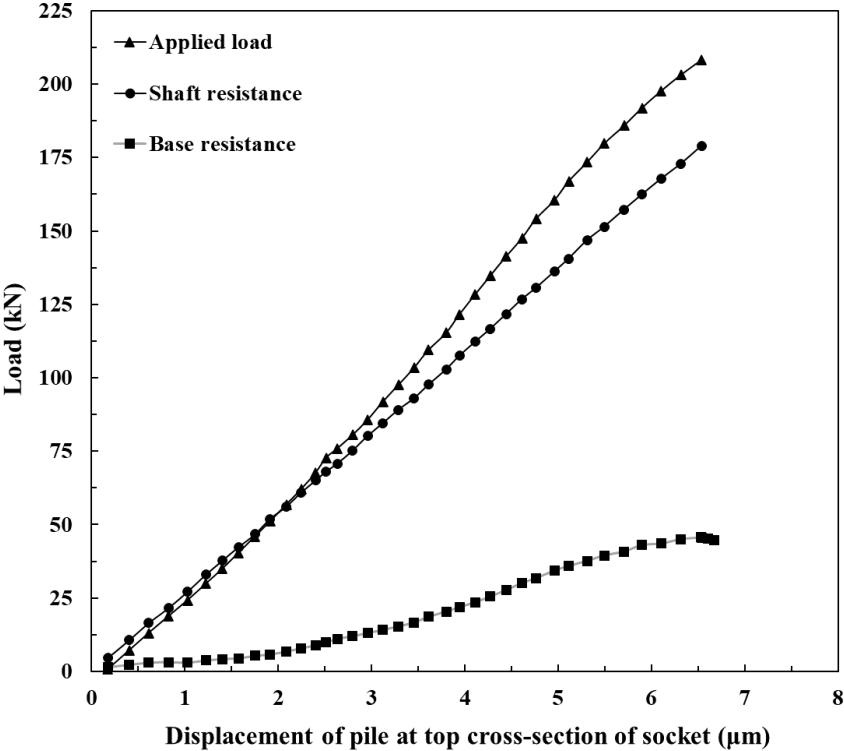


Figure 5.16 Shaft friction profiles of Pile 3 calculated from OFDR fiber section data under different loading levels



(a)



(b)

Figure 5.17 Socket response of Pile 3 under static loading: (a) mean shaft friction, end bearing and resistance percentage against static load and (b) shaft resistance and base resistance against displacement

CHAPTER 6: BEHAVIOUR OF FRP-SSC MODEL PILE IN MARINE SOILS INSTALLED IN ROCK-SOCKET

6.1 Introduction

In this chapter, the behavior of FRP composite SSC model pile ended in rock socket and surrounded by Hong Kong marine deposits is discussed to reveal the influence of soft soils consolidation on piles. Firstly, the model pile design and setup, transducers specifications, and instrumentations are introduced. Secondly, the bottom HKMD layer preparation and pre-consolidation results are discussed to reveal the settlement, pore pressure, and vertical stress variations under pre-consolidation pressure. Similarly, the upper HKMD layer preparation and pre-consolidation response is monitored under multistage surcharge loading to reveal the effects of different levels of surcharge pressure on pore pressure and settlement. After pre-consolidation, the HKMD was subjected to multistage surcharge loading to 150 kPa using air pressure cylinders on the top surface to reveal the settlement response of the two HKMD layers.

6.2 Model pile setup and instrumentations

6.2.1 Model pile setup

The model pile was made of SSC that is 100 mm in diameter with four longitudinal GFRP rebars embedded (a diameter of 9.5 mm and a length of 1460 mm). Above the rock socket, rebars were confined by circular stirrups of an outer diameter of 90 mm with a center-to-center spacing of 70 mm. The rebar cage was first fabricated and then fixed in the rock socket within the polyvinyl

CHAPTER 6: BEHAVIOUR OF FRP-SSC MODEL PILE IN MARINE SOILS INSTALLED IN ROCK-SOCKET

chloride formwork casing, followed by the casting of the SSC inside. The longitudinal rebars along with concrete contributed to the capacity of the pile against axial loads. Circular ties provided confinement to avoid the buckling and shear failure of longitudinal rebars.

The model pile was instrumented with both FBG sensors and OFDR fibers along the length. Eight FBGs were placed in the pile body above the rock socket and four FBGs within the rock socket, with a spacing of 160 and 35 mm, respectively. Two independent OFDR fibers were installed on the rebars and within the SSC, with six sections (S1 to S6, and F1-F6) for each fiber in the cross-section of the pile shown in Figure 6.1. The one independent fiber sections were not presented in the cross section, as the OFDR interrogator has one channel, hence only one fiber was used to monitor the deformation of pile. Since all the fibers worked as a sensor along the whole length, a section of the fiber (the slack fiber section) was kept free in the air to separate each measuring fiber. The photo of the physical model pile system is shown in Figure 6.2.

6.2.2 Instrumentations

The main transducers and dataloggers used in this physical model test are introduced in this section. For measuring earth pressure and pore-water within the HKMD during consolidation conventional electronic transducers were used. Three types of conventional transducers based on voltage signals were installed in the physical model test, namely pore pressure transducers, earth pressure cells, and linear variable differential transformers (LVDTs). The settlements were

CHAPTER 6: BEHAVIOUR OF FRP-SSC MODEL PILE IN MARINE SOILS INSTALLED IN ROCK-SOCKET

recorded by specially designed floating settlement plates and LVDTs. DM-YB1820 datalogger was used to record electronic signals from all conventional transducers and LVDTs.

Porewater pressure transducers (PPT)

The measurement of excess pore pressure in a physical modeling experiment was carried out using DMTY pore pressure transducers obtained from China. These transducers have a diameter of 32 mm and thickness of 15 mm and have a maximum capacity of 300 kPa. Their accuracy is reported to be $\leq 0.3\%$ F·S, where F·S denotes the output at the full measurement range. To ensure proper functioning, these transducers require full-bridge connection with an excitation voltage of 2V and a bridge resistance of 350 Ω . All the porewater pressure transducers were calibrated at the Soil Mechanics Laboratory before installation in the model for acute results.

Earth pressure cells (EPC)

In a physical modeling experiment, DMTY earth pressure cells manufactured in China were utilized for earth pressure measurement. The dimensions of these cells are 28 mm in diameter and 10 mm in thickness. The supplier recommended that the particle size of the soil should not exceed 1/20 of the transducer diameter for obtaining reliable data. The transducers used in this experiment have a maximum capacity of 300 kPa. These transducers have an accuracy of $\leq 0.3\%$ F·S and require full-bridge connection with an excitation voltage of 2V and a bridge resistance of 350 Ω for proper functioning. All the earth pressure cells were calibrated in the Soil Mechanics Laboratory before installing in the model.

CHAPTER 6: BEHAVIOUR OF FRP-SSC MODEL PILE IN MARINE SOILS INSTALLED IN ROCK-SOCKET

LVDTs

For the measurement of soil settlement in a physical modeling experiment, AML/SGD- 100 and DMWY-100 LVDTs manufactured in China were used. These LVDTs have a measurement range of 100mm and an accuracy of 0.2% F·S. The LVDTs require an excitation voltage ranging between 4 to 6V and have a resistance of 120 Ω . Besides, the LVDTs from GCTS actuator were also used to measure the surface settlement of soil. The LVDTs were calibrated for accurate results before the tests.

Consolidation loading setup

For the consolidation of HKMD, a special loading system was designed to apply the loading to the soil surface. Air cylinders utilizing air pressure were used for the loading application. The air cylinder was made from tyre's plastic material as shown in Figure 6.3(a). The air cylinders were first squeezed to extract the air and then positioned over the loading plate and connected to the air supply system. A total of 16 air cylinders were employed in the test as shown in Figures 6.3(b) and 6.4. The cylinders assembly was constrained from upward movement by a reaction frame fixed on the steel tank as shown in Figure 6.3(a). The air cylinders apply load on the wooden plate which transforms the loading uniformly to HKMD and it was designed with holes in it which facilitated water drainage during consolidation process.

6.3 Bottom layer HKMD preparation and pre-consolidation results

6.3.1 Bottom layer HKMD preparation

For conducting physical model tests, the bottom layer of Hong Kong marine deposits (HKMD) was filled inside the steel tank manually. The HKMD was dredged from the coastal area near the Lantau Island in Hong Kong and stored in the soil mechanics laboratory. The preparation of HKMD involved mixing water in it and stirring the mixture with a high-speed mixer to ensure uniform water distribution forming a slurry. The slurry was kept for three days allowing the soil particles to fully hydrate and subsequently an average 70% of water content was maintained for the first HKMD layer.

Before filling the prepared HKMD slurry, five pore water pressure and three earth pressure transducers were fixed at the desired locations at the bottom of the tank by epoxy to prevent any displacement during the filling of HKMD. The porewater pressure transducers were wrapped with a thin geotextile layer to avoid soil particles clogging covering the porous stone of each transducer shown in Figure 6.5. The layout of the transducers is presented in Figure 6.6. The HKMD slurry was mixed again to ensure homogeneity and poured in the steel tank manually as shown in Figure 6.7. The height gradient facilitated self-weight consolidation and uniform distribution.

Prefabricated vertical drains (PVDs) used in this model test were commercial PVDs named New Colbondrian CX1000 having a width and thickness of 100 mm and 5 mm respectively. The PVDs were tailored into small strips of width 33 mm to speed up the consolidation process as

CHAPTER 6: BEHAVIOUR OF FRP-SSC MODEL PILE IN MARINE SOILS INSTALLED IN ROCK-SOCKET

shown in Figure 6.8. The PVDs were installed through an aluminum mandril in a square pattern with 150 mm spacing as shown in Figures 6.9. The photo of bottom layer after PVDs insertion is shown in Figure 6.10. A layer of non-woven geotextile was placed over the HKMD after PVDs insertion to prevent slurry escape and uniform surface for consolidation pressure as shown in Figure 6.11.

6.3.2 Pre-consolidation loading system setup and loading program

For the pre-consolidation of bottom HKMD layer, the GCTS hydraulic actuator of the physical model was utilized for applying loading over the soil. A special loading transformation system was designed to transfer the loading from the loading cell (GCTS actuator) to the soil surface. The loading cell applies a load on the top aluminum plate which was transferred axially to the bottom aluminum plate through six steel bars as shown in Figure 6.12. The bottom aluminum plate transforms the loading uniformly to HKMD and it was designed with holes in it which facilitated water drainage during consolidation process.

In practical construction projects, surcharge loading is generally applied in multi stages, hence in this study, the HKMD was consolidated under multi-stage loading. The bottom HKMD layer was subjected to multi-stage ramp loading of 2 kPa, 6 kPa, and 10 kPa. Afterwards the surcharge loading was released to zero and loaded again from zero to 15 kPa and subsequently from 15 kPa to 20 kPa.

6.3.3 Responses of transducers during pre-consolidation of HKMD

To achieve reliable data during the tests, all the transducers were calibrated before the test. The responses of PPTs and EPCs in HKMD slurry during the consolidation process under multi-stage ramp loading were monitored consistently. The porewater pressure data from PPTs were used to determine the completion of pre-consolidation and dissipation of porewater pressure during each stage of loading. The indication of dissipation of porewater pressure was used to start subsequent surcharge loading.

The responses of three PPTs at the bottom of the tank are shown in Figure 6.14. Two PPTs data were excluded due to unreliable results because of electrical signals issue or porous stone soil clogging. The PPTs data present a good agreement of increase and dissipation of pore water pressure in each stage with each other. However, the changes in porewater pressure at different positions are possibly caused by filling HKMD manually leading to different initial hydraulic conditions. The dissipation of porewater pressure at PPT-B1 and PPT-B5 is faster than PPT-B2 which can be attributed to the locations of PPTs causing different drainage conditions because of closeness to the PVDs, pile and boundary of the steel tank.

Two PPTs measuring the horizontal pore water pressure were installed in the side wall of steel tank at a height of 22 cm from the bottom as shown in Figure 6.15. The responses of both side wall PPTs agree well with one another and show better dissipation and increasing trend in each stage of loading compared to the bottom PPTs. This can be attributed to less soil clogging possibility of PPT-S1 and PPT-S2, compared to bottom PPTs. Figure 6.16 shows the response of EPC-B2 at the bottom of the tank during pre-consolidation. Three EPCs were installed at the bottom, however due to unreliable results two EPCs were excluded possibly due to electrical

signal issues. The vertical stress measured by EPC-B2 agrees well with the surcharge loading during pre-consolidation process in each stage. When the loading was released to zero after 10 kPa surcharge, the water accumulated at the surface was drained out, hence slight decrease in subsequent measured vertical stress was detected.

6.3.4 Settlement during multi-stage pre-consolidation

The surface settlement of the bottom layer under pre-consolidation measured by LVDTs is shown in Figure 6.17. It can be found that during early surcharge loadings (0 to 10 kPa), the settlement increased at faster rate achieving 47 mm settlement till 10 kPa. However, when the loading was increased from 10 to 20 kPa, the settlement increased at slow rate from 47 mm to 71 mm. Initially, excess pore water pressures are high which causes significant decrease in effective stress and the soil exhibits predominantly liquid-like behavior. The Settlement is faster as the water drains out by PVDs. As the loading continues, excess pore pressures start dissipating due to consolidation and effective stress increases correspondingly, leading to slower settlement.

6.4 Upper layer HKMD preparation and pre-consolidation results

6.4.1 Upper layer HKMD preparation

After the pre-consolidation of the bottom layer, the loading assembly was removed to prepare the tank for the second HKMD layer. The same HKMD was used for the upper layer and preparation

CHAPTER 6: BEHAVIOUR OF FRP-SSC MODEL PILE IN MARINE SOILS INSTALLED IN ROCK-SOCKET

was carried out in the same way as for bottom layer, discussed in section 6.3.1. An average of 70% of water content was maintained for the second HKMD layer.

Before filling the prepared HKMD slurry, four PPTs and three EPCs were fixed at the desired locations at the top surface of the first layer to monitor the consolidation process. The pore water pressure transducers were wrapped with a thin geotextile layer to avoid soil particles clogging covering the porous stone of each transducer. The layout of the transducers is presented in Figure 6.13(b). The PVDs used for bottom layer consolidation were removed and new PVDs were installed using aluminum mandrel in a square pattern with 150 mm spacing as shown in Figure 6.10. The PVDs were fixed to the desired positions by clamps at the top edges of tank using plastic strips. The HKMD slurry was mixed again to ensure homogeneity and poured in the steel tank manually. The height gradient facilitated self-weight consolidation and uniform distribution.

6.4.2 Pre-consolidation loading system setup and loading program

For the pre-consolidation of upper HKMD layer, the GCTS hydraulic actuator of the physical model was utilized for applying loading over the soil as was used for first layer. The upper layer was pre-consolidated under multi-stage ramp loading of 2 kPa, 5 kPa, 10 kPa, 15kPa, and 20 kPa over a total duration of 32 days approximately.

6.4.3 Responses of transducers during pre-consolidation of HKMD

The responses of PPTs and EPCs in HKMD slurry during the consolidation process under multi-stage ramp loading were monitored consistently. The porewater pressure data from PPTs were

CHAPTER 6: BEHAVIOUR OF FRP-SSC MODEL PILE IN MARINE SOILS INSTALLED IN ROCK-SOCKET

used to determine the completion of pre-consolidation and dissipation of porewater pressure during each stage of loading. The indication of dissipation of porewater pressure was used to start subsequent surcharge loading during pre-consolidation.

The responses of two PPTs at the interface of upper and bottom layer are shown in Figure 6.18. Two PPTs data were excluded due to unreliable results because of electrical signals issue or porous stone soil clogging. The PPTs data present a good agreement of increase and dissipation of pore water pressure in each stage with each other. The porewater pressure at PPT-M1 is higher than PPT-M2 which can be attributed to its location, having different drainage conditions because of closeness to the pile boundary with less drainage path. The PPT-M2 is in the middle of the pile and tank, many PVDs surrounded there causing faster drainage resulting in higher dissipation and less pore pressure. The response of PPTs at the bottom of tank under pre-consolidation is shown in Figure 6.19. A good agreement of increase and dissipation of pore water pressure in each stage with each other was measured. However, the changes in porewater pressure initially are possibly caused by different drainage conditions due to closeness to PVDs or electrical signals shift for longer period of PPTs in soil.

Four PPTs (PPT-S1, PPT-S2, PPT-S3, and PPT-S4) measuring the horizontal pore water pressure of upper and bottom layer installed in the side wall of steel tank at a height of 22 cm (PPT-S1, PPT-S2) and 62 cm (PPT-S3, PPT-S4) from the bottom as shown in Figure 6.20. The responses of side wall PPTs agree well with one another and show better dissipation and increasing trend in each stage of loading compared to the vertical porewater pressure PPTs. This can be attributed to the quality and less soil clogging possibility of sidewall PPTs compared to the bottom and interface PPTs. Figure 6.21 shows the responses of two EPCs, measuring vertical stress at the

CHAPTER 6: BEHAVIOUR OF FRP-SSC MODEL PILE IN MARINE SOILS INSTALLED IN ROCK-SOCKET

interface of first and upper layer and bottom of the tank during pre-consolidation. Three EPCs were installed at the interface in the same way as those at bottom, however due to unreliable results, two EPCs were excluded possibly due to electrical signal issues. The vertical stress measured by both EPCs agrees well with the surcharge loading during pre-consolidation process in each stage. When the loading was released to zero after 10 kPa surcharge, the water accumulated at the surface was drained out, hence slight decrease in subsequent measured vertical stress was detected.

6.4.4 Settlement during multi-stage pre-consolidation

The settlement at surface of the upper layer under pre-consolidation measured by LVDTs is shown in Figure 6.22. It can be found that during surcharge loadings (0 to 15 kPa), the settlement increased at faster rate achieving 120 mm settlement till 15 kPa. However, when the loading was increased further to 20 kPa, the settlement increased gradually from 120 mm to 130 mm and become stable afterward. High excess pore water pressures initially reduce effective stress and when PVDs drain out water it accelerates settlement. As loading continues, consolidation dissipates excess pore pressures and effective stress increases which slows down settlement.

6.4.5 Review of simplified Hypothesis B method for soft soils under multi-stage loading and unloading

Due to the significant influence of creep effect on the consolidation settlement of soft soils, classical theories of one-dimensional consolidation are inadequate for accurate calculations. Consequently, researchers have shown considerable interest in this area and have investigated

CHAPTER 6: BEHAVIOUR OF FRP-SSC MODEL PILE IN MARINE SOILS INSTALLED IN ROCK-SOCKET

alternative approaches that incorporate creep considerations. Two distinct categories of viewpoints exist: Hypothesis A and Hypothesis B. Generally, engineers value simple methods that produce accurate results in practical applications, such as Hypothesis A method. Due to its simplicity, the method is commonly used by geotechnical engineers to calculate the consolidation settlements of soft soils (Shepherd and Williamson, 2018), but it has some contradictions with the principles of continuum mechanics (Degago et al. 2013).

The contradictions are based on the assumptions adopted in this method. It assumes that there are two stages of settlement independently, first stage is the primary consolidation stage and second is the secondary consolidation stage which are distinguished by a time point named as “End of Primary” (EOP) consolidation. Consolidation settlement is only induced prior to the so-called EOP by the dissipation of excess porewater. Following the completion of primary consolidation, the “secondary consolidation” induced by creep would begin due to the viscous properties of soft soils, such as soil particle bonding and viscous structure. Based on Hypothesis A, the consolidation settlement can be calculated as:

$$S_{totalA} = S_{primary} + S_{secondary} \quad (6.1)$$

$$= \begin{cases} U_v S_f & \text{for } t < t_{EOP,field} \\ U_v S_f + \frac{C_{ae}}{1+e_0} \log\left(\frac{t}{t_{EOP,field}}\right) H & \text{for } t > t_{EOP,field} \end{cases}$$

where $S_{primary}$ represents primary settlement, $S_{primary} = U_v S_f$, $S_{secondary}$ shows secondary

consolidation settlement given as $S_{secondary} = \frac{C_{ae}}{1+e_0} \log\left(\frac{t}{t_{EOP,field}}\right) H$, U_v is the average degree of

CHAPTER 6: BEHAVIOUR OF FRP-SSC MODEL PILE IN MARINE SOILS INSTALLED IN ROCK-SOCKET

consolidation, S_f is the final primary settlement, $C_{\alpha e}$ is the secondary compressive index, and e_0 is the initial void ratio. It should be noted that the time when excess porewater pressure was completely dissipated is infinite according to the classical one-dimensional consolidation theory, indicating that $t_{EOP,field}$ is infinite. Consequently, it is considered that soils reach 98% of average degree of consolidation at $t_{EOP,field}$.

Visco-plastic deformation (creep) occurs during the primary consolidation process, according to widely accepted Hypothesis B (Chen et al., 2021; Yin and Feng, 2017). The creep settlement can be considered during the consolidation analysis by using a simplified Hypothesis B method, which was first proposed by Yin and Feng (2017). With this simplified method, the total settlement for a normally consolidated soil can be calculated as:

$$S_{totalB} = S_{primary} + \begin{cases} \alpha \frac{C_{\alpha}}{1+e_0} H_0 \log \frac{t}{t_0}, & \text{for } t_0 \leq t < t_{EOP} \\ \alpha \frac{C_{\alpha}}{1+e_0} H_0 \log \frac{t}{t_0} + (1-\alpha) \frac{C_{\alpha}}{1+e_0} H_0 \log \frac{t}{t_{EOP}}, & \text{for } t \geq t_{EOP} \end{cases} \quad (6.2)$$

where α is an empirical correction factor (typically 0.8), U represents the overall degree of consolidation, C_{α} is the secondary consolidation coefficient, t_0 is the reference time (24 hours for standard oedometer tests), and t_{EOP} the time required for primary consolidation. The final term will be zero for loading time $t < t_{EOP}$.

6.5 Response of both HKMD layers under Consolidation loading

6.5.1 Consolidation loading program

A multistage loading test was carried out using a specially designed air cylinders loading system shown in Figure 6.3 following a loading sequence of 5 kPa, 10 kPa, 20 kPa, 30 kPa, 40 kPa, 50 kPa, 70 kPa, 90 kPa, and 150 kPa as shown in Figure 6.23. Before starting the above consolidation loading, as discussed previously in section 6.3.2 and 6.4.2, the upper and bottom layer have been subjected to pre-consolidation loading. In each stage, the loading lasted till the approximate dissipation of pore water pressure. The loading was increased during each stage from 5 to 90 kPa, however, after 90 kPa the loading was released to zero and reloaded to 150 kPa directly.

6.5.2 Porewater pressure and vertical stress

The responses of two PPTs (PPT-M1 and PPT-M2) with time placed at the interface of upper and bottom layer are shown in Figure 6.24. Both the PPTs data presented a clear response of increase and dissipation of pore water pressure in each stage of loading. When the applied loading is smaller than 20 kPa, the porewater pressure increases and dissipations measured by PPTs is smaller comparatively. However, upon increasing loading beyond 20 kPa, the increase in porewater pressure is significant with increase in loading. This can be attributed towards the pre-consolidation loading influence, during which the HKMD layers have experienced the loading till 20 kPa. Below 20 kPa loading, the soil structure has been densified and reinforced by pre-consolidation. However, once the load has increased the pre-consolidation pressure i.e., beyond 20 kPa till 90 kPa, it breaks down soil particle bonds and particles rearrange themselves causing

CHAPTER 6: BEHAVIOUR OF FRP-SSC MODEL PILE IN MARINE SOILS INSTALLED IN ROCK-SOCKET

reduction in volume and releasing more space for entrapped pore water. The porewater pressure at PPT-M1 is higher than PPT-M2 which can be attributed to its location, due to different drainage conditions near to pile boundary. The PPT-M2 is in the middle of the pile and tank horizontally, many PVDs surround there causing faster drainage resulting in higher dissipation and less pore pressure.

The response of the two PPTs (PPT-B2 and PPT-B5) at the bottom of tank under consolidation loading is shown in Figure 6.25. Both the PPTs response presented a clear trend of increase and dissipation of pore water pressure in each stage of loading. Below 20 kPa loading, the porewater pressure increase and dissipation is smaller, however, significant increase in porewater pressure was measured beyond 20 kPa due to prior pre-consolidation loading influence as discussed previously. The porewater pressure at PPT-B5 is higher than PPT-B2 which can be attributed to its location, due to different drainage conditions. The PPT-B2 is in the middle of the pile and tank horizontally, many PVDs surround there, causing faster drainage resulting in higher dissipation and less pore pressure. However, PPT-B5 is near the tank boundary causing less path for drainage of pore water hence measuring higher pore water pressure.

Four PPTs measuring the horizontal pore water pressure of upper and bottom layer installed in the side wall of steel tank at a height of 22 cm (PPT-S1, PPT-S2) and 62 cm (PPT-S3, PPR-S4) from the bottom as shown in Figure 6.26. The PPTs responded remarkably to the increase of loading in each stage showing a clear trend of increase and dissipation of pore water pressure.

CHAPTER 6: BEHAVIOUR OF FRP-SSC MODEL PILE IN MARINE SOILS INSTALLED IN ROCK-SOCKET

However, PPT-S3 showed a higher increase in porewater pressure than the PPT-S4, even though both were positioned at similar height. This could possibly be due to electrical signals disruption or different drainage conditions caused from the bending of PVDs strips in that area under loading. Likewise, vertical pore water pressure measuring PPTs, the horizontal PPTs showed significant increase in pore pressure response with increase in loading beyond 20 kPa due prior pre-consolidation loading.

Figure 6.27 shows the responses of two EPCs, measuring vertical stress at the interface of upper and bottom layer with EPC-M1 and at the bottom of tank with EPC-B2 during pre-consolidation. The vertical stress measured by both EPCs showed a clear increase with the increase of load during consolidation process in each stage. For both EPCs, the slight decrease in vertical stress during sustained load in respective stage is due to the porewater pressure dissipation over time. As porewater pressure decreases, the effective stress increases, as a result the soil supports the applied load with less vertical stress. Additionally, the creep effect under sustained loading further reinforces the soil, allowing stress redistribution through increase in shear strength. EPC-B2 stopped working after 50 kPa possibly due to electrical signals drop or cable damage.

6.5.3 Settlement of upper and bottom HKMD layers during consolidation

Four floating settlement plates were designed for measuring the settlement of upper and bottom HKMD layers. The floating settlement plate is designed with lower and upper steel plates having diameter of 100 mm and 50 mm connected by steel rod of diameter 6 mm shown in Figure

CHAPTER 6: BEHAVIOUR OF FRP-SSC MODEL PILE IN MARINE SOILS INSTALLED IN ROCK-SOCKET

6.13(a). The lower plate measures the soil settlement, and the upper plate provides a surface for the LVDT to monitor the settlement. Two floating settlement plates were installed on opposite sides of the pile at a horizontal distance of 12 cm from pile circumference and one on the other side at a distance of 29.5 cm at the interface of upper and bottom layers. Similarly, two floating settlement plates were placed on the opposite sides of pile at a similar distance of 19.5 cm from the pile circumference at the interface of sand and upper HKMD layer. The positions of the floating settlement plates are shown in Figure 6.13(b).

Figure 6.28 shows the settlement of upper and bottom layers with time under each stage loading measured by the floating settlement plates. Each settlement curve is the average value of two settlement plates at a similar height in the soil. It is observed that the incremental increase in settlement in each stage of loading measured at the interface of upper and bottom HKMD layer is smaller than the upper layer settlement. This can be attributed to the consolidation characteristics of bottom layer, as the pre-consolidation loading of bottom layer has influenced the compression index resulting in smaller settlements in each loading stage. The bottom layer has experienced the 20 kPa pre-consolidation loading twice compared to the upper layer, hence the stress history and stress distribution of the bottom layer induced smaller settlement.

When the applied loading is smaller than 20 kPa, the increase in settlement with loading for both layers is smaller comparatively. However, upon increasing loading beyond 20 kPa, the settlement increased significantly with increase in loading. This can be attributed towards the pre-consolidation loading influence, during which the HKMD layers have experienced the loading till 20 kPa. Below 20 kPa loading, the soil structure has been densified and reinforced by pre-consolidation. However, once the load has increased the pre-consolidation pressure i.e., beyond

CHAPTER 6: BEHAVIOUR OF FRP-SSC MODEL PILE IN MARINE SOILS INSTALLED IN ROCK-SOCKET

20 kPa till 90 kPa, it breaks down soil particle bonds and particles rearrange themselves causing reduction in volume resulting in higher settlement.

It can be found that during loadings (20 to 70 kPa), the settlement increased at faster rate achieving 25 mm and 75 mm settlement for the bottom and upper layers respectively. However, when the loading was increased from 70 to 90 kPa, the settlement increased at a slow rate. This can be attributed towards the excess pore water pressure which is high initially causing decrease in effective stress and the soil exhibits predominantly liquid-like behavior. The settlement is faster as the water drains out by PVDs initially. As the loading continues i.e., beyond 70 kPa, excess pore pressures start dissipating due to consolidation and effective stress increases correspondingly, leading to slower settlement.

The bottom and upper layer achieved a maximum settlement of 40 mm and 107 mm under 90 kPa loading respectively, showing 62% increase of the maximum settlement observed in the upper layer. The settlement curves from both the layer's floating settlement plates show similar trends proving their functionality and application to monitor the settlement at different heights in the soil. The classical consolidation theories might be validated with such instrumentation in the future.

Figure 6.28(b) shows the settlement of upper and bottom layers with time under loading from 0 to 150 kPa measured by the floating settlement plates. The settlement increased significantly in the first 3 days to 23 mm and 60 mm for the bottom and upper HKMD layers respectively. Afterwards under the same loading of 150 kPa, the settlement showed an approximately stable trend with constant value indicating a full dissipation of porewater pressure.

6.6 Summary

This chapter presents the experimental results of one-dimensional consolidation of the HKMD under multisatge loading to reveal its effect on the behaviour of FRP composie SSC model pile. During early surchage loadings, the settlement happened at faster rate due to high excess pore water pressure and as the surcharge loading continued to increase the settlement rate became slow due to the dissipation of pore water pressure. A good agreement of increase and dissipation of pore water pressure in each stage with each other was measured with pore pressure transducers. However, the changes in porewater pressure initially are possibly caused by different drainage conditions due to closeness to PVDs or electrical signals shift for longer period of PPTs in soil. The incremental increase in settlement in each stage of loading measured at the interface of upper and bottom HKMD layer is smaller than the upper layer settlement due to the consolidation characteristics of bottom layer. The pre-consolidation loading of bottom layer has influenced the compression index resulting in smaller settlements in each loading stage.

CHAPTER 6: BEHAVIOUR OF FRP-SSC MODEL PILE IN MARINE SOILS INSTALLED IN ROCK-SOCKET

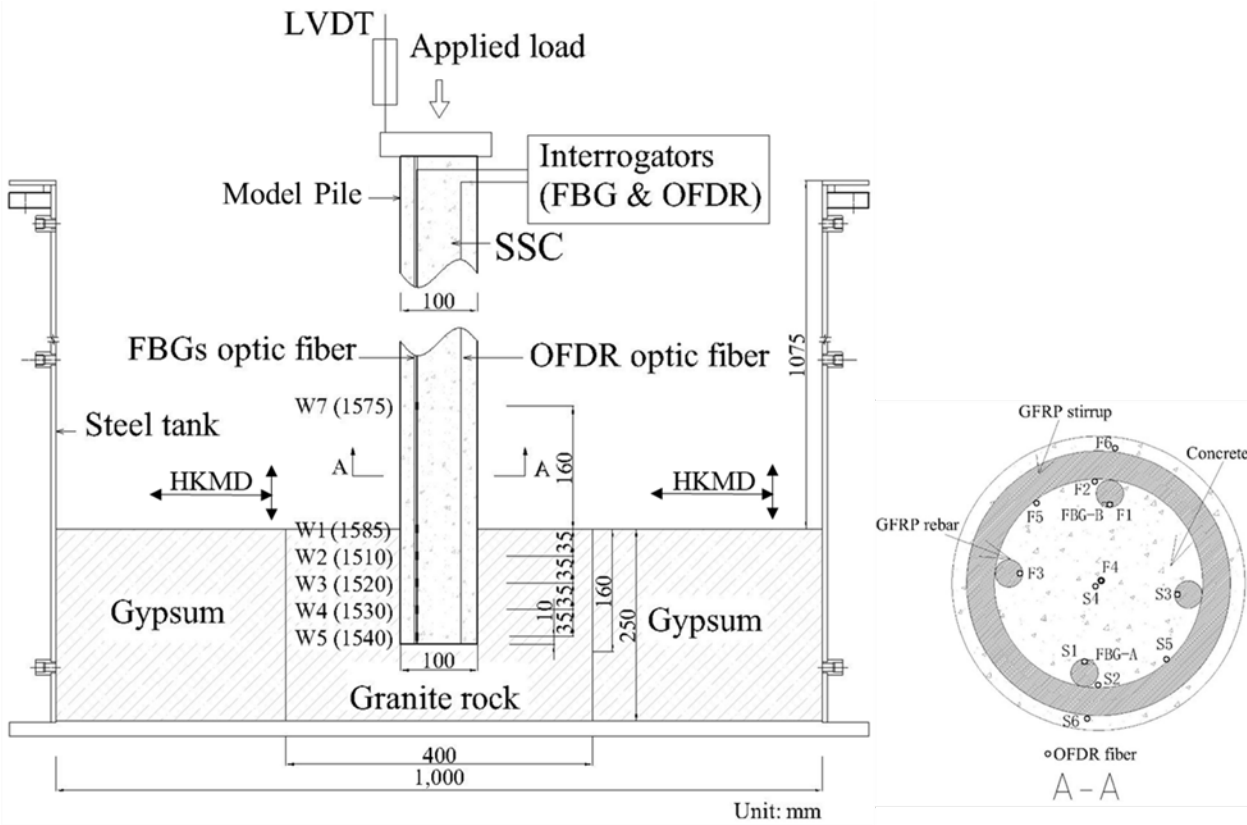


Figure 6.1 Model pile setup and instrumentation

CHAPTER 6: BEHAVIOUR OF FRP-SSC MODEL PILE IN MARINE SOILS INSTALLED IN ROCK-SOCKET

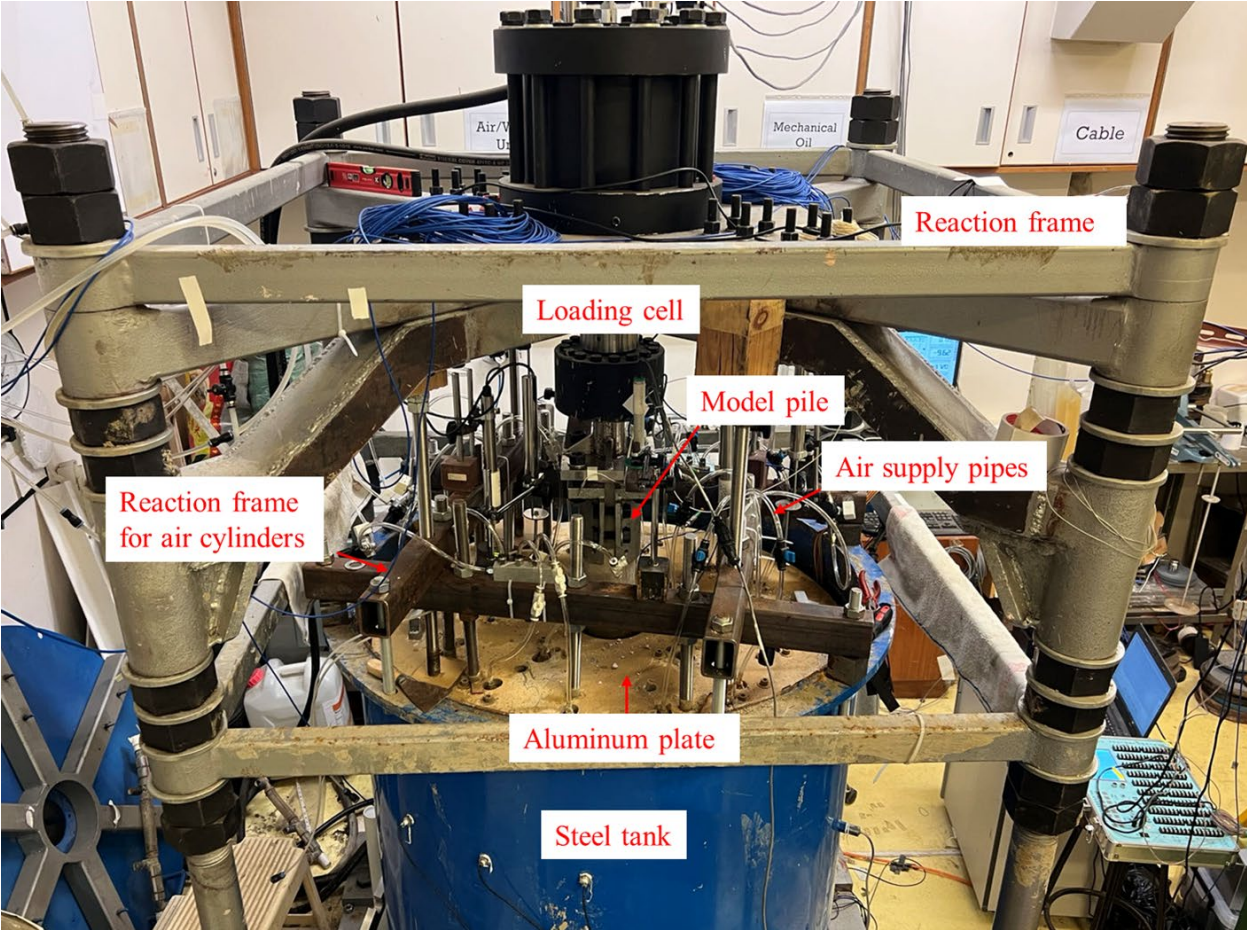


Figure 6.2 Photo of physical model pile and setup

CHAPTER 6: BEHAVIOUR OF FRP-SSC MODEL PILE IN MARINE SOILS INSTALLED IN ROCK-SOCKET

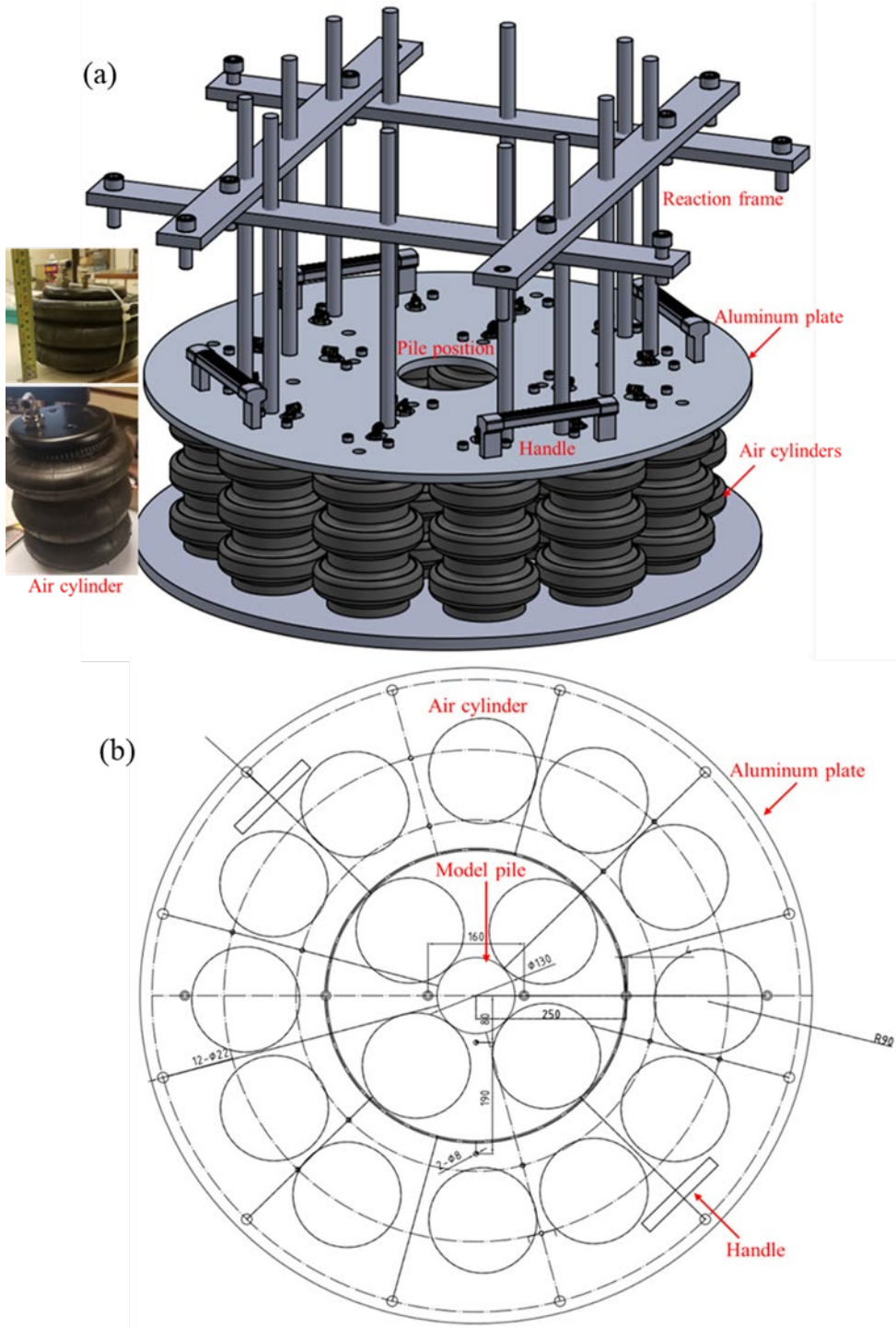


Figure 6.3 Air cylinders assembly and layout

CHAPTER 6: BEHAVIOUR OF FRP-SSC MODEL PILE IN MARINE SOILS INSTALLED IN ROCK-SOCKET



Figure 6.4 Photo of air cylinders layout in the physical model

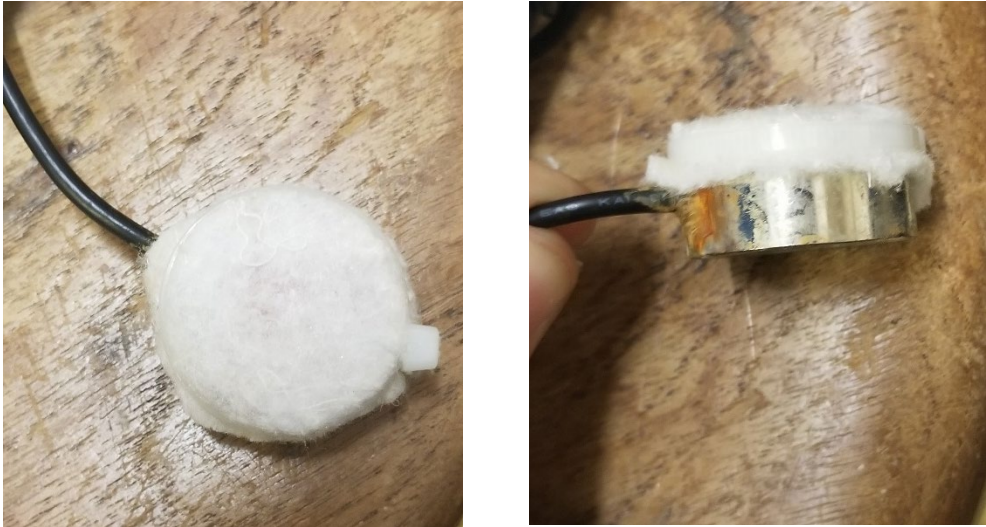


Figure 6.5 Porewater pressure transducer protective cotton covering

CHAPTER 6: BEHAVIOUR OF FRP-SSC MODEL PILE IN MARINE SOILS INSTALLED IN ROCK-SOCKET

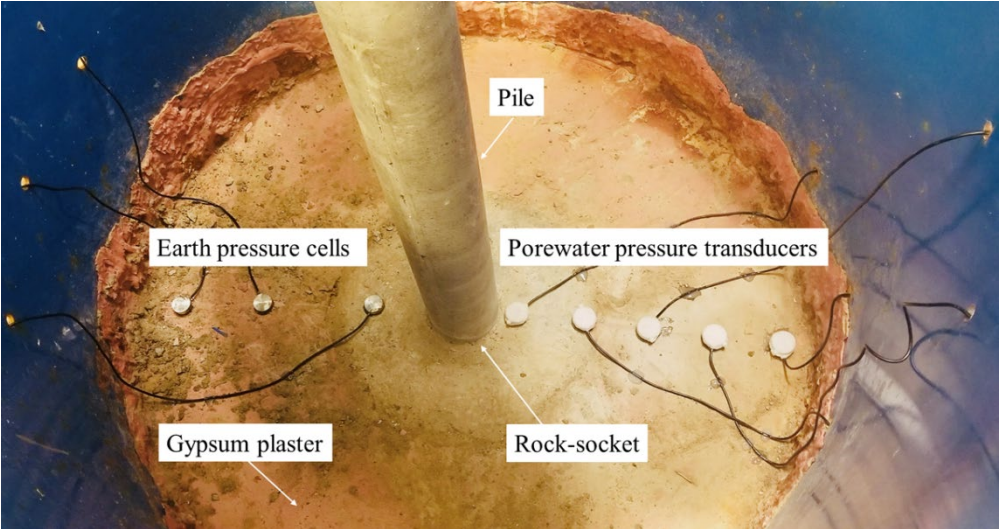


Figure 6.6 Bottom HKMD layer transducers layout



Figure 6.7 Photo after filling the first layer of HKMD slurry

CHAPTER 6: BEHAVIOUR OF FRP-SSC MODEL PILE IN MARINE SOILS INSTALLED IN ROCK-SOCKET

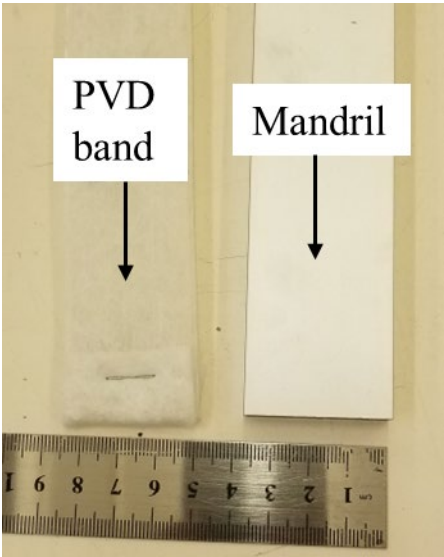


Figure 6.8 PVD band and aluminum mandril



Figure 6.9 Photo after installing the PVDs

CHAPTER 6: BEHAVIOUR OF FRP-SSC MODEL PILE IN MARINE SOILS INSTALLED IN ROCK-SOCKET

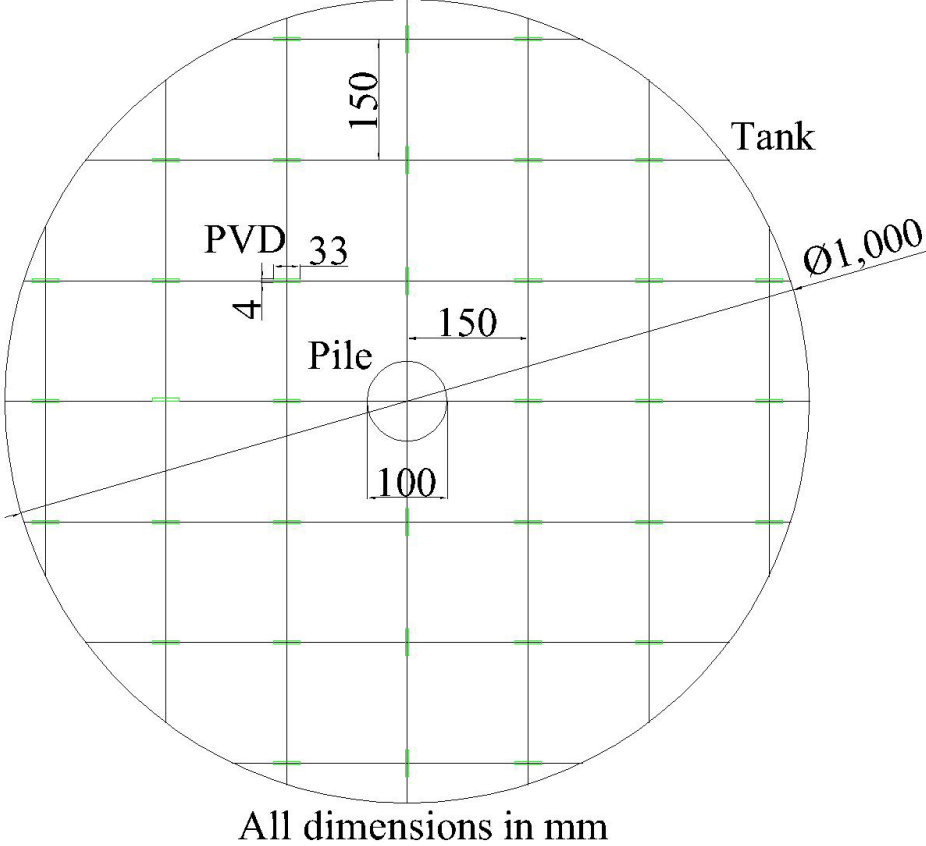
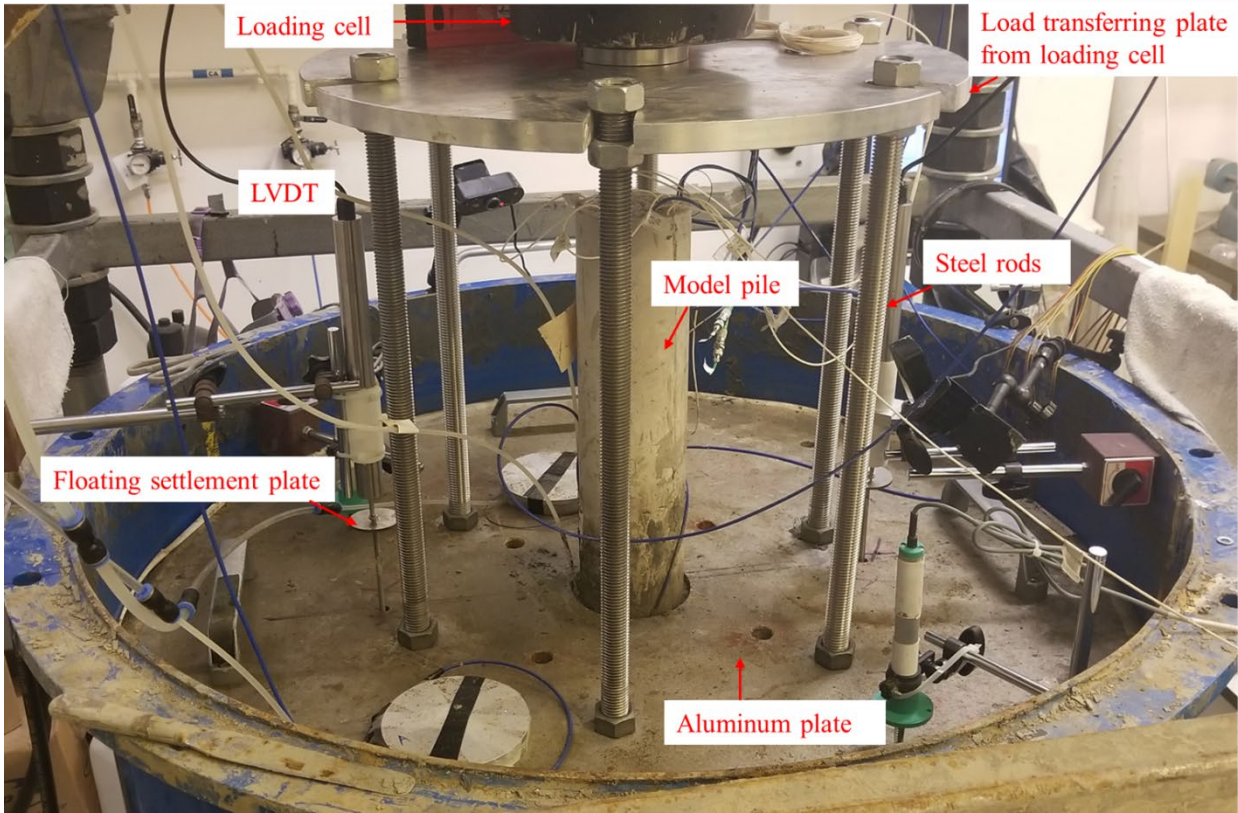


Figure 6.10 PVDs layout in the physical model

CHAPTER 6: BEHAVIOUR OF FRP-SSC MODEL PILE IN MARINE SOILS INSTALLED IN ROCK-SOCKET

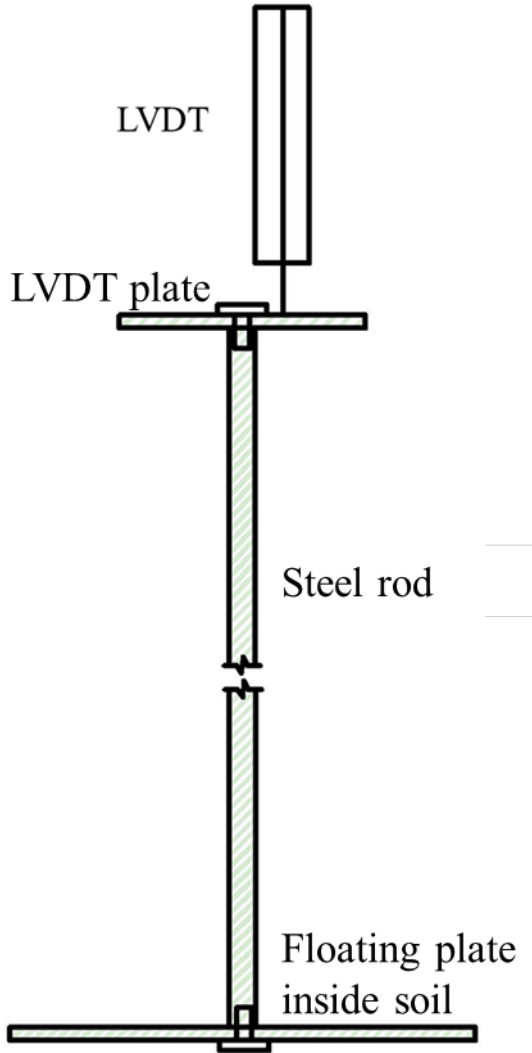


Figure 6.11 Geotextile layer



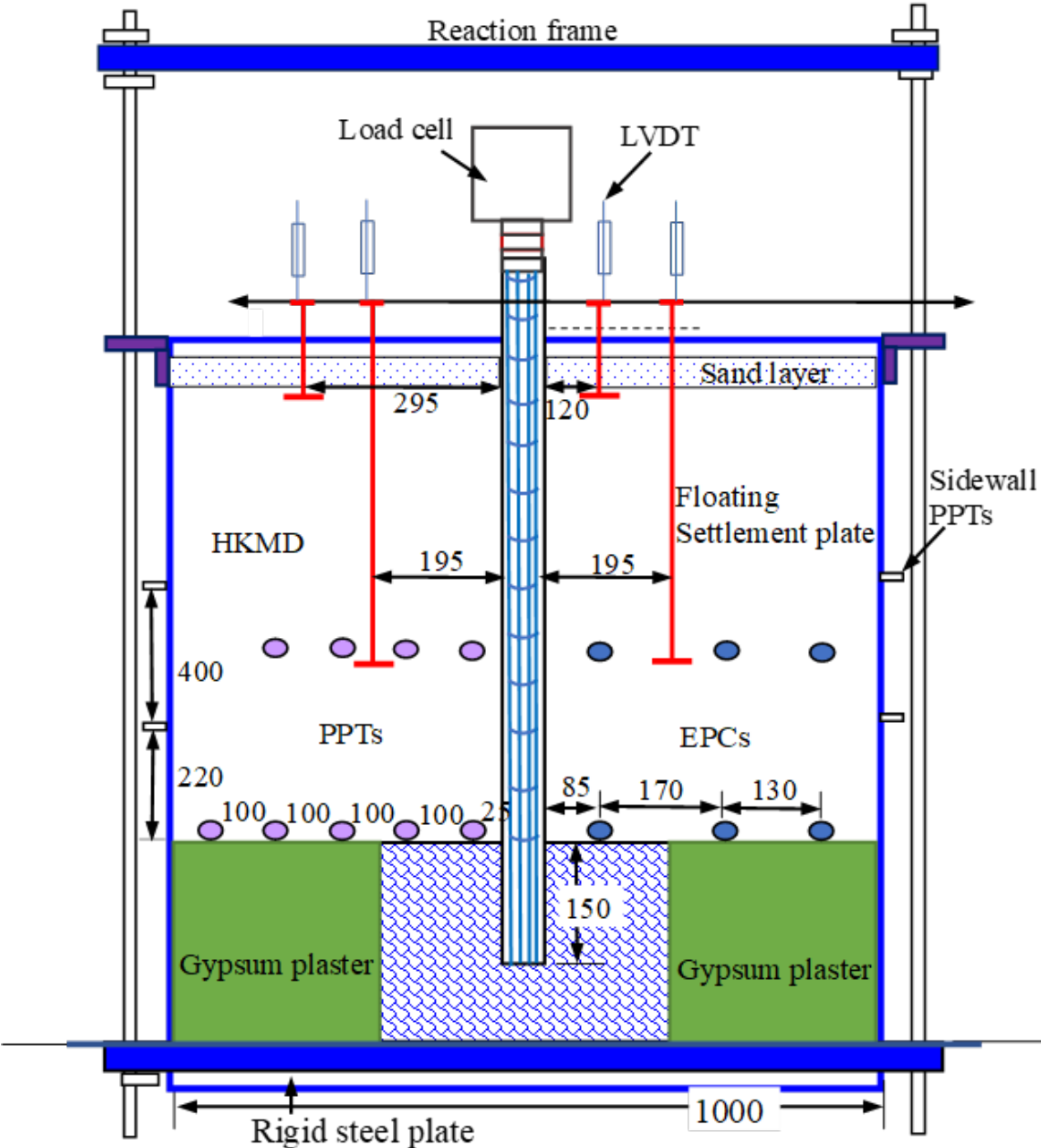
CHAPTER 6: BEHAVIOUR OF FRP-SSC MODEL PILE IN MARINE SOILS INSTALLED IN ROCK-SOCKET

Figure 6.12 Pre-consolidation loading setup



(a) Floating settlement plate design

CHAPTER 6: BEHAVIOUR OF FRP-SSC MODEL PILE IN MARINE SOILS INSTALLED IN ROCK-SOCKET



(b)

Figure 6.13 (a) Floating settlement plate design and (b) PPTs and EPCs layout

CHAPTER 6: BEHAVIOUR OF FRP-SSC MODEL PILE IN MARINE SOILS INSTALLED IN ROCK-SOCKET

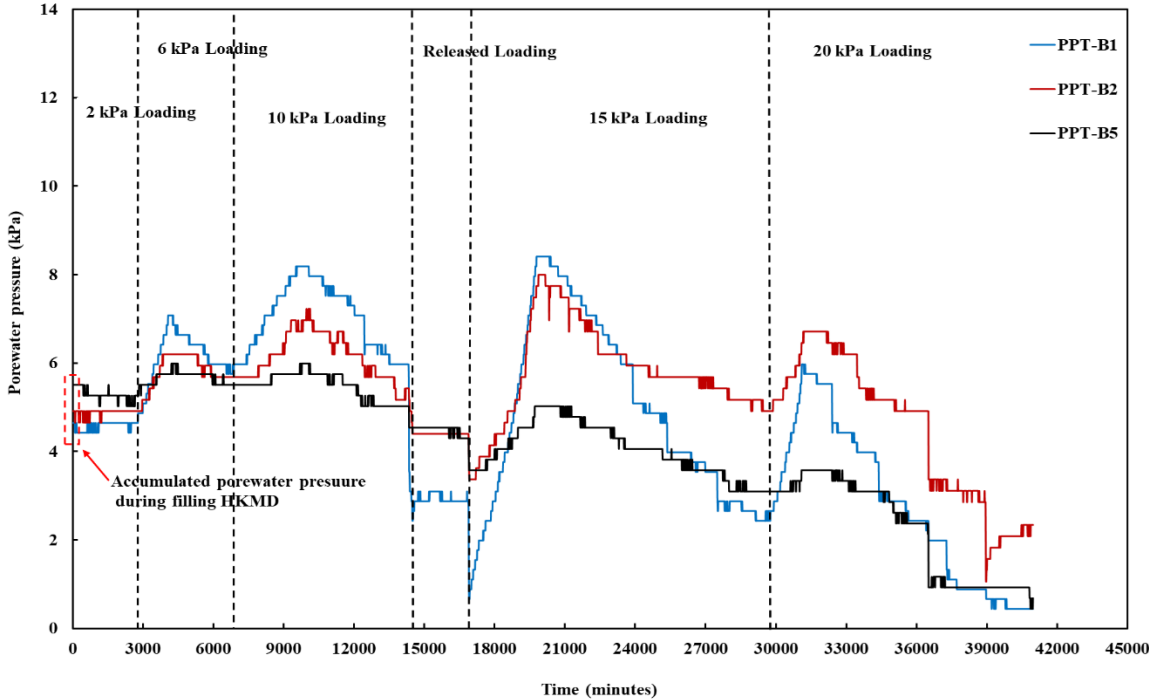
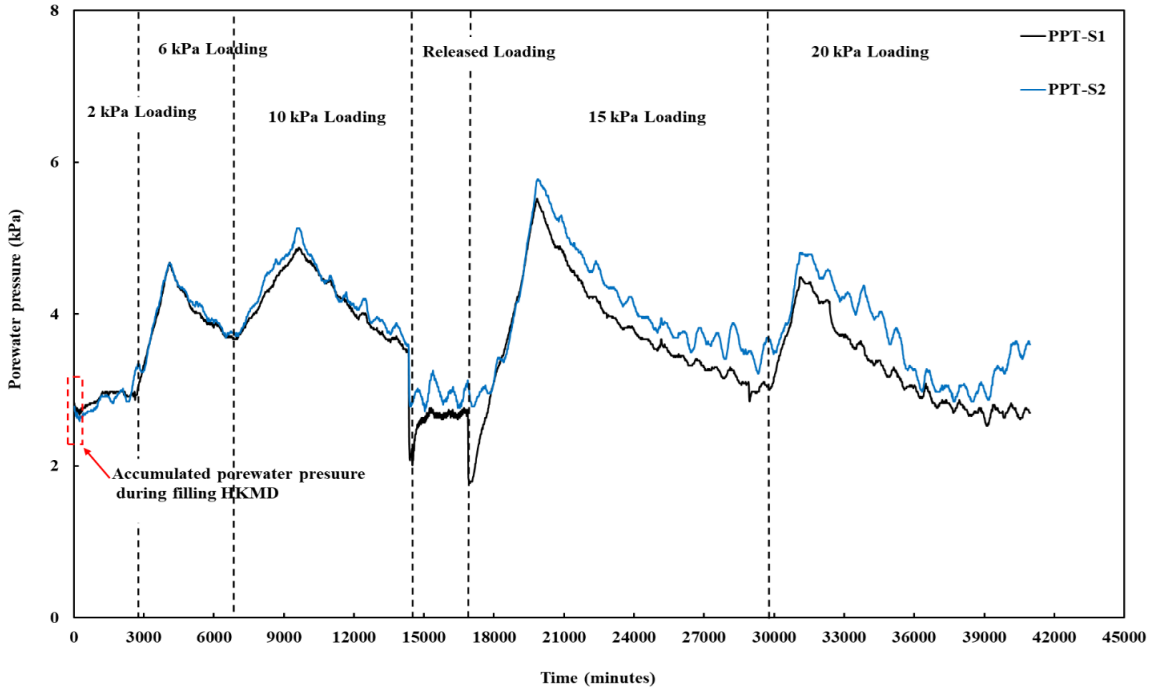


Figure 6.14 Porewater pressure variation at the bottom of tank during pre-consolidation measured with different PPTs



CHAPTER 6: BEHAVIOUR OF FRP-SSC MODEL PILE IN MARINE SOILS INSTALLED IN ROCK-SOCKET

Figure 6.15 Porewater pressure variation at the wall of tank during pre-consolidation measured with different PPTs

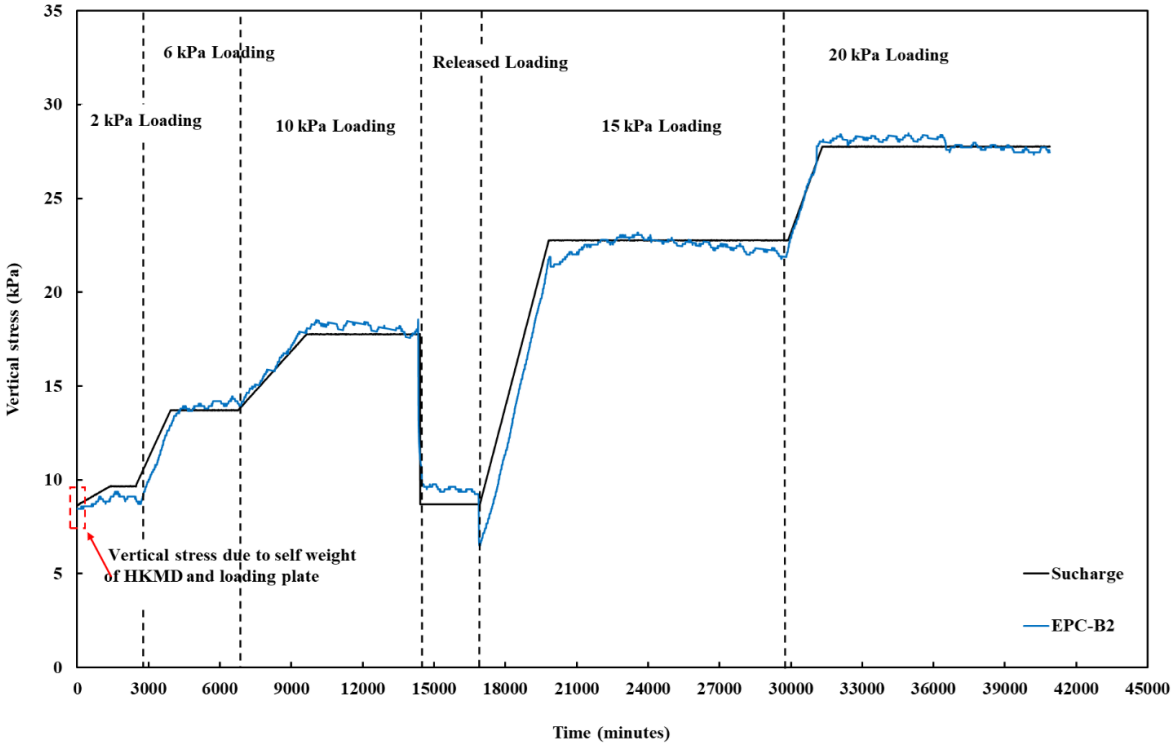


Figure 6.16 Vertical stress variation at the bottom of tank during pre-consolidation measured with EPC

CHAPTER 6: BEHAVIOUR OF FRP-SSC MODEL PILE IN MARINE SOILS INSTALLED IN ROCK-SOCKET

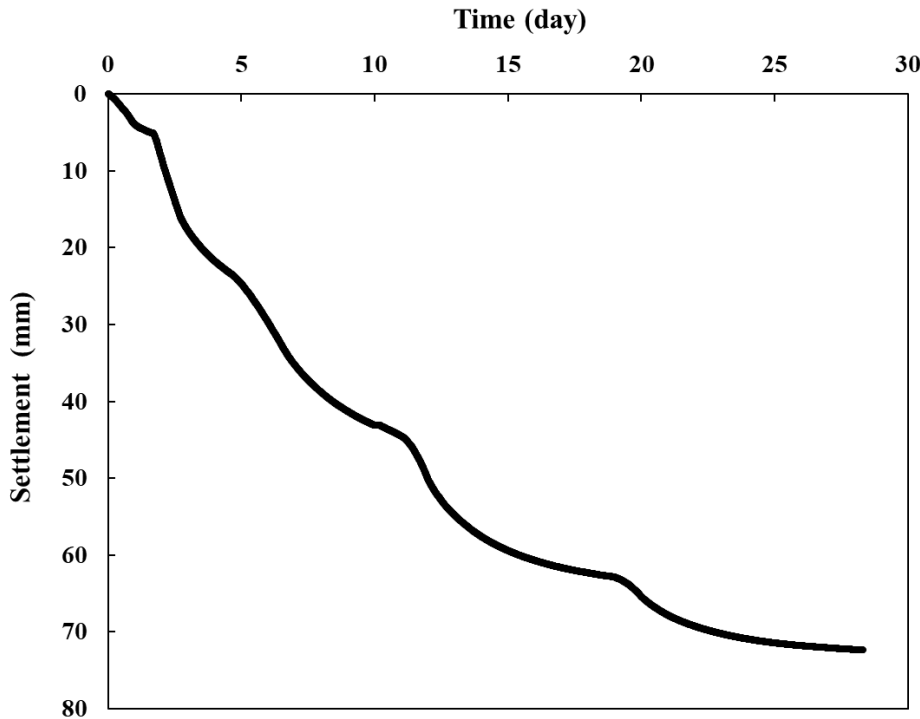
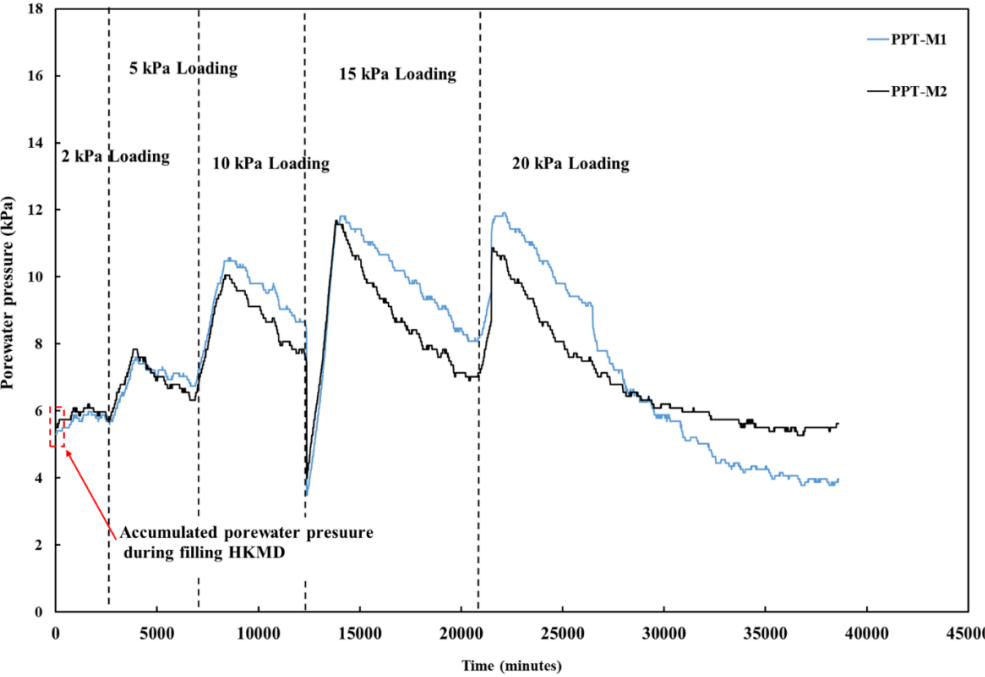


Figure 6.17 Measured settlement at the surface of bottom layer by LVDTs



CHAPTER 6: BEHAVIOUR OF FRP-SSC MODEL PILE IN MARINE SOILS INSTALLED IN ROCK-SOCKET

Figure 6.18 Porewater pressure variation at interface of upper and bottom HKMD layers during pre-consolidation measured with different PPTs

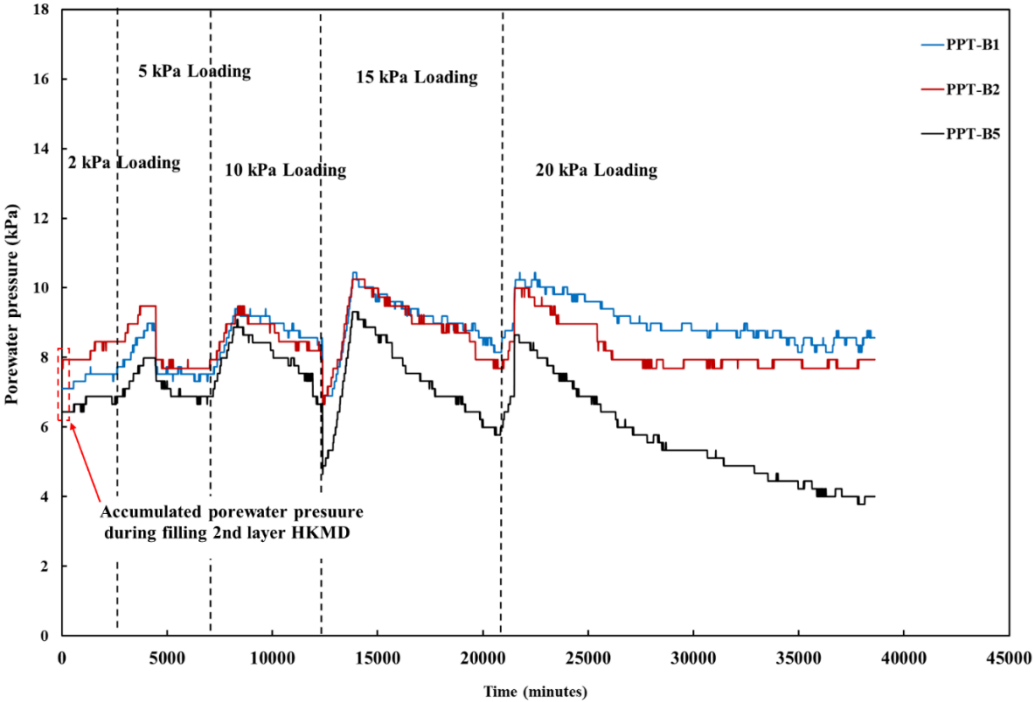


Figure 6.19 Porewater pressure variation at the bottom of tank during pre-consolidation measured with different PPTs

CHAPTER 6: BEHAVIOUR OF FRP-SSC MODEL PILE IN MARINE SOILS INSTALLED IN ROCK-SOCKET

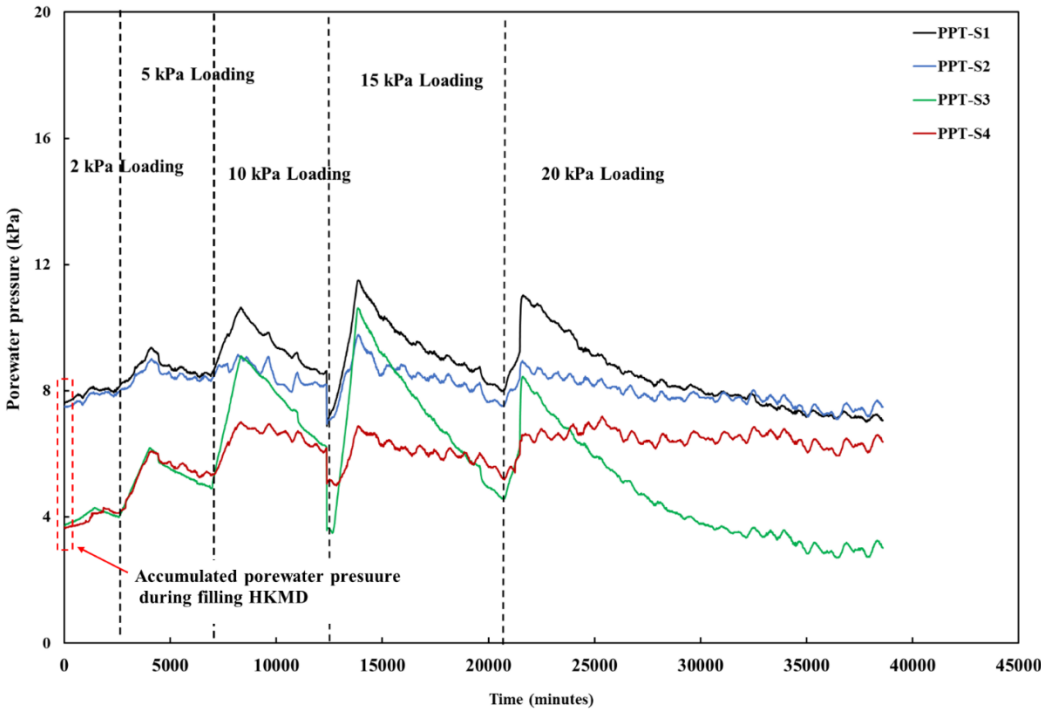
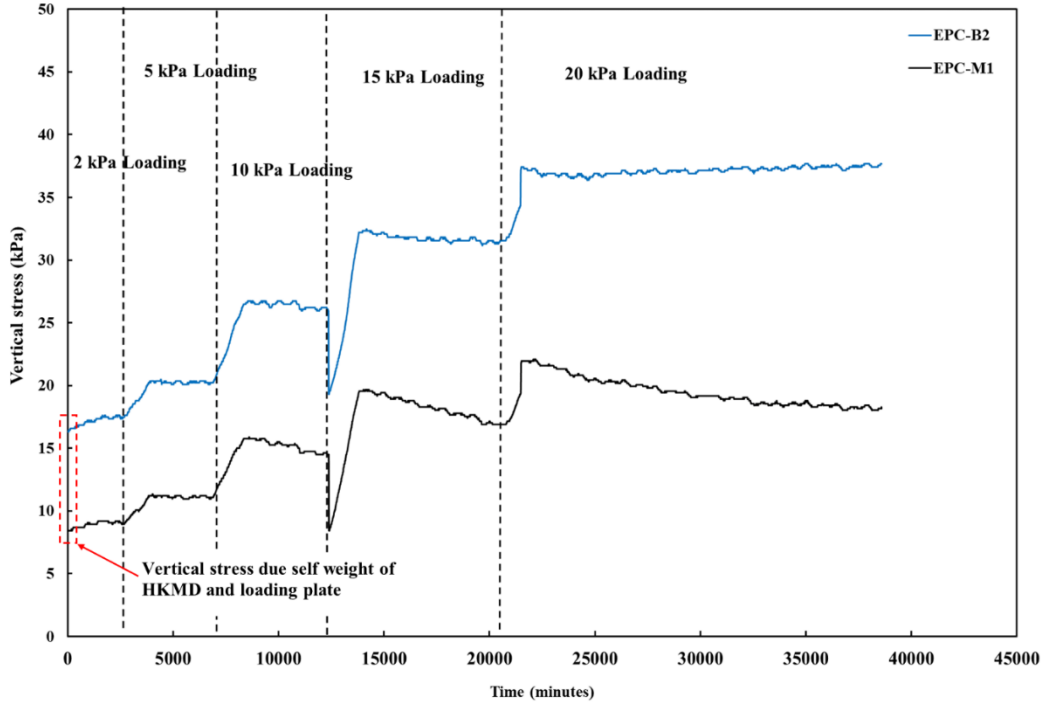


Figure 6.20 Porewater pressure variation at the wall of tank during pre-consolidation measured with different PPTs



CHAPTER 6: BEHAVIOUR OF FRP-SSC MODEL PILE IN MARINE SOILS INSTALLED IN ROCK-SOCKET

Figure 6.21 Vertical stress variation at the bottom and interface of upper and bottom HKMD layers during pre-consolidation measured with EPCs

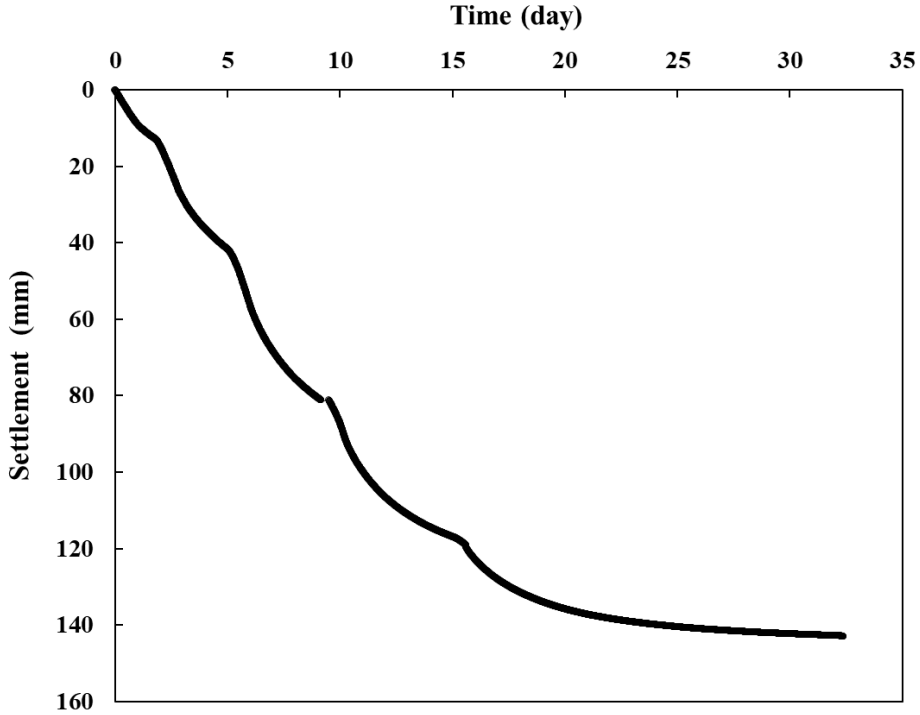


Figure 6.22 Measured settlement at the surface of upper layer by LVDTs

CHAPTER 6: BEHAVIOUR OF FRP-SSC MODEL PILE IN MARINE SOILS INSTALLED IN ROCK-SOCKET

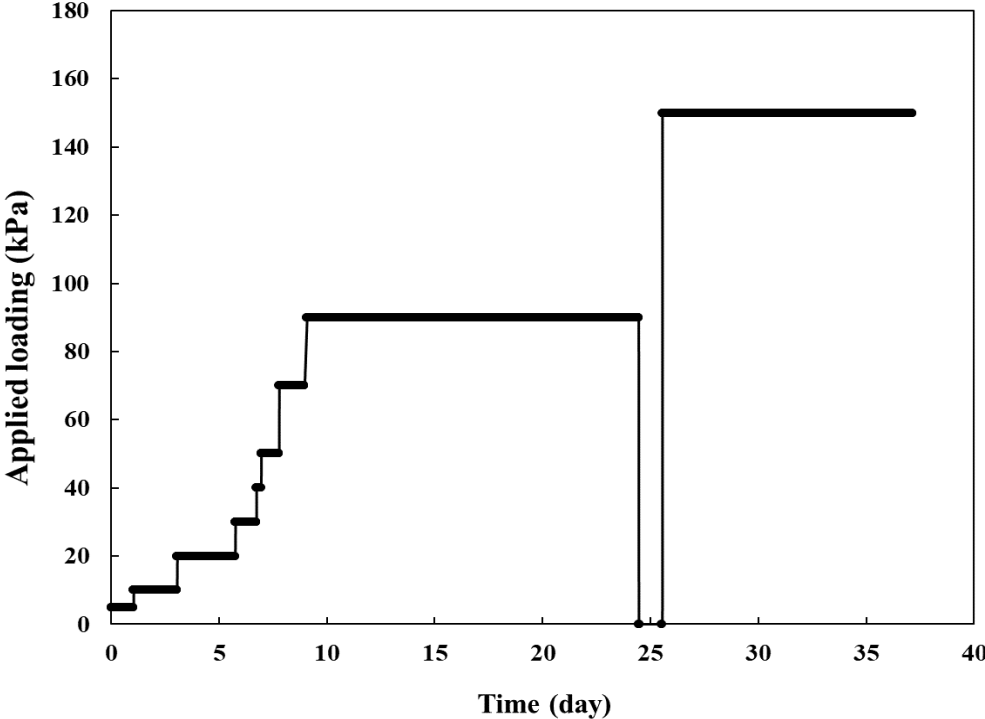
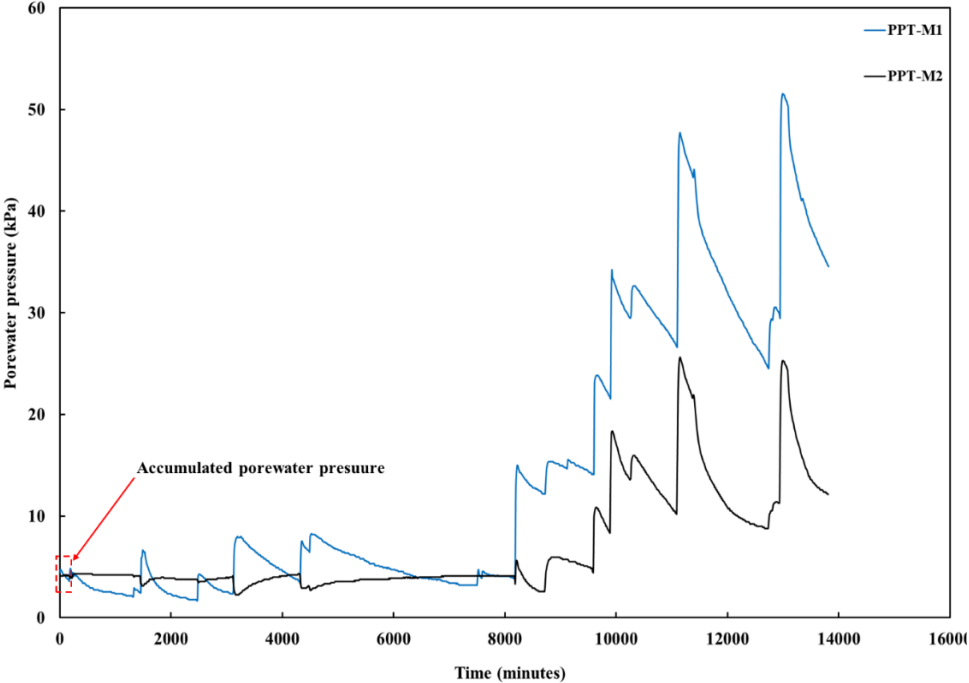


Figure 6.23 Applied surcharge loading for consolidation of HKMD



CHAPTER 6: BEHAVIOUR OF FRP-SSC MODEL PILE IN MARINE SOILS INSTALLED IN ROCK-SOCKET

Figure 6.24 Porewater pressure variation at interface of upper and bottom HKMD layers during consolidation measured with different PPTs

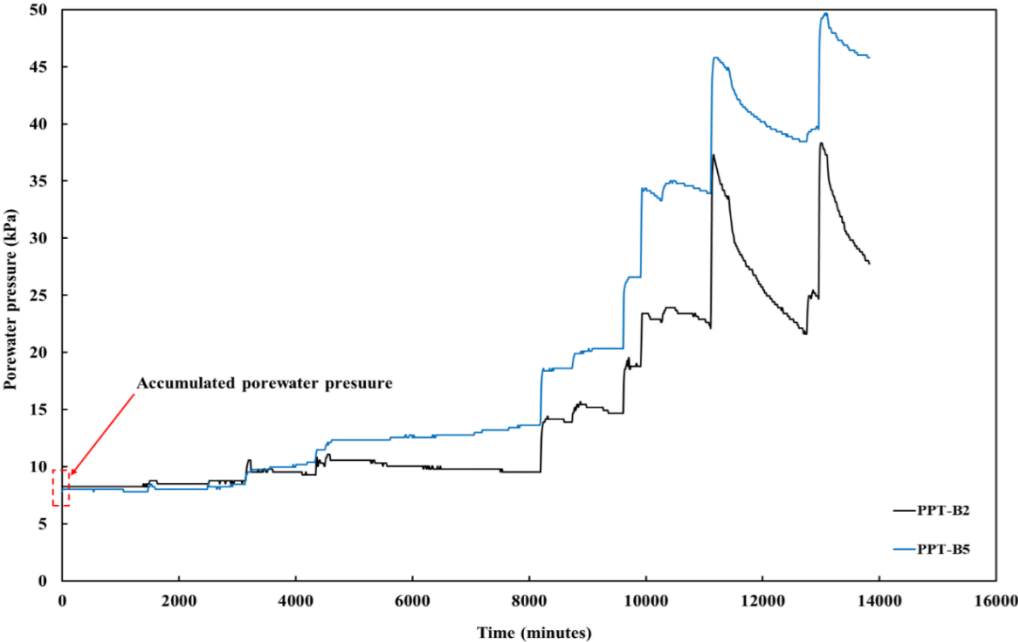


Figure 6.25 Porewater pressure variation at the bottom of tank during consolidation measured with dif

CHAPTER 6: BEHAVIOUR OF FRP-SSC MODEL PILE IN MARINE SOILS INSTALLED IN ROCK-SOCKET

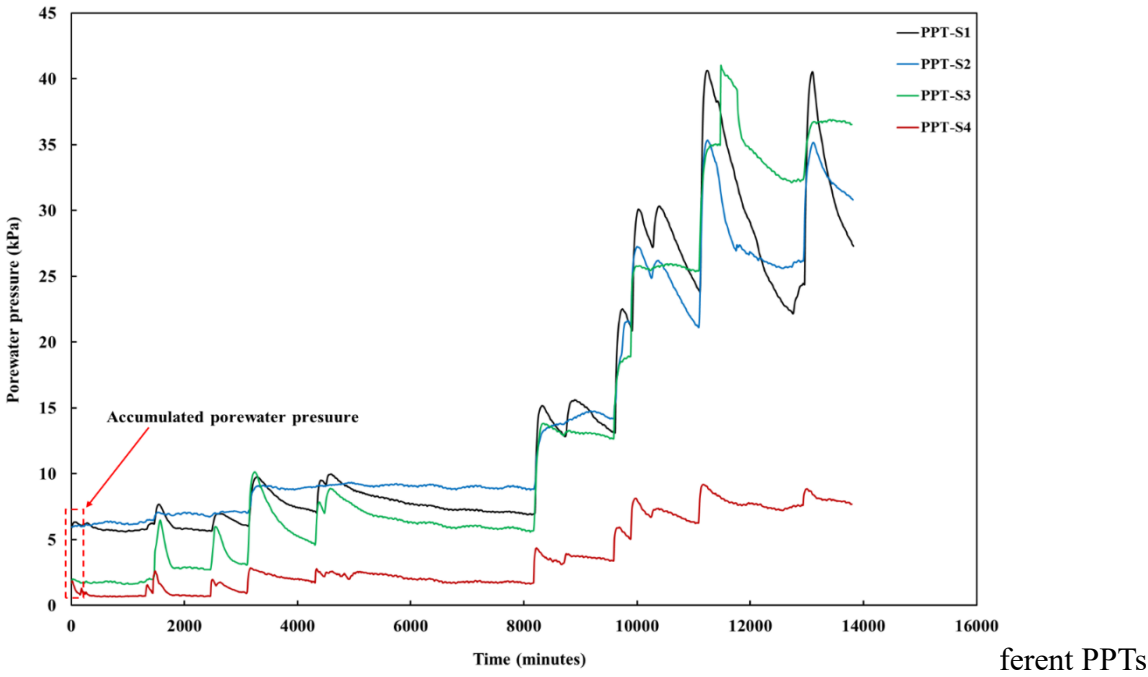
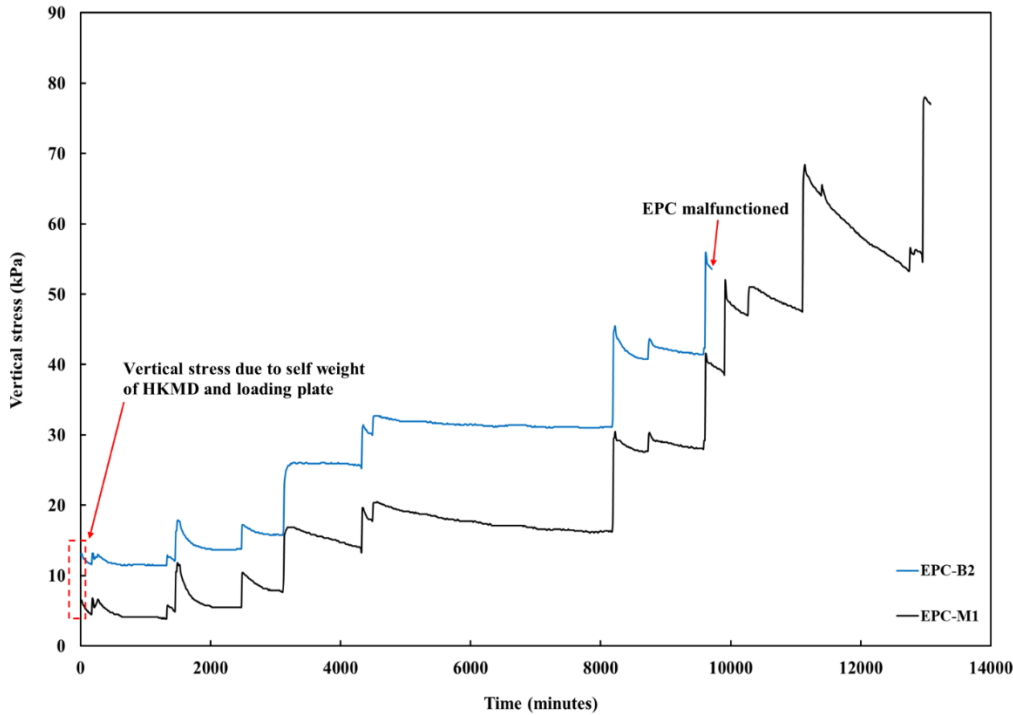
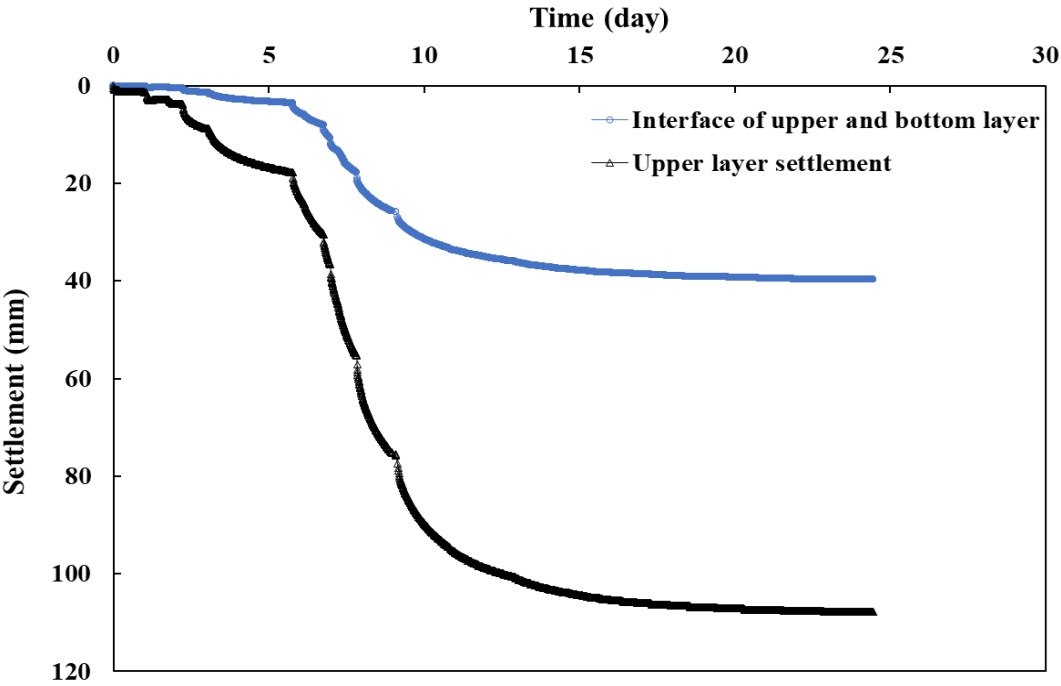


Figure 6.26 Porewater pressure variation at the wall of tank during consolidation measured with different PPTs



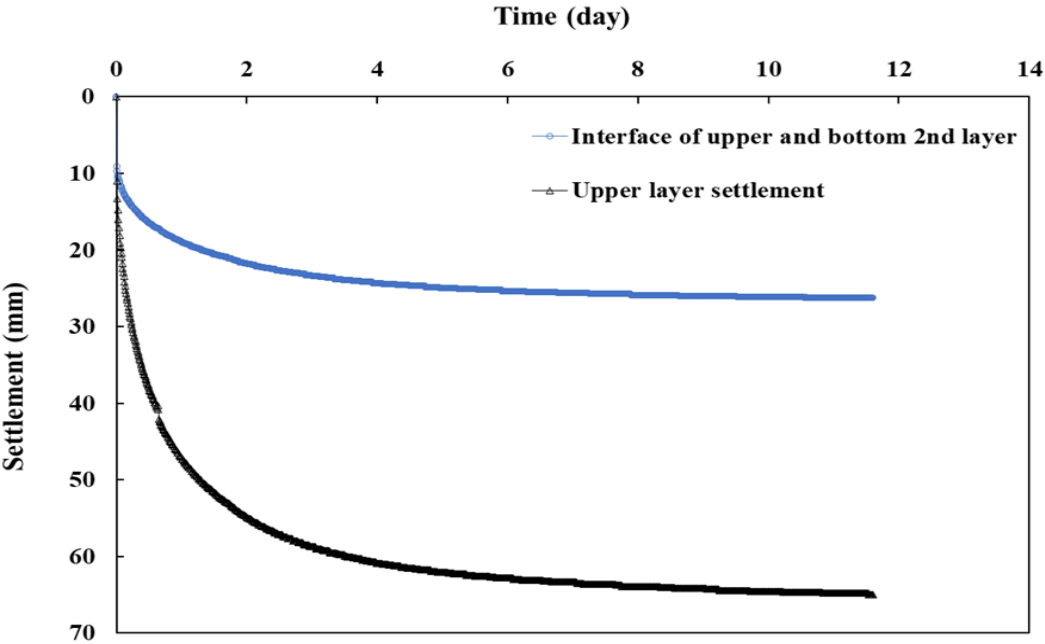
CHAPTER 6: BEHAVIOUR OF FRP-SSC MODEL PILE IN MARINE SOILS INSTALLED IN ROCK-SOCKET

Figure 6.27 Vertical stress variation at the bottom and interface of upper and bottom HKMD layers during consolidation measured with EPCs



(a)

CHAPTER 6: BEHAVIOUR OF FRP-SSC MODEL PILE IN MARINE SOILS INSTALLED IN ROCK-SOCKET



(b)

Figure 6.28 Measured settlement at the surface and interface of upper and bottom HKMD layers by floating settlement plates

CHAPTER 7: DISTRIBUTED FIBER OPTIC SENSING FOR PILE MONITORING

7.1 Introduction

This chapter compares different optic fiber sensing technologies and traditional LVDT monitored strain of model piles. Advantages and applications of each sensing method are emphasized for future studies to advance pile monitoring practices. The monitored data from OFDR sensors are analyzed and compared to the data measured by FBG sensors (discrete sensing method). The monitored axial strain data of different OFDR fiber sections at different locations of the pile cross-section is discussed in detail and compared. Besides, the distributed circumferential strain profiles around the pile at different positions along the depth are described. In addition, both the axial and circumferential strain distributions are compared and correlated with the strain localizations and failure modes of the model piles. Finally, the test findings are compared with the analytical solutions of partially embedded piles and found to be in good agreement.

7.2 Comparison of axial strain from optic fiber sensing (FBG and OFDR) and conventional LVDTs

7.2.1 Installation and instrumentation of OFDR optic fibers and FBGs in the model piles

The effectiveness of an optical fiber sensor to monitor strain profile of a structure is based on the bonding properties and bonding method between the structural material and the optical fiber.

CHAPTER 7: DISTRIBUTED FIBER OPTIC SENSING FOR PILE MONITORING

Optical fibers have the capability to be embedded within the structural material, like reinforced concrete section, or attached on the surface of structure using adhesives. In this study, optic fibers were embedded within the concrete and FRP, as well as attached to the surface using an ultra-high-strength epoxy adhesive to protect the fibers and ensure a good bond between the fiber and surface. A single mode silicon optical fiber coated with PVC having diameter of 1.8 mm (manufactured by YOFC Ltd., Wuhan, China) used by Hong et al. (2016) and P.-C. Wu et al. (2022) was used in this study.

Both the model piles were instrumented with OFDR and FBG optic fibers to monitor the behavior of piles. For Pile 2, one OFDR optic fiber was installed along the length of pile with six sections embedded at different positions. Four sections (S1, S9, S10, and S11) were placed longitudinally along the interface of FRP and SSC and two sections (S5, S6) were embedded within the SSC monitoring the strain at different positions of pile as shown in Figure 7.1(b). Additionally, seven OFDR optic fiber sections (S2 to S8) as shown in Figure 7.1(a) were installed horizontally on the outer circumferential surface of GFRP tube along the length of pile, monitoring the hoop strain distribution at different positions. Array of quasi-distributed FBGs were attached to the long aluminum channel with U-shaped cross section and placed within the SSC as shown in Figure 7.1(b). The aluminum channel was used to protect the vulnerable FBGs array while casting the concrete and to form a quasi-distributed sensing strip along the length of pile. Eight FBGs were installed in the pile body above the rock surface and four within the rock-socket at spacing of 160 mm and 35 mm respectively.

CHAPTER 7: DISTRIBUTED FIBER OPTIC SENSING FOR PILE MONITORING

For Pile 3, two independent OFDR optic fibers were installed on the rebars and within SSC along the length of pile, however one fiber damaged during the test preparation. The optic fiber has six sections (S1 to S6) for monitoring the strain of different locations of pile axially, as shown in Figure 7.2(b). Additionally, eight OFDR optic fiber sections (S7 to S14) as shown in Figure 7.2(a) were installed around the circumference at different positions at certain spacings along the depth of pile for monitoring the circumferential strain distribution. The longitudinal OFDR optic fibers attached to the rebars were glued within a notch of 3 mm depth on rebars while circumferential optic fibers were glued on the surface of concrete. Arrays of multiplexed FBGs were attached on the rebars as shown in Figure 7.2(b). Eight FBGs were placed in the pile body above rock surface at a spacing of 160 mm and four FBGs within the rock-socket at a spacing of 35 mm.

For both the piles, the measuring OFDR optic fibers were first pre-tensioned by 50 to 100 micro strain, before being glued on the structural surface. The purpose of pre-tensioning fiber was to ensure that it is in a known and stable state of tension prior to loading, thereby preventing unintentional changes in the position of fiber during casting concrete. To avoid imperfect strain transferring near the measuring fiber boundary and increase effective measuring fiber length, an additional 25% fiber length of the pile diameter was bonded for circumferential optic fiber sections (Lin et al., 2021). Additionally, the thickness of the adhesive layer was kept uniform and thin for reliable strain data. The whole length of the OFDR optic fiber worked as a distributed sensor, hence certain sections of the fiber were kept free in the air, called slack fiber section, for locating the measuring fiber sections along the length of fiber.

7.2.2 Comparison of OFDR and FBG strain profiles of Pile 2

Figure 7.3 shows the axial strain profile measured by OFDR and FBG optical fibers at different loading levels along the length of pile. Compressive strain is characterized as negative and tensile strain is positive in this study. The OFDR optic fiber strain profile was monitored by the fiber S12 embedded in the concrete at same position as of FBGs. While the FBGs strain profile was developed based on the data monitored by FBGs array attached to the aluminum channel as shown in Figure 7.1(b). The strain was measured at a spatial resolution of 10 mm by OFDR optic sensors along the depth. Both the distributed (OFDR) and discrete (FBG) sensing technologies showed similar strain profiles and generally were in good agreement with one another. It is observed that in Figure 7.3, the strain profile measured by both OFDR and FBG were generally in good agreement with one another.

7.2.3 Comparison of integrated axial strain from OFDR and FBGs with LVDTs for Pile 2

Figure 7.4 compares the axial strain measured by OFDR and FBG optical fibers at various loading levels to the strain data from LVDT. The OFDR sensing strain represents the mean strain of five fibers along the length of the pile. Similarly, FBGs strain data indicates the mean strain of twelve FBGs placed along the depth of pile on aluminum channel. The strain of LVDT was back-calculated from the mean displacement of two LVDTs positioned at the pile head. As found for Pile 2 measurement, the OFDR optic fibers data showed better agreement with LVDT results with higher level of linearity and similar coefficients.

7.2.4 Comparison of OFDR and FBG strain profiles of Pile 3

Figure 7.5 shows the axial strain profile measured by OFDR and FBG optical fibers at different loading levels along the length of pile. The axial strain by OFDR is calculated as the mean value from the two fibers in the pile body (S1 and S3) glued on two different rebars as shown in Figure 7.2(b). Similarly, the FBG data is the mean strain measured by two arrays, each glued on different rebars. The strain was measured at a spatial resolution of 10 mm by OFDR optic sensors along the depth. It is observed that in Figure 7.5, the strain profile measured by both OFDR and FBG were generally in good agreement with one another. The strain measured with OFDR optic fibers is relatively lower than that of FBGs which could potentially be attributed to the strain transferring mechanism of different optical fibers. The FBG and OFDR fiber protective coatings have different mechanical properties which influenced the strain transfer from substrate to the core of the respective optic fiber.

7.2.5 Comparison of integrated axial strain from OFDR and FBGs with LVDTs for Pile 3

Figure 7.6 presents the overall integrated axial strain measured by OFDR and FBG optic fibers at different loading levels against the LVDT data. The OFDR strain value at a specific depth is the mean strain of six fibers at the same level. The average of the results measured by two LVDTs fixed at the pile head is calculated and presented in Figure 7.6. It can be seen that the strain measured by both OFDR and FBG optic sensors have almost similar trends with that calculated from LVDTs. However, the OFDR strain data exhibited a higher correspondence with the data from LVDTs. In addition, the OFDR sensing technology provides distributed sensing, giving

more reliable data for analysis like necking, localized deformations, and cracks monitoring whereas such localized features would not be monitored by discrete sensing methods like FBGs or vibrating wire strain gauges. Therefore, this study will primarily discuss the OFDR sensing data to investigate the response of the model piles.

7.3 Comparison of axial strain distribution along the depth of model piles from different OFDR fiber sections

7.3.1 Axial strain profiles from different OFDR fiber sections of Pile 2

Figure 7.7 presents the strain profiles monitored by four independent OFDR fiber sections (S1, S9, S11, S12) along the pile length under different load levels. As shown in Figure 7.1(b), three of the sensing fibers monitored the strain profile at the interface of FRP tube and concrete and one fiber section within the concrete. Similar to the previous pile, the pile stiffness was constant above the socket because of no surrounding soil. Hence the strain profile was generally uniform from pile head to rock surface and decreased monotonically within the socket due to shaft resistance. However, the strain response monitored by the four fibers in Figures 7.7(a) to 7.7(d) between 200 and 400 mm exhibited larger localized strain values, which were clearly evident in the form of FRP tube buckling and concrete cracks at higher load levels during failure stage. The strain values monitored by fibers of S1, S11 and S12 showed smooth profiles, while the fiber S9 recorded some abrupt strain variations between 570 to 670 mm. This variation could be caused by the improper attachment of fiber onto FRP tube, resulting in irregularity and unreliable strain transformation. The fibers placed at the interface of concrete and FRP tube showed higher strain values because of the confinement action of FRP tube. The lateral expansion of the concrete

under axial compression was restrained by the FRP tube by providing confinement and recorded higher strains. However, the fiber section S12 embedded within the concrete monitored relatively small strain values.

7.3.2 Comparison of axial strain distribution at peak load of pile 2

The strain increased consistently with increasing load, with maximum strain values observed at maximum load 266 kN, as shown in Figure 7.8. The pile experienced buckling between 200 to 400 mm near the pile head, resulting in positive strain on the tension side as monitored by S10, and negative strain on the compression side as monitored by S11. The only fiber section S12 which monitored the pile socket strain distribution, showed a smooth decreasing trend between 1300 to 1460 mm because of shaft friction.

7.3.3 Axial strain profiles from different OFDR fiber sections of Pile 3

The strain distribution monitored with OFDR optical fiber sections (S1, S4, S5, and S6) along the pile length under different monotonic load levels are shown in Figure 7.9. There is no surrounding soil around the pile body making the axial load constant above the socket, and hence the strain was generally uniform from top to the rock surface under 30 kN and 60 kN load levels. However, between 200 to 400 mm, the strain response measured by the four fiber sections showed higher localized strain values, which were clearly observed in the form of cracks at higher load levels during failure of the pile. The strain increased with increase in load with maximum strain values measured at maximum load 213 kN. The strain profile monitored by

different fibers showed different types of curves. The fiber glued within the notch on the rebar recorded smoother strain curves under different loading levels as shown in Figure 7.2(b). The rebar provided a substrate with uniform modulus, enabling the fiber to record smoother strain data.

However, the fiber sections placed within the concrete showed obvious wavy strain curves, as shown in Figures 7.9(b), 7.9(c), and 7.9(d) due to the presence of stirrups. The lateral FRP reinforcement in the form of stirrups placed at 70 mm spacing generated the wavy strain profile. The stirrups provided lateral confinement; hence the fiber measurement points in contact with stirrups have higher strain values compared to the fiber section in between. Generally, under the axial load, the concrete expands laterally which is restrained by the FRP, hence the FRP experiences higher strain due to confining effect. When the axial load increases, the confining action of the FRP increases, which was confirmed by the OFDR optical fibers strain profile seen in Figures 7.9(b) and 7.9(c). From 1300 to 1450 mm is the socket, and the strain profile has smooth curves for all the fibers due to the absence of lateral FRP stirrups and high confinement effect from rock socket. The strain decreased monotonically along the depth due to the shaft resistance within the socket portion.

7.3.4 Comparison of axial strain distribution at peak load of pile 3

The strain profile measured by different fiber sections at peak load of 213 kN is shown in Figure 7.10. The fiber section S1, showed a smooth strain profile compared to the other fiber sections due to its placement on a FRP rebar with uniform modulus along the depth. The other fiber sections except S4 were attached to the ties longitudinally, therefore the profile recorded by these

fibers is wavy, indicating peaks at position where the fiber in contact with FRP stirrups and valleys showing the portion in concrete. The fiber section S6 outside the rebar cage in concrete cover showed higher strain values due to no confinement from FRP. The strain within the region 200 to 400 mm showed sudden increase indicating the weaker portion, which was confirmed by cracks in this region during failure of pile and will be showed in later sections. The strain within the socket followed a smooth decreasing trend along depth and all the fiber sections recorded same values of strain approximately.

7.4 Comparison of circumferential strain distribution of model piles from different OFDR fiber sections

7.4.1 Circumferential strain distribution from different OFDR fiber sections of Pile 2

The circumferential strain distribution monitored with OFDR optic fiber sections (S2, S5, S7, and S8) around the FRP tube confined pile at different positions along the depth are shown in Figure 7.11. The strain distribution run in the clockwise direction from 0° to 360° around the circumference of pile. The 0° position on pile circumference represents the actual North (N) direction in the laboratory, whereas 90° , 180° , and 270° positions refer to East (E), South (S), and West (W) directions, respectively. The 0° to 360° represents the circumferential length of pile (0 mm to 360 mm) and was presented in the form of angular directions for clear illustration. The tensile strain is positive which is similar to OFDR interrogator default measurement sign.

Figure 7.11(a) shows the circumferential strain distribution at the position of 200 mm from the pile head monitored by the fiber section S8 around the pile circumference under different loading

levels. The strain values appeared higher between the north and west sides compared to the other directions with a peak tensile strain of $2500 \mu\epsilon$ under 180 kN. At failure stage, the pile bent in the region (200 to 400 mm along the depth) towards west side, creating compression in the FRP tube on the westside and tension on the east side as shown in Figure 7.13. The higher strain on compression side is attributed towards the bulging of FRP tube and fiber matrix rupture, resulting in higher tensile stress in the circumferential fiber section. Under different loading levels, the stain contour remained the same in shape, but expanded in size with increasing load.

The circumferential strain distribution measured with the fiber section S7 placed at 400 mm around the circumference from the pile head is shown in Figure 7.11(b). The strain values appeared higher on the west side of the pile cross-section comparatively. This strain localizations were observed in the form of FRP tube buckling as discussed previously with tension and compression along the east and west sides respectively shown in Fig. 18. The strain pattern remained the same for different loads, but strain increased with increase in load.

The fiber section S5 placed near the middle of the pile length monitored the circumferential strain distribution as presented in Figure 7.11(c). The strain profile showed uniform pattern radially, however the strain values recorded were lower compared to other hoop sensing fiber sections. The circumferential strain monitored at 1100 mm depth from the pile head with fiber section S2 is shown in Figure 7.11(d). The higher strain values appeared in the southeast side comparatively. This strain concentration could possibly be attributed to the Euler deflection behavior of the pile as a column with one end (restrained to rotation and allowed to axial translation) and other end fixed support (under compression, the pile head acted as a support with no rotation but allowed to axial translation and the socket provided a fixed support to the pile).

7.4.2 Circumferential strain distribution from different OFDR fiber sections of Pile 3

The circumferential strain distributions monitored by four independent OFDR fiber sections (S8, S9, S12, and S14) around the pile circumference at different positions are shown in Figure 7.12. The strain distribution notations and signs are presented in Section 7.4.1. In general, the shape of strain profiles for different OFDR optical fiber sections placed at different positions varied. The circumferential strain distribution measured with the fiber section S8 under different load levels is shown in Figure 7.12(a). The strain distribution around the circumference fluctuated and showed higher strain values in the region between 240° to 260° mm and 320° to 350°. Under different loading levels, the strain distribution pattern around the circumference remained the same, but the strain values increased with the increase in load.

Figure 7.12(b) shows the hoop strain distribution at the position of 400 mm from the pile head, monitored by fiber section S9 around pile circumference under different load levels. The strain distribution around the circumference showed a uniform pattern. However, sudden increase in strain appeared in 210° to 280° region. This variation in the pattern can be attributed towards the strain localization towards the southwest side of the pile. The circumferential strain profile remained the same for different loads and increased with load level. The fiber section S12 positioned near the middle of the pile length monitored the circumferential strain distribution as shown in Figure 7.12(c). The hoop strain profile around the circumference of pile varied in southwest and northwest side, showing maximum strain values between 0° to 40° and 210° to 320° regions. The strain pattern remained the same for different loads and with the increase in load

strain values increased. Similarly, the circumferential strain monitored by the fiber section S14 at the position of 1100 mm from the pile head is shown in Figure 7.12(d). The strain profile around the circumference showed uniform pattern approximately with fluctuations in strain appeared between 30° to 60° and 250° to 290° mm regions. The maximum strain was recorded on the west side of the pile, corresponding to the strain localization in this region.

7.5 Analysis of axial and circumferential strain localizations in relation to failure mode of model piles

7.5.1 Comparison of axial and circumferential strain localizations with failure mode of Pile

2

The distributions of the axial strain along the pile depth and its circumferential strain at failure stage are shown in Figure 7.13. The axial and circumferential fiber sections were aligned in cardinal directions (N, E, S, and W) in similar manner as discussed for Pile 2 in Section 7.4.1. The pile failed as a result of buckling between 200 to 400 mm near pile head. The compression side of the buckled tube showed higher strain values due to FRP fibers and matrix damage which caused higher tensile strain concentration compared to the tension side. The strain localization was also observed between 900 to 1100 mm along the depth by circumferential fiber sections indicating Euler second mode buckling shape as shown in Figure 7.13.

7.5.2 Comparison of axial and circumferential strain localizations with failure mode of Pile

3

The distribution of the axial strain along pile length and hoop strain around the circumference of the pile at failure stage is shown in Figure 7.14. Three distributed fiber sections (S1, S3, and S5) present the axial strain response and five representative distributed circumferential fiber sections (S8, S9, S12, S13, and S14) presents circumferential strain distribution. The localized strain concentrations were successfully monitored by both axial and hoop optic fibers which is the primary concern of this study. The observed cracks at failure stage between 200 to 400 mm and 900 to 1100 along the depth were clearly detected by the optic fibers which are consistent with the monitored strain profiles. The localized strains and failure in the one third region of pile length near pile head and pile base, indicate Euler second buckling mode as shown in Figure 7.14.

7.6 Comparison with analytical solutions

The physical model piles in this study are considered as partially embedded piles, where the load is transferred to rock base through shaft friction in rock socket and serve as a column for the portion above the rock surface. The pile head was restrained to rotation but allowed for axial translation by the load transferring plate, while the pile bottom can be defined as fixed end due to the restraints of rotation and translation. However, the pile depth below the rock surface needs to be defined where it can be considered as fixed. This depth to fixity were predicted using analytical models which were derived using elastic Winkler foundation (Hetényi and Hetbenyi, 1946; Davisson and Robinson, 1965; Prakash, 1987; Heelis et al., 2004). The basic equation which defines moment equilibrium for partially embedded piles as

$$EI \frac{d^4 x}{dy^4} + \left[P - \int_0^y f(y) dx \right] \frac{d^2 x}{dy^2} - f(y) \frac{dx}{dy} + kx = 0 \quad (7.1)$$

where I is the moment of inertia of pile cross section, P is the axial compression applied at the pile head, x is the lateral deflection, $f(y)$ is the shaft friction along the depth y and k is modulus of subgrade reaction. k can be defined as $k = n_H y$. For granular soils, the k varies along the depth y , however in this study k is constant for rock mass hence $k = n_H$ and can be found as

$$k = n_H = \frac{E_m}{h} = \frac{0.5 \sigma_c MR}{h} \quad (7.2)$$

where E_m and σ_c is the modulus of deformation and UCS of rock mass respectively. MR is the modular ratio and h is the height of rock specimen. The value of $k = 0.21$ GPa/mm was found for the granite rock specimens from UCS tests based on ASTM C469. Davisson and Robinson (1965) proposed a solution for a partially embedded pile utilizing non-dimensional parameters where length of pile below rock surface, $Z_{\max} = L_b / T$, depth to fixity, $S_T = L_{b'} / T$, and column length above the rock surface, $J_T = L_u / T$, where $T = \sqrt[5]{\frac{EI}{n_H}}$, and $L_{b'} = 2T$. Figure 7.15 shows the equivalent embedded length ($L_{b'}$) of pile, where the total equivalent length is $L_e = L_{b'} + L_u$. The critical buckling load is then given as

$$P_{cr} = \frac{\pi^2 EI}{c(S_T + J_T)^2 T^2} \quad (7.3)$$

Since the pile cross sectional area A and radius of gyration r are constant, the critical buckling load may be computed by using Euler's formula for slender columns given as

$$P_{cr} = \frac{\pi^2 EA}{c(L_e / r)^2} \quad (7.4)$$

where c is the factor for unembedded pile end condition and is calculated as 0.25, 0.49, and 1 for fixed, pinned and translation-no-rotation respectively, using Euler formula, with the embedded end considered as fixed.

The experimental test results of both the model piles were compared with the above analytical solutions. The flexure rigidity EI of Pile 3 and Pile 2 determined from the optic fibers monitoring in the static compression tests were 6.4×10^{10} Nmm² and 8.6×10^{10} Nmm² respectively. The maximum load sustained by Pile 3 and Pile 2 under static monotonic compression test was 213 kN and 266 kN respectively. The theoretical buckling loads for both the model piles were calculated with embedded and unembedded ends considered as fixed and translation-no-rotation and end of fixity taken at pile base in rock-socket. The Davisson and Robinson (1965) analytical approach in Equation 7.3 predicted 252 kN and 340 kN buckling loads for Pile 3 and Pile 2, showing approximately 15% and 21% difference between the predicted and test results respectively. The difference in results shows good correlation for the model piles tests and can be explained from the monitored strain profiles of both piles. The higher localized strain concentrations between 200 to 400 mm depth monitored by distributed optic fiber sections shown in Figures 7.7 and 7.9 reduced the ultimate load carrying capacity of the piles. The localized strain concentrations can be attributed to reduced pile stiffness in this region due to low end fixity condition, degradation of modulus of pile due to pre-cyclic loading tests, and possibly low SSC density. The presence of the high localized strain values were monitored at the early stage under low load levels and hence were clearly observed in the form of cracks at higher load levels during failure of the piles.

Under same end conditions and fixity depth as above, the Euler formula in Equation 7.4 predicted 295 kN and 401 kN buckling loads for Pile 3 and 2, showing approximately 27% and 33 % difference between the predicted and test results respectively. As discussed previously, the difference in results can be attributed to localized strains, true mode shape prediction, and reduced pile stiffness at certain points.

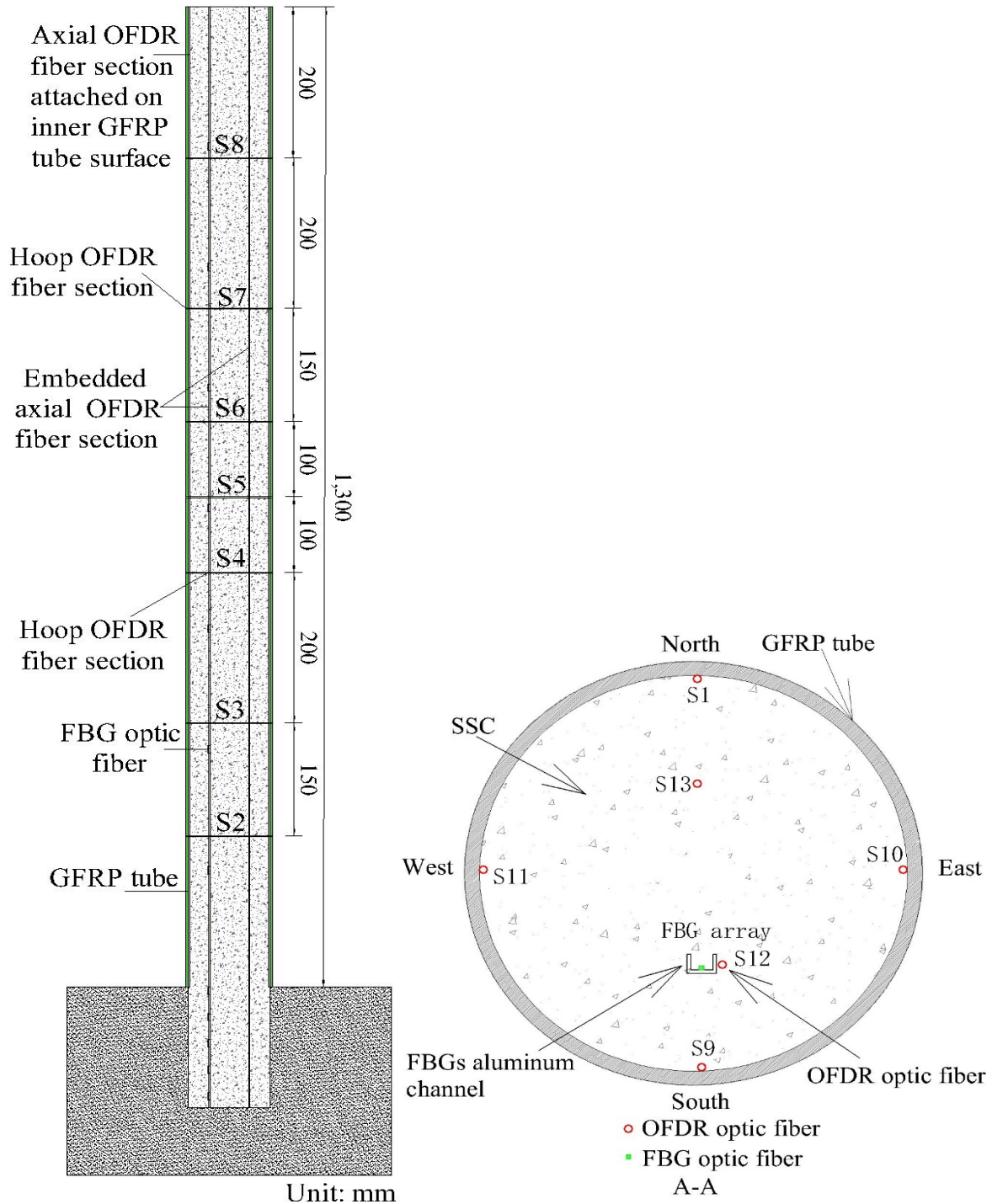
Both the model piles failed under Euler 2nd mode of buckling, with Pile II showed higher ductility comparatively. Pile 3 failed due to breakage of FRP rebars with obvious cracks, spalling and debonding of concrete from rebars as shown in Figure 7.14. For Pile 2, FRP tube provided better confinement effect, restrained concrete more uniformly and controlled the cracks propagation comparatively and failed due to the rupture and squeezing of FRP tube after full strain development shown in Figure 7.13.

7.7 Summary

Distributed OFDR and FBG sensing techniques were compared and analyzed in this chapter. Both sensing technologies showed similar strain profiles and generally were in good agreement with one another. The novel distributed sensing technique of distributed (OFDR) optic sensors is able to monitor the axial strain profiles along the FRP composite SSC piles, demonstrating good agreement with one another and with LVDT calculated strain data. The OFDR sensors monitor the distributed strain profiles with high spatial resolution providing load distribution of the entire pile, identifying any localized regions of weakness, strain concentrations, or pile shaft non-homogeneity with higher accuracy and hence overcoming the limitations of traditional monitoring techniques. The axial strain profiles measured by different fiber sections at different

CHAPTER 7: DISTRIBUTED FIBER OPTIC SENSING FOR PILE MONITORING

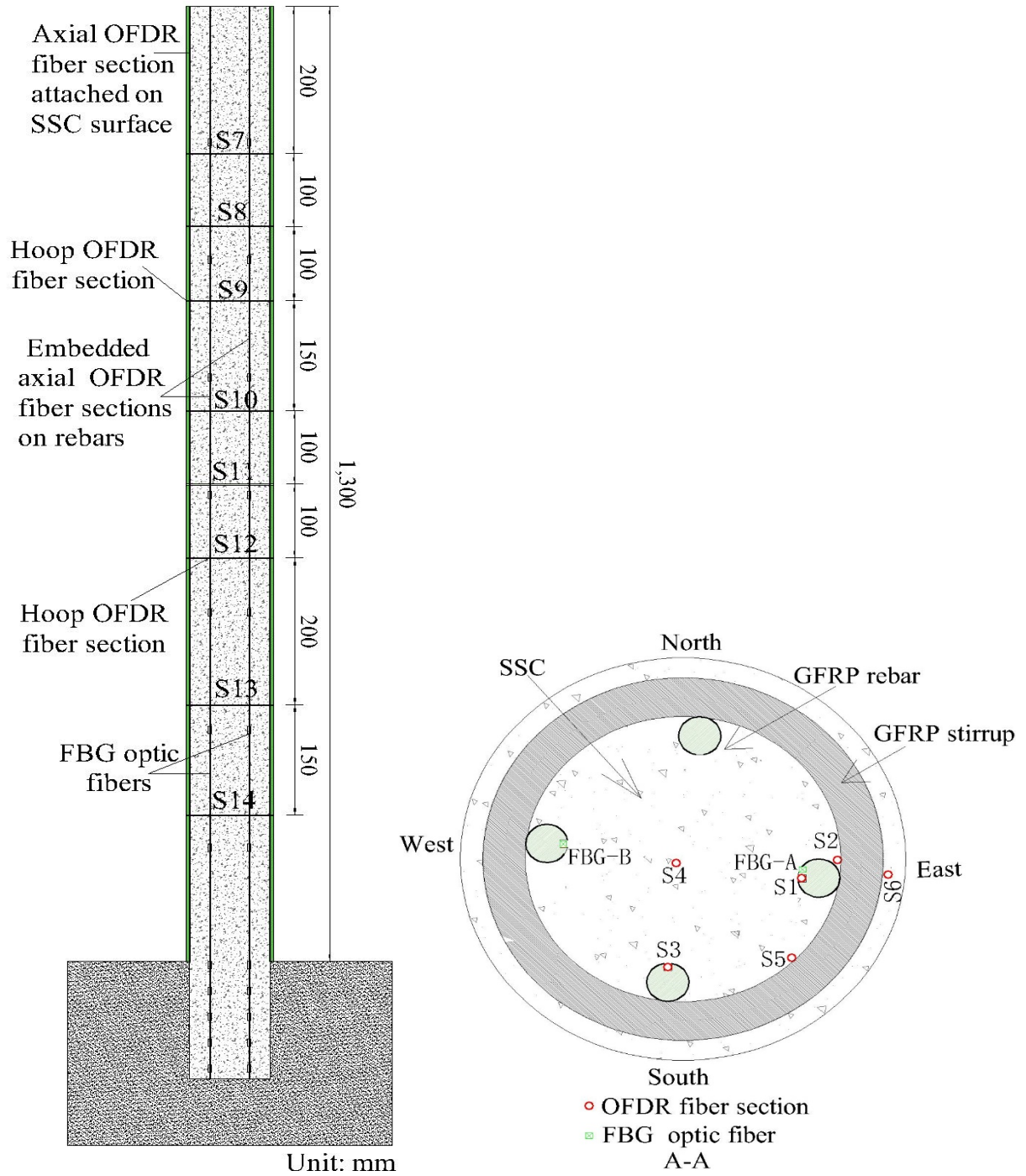
positions of the cross section along the depth of the piles showed a similar trend for model piles with higher localized strain values recorded in the upper one-third region near pile head. This localized strain concentration led to failure of both piles in the form of cracks and rebars crushing in both piles during failure stage. The distributed circumferential strain profiles provided reliable information of the localized strain concentrations around the pile circumference, showing early detection of pile shaft cracks, lateral deformation, and bending direction and position accurately. The predicted buckling load based on analytical solutions and actual buckling load from tests were in fair agreement with a minor discrepancy due to localized strains near the pile head.



(a)

(b)

Figure 7.1 Cross-section illustrations of Pile 2: (a) vertical profile, (b) horizontal profile



(a) (b)
 Figure 7.2 Cross-section illustrations of Pile 3: (a) vertical profile, (b) horizontal profile

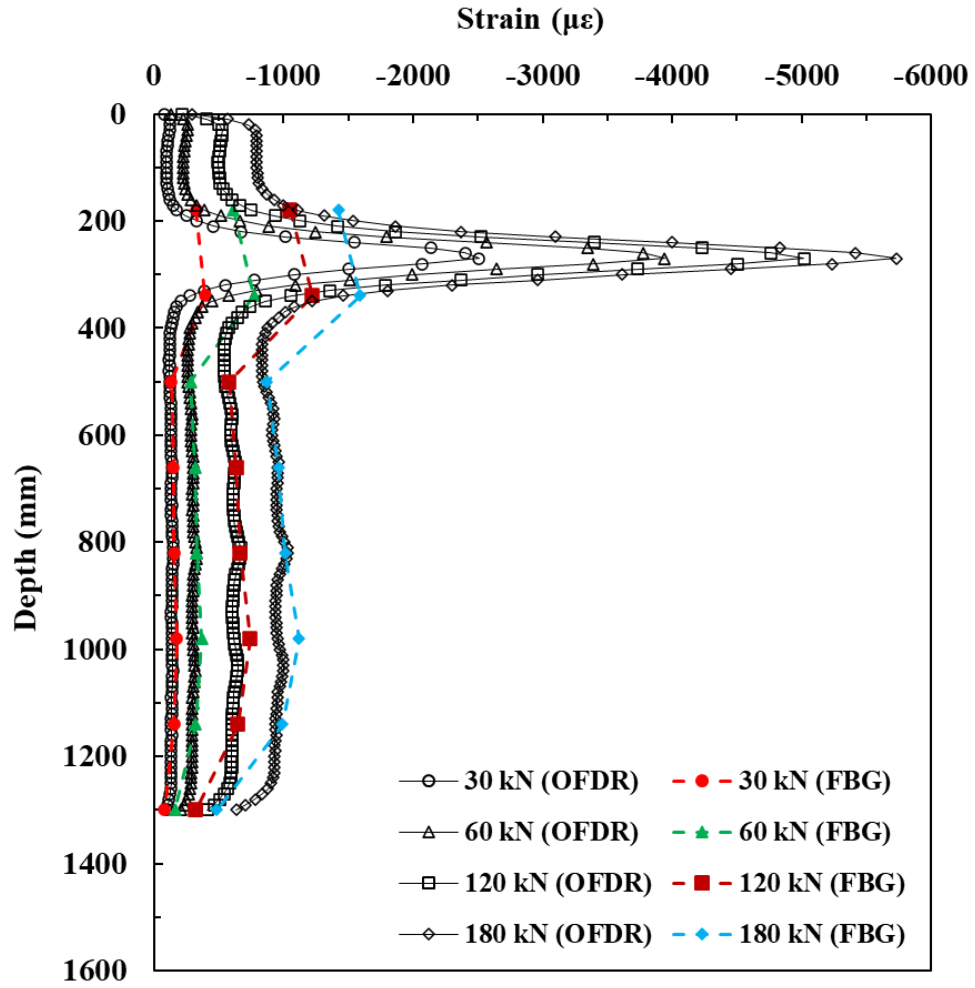


Figure 7.3 Comparison of axial strain distribution of Pile 2 measured from OFDR and FBGs

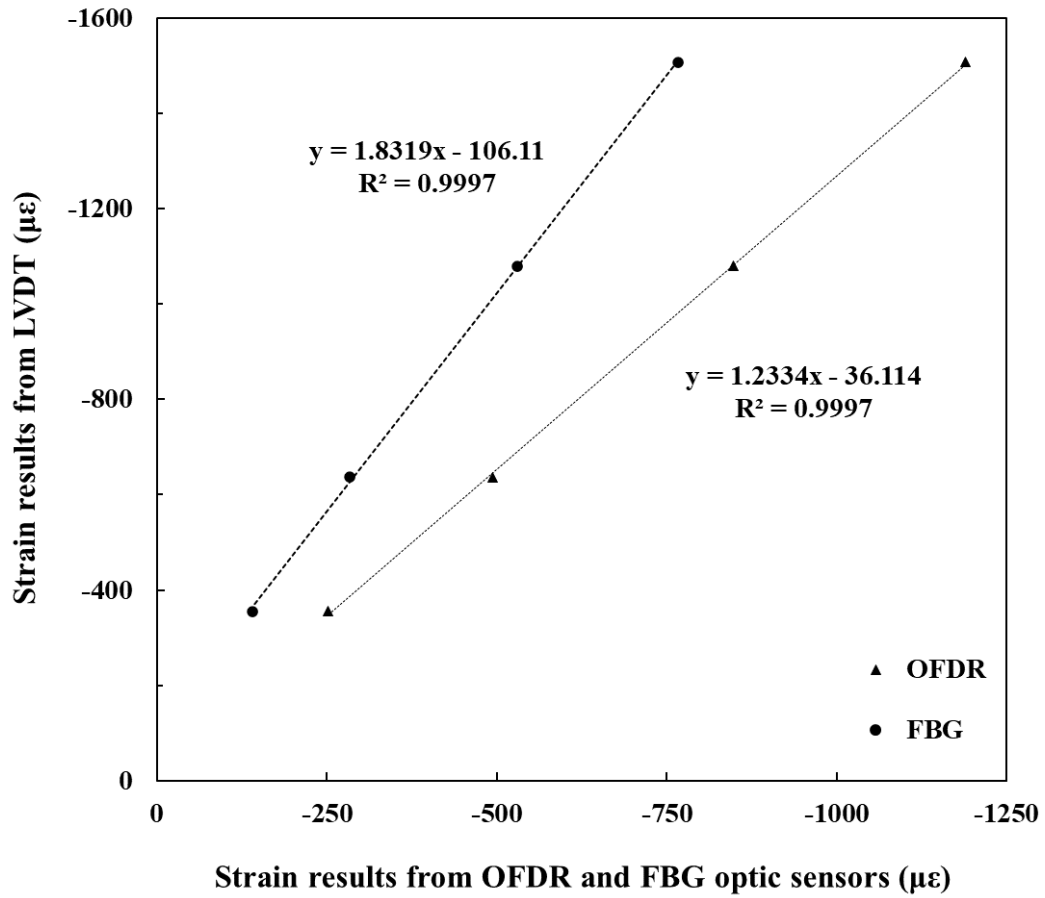


Figure 7.4 Overall integrated axial strain of Pile 2 from measured results from OFDR and FBGs versus the overall strain results from LVDT

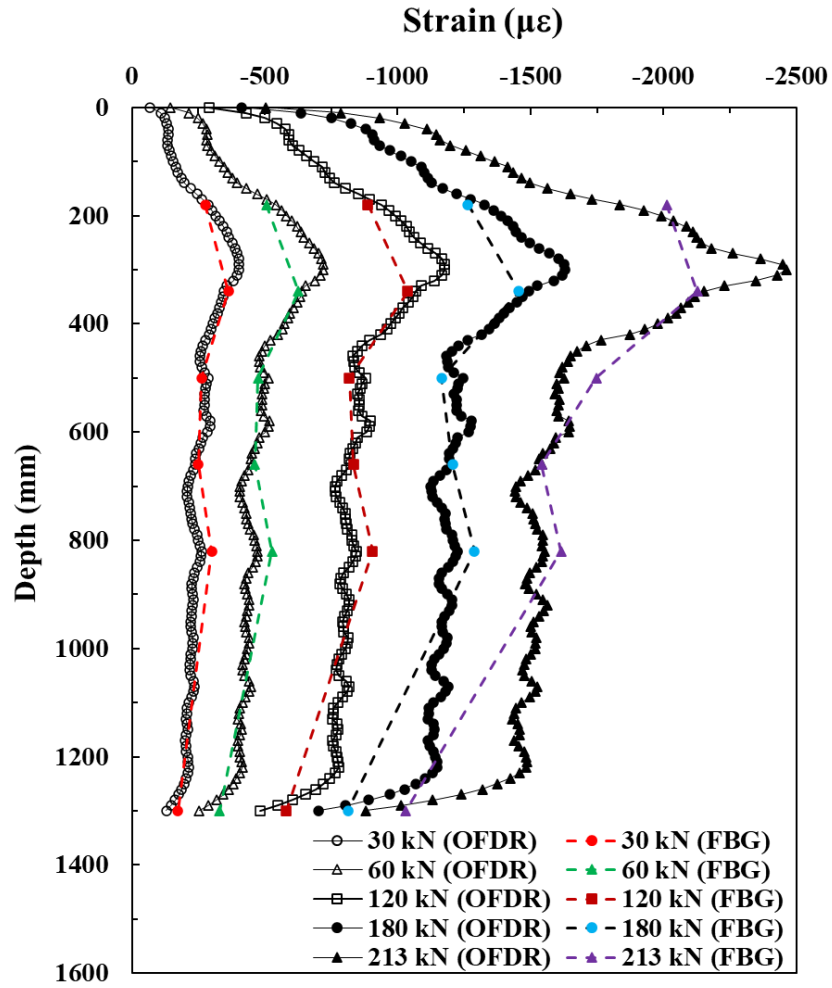


Figure 7.5 Comparison of axial strain distribution of Pile 3 measured from OFDR and FBGs

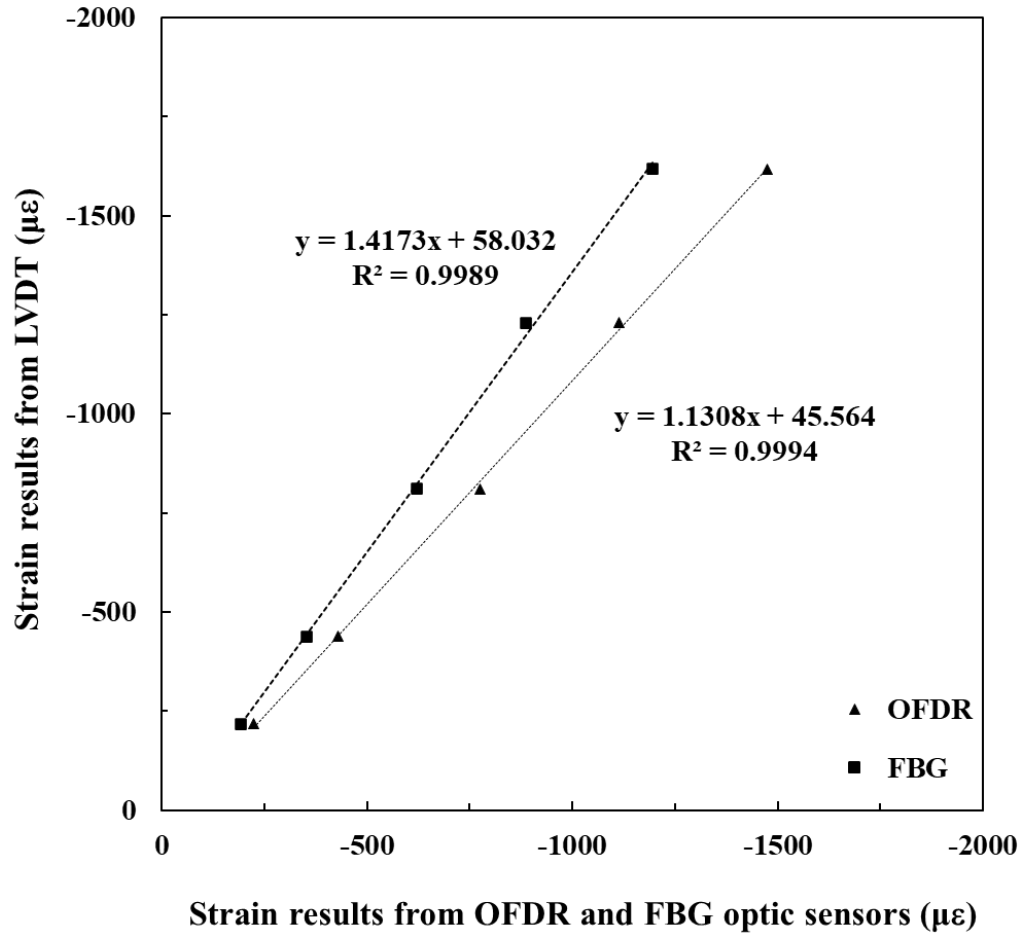
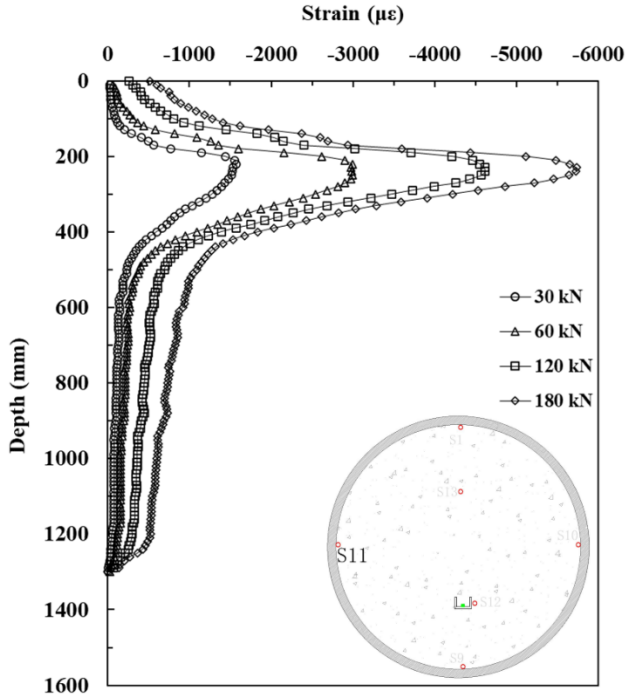
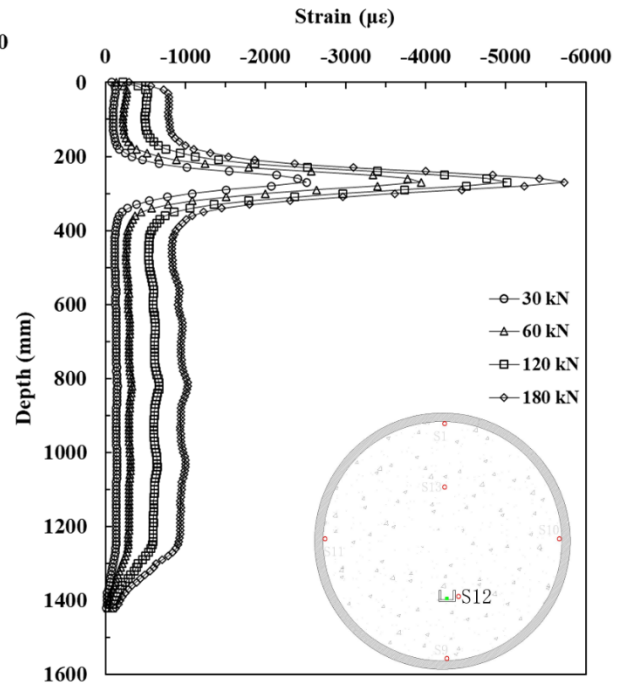


Figure 7.6 Pile 3 Overall integrated axial strain from measured results from OFDR and FBGs versus the overall strain results from LVDT

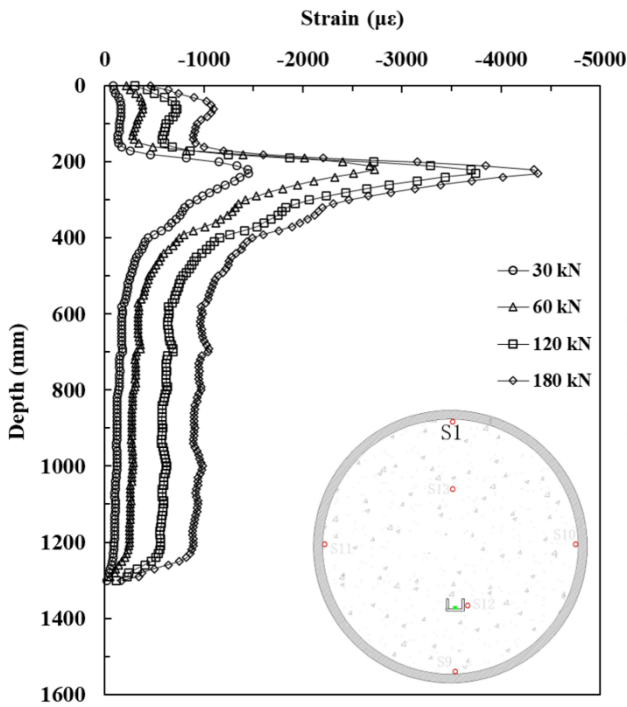
CHAPTER 7: DISTRIBUTED FIBER OPTIC SENSING FOR PILE MONITORING



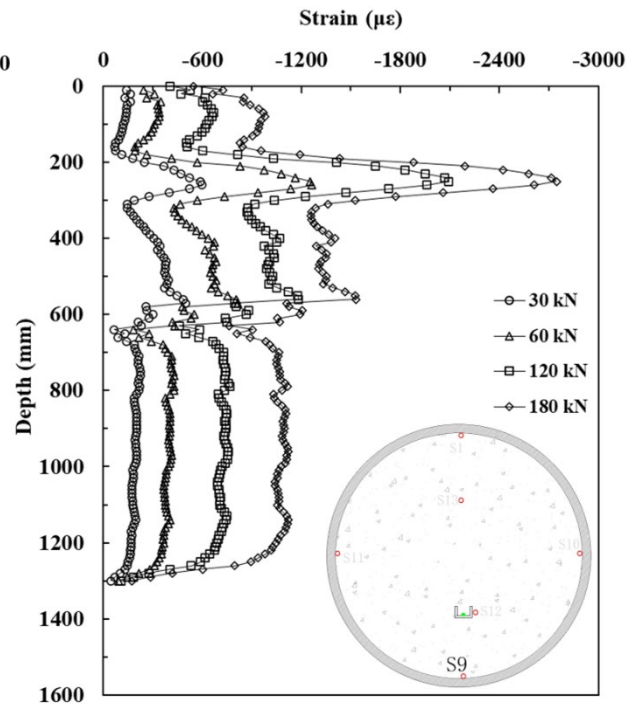
(a)



(b)



(c)



(d)

CHAPTER 7: DISTRIBUTED FIBER OPTIC SENSING FOR PILE MONITORING

Figure 7.7 Axial strain distribution of Pile 2 monitored with different OFDR fiber sections under different loading levels: (a) S1, (b) S9, (c) S11, and (d) S12

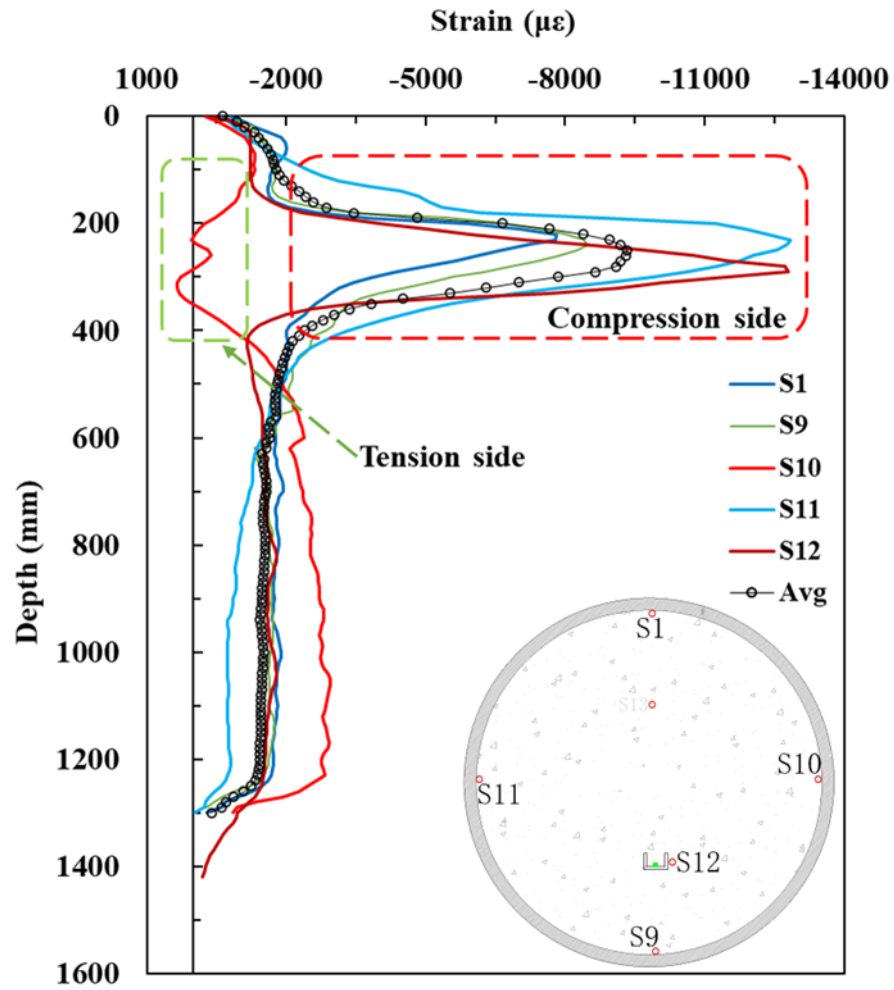
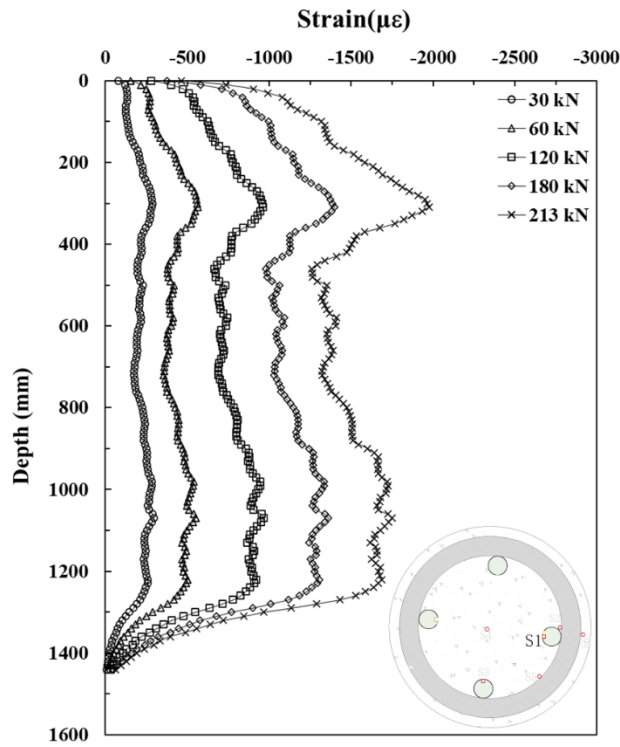


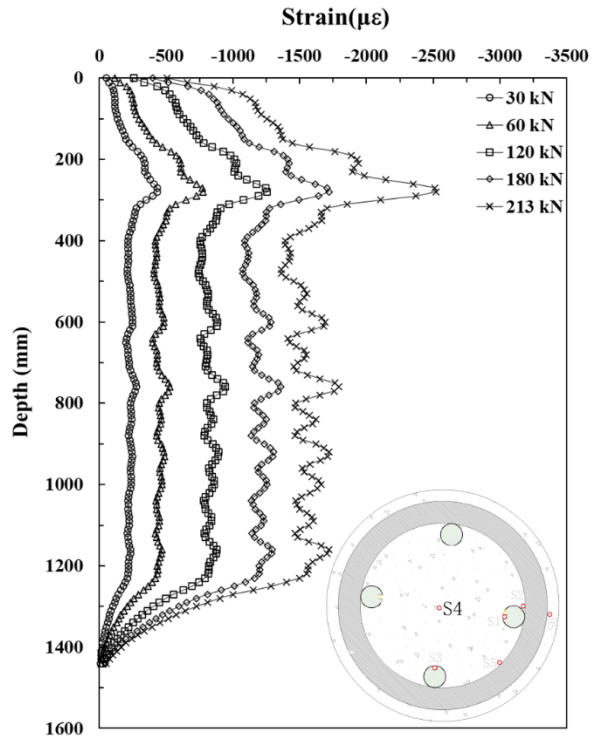
Figure 7.8 Axial strain profile of Pile 2 monitored with different fiber sections under peak load of

266 kN

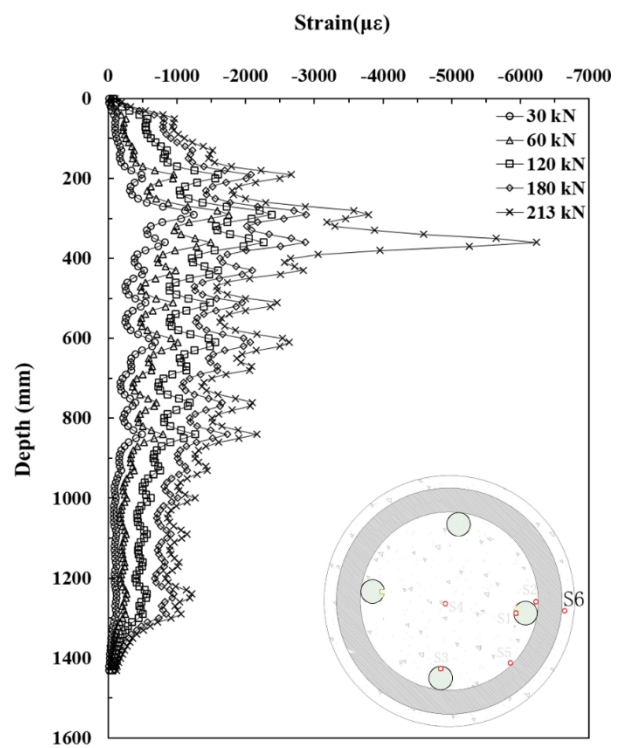
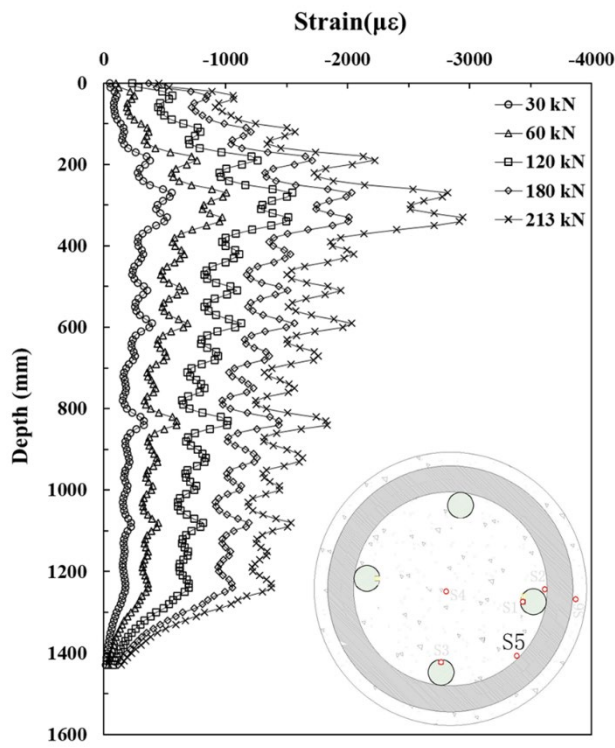
CHAPTER 7: DISTRIBUTED FIBER OPTIC SENSING FOR PILE MONITORING



(a)



(b)



(c)

(d)

Figure 7.9 Axial strain distribution of Pile I under different loading levels monitored with different OFDR fiber sections: (a) S1, (b) S4, (c) S5, and (d) S6

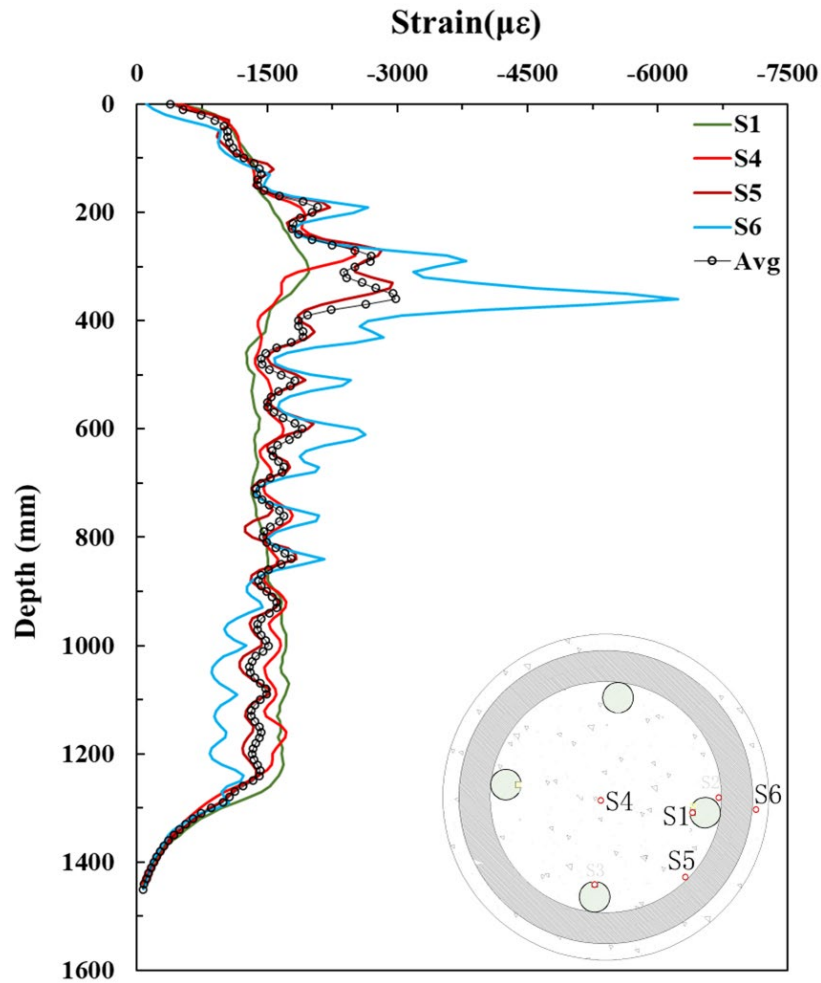
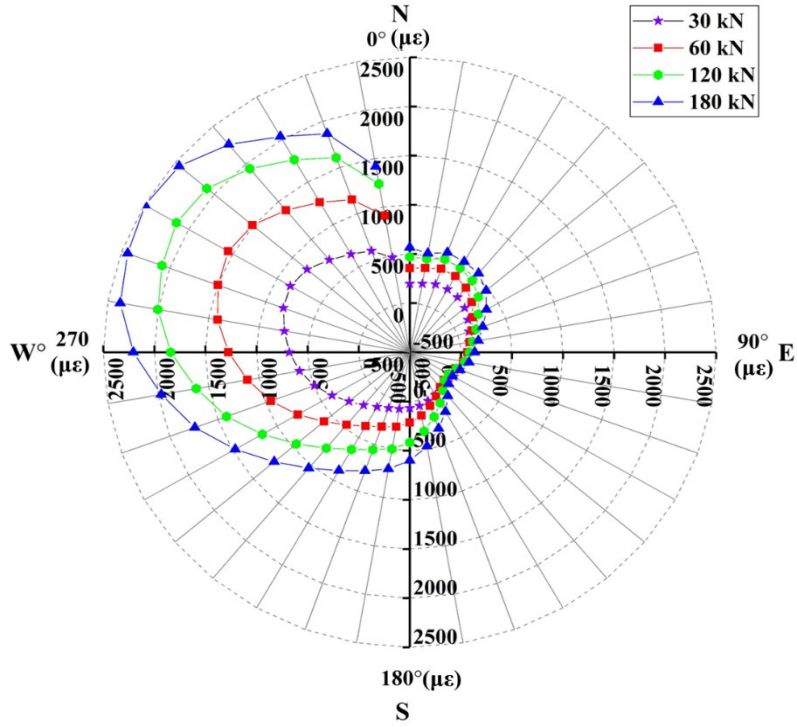
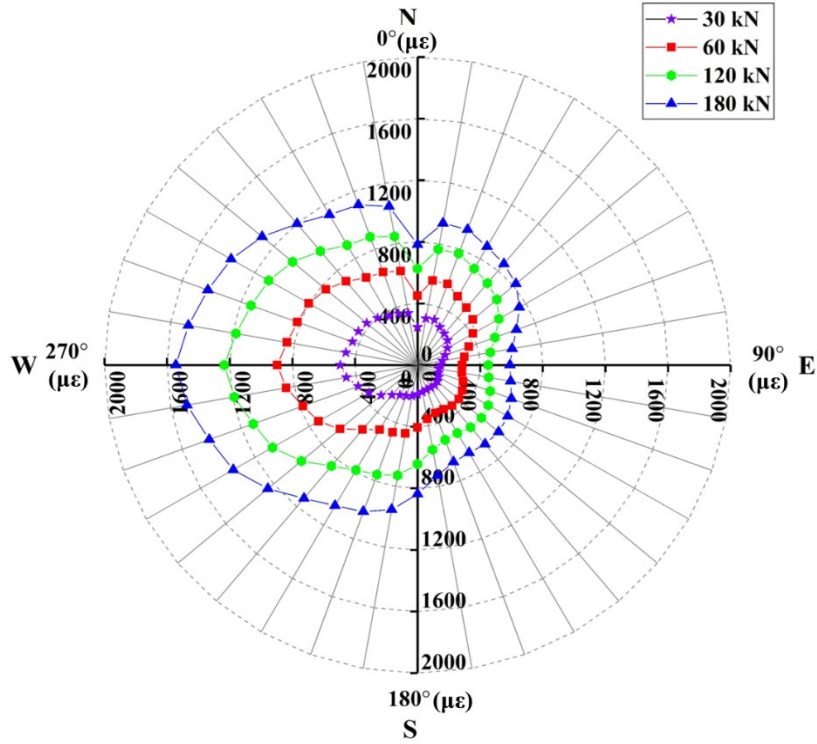


Figure 7.10 Axial strain profile of Pile 3 monitored with different fiber sections under peak load of 213 kN

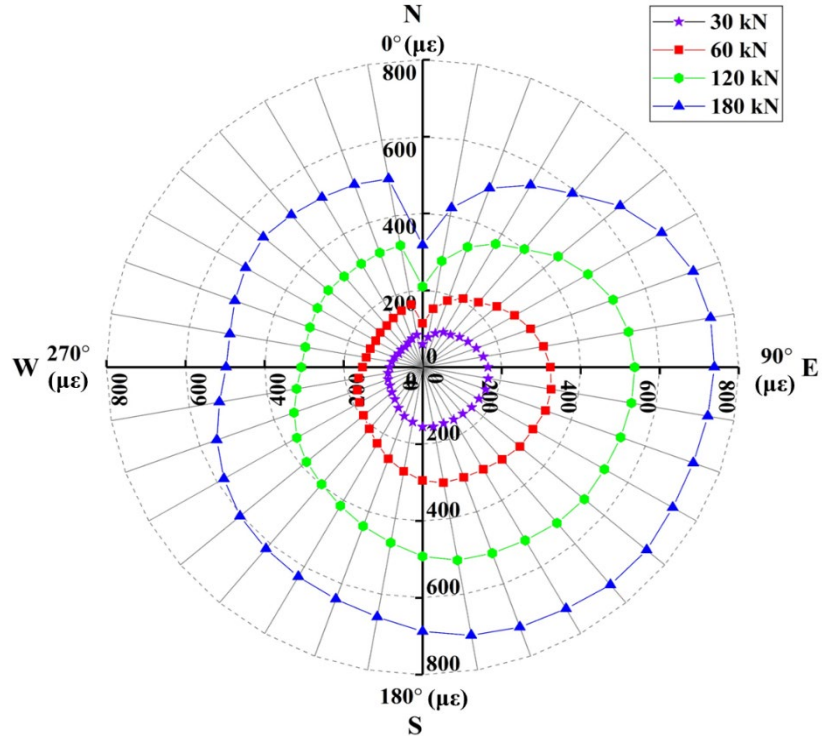
CHAPTER 7: DISTRIBUTED FIBER OPTIC SENSING FOR PILE MONITORING



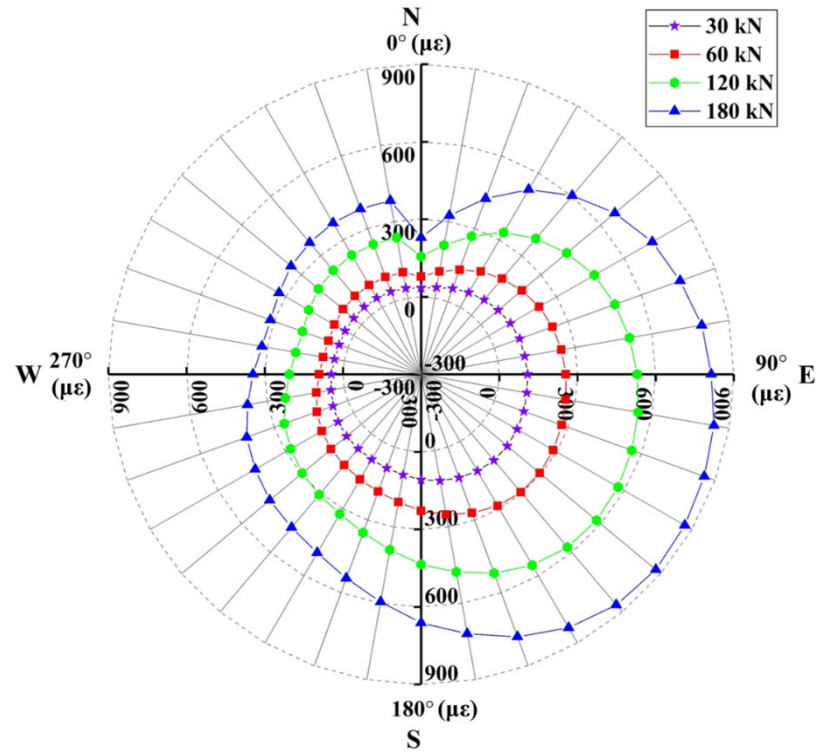
(a)



(b)

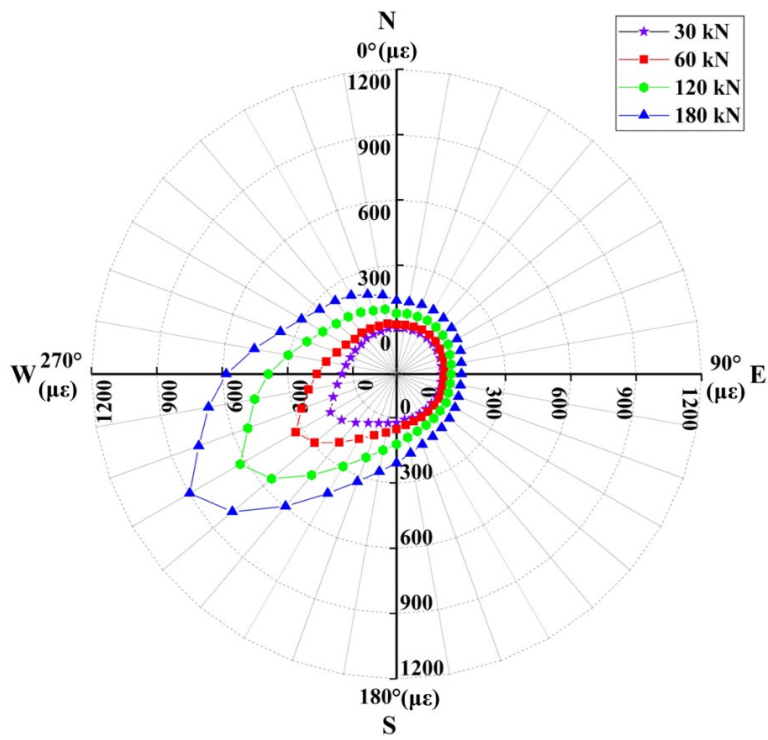


(c)

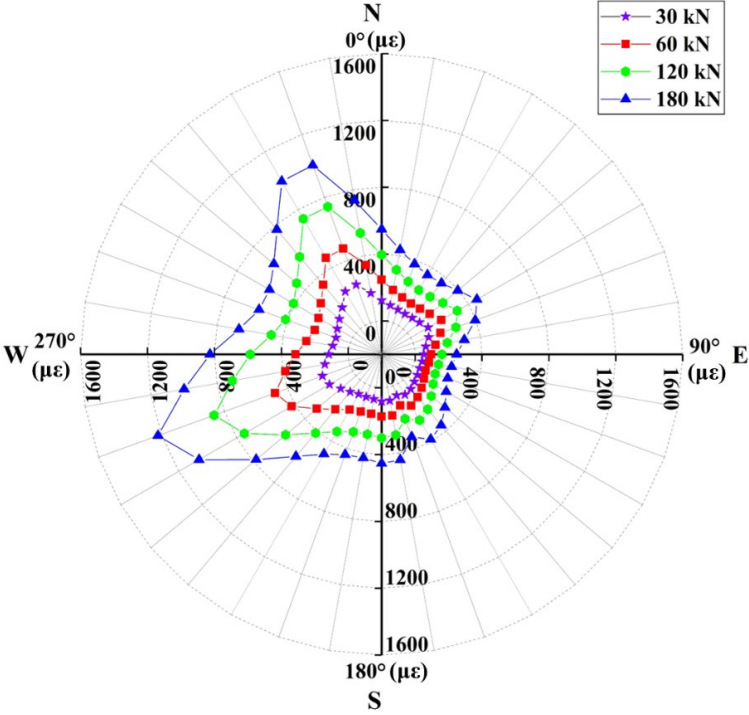


(d)

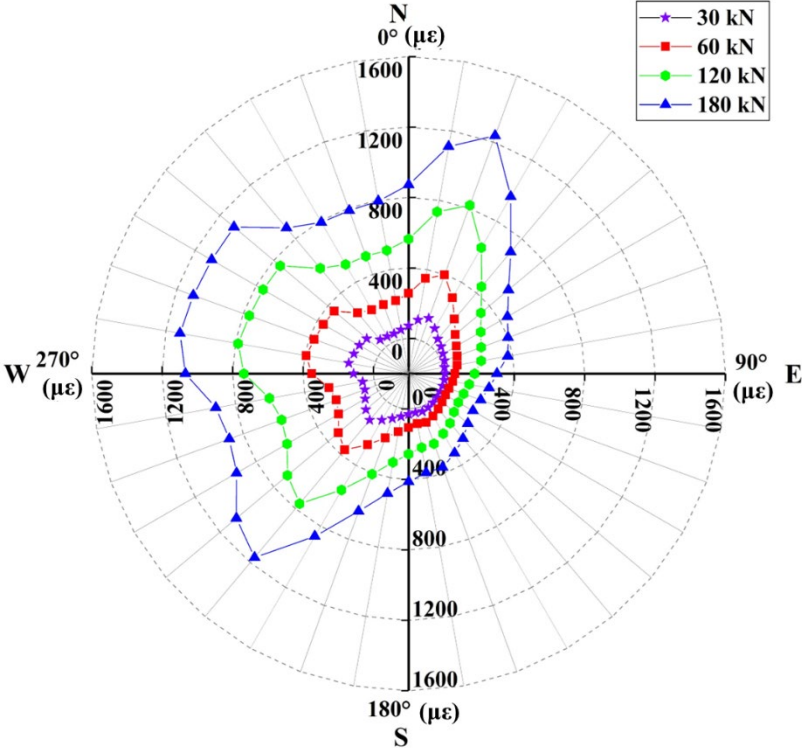
Figure 7.11 Circumferential strain distribution of Pile 2 monitored with different OFDR optic fibers at different loading levels; (a) S8; (b) S7; (c) S5; and (d) S2



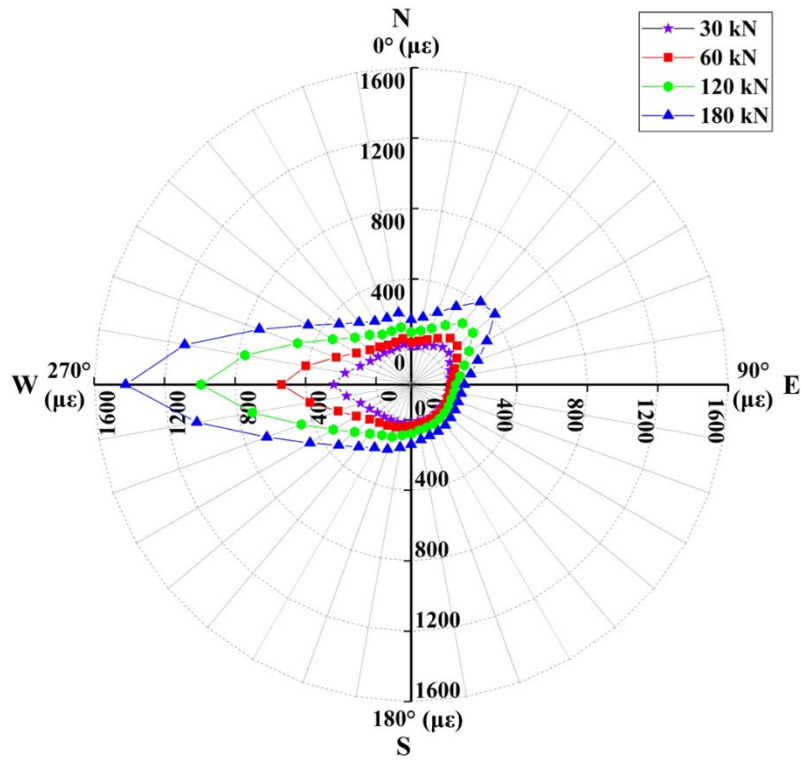
(a)



(b)



(c)



(d)

Figure 7.12 Circumferential strain distribution of Pile 3 monitored with different OFDR optic fibers at different loading levels; (a) S8; (b) S9; (c) S12; and (d) S14

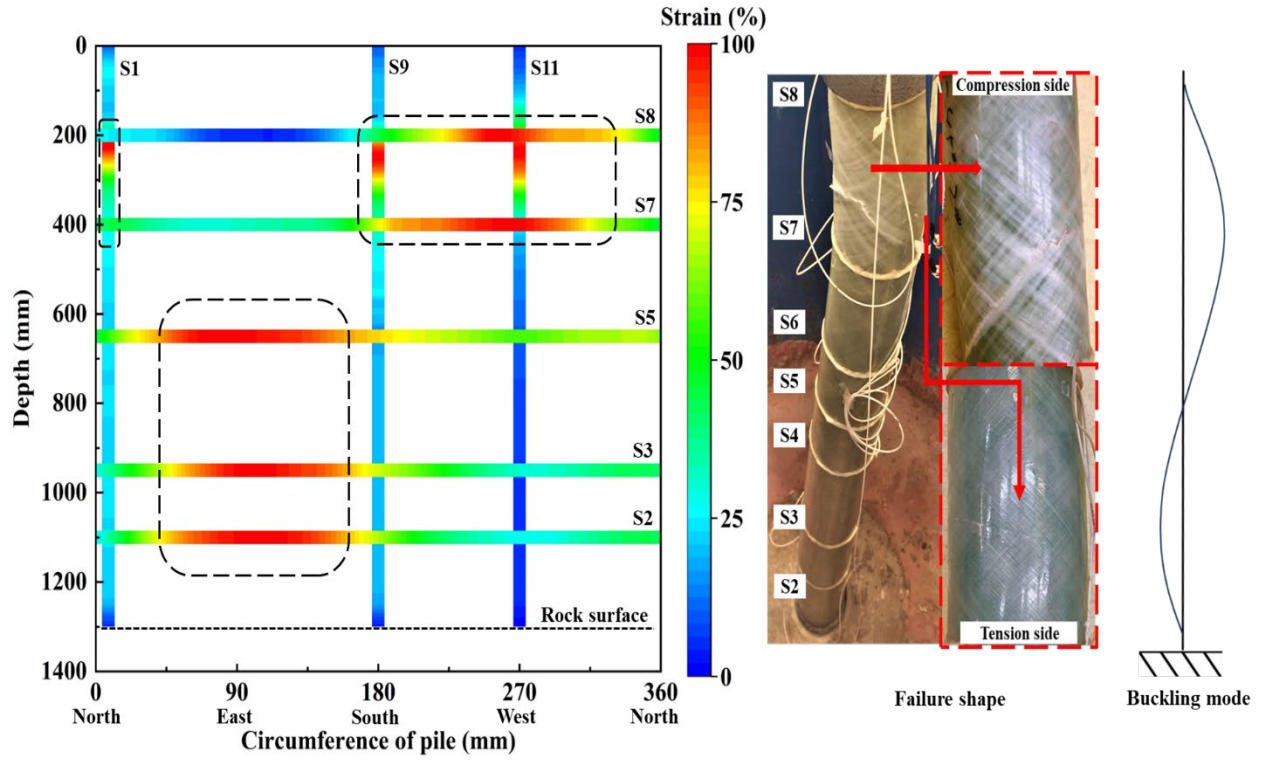


Figure 7.13 Comparison of axial and circumferential strain profiles of Pile 2 with final failure shape and buckling mode

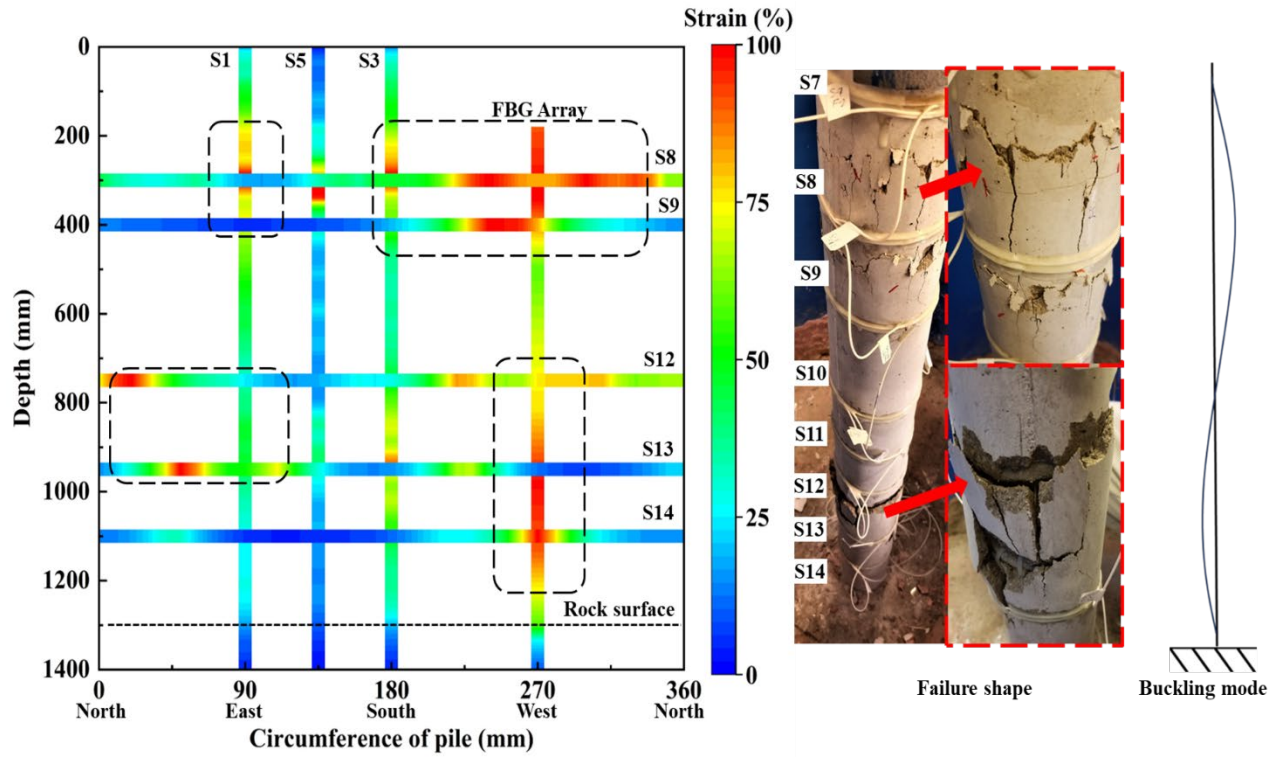


Figure 7.14 Comparison of axial and circumferential strain profiles of Pile 3 with final failure shape and buckling mode

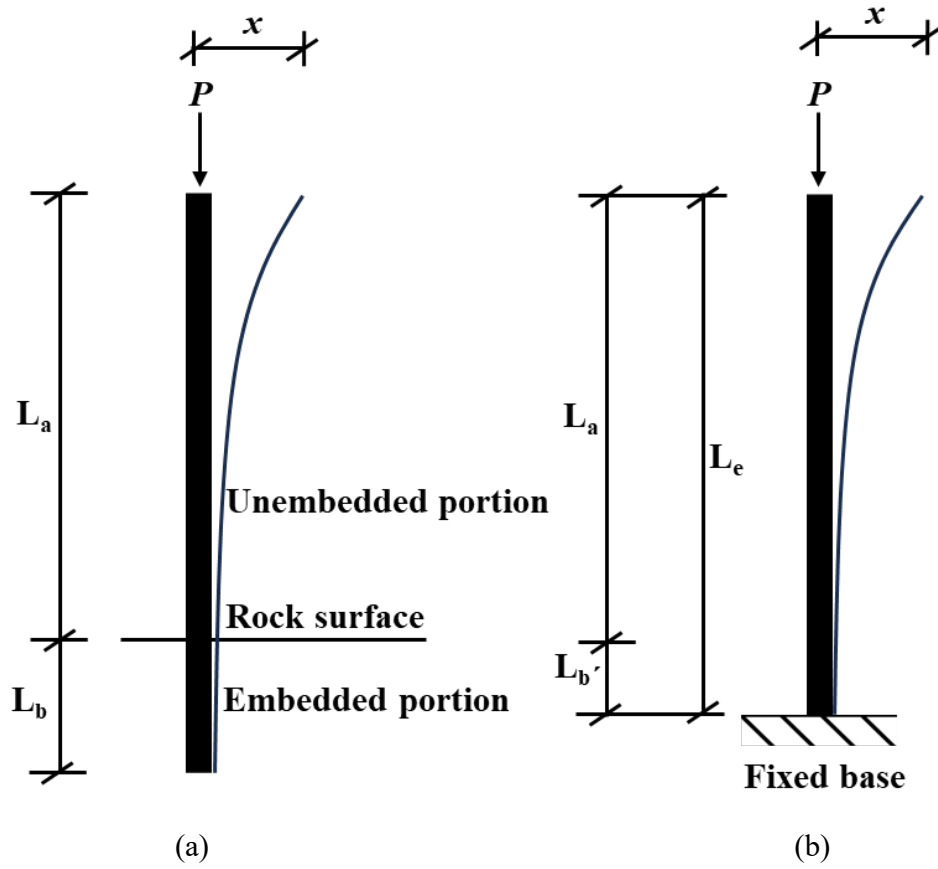


Figure 7.15 Partially embedded pile system: (a) actual pile, and (b) equivalent system based on (after Heelis et al., 2004)

CHAPTER 8: CONCLUSIONS AND RECOMMENDATIONS

8.1 Conclusions

This study conducted six physical model pile tests which provided valuable data that can be used to improve the design, construction, and performance of FRP-SSC piles in real field applications. The behavior of different model piles was investigated under a wide range of loading conditions, allowing for the identification of potential issues and optimization of the respective pile design. The results can be used to validate and improve numerical models used for predicting the behavior of FRP-SSC piles in real field applications. Compared to full-scale field tests, the physical model tests conducted are more cost-effective and conducted in a controlled laboratory environment, allowing for the simulation of various pile configurations, and loading conditions. More importantly, advanced optical sensing techniques (OFDR and FBG optic sensors) were employed to monitor the response of model piles, providing reliable results that were rare in previous studies. Both static and different cyclic loading conditions were employed and compared in all model tests. Hence, the results of our FRP-SSC physical model tests on rock-socketed piles have significant implications on respective pile design.

This study is also closely related to engineering practice, particularly focusing on rock-socketed piles, which are widely adopted in many regions including Hong Kong. The optimization of pile design is important for engineering projects. The data from experiments have provided the first systematic study on the performance of the FRP-SSC composite model piles installed in rock socket under static and axial cyclic loadings. The findings from this study are significant for

formulating a potential predictive method for estimating pile settlement and capacity, leading to better designs for rock-socketed piles in the future. Therefore, the results can be generalized considering the scale effects, test conditions, and parameters for the actual field conditions.

8.1.1 Axial cyclic stiffness of model piles

Pile foundations supporting high-rise buildings are generally subject to cyclic loading because of dynamic loading. In this study, a series of cyclic loading tests on the model piles made of fiber-reinforced polymer (FRP) and sea sand-seawater concrete (SSC) and ended in a rock socket were reported. The axial cyclic stiffness of piles under different modes of axial cyclic loading were analyzed and explored in detail in this study. The stiffness of a pile plays a crucial role in determining the load transfer mechanism and the distribution of stresses and strains along its length. Understanding and characterizing the stiffness behavior of piles is essential for various reasons. Firstly, the axial cyclic stiffness of driven piles serves as a significant indicator of pile stability. By analyzing the variation in axial cyclic stiffness, valuable insights can be gained regarding the performance and behavior of piles under cyclic loading conditions. Moreover, experimental results on pile stiffness provide important data that can be used to validate and enhance numerical models and theoretical predictions. By comparing model predictions with measured stiffness values, engineers can refine their models and improve the accuracy of future design calculations. This iterative process ultimately leads to more efficient and cost-effective foundation designs that are better suited to the specific site conditions and loading requirements.

CHAPTER 8: CONCLUSIONS AND RECOMMENDATIONS

The test results indicate that the FRP tube confined model pile showed higher confinement and cyclic capacity and lower stiffness degradation, leading to relatively more stable behavior. A high level of cyclic loading can cause micro-cracks to form and grow within the pile material, thereby decreasing the pile stiffness. The cyclic stiffness showed gains initially when cyclic load conditions were below a certain threshold level but degraded when loading was increased beyond it. The pile body gained cyclic stiffness when the maximum cyclic load level ($Q_{mean} + Q_{cyc}$) was below 30% of Q_{us} , and degradation was observed under higher load conditions. The stiffness of the pile body showed gains of up to 5% for the mentioned load levels, with the maximum stiffness observed on the FRP tube confined pile. The cyclic stiffness of the socket section increased linearly with the increase in cyclic load levels due to the high modulus and strength of the rock. Both Q_{mean} and Q_{cyc} levels influenced the deformation accumulation, with the maximum deformation accumulated within the pile body, around the threshold loading for the FRP tube confined pile.

8.1.2 Static axial behavior of model piles under static loading

FRP-SSC piles with a center FRP rebar exhibited the highest initial modulus in contrast to the piles with FRP tube or FRP stir-ups, while the former showed continuous strain softening and strain hardening for the latter ones with the increase of compression. The FRP tube confined pile showed higher ductility and capacity comparatively, suggesting the best solution for field applications in terms of mechanical performance. The predicted buckling load based on analytical solutions and actual buckling load from tests were in fair agreement with a minor discrepancy due to localized strains near the pile head. The OFDR sensors monitored the

distributed strain profiles with high spatial resolution providing load distribution of the entire pile, identifying any localized regions of weakness, strain concentrations, or pile shaft non-homogeneity with higher accuracy and hence overcoming the limitations of traditional monitoring techniques.

8.1.3 Strain profiles measured with OFDR and FBG optic sensors comparison

Fiber Bragg grating (FBG) optic sensors provide discrete strain information along the length of piles. Therefore, a novel fully distributed sensing technology named optical frequency domain reflectometry (OFDR) with a higher spatial resolution of 1 mm and a high sensing accuracy of $\pm 1 \mu\epsilon$ was used to monitor the fully distributed axial and circumferential strain profiles of piles.

The novel distributed sensing technique of distributed (OFDR) optic sensors is able to monitor the axial strain profiles along the FRP composite SSC piles, demonstrating good agreement with FBGs data and with LVDT calculated strain data. The axial strain profiles measured by different OFDR fiber sections at different positions of the cross section along the depth of the piles showed a similar trend for model piles. The axial strain distribution along the depth of piles showed a similar trend for the model piles, with higher strains recorded in the region $(0 - l_d/4)$ from the pile head. The failure of FRP tube confined and centered FRP rebar-reinforced SSC piles happened within this region near the pile head. However, the FRP rebar cage reinforced SSC pile showed the maximum compression in the same region near the pile head and rock surface. The distributed circumferential strain profiles provided reliable information of the localized strain concentrations around the pile circumference, showing early detection of pile shaft cracks, lateral deformation, and bending direction and position accurately. The axial and

circumferential strain profiles corresponded well with each other in terms of detecting the localized potential failures along the pile length and around its circumference.

8.1.4 Shaft friction mobilization in rock-socket

The axial strain profiles monitored with fiber optic sensors within rock-socket were utilized to develop load transfer curves to calculate reliable shaft friction values that may be used in future pile design of similar conditions. The maximum shaft friction was mobilized in the upper one-third region of the socket. Shaft resistance in rock socket increased with $(Q_{mean} + Q_{cyc})$. The pile-rock interface at the upper portion mobilized largely with more significant asperities breakage and an obvious increase in confinement from rock to pile due to the dilation effect of broken-out small particles. The magnitude changed less markedly with cycles in the lower section of the rock socket but increased with an increase in cycle number at the upper portion. Under static loading, the mean shaft friction mobilized early at smaller displacement with maximum up to 3.3 MPa and 4 MPa compared to end bearing pressure which mobilized at higher displacement with maximum up to 4.85 MPa and 5.5 MPa for Pile 3 and 2 respectively. The observed shaft friction values between the rock and pile shaft were higher compared to conventional designs showing underestimation of actual values. The maximum resistance was provided by the pile shaft compared to the base, accounting for approximately 80% of the total resistance. These findings are consistent with the field design approach proposed by Haberfield and Collingwood (2006) and with the field load tests results of drilled shaft foundations socketed into rock (Carter and Kulhawy, 1988).

8.1.5 Settlement response due to consolidation of HKMD

During multistage consolidation, the incremental increase in settlement in each stage of loading measured at the interface of upper and bottom HKMD layer is smaller than that of upper layer possibly due to the different consolidation characteristics of bottom layer. The pre-consolidation loading of bottom layer has influenced the compression index resulting in smaller settlements in each loading stage. The bottom and upper layer achieved a maximum settlement of 40 mm and 107 mm under 90 kPa loading respectively, showing 62% increase of the maximum settlement observed in the upper layer. The settlement curves from both the layer's floating settlement plates show similar trends proving their functionality and application to monitor the settlement at different heights in the soil. The classical consolidation theories might be validated with such instrumentation in the future.

8.2 Recommendations and future studies

8.2.1 Behavior of model piles under lateral loading

This thesis mainly focuses on the axial cyclic and static behavior of FRP-SSC model piles installed in rock socket surrounded by marine soils through a series of physical model tests. Different pile configurations were adopted for the model piles to investigate the stiffness variation, shaft friction mobilization and load transfer mechanism .

For further studies, it is necessary to perform additional experiments to investigate the effect of diverse cyclic loading parameters, and the impact of combined lateral and vertical loadings on model piles. Both lateral and axial cyclic loads should be independently applied to model piles to

isolate directional effects and response under different loadings. Additionally, experiments imposing combined lateral and axial cyclic loads by simulating more complex loading scenarios which will provide valuable insight into pile-soil interaction, deformation accumulation, and pile stiffness variations. Pile may experience large number of cycles and varied frequencies in the field conditions. It is recommended to conduct experiments with large number of cycles and different frequencies. This will help to provide design and analysis guidelines for future pile foundations supporting critical infrastructure subject to seismic or other cyclic loads.

8.2.2 NSF for FRP tube confined model pile

In this study, NSF development due to soft consolidating soils on FRP rebars reinforced SSC pile was investigated under different surcharge loadings. However, FRP tube confined pile is one of the commonly adopted configurations for composite piles. Hence, it is recommended to investigate the NSF development on the FRP tube confined pile in soft consolidating soils under different surcharge loadings. The emergence of machine learning methodologies in DFOSs has been driven by several important factors. First, state-of-the-art DFOS systems allow for continuous and long-range monitoring, generating massive amounts of data that are difficult and time consuming to analyze manually.

8.2.3 Machine learning methods for interpretation of OFDR distributed monitoring data

In recent years, machine learning has demonstrated considerable potential for advanced signal processing methods. This progress creates novel opportunities to apply machine learning

CHAPTER 8: CONCLUSIONS AND RECOMMENDATIONS

methods to effectively extract meaningful data from large volume of OFDR based monitored sensing data. The algorithms can be used to extract unusual events, strain concentrations, and temperature variations from continuous monitored data collected over long time from different civil infrastructures such as bridges, building, buried pipelines or retaining walls. Therefore, it is recommended to study and implement machine learning methods for interpretation of distributed sensing data.

List of notations and abbreviations

A_c	cross-sectional area of concrete
A_f	cross-sectional area of FRP rebars
c_1	strain coefficient
c_2	temperature coefficient
C_ε	strain coefficient
C_T	temperature coefficient
D	pile diameter
E_c	elastic modulus of concrete
E_f	elastic modulus of FRP rebar
E	young's modulus
E_t	tangent modulus
f	shaft resistance
f_{cm}	peak stress
ΔF	change in axial force
Δh	distance between the two sensing points
i	initial state
l_a	length of pile from pile head to rock surface
$k_{cyc,pb}$	cyclic stiffness of the pile body above the rock socket
N	number of cycles
n	scale factor

List of notations and abbreviations

Q_{cyc}	axial cyclic amplitude
Q_{max}	maximum cyclic load
Q_{mean}	mean axial cyclic load
Q_{min}	minimum cyclic load
Q_{us}	post cyclic compression capacity
ΔT	temperature change
UCS	unconfined compressive strength
$u_{cyc,pb}$	change in the compression of the pile body in the respective cycle
u_{pb}	pile body compression
z	depth below pile head
ε_c	axial strain
ε_{cm}	strain at peak stress
$\varepsilon(z)$	strain at depth below pile head
η	ratio of axial strain to strain at peak stress
σ_c	axial stress of concrete
$\Delta\sigma_c$	change in axial stress of concrete
$\Delta\sigma_f$	change in axial stress of FRP rebars
$\Delta\varepsilon$	strain change
Δv	Rayleigh spectrum
λ	reflected light wavelength
$\Delta\lambda$	change in wavelength

λ_i

initial wavelength

REFERENCES

REFERENCES

- ANDERSEN, K. (2013). Cyclic resistant geotechnical design and parameter selection for offshore engineering and other applications.(A. Puech, Ed.) In: TC 209 Workshop 18th ICSMGE: Desing for cyclic loading: Piles and other foundations, September, Paris. *Anais... Paris.*
- Bersan, S., Bergamo, O., Palmieri, L., Schenato, L., and Simonini, P. (2018). Distributed strain measurements in a CFA pile using high spatial resolution fibre optic sensors. *Engineering Structures, 160*, 554-565.
- Broms, B. B. (1988). Design and construction of anchored and strutted sheet pile walls in soft clay.
- Carter, J., and Kulhawy, F. H. (1988). *Analysis and design of drilled shaft foundations socketed into rock.*
- Chan, S.-F., and Hanna, T. H. (1980). Repeated loading on single piles in sand. *Journal of the Geotechnical Engineering Division, 106*(2), 171-188.
- Chen, Z., Chen, W.-B., Yin, J.-H., and Malik, N. (2021). Shaft Friction Characteristics of Two FRP Seawater Sea–Sand Concrete Piles in a Rock Socket with or without Debris. *International Journal of Geomechanics, 21*(7), 06021015.
- Code, C.-F. M. (1990). CEB-FIP model code for concrete structures, euro-international committee for concrete. *Bulletin*(213/214).
- Copsey, J., Hulme, T., Kraft, B., and Sripathy, P. (1989). Singapore mass rapid transit system: design. *Proceedings of the Institution of Civil Engineers, 86*(4), 667-707.

REFERENCES

- Davissou, M., and Robinson, K. (1965). Bending and buckling of partially embedded piles. *Soil Mech & Fdn Eng Conf Proc/Canada/*,
- De Battista, N., Kechavarzi, C., Seo, H., Soga, K., and Pennington, S. (2016). Distributed fibre optic sensors for measuring strain and temperature of cast-in-situ concrete test piles. *Transforming the Future of Infrastructure through Smarter Information: Proceedings of the International Conference on Smart Infrastructure and Construction*, 27–29 June 2016,
- Fam, A., Flisak, B., and Rizkalla, S. (2003). Experimental and analytical modeling of concrete-filled FRP tubes subjected to combined bending and axial loads. *ACI Struct. J*, 100(4), 499-509.
- Fardis, M. N., and Khalili, H. (1981). Concrete encased in fiberglass-reinforced plastic. *Journal Proceedings*,
- Feng, W. Q., and Yin, J. H. (2017). A new simplified Hypothesis B method for calculating consolidation settlements of double soil layers exhibiting creep. *International journal for numerical and analytical methods in geomechanics*, 41(6), 899-917.
- Fleming, K., Weltman, A., Randolph, M., and Elson, K. (2008). *Piling engineering*. CRC press.
- Haberfield, C., and Collingwood, B. (2006). Rock-socketed pile design and construction: a better way? *Proceedings of the Institution of Civil Engineers-Geotechnical Engineering*, 159(3), 207-217.
- Han, J., Frost, J. D., and Brown, V. L. (2003). Design of fiber-reinforced polymer composite piles under vertical and lateral loads. *Transportation research record*, 1849(1), 71-80.

REFERENCES

- Hauswirth, D., Puzrin, A. M., Carrera, A., Standing, J., and Wan, M. (2014). Use of fibre-optic sensors for simple assessment of ground surface displacements during tunnelling. *Géotechnique*, 64(10), 837-842.
- HAUSWIRTH, D., PUZRIN, A. M., CARRERA, A., STANDING, J. R., and WAN, M. S. P. (2014). Use of fibre-optic sensors for simple assessment of ground surface displacements during tunnelling. *Géotechnique*, 64(10), 837-842. <https://doi.org/10.1680/geot.14.T.009>
- Heelis, M., Pavlović, M., and West, R. (2004). The analytical prediction of the buckling loads of fully and partially embedded piles. *Géotechnique*, 54(6), 363-373.
- Hetényi, M., and Hetbenyi, M. I. (1946). *Beams on elastic foundation: theory with applications in the fields of civil and mechanical engineering* (Vol. 16). University of Michigan press Ann Arbor, MI.
- Hong, C.-Y., Zhang, Y.-F., and Liu, L.-Q. (2016). Application of distributed optical fiber sensor for monitoring the mechanical performance of a driven pile. *Measurement*, 88, 186-193.
- Hong, C., Wang, X., Han, K., Su, D., and Chen, Z. (2022). Performance investigation of 3D printed clay soil using fiber Bragg grating technology. *Acta Geotechnica*, 17(2), 453-462.
- Horvath, R., Kenney, T., and Kozicki, P. (1983). Methods of improving the performance of drilled piers in weak rock. *Canadian Geotechnical Journal*, 20(4), 758-772.
- Horvath, R. G., and Kenney, T. C. (1979). Shaft resistance of rock-socketed drilled piers. Symposium on Deep Foundations,
- Iskander, M. G., and Hassan, M. (1998). State of the practice review in FRP composite piling. *Journal of Composites for Construction*, 2(3), 116-120.
- Iskander, M. G., and Stachula, A. (2002). Wave equation analyses of fiber-reinforced polymer composite piling. *Journal of Composites for Construction*, 6(2), 88-96.

REFERENCES

- Iten, M., Puzrin, A. M., and Schmid, A. (2008a). Landslide monitoring using a road-embedded optical fiber sensor. *Smart Sensor Phenomena, Technology, Networks, and Systems 2008*,
- Iten, M., Puzrin, A. M., and Schmid, A. (2008b). Landslide monitoring using a road-embedded optical fiber sensor. *Smart Sensor Phenomena, Technology, Networks, and Systems 2008*,
- Jardine, R., Zhu, B., Foray, P., and Yang, Z. (2013). Interpretation of stress measurements made around closed-ended displacement piles in sand. *Géotechnique*, 63(8), 613-627.
- Jardine, R. J., Standing, J. R., and Chow, F. C. (2006). Some observations of the effects of time on the capacity of piles driven in sand. *Géotechnique*, 56(4), 227-244.
- Juran, I., and Komornik, U. (2006). *Behavior of fiber-reinforced polymer composite piles under vertical loads*.
- Kaderabek, T. J., and Reynolds, R. T. (1981). Miami limestone foundation design and construction. *Journal of the Geotechnical Engineering Division*, 107(7), 859-872.
- Khare, M. G., and Gandhi, S. R. (2001). Behavior of coated piles under dragload.
- Koutsoftas, D. C., Foott, R., and Handfelt, L. D. (1987). Geotechnical investigations offshore Hong Kong. *Journal of Geotechnical Engineering*, 113(2), 87-105.
- Krauss, P. D., and Nmai, C. K. (1996). Preliminary corrosion investigation of prestressed concrete piles in a marine environment: Deerfield beach fishing pier. *ASTM special technical publication*, 1276, 161-172.
- Kulhawy, F. H., and Phoon, K.-K. (1993). Drilled shaft side resistance in clay soil to rock. *Design and performance of deep foundations: Piles and piers in soil and soft rock*,
- Lau, A., and Hui, D. (2002). Strength and durability performance of concrete axially loaded members confined with AFRP composite sheets. *Compos. Part B*, 33, 263-277.

REFERENCES

- Le Kouby, A., Canou, J., and Dupla, J. (2004). Behaviour of model piles subjected to cyclic axial loading. *Cyclic behaviour of soils and liquefaction phenomena*, 159-166.
- Lee, C. J., and Ng, C. W. (2004). Development of downdrag on piles and pile groups in consolidating soil. *Journal of Geotechnical and Geoenvironmental Engineering*, 130(9), 905-914.
- Li, Y., Zhao, X., and Raman, R. S. (2018). Mechanical properties of seawater and sea sand concrete-filled FRP tubes in artificial seawater. *Construction and Building Materials*, 191, 977-993.
- Manceau, S., Klapper, J., Jardine, R., Hall, A., and Barbosa Moreira, P. (2021). The Field Behaviour of Drilled and grouted piles in rock. *Piling 2020: Proceedings of the Piling 2020 Conference*,
- Mandolini, A., Russo, G., and Viggiani, C. (2005). Pile foundations: Experimental investigations, analysis and design. *Proceedings of the international conference on soil mechanics and geotechnical engineering*,
- McVay, M., Townsend, F., and Williams, R. (1992). Design of socketed drilled shafts in limestone. *Journal of Geotechnical Engineering*, 118(10), 1626-1637.
- Mirmiran, A., and Shahawy, M. (1997). Behavior of concrete columns confined by fiber composites. *Journal of structural engineering*, 123(5), 583-590.
- Mirmiran, A., Shahawy, M., and Samaan, M. (1999). Strength and ductility of hybrid FRP-concrete beam-columns. *Journal of structural engineering*, 125(10), 1085-1093.
- Mohamad, H., and Tee, B. P. (2015). Instrumented pile load testing with distributed optical fibre strain sensor. *Jurnal Teknologi*, 77(11).

REFERENCES

- Mousa, S., Mohamed, H. M., and Benmokrane, B. (2018). Flexural Strength and Design Analysis of Circular Reinforced Concrete Members with Glass Fiber-Reinforced Polymer Bars and Spirals. *ACI Structural Journal*.
- Ng, C. W., Yau, T. L., Li, J. H., and Tang, W. H. (2001). Side resistance of large diameter bored piles socketed into decomposed rocks. *Journal of Geotechnical and Geoenvironmental Engineering*, 127(8), 642-657.
- Nolan, S., Rossini, M., Knight, C., and Nanni, A. (2021). New directions for reinforced concrete coastal structures. *Journal of Infrastructure Preservation and Resilience*, 2(1), 1-12.
- O'Neill, M., Townsend, F., Hassan, K., Buller, A., and Chan, P. (1996). *Load transfer for drilled shafts in intermediate geomaterials*.
- O'Neill, M. W., and Hassan, K. M. (1993). Perimeter load transfer in drilled shafts in the Eagle Ford formation. *Design and Performance of Deep Foundations: Piles and Piers in Soil and Soft Rock*,
- Pando, M. A., Ealy, C. D., Filz, G. M., Lesko, J., and Hoppe, E. (2006). *A laboratory and field study of composite piles for bridge substructures*.
- Park, J.-H., Jo, B.-W., Yoon, S.-J., and Park, S.-K. (2011). Experimental investigation on the structural behavior of concrete filled FRP tubes with/without steel re-bar. *KSCE Journal of Civil Engineering*, 15(2), 337-345.
- Pelecanos, L., Soga, K., Elshafie, M. Z., de Battista, N., Kechavarzi, C., Gue, C. Y., Ouyang, Y., and Seo, H.-J. (2018). Distributed fiber optic sensing of axially loaded bored piles. *Journal of Geotechnical and Geoenvironmental Engineering*, 144(3), 04017122.

REFERENCES

- Pitarresi, G., Scalici, T., Dellaira, M., and Catalanotti, G. (2019). A methodology for the rapid characterization of Mode II delamination fatigue threshold in FRP composites. *Engineering Fracture Mechanics*, 220, 106629.
- Prakash, S. (1987). Buckling loads of fully embedded vertical piles. *Computers and Geotechnics*, 4(2), 61-83.
- Reese, L. (1988). Drilled shafts: Construction procedures and design methods. *FHWA A Publication*, 88.
- Richart, F. E., Brandtzæg, A., and Brown, R. L. (1929). Failure of plain and spirally reinforced concrete in compression. *University of Illinois. Engineering Experiment Station. Bulletin; no. 190*.
- Rosenberg, P., and Journeaux, N. L. (1976). Friction and end bearing tests on bedrock for high capacity socket design. *Canadian Geotechnical Journal*, 13(3), 324-333.
- Rowe, R., and Armitage, H. (1987). A design method for drilled piers in soft rock. *Canadian Geotechnical Journal*, 24(1), 126-142.
- Saafi, M., Toutanji, H., and Li, Z. (1999). Behavior of concrete columns confined with fiber reinforced polymer tubes. *Materials Journal*, 96(4), 500-509.
- Sakr, M., Naggar, M. H. E., and Nehdi, M. (2004). Novel toe driving for thin-walled piles and performance of fiberglass-reinforced polymer (FRP) pile segments. *Canadian Geotechnical Journal*, 41(2), 313-325.
- Sargin, M., and Handa, V. (1969). A general formulation for the stress-strain properties of concrete. *SM Report Solid Mechanics Division, University of Waterloo, Canada*(3).
- Schenato, L. (2017). A review of distributed fibre optic sensors for geo-hydrological applications. *Applied Sciences*, 7(9), 896.

REFERENCES

- Schoeppner, G. A., and Abrate, S. (2000). Delamination threshold loads for low velocity impact on composite laminates. *Composites Part A: applied science and manufacturing*, 31(9), 903-915.
- Seidel, J., and Collingwood, B. (2001). A new socket roughness factor for prediction of rock socket shaft resistance. *Canadian Geotechnical Journal*, 38(1), 138-153.
- Sen, R., and Mullins, G. (2007). Application of FRP composites for underwater piles repair. *Composites Part B: Engineering*, 38(5-6), 751-758.
- Shaia, H. (2013). *Behaviour of Fibre Reinforced Polymer Composite Piles: Experimental and Numerical Study*. The University of Manchester (United Kingdom).
- SharnoubyM.M., E., and NaggarM.H., E. (2012). Axial monotonic and cyclic performance of fibre-reinforced polymer (FRP) – steel fibre–reinforced helical pulldown micropiles (FRP-RHPM). *Canadian Geotechnical Journal*, 49(12), 1378-1392. <https://doi.org/10.1139/cgj-2012-0009>
- Soga, K. (2014a). Understanding the real performance of geotechnical structures using an innovative fibre optic distributed strain measurement technology. *Riv. Ital. Geotech*, 4, 7-48.
- Soga, K. (2014b). Understanding the real performance of geotechnical structures using an innovative fibre optic distributed strain measurement technology. *Rivista Italiana di Geotechnica*, 4, 7-48.
- Sze, J. W. (2015). Deep Foundations for High-Rise Buildings in Hong Kong. *International Journal of High-Rise Buildings*, 4(4), 261-270.

REFERENCES

- Toh, C., Ooi, T., Chiu, H., Chee, S., and Ting, W. (1989). Design parameters for bored piles in a weathered sedimentary formation. *Congrès international de mécanique des sols et des travaux de fondations*, 12,
- Tomblin, J., and Barbero, E. (1994). Local buckling experiments on FRP columns. *Thin-Walled Structures*, 18(2), 97-116.
- Wilkinson, T. L. (1968). *Strength evaluation of round timber piles* (Vol. 101). Forest Products Laboratory.
- Williams, A., and Pells, P. (1981). Side resistance rock sockets in sandstone, mudstone, and shale. *Canadian Geotechnical Journal*, 18(4), 502-513.
- Wu, J., Liu, H., Yang, P., Tang, B., and Wei, G. (2020). Quantitative strain measurement and crack opening estimate in concrete structures based on OFDR technology. *Optical Fiber Technology*, 60, 102354.
- Wu, P.-C., Chen, W.-B., Yin, J.-H., Pan, Y., Lou, K., and Feng, W.-Q. (2022). A Novel Sensor for Undrained Shear Strength Measurement in Very Soft to Soft Marine Sediments Based on Optical Frequency Domain Reflectometry Technology. *Sensors*, 22(15), 5530.
- Wu, P.-C., Tan, D.-Y., Chen, W.-B., Malik, N., and Yin, J.-H. (2021). Novel fiber Bragg Grating-based strain gauges for monitoring dynamic responses of *Celtis sinensis* under typhoon conditions. *Measurement*, 172, 108966.
- Wu, P. (2021). Physical and numerical modelling study of Hong Kong marine deposits improved by reinforcements and vertical drains.
- Wu, P., Guo, Y., Zhu, D., Jin, W., Zhang, Z., and Liang, R. (2020). Flexural performances of prestressed high strength concrete piles reinforced with hybrid GFRP and steel bars. *Marine Georesources & Geotechnology*, 38(5), 518-526.

REFERENCES

- Wu, P., Tan, D., Lin, S., Chen, W., Yin, J., Malik, N., and Li, A. (2022). Development of a monitoring and warning system based on optical fiber sensing technology for masonry retaining walls and trees. *Journal of Rock Mechanics and Geotechnical Engineering*, 14(4), 1064-1076.
- Xiao, J., Qiang, C., Nanni, A., and Zhang, K. (2017). Use of sea-sand and seawater in concrete construction: Current status and future opportunities. *Construction and Building Materials*, 155, 1101-1111.
- Xiao, Y., Stuedlein, A. W., Pan, Z., Liu, H., Matthew Evans, T., He, X., Lin, H., Chu, J., and Van Paassen, L. A. (2020). Toe-bearing capacity of precast concrete piles through biogrouting improvement. *Journal of Geotechnical and Geoenvironmental Engineering*, 146(12), 06020026.
- Yin, J.-H., and Graham, J. (1994). Equivalent times and one-dimensional elastic viscoplastic modelling of time-dependent stress–strain behaviour of clays. *Canadian Geotechnical Journal*, 31(1), 42-52.
- Yin, J.-H., and Graham, J. (1999). Elastic viscoplastic modelling of the time-dependent stress-strain behaviour of soils. *Canadian Geotechnical Journal*, 36(4), 736-745.
- Yin, J.-H., Zhu, J.-G., and Graham, J. (2002). A new elastic viscoplastic model for time-dependent behaviour of normally and overconsolidated clays: theory and verification. *Canadian Geotechnical Journal*, 39(1), 157-173.
- Zhan, C., and Yin, J.-H. (2000). Field static load tests on drilled shaft founded on or socketed into rock. *Canadian Geotechnical Journal*, 37(6), 1283-1294.

- Zhang, B.-j., Huang, B., Mei, C., Fu, X.-d., Luo, G., and Yang, Z.-j. (2016). Dynamic behaviours of a single soft rock-socketed shaft subjected to axial cyclic loading. *Advances in Materials Science and Engineering*, 2016.
- Zhang, D., Shi, B., Sun, Y., Tong, H., and Wang, G. (2015a). Bank slope monitoring with integrated fiber optical sensing technology in Three Gorges Reservoir Area. In *Engineering Geology for Society and Territory-Volume 2* (pp. 135-138). Springer.
- Zhang, D., Shi, B., Sun, Y., Tong, H., and Wang, G. (2015b). Bank slope monitoring with integrated fiber optical sensing technology in Three Gorges Reservoir Area. *Engineering Geology for Society and Territory-Volume 2: Landslide Processes*,
- Zheng, X., Shi, B., Zhu, H.-H., Zhang, C.-C., Wang, X., and Sun, M.-Y. (2021). Performance monitoring of offshore PHC pipe pile using BOFDA-based distributed fiber optic sensing system. *Geomechanics and Engineering*, 24(4), 337-348.
- Zyka, K., and Mohajerani, A. (2016). Composite piles: A review. *Construction and Building Materials*, 107, 394-410.